

Effects of Boria on Environmental Barrier Coating Systems

A

Dissertation

Presented to
the faculty of the School of Engineering and Applied Science
University of Virginia

in partial fulfillment
of the requirements for the degree

Doctor of Philosophy

by

Rachel Guarriello

August 2021

APPROVAL SHEET

This
Dissertation
is submitted in partial fulfillment of the requirements
for the degree of
Doctor of Philosophy

Author: Rachel Guarriello

This Dissertation has been read and approved by the examining committee:

Advisor: Elizabeth Opila

Advisor:

Committee Member: Chris Benmore

Committee Member: Andres Clarens

Committee Member: Jon Ihlefeld

Committee Member: Bicheng Zhou

Committee Member:

Committee Member:

Accepted for the School of Engineering and Applied Science:

A handwritten signature in black ink, appearing to read 'CHB', is written over a faint, light gray signature line.

Craig H. Benson, School of Engineering and Applied Science

August 2021

Acknowledgements

This work was funded by Rolls-Royce. I would like to thank my program manager from Rolls-Royce, Dr. Adam Chamberlain. I would also like to thank Dr. James Keiser at The Oak Ridge National Laboratory for the testing conducted in the Keiser Rig.

I would like to thank my adviser, Dr. Elizabeth Opila for the opportunity to conduct this research and for her support throughout the PhD process.

A huge thank-you to the other members of the Opila High Temperature Materials Research Group, both past and present for all the support, discussion and help throughout my time at UVA. A special thank-you to undergraduate students Rachel MacNamara and Dominic Pinnisi for their assistance with programming and image analysis. Also thank you to my other coworkers, friends and roommates who have always been there to support me.

Finally, I would like to thank my family- my mother Beth, father Henry, and my siblings Marissa and David for their love and unwavering support throughout my graduate school journey. I could not have gotten this far without them.

Contents

Acknowledgements.....	1
List of Figures	5
List of Tables	12
1 Introduction.....	13
1.1 CMC/ EBC System Overview	13
1.2 Project Objectives	20
1.3 References.....	22
2 Idealized Interfacial Reactions between B_2O_3 and Yb-Silicates.....	25
2.1 Introduction.....	25
2.2 Materials & Experimental Setup	27
2.3 Results	31
2.3.1 $Yb_2Si_2O_7$ Substrates	31
2.3.2 Yb_2SiO_5 & Yb_2O_3 Substrates	41
2.4 Discussion.....	47
2.5 Summary and Conclusions	50
2.6 References.....	51
3 Phase Diagram Determination for the $Yb_2O_3 - B_2O_3$ and $Yb_2O_3 - SiO_2 - B_2O_3$ systems.....	53
3.1 Introduction.....	53
3.1.1 Computational Predictions for the $Yb_2O_3 - SiO_2 - B_2O_3$ System	56
3.1.2 Phase Equilibria Testing Methods.....	57
3.2 Experimental Methods.....	58
3.2.1 Materials and Sample Preparation Methods.....	60
3.2.2 Differential Scanning Calorimetry.....	61
3.2.3 High Energy X-ray Diffraction.....	61
3.3 Results	63
3.3.1 Binary Phase Studies	63
3.3.2 Ternary Phase Studies.....	65
3.4 Discussion.....	71
3.4.1 Binary Compositions	71
3.4.2 Ternary Compositions	72

3.5	Conclusions.....	77
3.6	References.....	78
4	Thermal and Physical Properties of YbBO ₃	80
4.1	Introduction.....	80
4.2	Experimental Procedures	83
4.2.1	DSC and Pt encapsulation	83
4.2.2	Bulk Borate Tests- CTE & Physical Properties	85
4.3	Results	87
4.3.1	DSC	87
4.3.2	Hot Stage Lattice Parameter and CTE Results	89
4.3.3	Static Equilibrium Testing	92
4.3.4	Solid YbBO ₃ Samples	94
4.4	Discussion	98
4.5	Conclusions.....	101
4.5.1	Future Work	103
4.6	References.....	104
5	Effects of Boria on the Si Bond Coat Oxidation and Yb ₂ Si ₂ O ₇ EBCs.....	106
5.1	Introduction.....	106
5.2	Experimental Procedure.....	110
5.2.1	Materials and Test Matrix.....	110
5.2.2	Sample Testing and Characterization	111
5.3	Results	117
5.3.1	RBSiC and CMC Oxidation: TGA Data.....	117
5.3.2	Complexities in Experimental Setup	123
5.3.3	RBSiC and CMC Oxidation: Benchtop Weight Changes	124
5.3.4	Dragonfly Segmentation and TGO Morphology	127
5.3.5	TGA & Keiser Rig Exposure Comparison	133
5.3.6	B Effects on Yb ₂ Si ₂ O ₇ EBC.....	136
5.4	Discussion	138
5.4.1	Oxidation Kinetics and Experimental Discrepancies.....	138
5.4.2	Dragonfly Application to TGO analysis	140
5.5	Conclusions.....	143
5.5.1	Suggested Future Work	145

5.6	References.....	146
6	Summary and Conclusions	148
6.1	Objectives and Summary	148
6.2	Impact.....	153
6.3	Suggestions for Future Work	154
7	Appendix A: DSC Data.....	155
7.1	Baseline DSC Scans.....	155
7.2	Binary Composition DSC Scans.....	158
7.3	Ternary Composition DSC Scans	163
8	Appendix B: Beamline Scans.....	174
8.1	Binary Composition Scans.....	174
8.2	Ternary Composition Scans.....	179
9	Appendix C: Dragonfly Segmentations for TGA & Keiser Rig Exposed Samples	200
9.1	900°C Exposures, 100h, 1 atm O ₂	200
9.2	1050°C Exposures, 100h 1 atm O ₂	204
9.3	1200°C Exposures, 100h 1 atm O ₂	208

List of Figures

Figure 1.1: Cross section micrograph of a SiC/BN/SiC CMC showing the SiC fibers surrounded by the BN interphase in the Si/SiC matrix. (Image courtesy of Rolls-Royce)	14
Figure 1.2 (Left) SiO_2 - B_2O_3 system phase diagram from Rockett & Foster. (Right) Structural image of SiO_2 - B_2O_3 glass with Na ions (yellow) showing how the B_2O_3 triangles (green) lower connectivity of the glass network from pure SiO_2 tetrahedra (blue). (21,22)	15
Figure 1.3 Yb_2O_3 - SiO_2 system phase diagram from Toropov (26)	16
Figure 1.4: (Left) YbBO_3 – B_2O_3 system phase diagram from Levin (27,29,35) (Right) CaCO_3 Vaterite crystal structure showing different possible configurations of the CO_3 triangles within a unit cell, analogous to BO_3 in YbBO_3 (36). ..	17
Figure 1.5: Dendritic structures (Left) and spinodal decomposition (Right) observed in $\text{Yb}_2\text{Si}_2\text{O}_7$ EBCs after exposure at 1150°C for 100h in a 12atm combustion environment. [Images from Rolls-Royce Statement of Work for this research program]	20
Figure 2.2.1: A backscatter electron micrograph showing the initial morphology and splat structure in a polished cross section of dense APS $\text{Yb}_2\text{Si}_2\text{O}_7$ coatings provided by Rolls-Royce (1) $\text{Yb}_2\text{Si}_2\text{O}_7$ splats are the darkest grey, Yb_2SiO_5 the medium grey, and Yb_2O_3 the lightest grey.	26
Figure 2.2: Well test setup schematic showing dimensions of SPS substrate, drilled hole and boria plug.	29
Figure 2.3 Plan-view SEM image of $\text{Yb}_2\text{Si}_2\text{O}_7$ sample after exposure to B_2O_3 for 24 h at 1000°C	31
Figure 2.4 Plan-view SEM back-scattered image of dendrites in a surface “pool” of glass after $\text{Yb}_2\text{Si}_2\text{O}_7$ exposure to B_2O_3 at 1000°C for 24 hours. The high contrast from the backscattered electron image suggests that the dendrites are Yb-rich.	32
Figure 2.5 Plan-view BSE SEM images of $\text{Yb}_2\text{Si}_2\text{O}_7$ well surface after 24 h exposure to B_2O_3 at 800° , 1000° , and 1200°C , and post-soak in 80°C DI H_2O for 48 hours. More glass remains on the surface with increasing exposure temperature, indicating that the glass becomes more silica rich.	33
Figure 2.6: Plan-view BSE SEM images of $\text{Yb}_2\text{Si}_2\text{O}_7$ well surface after 3, 8, and 24 h exposure to B_2O_3 at 1000°C , post-soak in 90°C DI H_2O for 48 hours. More glass remains on the surface with increasing exposure time, indicating that the glass becomes more silica rich.	33
Figure 2.7: (Left) Plan-view SEM BSE imaging shows charging glass and exposed ring of substrate surrounding the drilled well following 24h $\text{Yb}_2\text{Si}_2\text{O}_7$ furnace exposure to B_2O_3 at 1000°C and removal of soluble glass via water soaking. (Right) Higher magnification imaging of the exposed surface shows pores inside the grains.	34
Figure 2.8: Micro-XRD data taken from the surface of $\text{Yb}_2\text{Si}_2\text{O}_7$ + B_2O_3 after exposure for 24 h at 1000°C and post-soak in 80°C DI water for 48 hours.	34
Figure 2.9: Silicon to boron ratio (Si: B) as a function of time and temperature from ICP-OES analysis of water-soluble glasses/reaction products dissolved from $\text{Yb}_2\text{Si}_2\text{O}_7$ sample surfaces after exposure to B_2O_3 . Note the error bars for the data at 800 and 1000°C are smaller than the symbols.	36
Figure 2.10: Diagram of a cross-sectioned well test sample (not soaked in DI H_2O) showing well, residual glass, and reaction layers penetrating the cracks remaining from SPS processing.	37

Figure 2.11 Cross-section BSE SEM image showing the YbBO_3 reaction layers (B_2O_3 exposure, 1000°C, 24 hours) along the edge of the $\text{Yb}_2\text{Si}_2\text{O}_7$ well (Top right) and in processing cracks leading away from the well. Reaction layers show a columnar structure at the interface with porous clusters of glass overtop in the well. Glass has filled the processing cracks leading away from the well.	37
Figure 2.12: 1000°C, 24-hour Exposure. Higher magnification cross-section BSE SEM image of a glass-filled crack. Elemental mapping shows that remaining glass is silicon-rich and that reaction layers are depleted in silicon and enriched in boron.	38
Figure 2.13 (Left) 1000°C, 24h $\text{Yb}_2\text{Si}_2\text{O}_7$ – B_2O_3 sample exposure. FIB Section taken across the glass-filled branching crack/ reaction layer interface. (Right) Higher magnification micrograph highlighting the area in which SAED was conducted.	39
Figure 2.14: TEM SAED patterns of a reaction layer from $\text{Yb}_2\text{Si}_2\text{O}_7$ sample exposed to B_2O_3 at 1000°C for 24 hours. (a&c) The pattern obtained from boxed area in Figure 2.13 (Right) of the reaction layer adjacent to the glass-filled branching cracks. (b&d) Simulated patterns of hexagonal YbBO_3 . (Top) $\langle 0001 \rangle$ zone axis. (Bottom) $\langle 2243 \rangle$ zone axis. (9–11).....	40
Figure 2.15: Comparison of $\text{Yb}_2\text{Si}_2\text{O}_7$, Yb_2SiO_5 , and Yb_2O_3 (Left-Right) substrates in plan view pre-soak showing the well and the ring of boria-rich glass surrounding it after exposure at 1000°C for 24 hours in the stagnant air box furnace.....	41
Figure 2.16: Comparison of outer edges of wells in plan view post-soak of the $\text{Yb}_2\text{Si}_2\text{O}_7$, Yb_2SiO_5 , and Yb_2O_3 substrates (Left – Right) show the reaction layers and exposed substrate rings after the water-soluble products were removed. No glass remains on the surface of the Yb_2O_3 substrate due to a lack of silica in the system.	42
Figure 2.17: Close ups of the well test top surfaces (L: Yb_2SiO_5 , R: Yb_2O_3) post-soak in 80°C DI H_2O for 48 hours showing a small, granulated grain structure with residual borate & glassy phases.	42
Figure 2.18: Amount of material measured in ICP for two Yb_2SiO_5 substrates exposed at each 8h and 24h with B_2O_3 at 1000°C. Linear fits shown to guide the eyes.	43
Figure 2.19: Amount of material measured in ICP for two Yb_2O_3 substrates exposed at each 8h and 24h with B_2O_3 at 1000°C. Linear fits shown to guide the eyes.	44
Figure 2.20: Reaction layers in cracks for Yb_2SiO_5 substrate exposed to B_2O_3 at 1000°C for 24 hours with EDS maps showing depletion of silica from reaction layers and into the glass-filled crack.	45
Figure 2.21: Micro-focus XRD results showing presence of YbBO_3 phase in the Yb_2SiO_5 reaction layers after substrate was exposed to B_2O_3 for 24h at 1000°C.	45
Figure 2.22: Yb_2O_3 substrate in cross section showing reaction layer with EDS after 24h to B_2O_3 at 1000°C.	46
Figure 2.23: Micro-focus XRD results showing presence of YbBO_3 phase in the Yb_2O_3 reaction layers after substrate exposure to B_2O_3 for 24h at 1000°C.	46
Figure 2.24: FactSage Simulation of $\log(\text{activity})$ vs. temperature for B_2O_3 in O_2	48
Figure 3.1: (Left) SiO_2 – B_2O_3 phase diagram from Rockett & Foster (1). (Right) Yb_2O_3 – SiO_2 phase diagram from Toropov & Bondar (2). Diagrams # 2353, 2391 from ACERS-NIST database (29).....	53
Figure 3.2: Boria rich half of the Yb_2O_3 – B_2O_3 system phase diagram from Levin (7).....	54

Figure 3.3 $\text{La}_2\text{O}_3 - \text{B}_2\text{O}_3$ phase diagram from Dmitruk (9)	55
Figure 3.4: (Left) ball and stick model of vaterite showing the CO_3 triangular groups. (19) (Center) Side view of vaterite CaCO_3 showing the layering between oxide groups and varied orientations of the CO_3 groups (colored triangles). (Right) top-down views of CaCO_3 vaterite showing the number of different orientation that the CO_3 groups can take within the unit cell. (16)	56
Figure 3.5: Predicted phase diagrams via convex hull theory at 0K for the $\text{Yb}_2\text{O}_3 - \text{SiO}_2 - \text{B}_2\text{O}_3$ ternary system. Blue points indicate stable phases, and red dots indicate metastable phases according to convex hull predictions for 0K. The blue lines are Alkemade lines indicating equilibrium between phases.	57
Figure 3.6 $\text{B}_2\text{O}_3 - \text{SiO}_2 - \text{Yb}_2\text{O}_3$ ternary compositions of interest overlaid on a partial ternary phase diagram showing tie Alkemade lines of equilibrium reactions identified with idealized interfacial reaction tests (Chapter 2).	59
Figure 3.7: Pictures of the 6-ID-D Beamline at Argonne National Lab showing (from left to right) the beamline setup, inside of the sample chamber, and diagram of the sample during the experiment.	62
Figure 3.8: Raw .tif File of composition B3 taken at 1300°C and resultant integrated XRD pattern for analysis in HighScore Plus.	63
Figure 3.9: DSC scan of composition B5, 50 mol% B_2O_3 and 50 mol% Yb_2O_3 showing PVA burnout at ~200°C on heating, an exothermic event at 733°C on heating, and an exothermic event at 598°C on cooling.	64
Figure 3.10: Stacked XRD scans of composition B5- 50 mol% B_2O_3 and 50 mol% Yb_2O_3 with reference patterns for Yb_2O_3 and the two polymorphs of YbBO_3	65
Figure 3.11: DSC Scan of T19 (40 mol% Yb_2O_3 , 30 mol% SiO_2 , and 30 mol% B_2O_3) showing PVA burnout below 200°C on heating, an exothermic event at 733°C on heating, melting at 1454°C on heating, solidification at 1436°C on cooling, and a phase transition at 559°C on cooling.	66
Figure 3.12: Expected equilibrium phase fields for the $\text{Yb}_2\text{O}_3 - \text{SiO}_2 - \text{B}_2\text{O}_3$ ternary system based on Alkemade lines from the equilibrium reactions discussed in the idealized interfacial reactions studies in Chapter 2. $\text{YbDS} = \text{Yb}_2\text{Si}_2\text{O}_7$ and $\text{YbMS} = \text{Yb}_2\text{SiO}_5$	67
Figure 3.13: Phase identification results for the $\text{Yb}_2\text{O}_3 - \text{SiO}_2 - \text{B}_2\text{O}_3$ ternary system from HE-XRD scans taken at 1100°C.	67
Figure 3.14: Phase identification results for the $\text{Yb}_2\text{O}_3 - \text{SiO}_2 - \text{B}_2\text{O}_3$ ternary system from HE-XRD scans taken at 1200°C.	68
Figure 3.15: Phase identification results for the $\text{Yb}_2\text{O}_3 - \text{SiO}_2 - \text{B}_2\text{O}_3$ ternary system from HE-XRD scans taken at 1300°C.	68
Figure 3.16 Phase identification results for the $\text{Yb}_2\text{O}_3 - \text{SiO}_2 - \text{B}_2\text{O}_3$ ternary system from HE-XRD scans taken at 1400°C.	69
Figure 3.17: Phase identification results for the $\text{Yb}_2\text{O}_3 - \text{SiO}_2 - \text{B}_2\text{O}_3$ ternary system from HE-XRD scans taken at 1500°C.	69
Figure 3.18: Composition T25 (40% Yb_2O_3 40% SiO_2 and 20% B_2O_3) individual HE-XRD scans stacked according to increasing time held at 1000°C with reference patterns for YbBO_3 and Yb_2O_3	70

Figure 3.19: $P_2O_5 - SiO_2 - B_2O_3$ and $P_2O_5 - B_2O_3$ phase diagrams used for reference due to equilibrium phase similarities to the $Yb_2O_3 - SiO_2 - B_2O_3$ system.(28)	73
Figure 3.20: Predicted liquidus boundary (orange line) at 1200°C based on HE-XRD scans showing melting in compositions T16 and T30.	74
Figure 3.21: Predicted liquidus boundary (dashed orange line) at 1300°C based on HE-XRD scans showing melting in compositions T25 and T31.	74
Figure 3.22: Predicted liquidus boundary (dotted orange line) at 1400°C based on HE-XRD scans showing melting in compositions T18, T24, and T32. Some melting was also seen in compositions T20, T21, T28, and T36.	75
Figure 3.23: Predicted liquidus surface of $Yb_2O_3 - SiO_2 - B_2O_3$ phase diagram with boundary lines shown in thick orange, ternary eutectic shown in blue, and regions of possible liquid immiscibility shown in grey. Alkemade lines for equilibrium reactions are shown in purple and green.	76
Figure 4.1: Comparison of the two $YbBO_3$ structures generated in CrystalMaker. Two unit cells shown for each structure. (Left) Low temperature polymorph. (Right) High temperature polymorph. Yb = Blue, O=Red, B=grey. Note the differences in the bonding state of the B to the O as circled in green.	81
Figure 4.2: (Left) three-fold crimp & welds on the bottom of the platinum equilibration packet. (Right) Filled & sealed platinum packet in drilled alumina holder for exposure in stagnant air box furnace.	85
Figure 4.3: (left) $YbBO_3$ formed after 24-hour exposure of mechanically mixed 40 mol% Yb_2O_3 and 60 mol% B_2O_3 powders at 800°C in a stagnant air box furnace. (Right) XRD of the bulk $YbBO_3$ showing that it is phase pure $YbBO_3$	86
Figure 4.4: 1 st DSC results of Yb_2O_3 and B_2O_3 equimolar mixture showing PVA burnout at 200°C on heating, exothermic formation reaction at 733°C on heating, and exothermic phase transition at 599°C on cooling.	88
Figure 4.5: Repeat of DSC run from sample in Figure 4.4 above, now $YbBO_3$, showing endothermic phase change at 995°C on heating and exothermic phase change at 540°C on cooling.	88
Figure 4.6: Hot Stage XRD scan showing both $YbBO_3$ polymorphs at 500°C on cooling.	89
Figure 4.7 : Cubic Yb_2O_3 lattice parameters taken from hot-stage XRD on heating compared to Stectura data for Yb_2O_3 CTE taken in 1961 (20)	90
Figure 4.8: Unit cell expansion data for both $YbBO_3$ vaterite polymorphs. (Left) Unit cell expansion in “a” basal plane direction. (Right) expansion in “c” direction. High temperature polymorph data taken in two separate runs shown in red. Low temperature polymorph data shown in black.	91
Figure 4.9: Backscatter electron micrographs of the $YbBO_3$ samples inside the platinum packets. Equimolar mixtures of Yb_2O_3 and B_2O_3 were first equilibrated at 800°C for 24 hours before a secondary 24h equilibration at the temperatures of interest. (Left) 500°C, note the stringing in the crack. (Right)- 600°C, note the bright phase is more prevalent after equilibration at the higher temperature.	93
Figure 4.10: Micro focus XRD scans of static equilibration of equimolar Yb_2O_3 and B_2O_3 mixtures after reaction at 800°C (Top) and 24h equilibrations. Note the presence of $YbBO_3$ in the 800°C exposure and the presence of both $YbBO_3$ and Yb_2O_3 in the 500°C (Left) and 600°C (Right) exposures.	94
Figure 4.11: Pressed, polished, and sectioned $YbBO_3$ puck piece (Left) swelling after 10 min exposure at 1200°C in stagnant air box furnace (Right).	95

Figure 4.12: YbBO ₃ ceramic puck sample after manipulation with tweezers while hot (30 minutes at 1200°C) and backscatter electron micrograph of sample surface.	96
Figure 4.13: XRD scans of YbBO ₃ pucks from the pre-reacted YbBO ₃ powder reacted post-anneal for 1 hour at 475°C (left) and 500°C (right) showing both YbBO ₃ and Yb ₂ O ₃ present in the samples.	97
Figure 4.14: XRD scan of YbBO ₃ puck from the pre-reacted YbBO ₃ powder after annealing at 1200°C for 10 minutes showing only the YbBO ₃ phase present.	97
Figure 4.15: Stacked XRD patterns of the YbBO ₃ samples in various stages of processing and testing. Yb ₂ O ₃ -specific peaks are highlighted with vertical blue lines and the measured Yb ₂ O ₃ content via Rietveld refinement is shown under the sample identification to the right of each scan.	100
Figure 5.1: Diagram of APS process illustrating torch & powder feeds (14).....	108
Figure 5.2: Yb ₂ Si ₂ O ₇ coatings fabricated via APS processes showing pores, microcracking, and multiple Yb-silicate phases with varying SiO ₂ content (16).	109
Figure 5.3: (Left) RBSiC and (Right) CMC coupons with Si bond coat and Yb ₂ Si ₂ O ₇ topcoat.	111
Figure 5.4: Keiser Rig Sample setup showing the hanging coupons and furnace setup of the coupon hangers inserted into Hexoloy™ SiC chambers.	112
Figure 5.5: Photograph and hot zone schematic of a SiC coupon in the TGA	113
Figure 5.6: Masked image for Dragonfly (L: starting image- CMC with Si bond coat and EBC exposed in 4.4 atm O ₂ at 900°C for 500h, R: Masked image showing that only the TGO and bond coat have been selected for segmentation).....	115
Figure 5.7: Si bond coat in CMC/ EBC coupon exposed in 4.4 atm O ₂ at 900°C for 500h. Segmented in Dragonfly. Yellow is the Si bond coat, blue is the TGO, and red is the pores.....	116
Figure 5.8: Segmentation of Si bond coat (yellow) TGO (blue) and pores (red) before and after manual touch-ups, micrograph layer hidden.....	117
Figure 5.9: 100h TGA data of coated 0%B and 4%B RBSiC coupons at 900°C in O ₂ shown with forced linear fits for parabolic rate constants.	118
Figure 5.10: 100h TGA data of coated 0%B and 4%B RBSiC coupons at 1050°C in O ₂ shown with forced linear fits for parabolic rate constants.	119
Figure 5.11: 100h TGA data of coated 0%B and 4%B RBSiC coupons and CMC coupons at 1200°C in O ₂ with forced linear fits for parabolic rate constants.....	119
Figure 5.12: TGA data comparing 0%B coated RBSiC samples to uncoated samples exposed at 900°C for 100h in O ₂	120
Figure 5.13: TGA data comparing 4%B coated RBSiC samples to uncoated samples exposed at 900°C for 100h in O ₂	121
Figure 5.14: TGA data comparing 0%B coated RBSiC samples to uncoated samples exposed at 1200°C for 100h in O ₂	121

Figure 5.15: TGA data comparing 4%B coated RBSiC samples to uncoated samples exposed at 1200°C for 100h in O ₂ .	122
Figure 5.16: TGA data comparing CMC coated RBSiC samples to uncoated samples exposed at 1200°C for 100h in O ₂ .	122
Figure 5.17: 1050°C dry O ₂ benchtop weight changes for samples exposed in the Keiser Rig with forced linear fits to parabolic kinetics. (Left) 1 atm exposure. (Right) 4.4 atm exposure	125
Figure 5.18: 1200°C dry O ₂ benchtop weight changes for samples exposed in the Keiser Rig with forced linear fits. (Left) 1 atm exposure. (Right) 4.4 atm exposure	125
Figure 5.19: Backscatter electron and elemental maps of a tortuous TGO and glassy inclusion in coated CMC sample exposed at 900°C for 500 h at 4.4 atm O ₂ .	127
Figure 5.20: Backscatter electron micrograph of the TGO in a coated CMC exposed at 1200°C in 4.4 atm O ₂ for 500h in the Keiser rig.	128
Figure 5.21: Backscatter electron micrograph of Si/ EBC coated CMC coupons with segmented overlay of the bond coat (yellow), TGO (blue), and pores (red).	129
Figure 5.22: 900°C 500h 4.4 atm O ₂ segmentation of the bond coat (yellow), TGO (blue), and pores (red) with resultant histogram of TGO distribution through the depth of the bond coat	130
Figure 5.23: Histograms of TGO distribution in the Si bond coat for EBC coated CMCs tested in the Keiser Rig at 4.4 atm O ₂ for 500h. They have been rotated 90° for ease of reading with the bond coat/ EBC interface on the left and bond coat/ CMC interface on the right. They are presented in the same order as their corresponding segmentations in Figure 5.21.	131
Figure 5.24: Comparison of TGO depth penetration concentrations for the CMC samples exposed in the Keiser Rig for 500h in 4.4 atm dry O ₂ . Numbers refer to % depth of Si bond coat at which 80% of the TGO is formed.	132
Figure 5.25: Defect variations observed in the silicon bond coats of CMC and RBSiC samples that were characterized for segmentation in Dragonfly. (Left) Large and numerous pores in the bond coat of the CMC (top) and RBSiC sample (bottom). (Top Right) crumbly microstructure of the bond coat and small EBC inclusions. (Bottom Right) Numerous EBC inclusions.	133
Figure 5.26: TGO depth concentration curves for EBC/ Si coated 0%B and 4%B RBSiC coupons exposed in the Keiser Rig and TGA at 900°C for 100h in 1 atm O ₂ . Numbers refer to % depth of Si bond coat at which 80% of the TGO is formed.	134
Figure 5.27: TGO depth concentration curves for EBC/Si coated 0%B and 4%B RBSiC coupons exposed in the Keiser Rig and TGA at 1050°C for 100h in 1 atm O ₂ . Numbers refer to % depth of Si bond coat at which 80% of the TGO is formed.	135
Figure 5.28: TGO depth concentration curves for EBC/Si coated 0%B and 4%B RBSiC coupons exposed in the Keiser Rig and TGA at 1200°C for 100h in 1 atm O ₂ . Numbers refer to % depth of Si bond coat at which 80% of the TGO is formed.	135
Figure 5.29: 4%B RBSiC cross section of the EBC showing features similar to the reaction layers seen in the well tests.	136

<i>Figure 5.30: FIB section of porous reaction phase taken from the red rectangle in Figure 19 right, SAED pattern, and reference diffraction pattern showing that the grains are $\text{Yb}_2\text{Si}_2\text{O}_7$.</i>	136
<i>Figure 5.31: Silica pools and porous EBC grain structure features reminiscent of YbBO_3 from well tests was found in samples of all characterized boron contents and both exposure apparatuses. These RBSiC samples are from 1200°C, 100h, 1 atm dry O_2 exposures. (Top) Samples exposed in Keiser Rig. (Bottom) Sample exposed in TGA. (Left) 0%B RBSiC Samples. (Right) 4%B RBSiC Samples.</i>	137
<i>Figure 5.32: Micrograph of 0%B RBSiC coupon exposed in the TGA at 1050°C for 100h in dry O_2.</i>	139
<i>Figure 5.33: FactSage Simulation of $\log(\text{activity})$ vs. temperature for B_2O_3 in O_2.</i>	140
<i>Figure 6.1: Predicted liquidus surface of $\text{Yb}_2\text{O}_3 - \text{SiO}_2 - \text{B}_2\text{O}_3$ phase diagram with boundary lines shown in thick orange, ternary eutectic shown in blue, and regions of possible liquid immiscibility shown in grey. Alkemade lines for equilibrium reactions are shown in purple and green.</i>	150

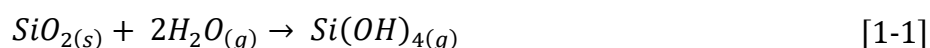
List of Tables

<i>Table 2-1 Praxair powders used for SPS substrates.</i>	27
<i>Table 2-2: SPS procedures for well test substrates and their resultant final densities taken by Archimedes measurements.</i>	28
<i>Table 2-3: Well testing exposure parameters</i>	29
<i>Table 2-4: Ratio values and Calculated errors for ICP measurements of the B:Si ratio in the glass removed during the soak</i>	35
<i>Table 2-5: Possible Yb-borate phase candidates for SAED analysis including space groups and g-spacings for comparison. Potential as a match and associated reasoning shown in the right two columns.</i>	39
<i>Table 3.1: Binary Yb₂O₃ – B₂O₃ compositions of interest in both molar and weight percent</i>	59
<i>Table 3.2: Ternary sample compositions of interest by both molar and weight percent</i>	60
<i>Table 3.3: Powder information for oxides used in phase diagram experiments.</i>	61
<i>Table 4-1: Comparison of YbBO₃ polymorph crystal structures from HighScore PDF cards 00-019-1426 and 00-019-1427(2,3)</i>	81
<i>Table 4-2: Powders used for preparation of YbBO₃ bulk samples and Pt encapsulation samples.</i>	83
<i>Table 4-3: Calculated CTEs for YbBO₃ and material components of EBC/ CMC systems. CTE for individual lattice directions are reported for the YbBO₃ polymorphs while data reported for other constituents are the average linear CTE for the phase. (21,23,24)</i>	91
<i>Table 4-4: Calculated volumes for assorted phases of interest and difference in volumes relative to low-temperature YbBO₃ polymorph</i>	92
<i>Table 5-1: TGA and Keiser Rig (ORNL) testing conditions for characterized RBSiC & CMC samples</i>	111
<i>Table 5-2: Parabolic Oxidation rates (mg²/cm⁴·h) calculated from TGA exposures.</i>	123
<i>Table 5-3: Calculated parabolic rate constants (mg²/cm⁴·h) and pressure dependence.</i>	126
<i>Table 5-4: Calculated parabolic rate constants and pressure effects on uncoated RBSiC coupons. (20)</i>	126
<i>Table 5-5: TGO Area Fractions from Dragonfly Segmentations of the micrographs in Figure 5.23</i>	129
<i>Table 5-6: Area fraction comparisons for RBSiC and CMC samples exposed in the Keiser Rig & TGA for 100h in dry O₂</i>	134

1 Introduction

1.1 CMC/ EBC System Overview

Silicon carbide-based ceramic matrix composites (CMCs) entered service in the hot section of turbine engines for civilian use in 2016 (1). The use of CMCs allows for both a reduction in weight of the engine as well as an increase in operating temperature relative to the nickel-base superalloys that are currently employed, both of which in turn lead to improved fuel efficiency and lower emissions. In the presence of water vapor or oxygen, SiC is known to oxidize to form silica (SiO_2) and carbon monoxide. The thermally grown oxide (TGO) is volatile in the presence of water vapor, a by-product of fuel combustion process(2). This volatilization reaction, Equation [1-1] below, results in an unacceptable rate of material loss from the composite.



Environmental barrier coatings (EBCs) are thus used to limit the reaction between the CMC and water vapor. State of the art EBCs are based on rare earth silicate systems with ytterbium disilicate ($\text{Yb}_2\text{Si}_2\text{O}_7$) being a favored candidate due to a lack of polymorphs, good environmental stability, and a coefficient of thermal expansion close to that of the other CMC/ EBC system components, namely the silicon bond coat (3,4). Both the bond coat and the EBC are applied to the composite substrate using atmospheric plasma spraying (APS) techniques. The Si bond coat is necessary between the CMC and the EBC to improve adhesion of the EBC, limiting oxidation of the underlying SiC composite and the resultant formation of $\text{CO}_{(g)}$ (5).

Current CMCs are comprised of SiC fibers that are coated with a boron nitride (BN) interphase followed by chemical vapor infiltration of more SiC and silicon melt infiltration to form the matrix of the CMC as shown below in Figure 1.1.

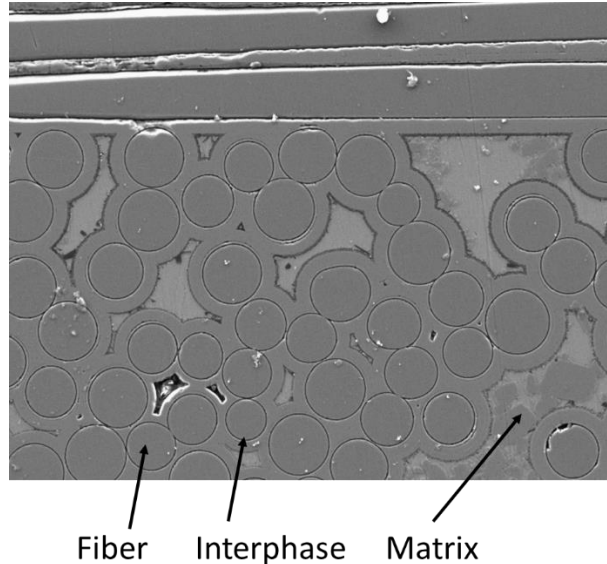
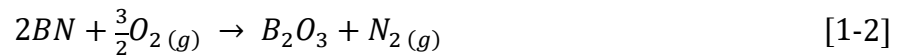


Figure 1.1: Cross section micrograph of a SiC/ BN/SiC CMC showing the SiC fibers surrounded by the BN interphase in the Si/SiC matrix. (Image courtesy of Rolls-Royce)

The BN interphase is critical to the mechanical properties of the CMC, however BN and other boron-rich phases are known to oxidize to form boria (B_2O_3) at temperatures above 400°C as shown in Equation 1-2 (6).



Boria is a strong glass-former and is volatile in H_2O -containing environments (7–10). Boria will react with the SiO_2 in the TGO from the bond coat or CMC to form borosilicate glass (7,11,12), drastically lowering its melting temperature (Figure 1.2) and viscosity and increasing its reactivity compared to pure silica (13–19). The boron oxide triangular, planar groups open the tetrahedrally coordinated silica glass network as shown below in Figure 1.2 , reducing the

dimensionality and bonding of the glass network from a true 3D network, making it less viscous and lowering the melting temperature(20).

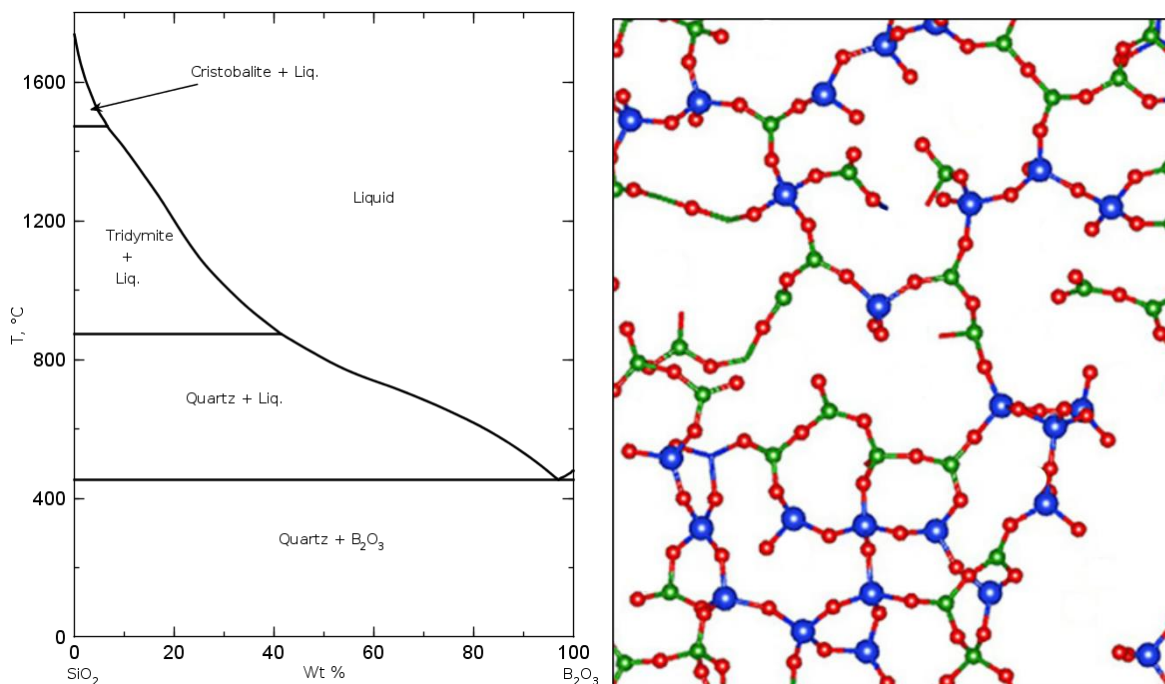


Figure 1.2 (Left) SiO_2 - B_2O_3 system phase diagram from Rockett & Foster. (Right) Structural image of SiO_2 - B_2O_3 glass with Na ions (yellow) showing how the B_2O_3 triangles (green) lower connectivity of the glass network from pure SiO_2 tetrahedra (blue). (21,22)

Borates have been used as solvents in high-temperature calorimetry for oxides and silicate since the early 20th century (17,23–25). It follows then that boria in the CMC/ EBC system will readily react with the oxides and silicates present, potentially forming glassy, amorphous phases that will contribute to a reduction in the high-temperature capabilities of the system.

The focus of this work is to explore the interactions between boria and EBC silicate materials, specifically $\text{Yb}_2\text{Si}_2\text{O}_7$. No data are currently available on the Yb_2O_3 / SiO_2 / B_2O_3 pseudo-ternary oxide system, and little are available on the Yb_2O_3 / B_2O_3 pseudo-binary system. Phase diagrams

exist for the SiO_2 - B_2O_3 system as shown in Figure 1.2, as well as for the SiO_2 – Yb_2O_3 system as shown in Figure 1.3 below.

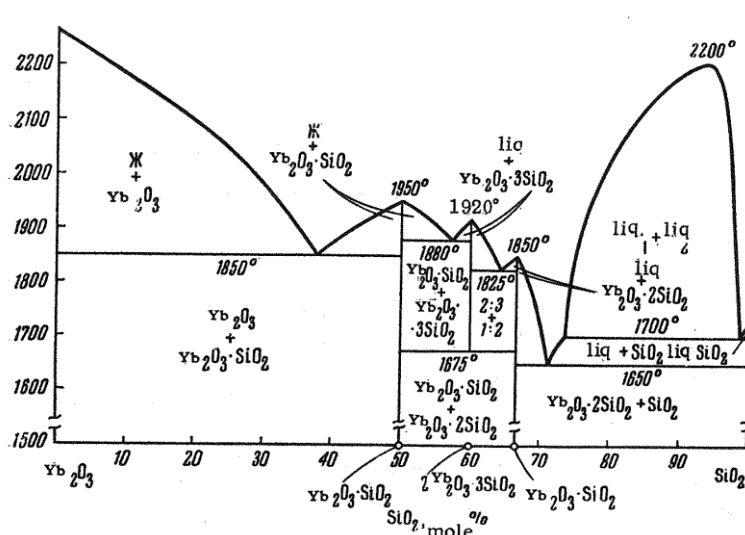


Figure 1.3 Yb_2O_3 - SiO_2 system phase diagram from Toropov (26)

Rare earth borates were first studied in the 1960s by E.M. Levin and based on phase diagram liquidus determination studies originally conducted by G.W. Morey in 1923(27–29). The focus of these studies by Levin was mostly on liquid immiscibility. As such, they focused on high temperatures and boria contents. As a result, the boria-rich side of the B_2O_3 – Yb_2O_3 diagram was explored as shown in Figure 1.4 below. The diagram indicates the suspected phase equilibria and liquid immiscibility, though only the solid lines have been confirmed experimentally.

Rare earth borates (REBO_3) are found to take the same crystal structures as the CaCO_3 system. The orthoborates with rare earth cations of larger radii, such as ytterbium, take the vaterite structure (14,30–34). This structure shows two polymorphs in the rare earth borates, a high

temperature and a low temperature polymorph, with the transition between the two requiring a reconstruction of the B-O bonding in the borate groups. However, the system remains relatively un-studied.

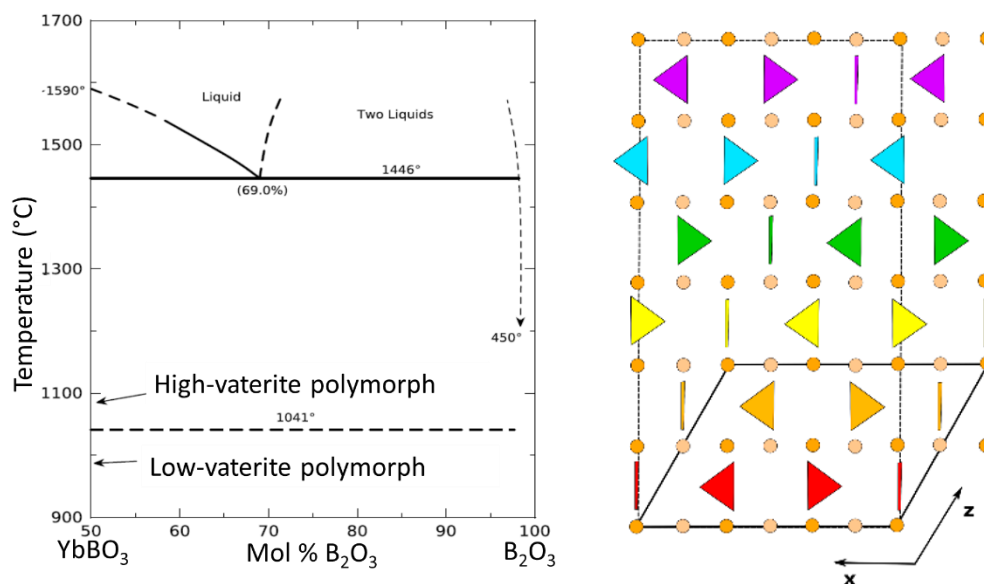


Figure 1.4: (Left) $\text{YbBO}_3 - \text{B}_2\text{O}_3$ system phase diagram from Levin (27,29,35) (Right) CaCO_3 vaterite crystal structure showing different possible configurations of the CO_3 triangles within a unit cell, analogous to BO_3 in YbBO_3 (36).

The listed crystal structures for YbBO_3 , high temperature and low temperature polymorphs of the vaterite type, are highly controversial hexagonal structures (31,36–40). There is debate about the superlattice of the CaCO_3 vaterite due to orientational disordering of the carbonate triangular groups found in this metastable phase. These CO_3 groups can rotate in the space between the Ca atoms and can take different orientations within a single unit cell or throughout the larger crystal as shown above in Figure 1.4. For the rare earth borates with an analogous crystal structure to vaterite, the rare earth cations sit on the calcium sites and triangular borate groups sit in the carbonate sites. The borate groups exhibit the same disordering as the carbonate groups, and though both the borate and carbonate vaterite

analogs have been well-studied, the exact superlattice structure remains unknown. Sixteen distinct ordered superstructures having been proposed to date (14,27,30–32,34). Given the lack of thermodynamic information on the $\text{Yb}_2\text{O}_3 - \text{B}_2\text{O}_3$ system, no ternary phase diagram for the $\text{Yb}_2\text{O}_3 - \text{SiO}_2 - \text{B}_2\text{O}_3$ system currently exists.

The effects of the boria in the system on the growth of the SiO_2 bond coat and the phase stability of the rare earth EBC have not previously been investigated. Previous studies have shown that both Si and SiC will oxidize to form silica as described by the Deal & Grove model.

This study describes the overall silicon oxidation as following the relationship:

$$x_0^2 + Ax_0 = B(t + \tau) \quad [1 - 3]$$

Where x_0 is the oxide thickness, t is time, and τ corrects for any native oxide layer. In this case, A and B are constants. For short times or thin oxides, the relationship in Equation [1-3] can be reduced to a linear rate law (below) where B/A is the linear rate constant, often denoted k_l .

The oxidation rates in this case are surface-reaction controlled.

$$x_0 \cong \frac{B}{A}(t + \tau) \quad [1 - 4]$$

For thick oxides or longer exposure times, the relationship in Equation [1-3] reduces to describe parabolic oxidation as shown in Equation [1-5] where B is the parabolic rate constant, often denoted as k_p . In this case, the oxidation rate is diffusion-controlled by the transport of oxidant through the oxide scale.

$$x_0 \cong \sqrt{Bt} \quad [1 - 5]$$

An early study by Schlichting (42) found that the oxidation of Si coupons coated in borosilicate glasses containing up to 30 mol% B_2O_3 exhibited parabolic rate constants up to four orders of magnitude higher than that of Si coupons coated only in Si glass. Later work by McFarland showed that the SiO_2 grown from SiC oxidation in the presence of boria was substantially thicker and accompanied by a greater weight change than oxides grown from pure SiC. McFarland proposed that this accelerated oxidation was due to the boria etching in the interface(41). This study was only conducted with pure SiC substrates and did not include any coatings. The effects of B_2O_3 on APS Si bond coat oxidation or the $Yb_2Si_2O_7$ EBCs have not yet been investigated.

1.2 Project Objectives

The aim of this project is to elucidate the effects of boria on the $\text{Yb}_2\text{Si}_2\text{O}_7$ EBC system. Previous studies of boron-containing CMC/ EBC systems have shown the formation of dendritic structures and spinodal decomposition during combustion rig testing at 1150°C as shown below in Figure 1.5. The spinodal decomposition and dendritic structures were attributed to the presence of B_2O_3 , however the lack of thermodynamic information available or fundamental studies on the system prevented any definitive conclusions.

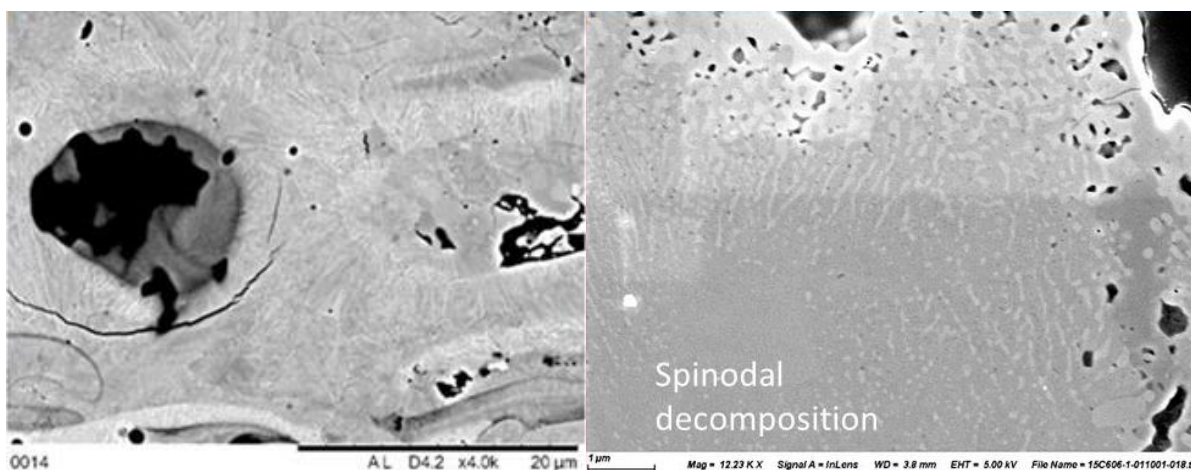


Figure 1.5: Dendritic structures (Left) and spinodal decomposition (Right) observed in $\text{Yb}_2\text{Si}_2\text{O}_7$ EBCs after exposure at 1150°C for 100h in a 12atm combustion environment. [Images from Rolls-Royce Statement of Work for this research program]

Due to the lack of information on the B_2O_3 - SiO_2 - Yb_2O_3 pseudo-ternary oxide system, this body of work aims to do the following:

1. Understand the reactions and equilibrium phases that occur when B_2O_3 reacts with the phases found in the rare earth silicate EBC; $\text{Yb}_2\text{Si}_2\text{O}_7$, Yb_2SiO_5 , and Yb_2O_3 .
2. Develop a phase diagram for the Yb_2O_3 - SiO_2 - B_2O_3 ternary system.

3. Determine the properties of any reaction products and equilibrium phases that are found to form in the $\text{Yb}_2\text{O}_3 - \text{SiO}_2 - \text{B}_2\text{O}_3$ ternary system.
4. Determine the impact of the formation of these reaction products on the oxidation of SiC/BN/SiC CMC, Si bond coat, and $\text{Yb}_2\text{Si}_2\text{O}_7$ EBC systems.

For the first objective, idealized interfacial reaction tests between B_2O_3 and $\text{Yb}_2\text{Si}_2\text{O}_7$ (YbDS), Yb_2SiO_5 (YbMS), and Yb_2O_3 , referred to as “well tests”, were used to investigate the reactions that occur between boria and the rare earth oxides and silicates. The phase equilibria were then studied through a series of differential scanning calorimetry (DSC) and high-energy x-ray diffraction (HE-XRD) investigations of compositions from the binary $\text{Yb}_2\text{O}_3 - \text{B}_2\text{O}_3$ system as well as compositions from the ternary $\text{Yb}_2\text{O}_3 - \text{SiO}_2 - \text{B}_2\text{O}_3$ system with up to 30 mol% B_2O_3 at temperatures up to 1500°C. The resultant reaction product, ytterbium borate, was then produced in bulk. Its physical and thermal properties were studied through use of DSC to determine reaction temperatures and enthalpies, platinum encapsulations for static equilibrium testing, and hot stage X-ray diffraction for CTE measurements. Finally, both thermogravimetric analysis and high-temperature, high-pressure exposures were conducted on $\text{Yb}_2\text{Si}_2\text{O}_7$ coated reaction-bonded SiC (RBSiC) and CMC samples to determine the effects of boria on the oxidation of the Si bond coat and the EBC phase stability.

1.3 References

1. Zok F. Ceramic-matrix composites enable revolutionary gains in turbine engine efficiency. American Ceramic Society Bulletin. 2016;95(5).
2. Opila EJ, Hann RE. Parabolic oxidation of CVD SiC in water vapor. Journal of the American Ceramic Society. 1997;80(1):197–205.
3. Lee KN. Current status of environmental barrier coatings for Si-based ceramics. Surface and Coatings Technology. 2000;133–134:1–7.
4. Turbines G, Lee KN. Protective Coatings for Gas Turbines 4.4.2-1 Introduction. :419–37.
5. Lee KN, Opila EJ, Miller R. Oxidation and pore formation at the Mullite/SiC interface in air and water vapor. Fundamental Aspects of High Temperature Corrosion. 1996 Oct:124–38.
6. Ruggles-Wrenn MB, Jones TP. Tension-compression fatigue of a SiC/SiC ceramic matrix composite at elevated temperature. Journal of Engineering for Gas Turbines and Power. 2012;134(9).
7. Priest DK, Levy AS. Effect of Water Content on Corrosion of Borosilicate Glass. Journal of the American Ceramic Society [Internet]. 1960 Jul 1 [cited 2021 May 24];43(7):356–8. Available from: <https://ceramics.onlinelibrary.wiley.com/doi/full/10.1111/j.1151-2916.1960.tb13671.x>
8. Kracek FC, Morey GW, Merwin HE. The system, water - boron oxide. American Chemical Society Spring Meeting [Internet]. 1938 [cited 2021 Mar 14];(April):1–29. Available from: <http://earth.geology.yale.edu/~ajs/1938-A/143.pdf>
9. Meller F, Milberg ME. The Structure of Some B₂O₃-H₂O Glasses. Journal of the American Ceramic Society [Internet]. 1960 Jul 1 [cited 2021 May 24];43(7):353–6. Available from: <https://ceramics.onlinelibrary.wiley.com/doi/full/10.1111/j.1151-2916.1960.tb13670.x>
10. Stackelberg M v., Quatram F, Dressel J. Die Flüchtigkeit der Borsäuren mit Wasserdampf. Das System B₂O₃-Wasser. Zeitschrift für Elektrochemie und angewandte physikalische Chemie [Internet]. 1937 Jan 1 [cited 2021 May 24];43(1):14–28. Available from: <https://onlinelibrary.wiley.com/doi/full/10.1002/bbpc.19370430104>
11. Advocat T, Crovisier JL, Fritz B, Vernaz E. Thermokinetic Model of Borosilicate Glass Dissolution: Contextual Affinity. MRS Proceedings. 1989;176.
12. Bunker BC, Arnold GW, Day DE, Bray PJ. The effect of molecular structure on borosilicate glass leaching. Journal of Non-Crystalline Solids. 1986;87(1–2):226–53.
13. Brosh E, Pelton AD, Decterov SA. A model to calculate the viscosity of silicate melts: Part IV: Alkali-free borosilicate melts. International Journal of Materials Research. 2012;103(4):494–501.
14. Heller G. A survey of structural types of borates and polyborates. 1986;39–98.

15. Shelby JE. Thermal Expansion of Alkali Borate Glasses. *Journal of the American Ceramic Society*. 1983;66(3):225–7.
16. Ahmed AA, Abbas AF, Salman SM. Thermal Expansion of Mixed Alkali Borate Glasses. *Physics and Chemistry of Glasses*. 1985;26(1):17–23.
17. Zhang Z, Hirao K, Soga N. Water corrosion behavior of densified glass. II. Borate glasses. *Journal of Non-Crystalline Solids*. 1991;135(1):62–6.
18. Avramov I, Vassilev T, Penkov I. The glass transition temperature of silicate and borate glasses. *Journal of Non-Crystalline Solids*. 2005;351(6–7):472–6.
19. Amietszajew T, Seetharaman S, Bhagat R. The Solubility of Specific Metal Oxides in Molten Borate Glass. *Journal of the American Ceramic Society*. 2015 Oct 1;98(10):2984–7.
20. Introduction to Glass Science and Technology Second Edition.
21. Rockett TJ, Foster WR. Phase Relations in the System Boron Oxide–Silica. *Journal of the American Ceramic Society*. 1965;48(2):75–80.
22. Ren M, Deng L, Du J. Surface structures of sodium borosilicate glasses from molecular dynamics simulations. *Journal of the American Ceramic Society*. 2017 Jun 1;100(6):2516–24.
23. Amietszajew T, Seetharaman S, Bhagat R. The Solubility of Specific Metal Oxides in Molten Borate Glass. *Journal of the American Ceramic Society*. 2015;98(10):2984–7.
24. Konijnendijk WL, Stevels JM. The structure of borate glasses studied by Raman scattering. *Journal of Non-Crystalline Solids*. 1975;18(3):307–31.
25. Kamitsos EI. Infrared studies of borate glasses. *Physics and Chemistry of Glasses*. 2003;44(2):79–87.
26. Toropov NA, Bondar' IA. Silicates of the rare earth elements. *Bulletin of the Academy of Sciences of the USSR Division of Chemical Science*. 1961;10(8):1278–85.
27. Levin EM, Roth RS, Martin JB. Polymorphism of ABO₃ Type Rare Earth Borates. the *American Mineralogist* [Internet]. 1961;46(1954):1030–55. Available from: http://www.minsocam.org/ammin/AM46/AM46_1030.pdf
28. Academy W, Academy W. A comparison of the heating-curve and quenching methods of melting-point determinations Author (s): George W . Morey Source: *Journal of the Washington Academy of Sciences*, August 19 , 1923 , Vol . 13, No. Published by: Washington Academy of Science. 1923;13(14):326–9.
29. Levin EM. Liquid immiscibility in oxide systems. *Phase Diagrams Materials Science and Technology*. 2012; 3:143–236.
30. Weir CE, Schroeder RA. Infrared spectra of the crystalline inorganic borates. *Journal of Research of the National Bureau of Standards Section A: Physics and Chemistry*. 1964;68A(5):465.

31. Weir CE, Lippincott ER. Infrared studies of aragonite, calcite, and vaterite type structures in the borates, carbonates, and nitrates. *Journal of Research of the National Bureau of Standards Section A: Physics and Chemistry*. 1961;65A (3):173.
32. Newnham RE, Redman MJ, Santoro RP. Crystal Structure of Yttrium and Other Rare-Earth Borates. *Journal of the American Ceramic Society*. 1963;46(6):253–6.
33. Joubert J-C, White WB, Roy R. Synthesis and crystallographic data of some rare earth–iron borates. *Journal of Applied Crystallography*. 1968;1(5):318–9.
34. Bradley WF, Graf DL, Roth RS. The vaterite-type ABO₃ rare-earth borates. *Acta Crystallographica*. 1966;20(2):283–7.
35. Levin EM, Robbins CR, Waring JL. Immiscibility and the System Lanthanum Oxide–Boric Oxide. *Journal of the American Ceramic Society*. 1961;44(2):87–91.
36. Christy AG. A Review of the Structures of Vaterite: The Impossible, the Possible, and the Likely. *Crystal Growth and Design*. 2017;17(6):3567–78.
37. Jacob DE, Wehrmeister U, Soldati AL, Hofmeister W. Spectroscopic characterisation of biological vaterite: relations to synthetic and geological vaterites. *Geophysical Research Abstracts*. 2009; 11:2006–7.
38. Demichelis R, Raiteri P, Gale JD, Dovesi R. The multiple structures of vaterite. *Crystal Growth and Design*. 2013;13(6):2247–51.
39. Burgess KMN, Bryce DL. On the crystal structure of the vaterite polymorph of CaCO₃: A calcium-43 solid-state NMR and computational assessment. *Solid State Nuclear Magnetic Resonance* [Internet]. 2015; 65:75–83. Available from: <http://dx.doi.org/10.1016/j.ssnmr.2014.08.003>
40. Ševčík R, Šašek P, Viani A. Physical and nanomechanical properties of the synthetic anhydrous crystalline CaCO₃ polymorphs: vaterite, aragonite and calcite. *Journal of Materials Science*. 2018;53(6):4022–33.
41. McFarland B, Angelici Avincola V, Morales M, Opila E. Identification of a new oxidation/dissolution mechanism for boron-accelerated SiC oxidation. *Journal of the American Ceramic Society*. 2020;103(9):5214–31.
42. Schlichting J. Oxygen transport through glass layers formed by a gel process. *Journal of Non-Crystalline Solids*. 1984 Feb 1;63(1–2):173–81.

2 Idealized Interfacial Reactions between B_2O_3 and Yb-Silicates

2.1 Introduction

Idealized interfacial interaction tests were used to determine the direct interactions between B_2O_3 and the phases found in the rare earth EBC; $Yb_2Si_2O_7$, Yb_2SiO_5 , and Yb_2O_3 . These tests, referred to as “well tests” were conducted with substrates made via spark plasma sintering of the three ytterbium-containing phases and boria glass inserts. In this case, the amounts of boria glass used are significantly higher than would be found in a CMC/ EBC system. The interactions of these materials have never been studied before, therefore these high ratios were used to ensure observation of any reactions that occurred between the B_2O_3 and the EBC materials.

The EBC materials used as substrates for these tests ($Yb_2Si_2O_7$, Yb_2SiO_5 , and Yb_2O_3) were processed via spark plasma sintering (SPS) rather than the atmospheric plasma spraying techniques usually used to apply the EBCs to the CMC substrates. APS is not an equilibrium process which results in all three phases mentioned above being present in the as sprayed EBC. An example of the cross-section structure of these APS coatings can be seen below in Figure 2.2.1 with all three ytterbium-based phases identifiable. SPS processing of each of these phases allows interactions with B_2O_3 to be tested individually.

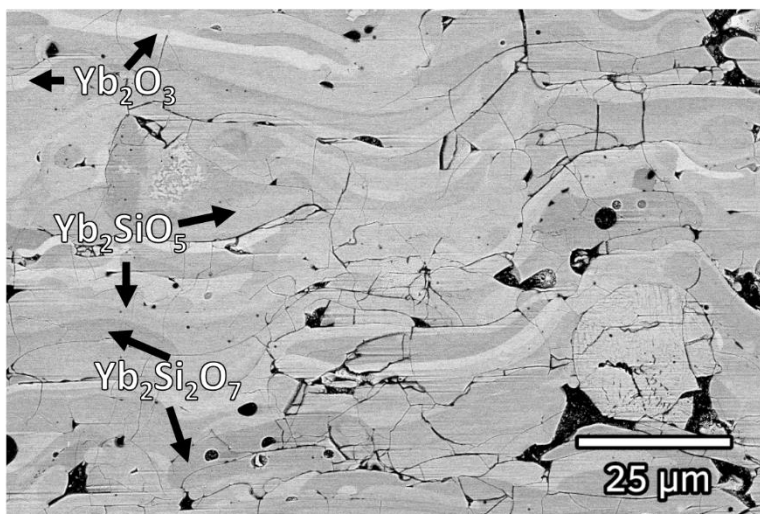


Figure 2.2.1: A backscatter electron micrograph showing the initial morphology and splat structure in a polished cross section of dense APS $\text{Yb}_2\text{Si}_2\text{O}_7$ coatings provided by Rolls-Royce (1) $\text{Yb}_2\text{Si}_2\text{O}_7$ splats are the darkest grey, Yb_2SiO_5 the medium grey, and Yb_2O_3 the lightest grey.

The interfacial interaction tests were designed to avoid both contamination and reaction of the materials surrounding the interfacial test as well as excessive loss of boria by vaporization from the samples being tested. The “well test” setup utilized in this study has been used previously for calcium magnesium aluminosilicate (CMAS) interaction studies to look at the interactions of the vitreous CMAS with the CMC/ EBC component materials.(2) The well configuration here was chosen over the pellet configuration to prevent loss of as much boria as possible via either volatilization or wicking. Boria has previously been found to be highly wetting when molten, readily wicking along surfaces, through pore networks, and up the sides of vessels in which it is contained (3–6).

2.2 Materials & Experimental Setup

$\text{Yb}_2\text{Si}_2\text{O}_7$, Yb_2SiO_5 , and Yb_2O_3 powders were obtained from Praxair and are listed in Table 2-1 below.

Table 2-1 Praxair powders used for SPS substrates.

<i>Powder Formulation</i>	<i>Chemical Purity</i>	<i>Manufacturer</i>
$\text{Yb}_2\text{Si}_2\text{O}_7$	99.9%	Praxair Surface Technologies Indianapolis, IN
Yb_2SiO_5	99.9%	
Yb_2O_3	99.9%	

As these powders were intended for use in atmospheric plasma spray (APS) processes, they were first baked out to remove any polymers and plasticizers added to assist in the spraying process. They were placed in a platinum crucible and exposed at 900°C for 15 minutes in a stagnant air box furnace (CM furnaces, Bloomfield NJ). After burnout, powders were transferred in 25g batches to a HDPE bottle with zirconia milling media (>95% purity, Glen Mills, Clifton NJ) and ball milled for 12 hours. The powders are then packed into 25.4mm diameter graphite dies (Beumac Company Inc., Epsom NH) lined with graphite foil (Thermal Technologies LLC). The powder was then consolidated into dense pucks by spark plasma sintering (SPS; Thermal Technologies LLC, Model SPS 25-10, Santa Rosa CA) according to the heat treatments outlined in Table 2-2 below. Final densities as listed in Table 2-2 for each of the substrates were obtained via Archimedes measurements.

Table 2-2: SPS procedures for well test substrates and their resultant final densities taken by Archimedes measurements.

<i>Puck Material</i>	<i>Hold Time</i>	<i>Target Temperature</i>	<i>Pressure</i>	<i>Ramp Rate</i>	<i>Final Density</i>
$Yb_2Si_2O_7$	15 min	1500° C	65 MPa	150K/min	92-96%
Yb_2SiO_5	10 min	1500°C	65 MPa	150 K/min heating, 25 K/ min cooling	85-90%
Yb_2O_3	7 min	1800°C	65 MPa	150 K/ min heating, 50 K/min cooling	90-95%

The pucks prepared via SPS were sectioned into 10x10x5 mm samples using a low-speed saw with a 4" diamond-embedded blade. A 3 mm deep well was then drilled into each sample using a standard drill press with a tapered diamond Dremel bit (Dremel bit #7134) and deionized water as a drilling lubricant. Samples were annealed at 1500°C for 72 hours in the stagnant air box furnace to ensure phase uniformity and to bake out any carbon remaining from the SPS process.

Boria glass was prepared by melting anhydrous boric oxide in a platinum crucible at 1000°C in a stagnant air box furnace until fully melted (~ 0.5h). While still molten, borosilicate stir rods (Kimble KIMAX solid stirring rods) were inserted into the melt then slowly withdrawn to pull a fiber of molten boria glass ~2mm in diameter.

Boria plugs were prepared from the boria fibers drawn from the melt. The fiber diameter was measured to find a region that would fit into the drilled well (~2mm in diameter). That region was then cut into 3mm lengths averaging 4mg in weight. A schematic drawing of the well test prepared for exposure is shown in Figure 2.2 below.

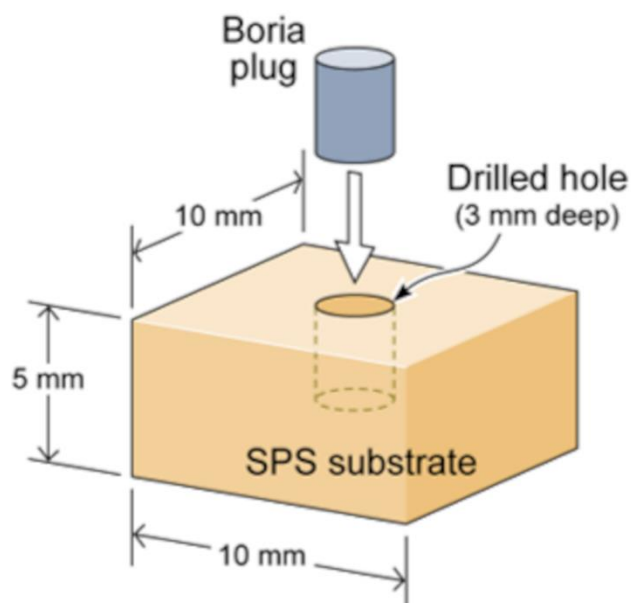


Figure 2.2: Well test setup schematic showing dimensions of SPS substrate, drilled hole and boria plug.

Samples were heated in the stagnant air box furnace according to the test matrix in Table 2-3 below. For $\text{Yb}_2\text{Si}_2\text{O}_7$, multiple times and temperatures were chosen to fully explore the extent of reaction with B_2O_3 while 1000°C and 24 hours was chosen for the Yb_2O_3 and Yb_2SiO_5 substrates for comparison to the $\text{Yb}_2\text{Si}_2\text{O}_7$ results.

Table 2-3: Well testing exposure parameters

Substrate	Exposure Temperature	Exposure Times
SPS $\text{Yb}_2\text{Si}_2\text{O}_7$	800°	1h, 3h, 8h, 24h
SPS $\text{Yb}_2\text{Si}_2\text{O}_7$	900°	1h, 3h, 8h, 24h
SPS $\text{Yb}_2\text{Si}_2\text{O}_7$	1000°	1h, 3h, 8h, 24h
SPS $\text{Yb}_2\text{Si}_2\text{O}_7$	1200°	1h, 3h, 8h, 24h
SPS Yb_2SiO_5	1000°	8h, 24h
SPS Yb_2O_3	1000°	8h, 24h

The samples were placed in the furnace at temperature and air quenched after exposure. Post-exposure, scanning electron microscopy (SEM; FEI Quanta 650, Hillsboro, Oregon) and

standardless energy dispersive spectroscopy (EDS; Oxford Instruments Aztec X-MaxN 150, Abingdon, Oxfordshire, UK) were used to characterize remaining glass on the surface of samples in plain view.

Selected samples were cross-sectioned using a low-speed saw with a diamond-embedded wafering blade and ethylene glycol to minimize loss of water-soluble phases. The cut samples were mounted in epoxy and ground down to the center of the well, then polished in ethylene glycol to a 0.25 μm diamond finish. Samples were then sputter coated with Au/Pd for further imaging and analysis via SEM and EDS. Selected samples were also sectioned using a dual-beam focused ion beam (FIB; Helios UC G4, Thermo Fischer Scientific) for transmission electron microscopy and selected area diffraction (TEM; Titan 80-300 STEM, FEI, Hillsboro, Oregon).

Additional samples were soaked in 15 mL of deionized water for 24 h at 80°C to remove any water-soluble glass/reaction products after plan view imaging. The solutions were retained for spectroscopic elemental analysis by Inductively coupled plasma optical emission spectroscopy (ICP-OES: iCAP 6000, Thermo Scientific, Cambridge UK). This technique utilizes calibration curves for element-specific wavelengths with a sensitivity of ppmw. Yb, Si, and B concentrations were determined using three repeats each of four or five calibration wavelengths for each element achieving average values within 1.0 ppm of the average for each cation present in the solution.

Post-soak, reaction products on the sample surfaces were imaged in SEM in both plan view and cross-section and identified using micro-focus x-ray diffraction (μ -XRD; PANalytical Empyrean, Royston, UK) which allows for analysis of interaction areas with a width as small as 130 μm .

The areas of interest included the exposed substrate surface after water-soluble phases were removed, as well as any glass remaining on the sample surface.

2.3 Results

2.3.1 $\text{Yb}_2\text{Si}_2\text{O}_7$ Substrates

2.3.1.1 Plan View SEM/EDS

Figure 2.3 shows a plan view of the $\text{Yb}_2\text{Si}_2\text{O}_7$ well test surface after exposure at 1000°C for 24 hours. Post-exposure, all samples exhibited surface morphologies like that shown in Figure 2.3, regardless of exposure time or temperature. While some glass remained in the well, glass was observed to wick over the edges of the well to cover the surface of the $\text{Yb}_2\text{Si}_2\text{O}_7$ sample. SEM backscatter electron (BSE) imaging of the well surface shows charging immediately around the edge of the well, indicating the presence of a thick ring of glass. EDS mapping shows consistent O signal across the surface, with slight drop-out of the Si and increase in the B signal in the ring of glass surrounding the well.

1000°C 24 hours

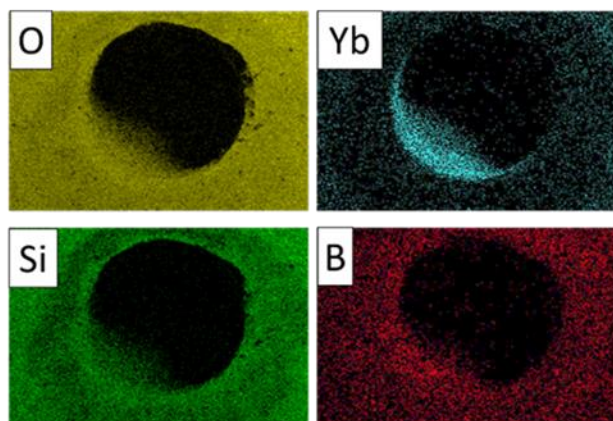
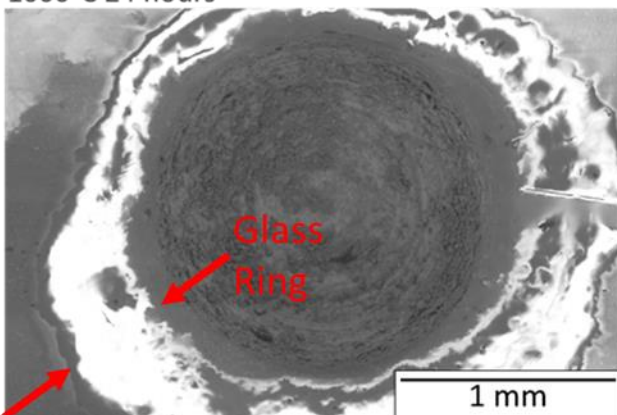


Figure 2.3 Plan-view SEM image of $\text{Yb}_2\text{Si}_2\text{O}_7$ sample after exposure to B_2O_3 for 24 h at 1000°C .

The EDS signal drops out inside of the well due to the depth and angle of the EDS detector.

While only observed in one instance, Figure 2.4 shows small dendrites in surface glass “pools” that had collected in dimpled surface features roughly 2 mm from the well edge in a 24h exposure at 1000°C. The high contrast in the backscattered electron images within the surrounding glass suggests that these are Yb-rich dendrites.

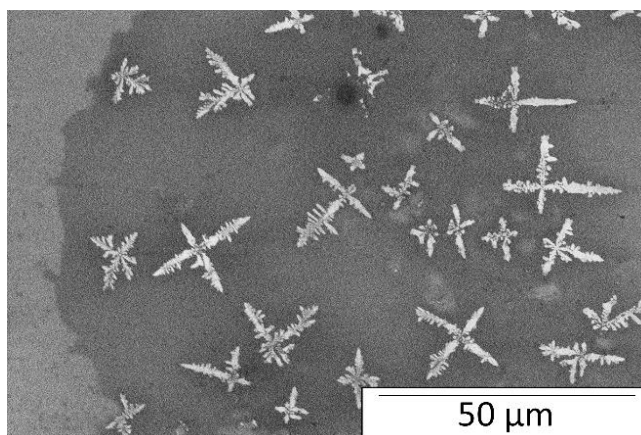


Figure 2.4 Plan-view SEM back-scattered image of dendrites in a surface “pool” of glass after $\text{Yb}_2\text{Si}_2\text{O}_7$ exposure to B_2O_3 at 1000°C for 24 hours. The high contrast from the backscattered electron image suggests that the dendrites are Yb-rich.

Samples were examined in plan-view post-soak to qualitatively observe differences in the composition of the glass remaining on the surface of samples. Not all the surface glass was removed during the water soak. The solubility of borosilicate glasses in water is known to decrease with increasing silica content (7). Increasing amounts of glass remained on the sample surface post-soak with both increasing temperature and time indicating that the glass is becoming more silica rich. Plan-view BSE SEM images after exposure for 24 h at 800°C, 1000°C, and 1200°C are shown in Figure 2.5 to demonstrate temperature-dependent changes in surface glass composition. Plan-view BSE SEM images after exposure for 3, 8, and 24 h at 1000°C are shown in Figure 2.6 to demonstrate time-dependent changes in surface glass composition.

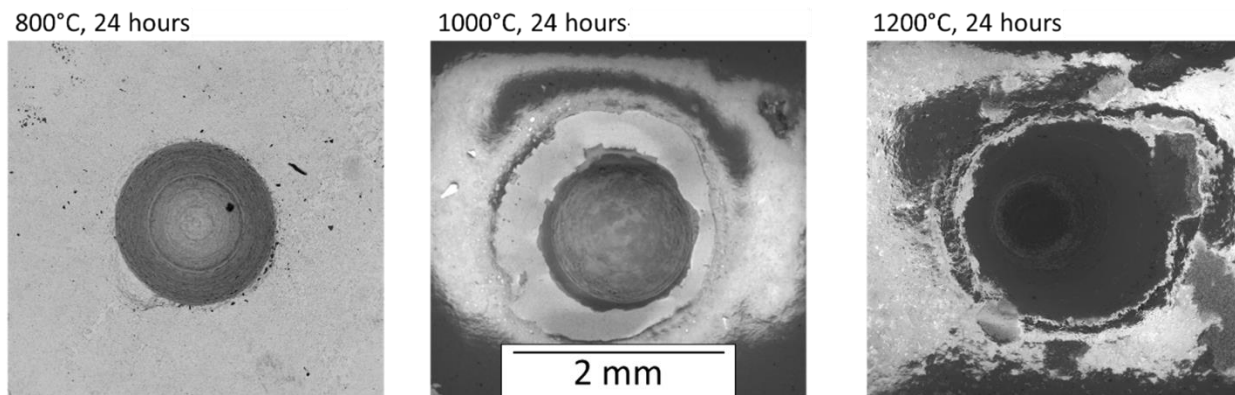


Figure 2.5 Plan-view BSE SEM images of $\text{Yb}_2\text{Si}_2\text{O}_7$ well surface after 24 h exposure to B_2O_3 at 800°, 1000°, and 1200°C, and post-soak in 80°C DI H_2O for 48 hours. More glass remains on the surface with increasing exposure temperature, indicating that the glass becomes more silica rich.

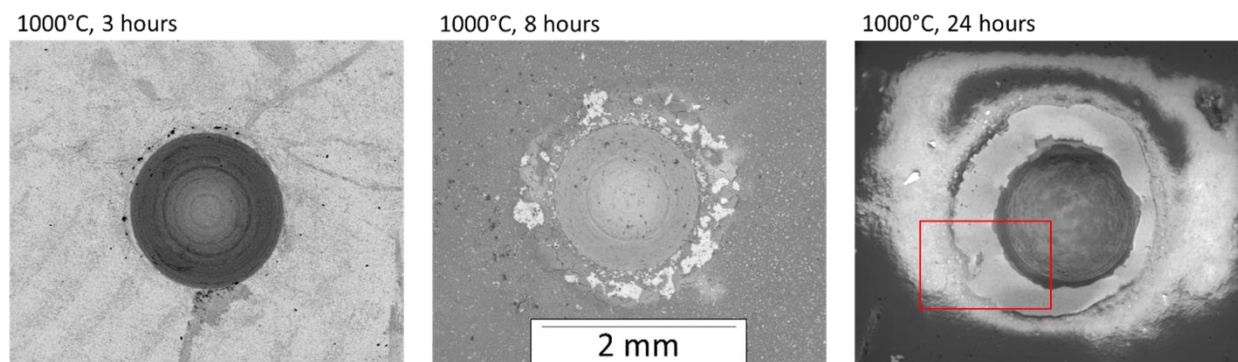


Figure 2.6: Plan-view BSE SEM images of $\text{Yb}_2\text{Si}_2\text{O}_7$ well surface after 3, 8, and 24 h exposure to B_2O_3 at 1000°C, post-soak in 90°C DI H_2O for 48 hours. More glass remains on the surface with increasing exposure time, indicating that the glass becomes more silica rich.

In the case of the 1000°C, 24 h test, the glass is completely removed from the area outside the ring surrounding the well post-soak, exposing the underlying $\text{Yb}_2\text{Si}_2\text{O}_7$ as shown in Figure 2.7 (left) below which is a higher magnification image of the area outlined in red in Figure 2.6. This exposed substrate, marked with a red box in Figure 2.7 was the area in which the micro-XRD scans were performed. A higher magnification micrograph is shown in Figure 2.7 (right).

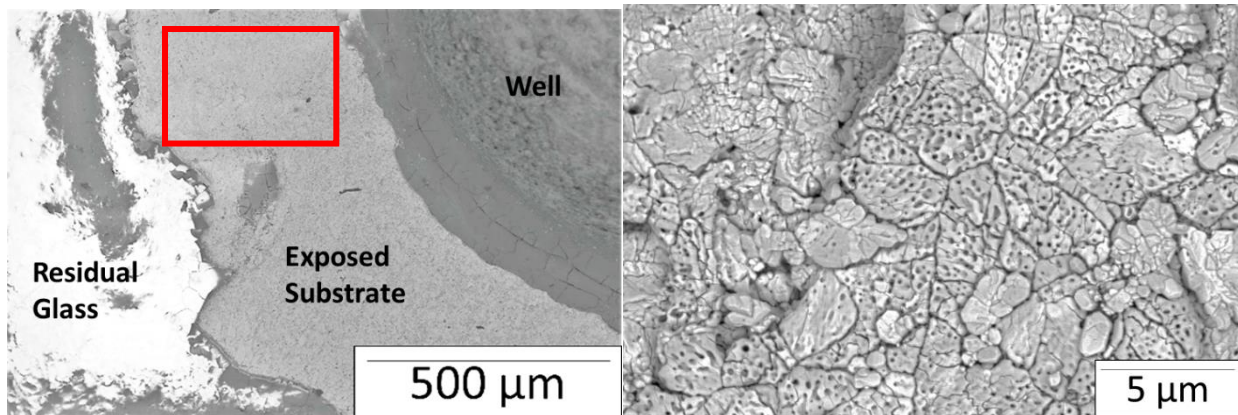


Figure 2.7: (Left) Plan-view SEM BSE imaging shows charging glass and exposed ring of substrate surrounding the drilled well following 24h $\text{Yb}_2\text{Si}_2\text{O}_7$ furnace exposure to B_2O_3 at 1000°C and removal of soluble glass via water soaking. (Right) Higher magnification imaging of the exposed surface shows pores inside the grains.

As shown in Figure 2.7, there are pores visible within the surface grains following exposure and post-soak, suggesting a volume change accompanying phase change or a selective leeching process. Micro-XRD results, shown in Figure 2.8, of this exposed surface confirm that these phases consist of a reaction product, ytterbium borate (YbBO_3), and minor amounts of the initial reactant, $\text{Yb}_2\text{Si}_2\text{O}_7$.

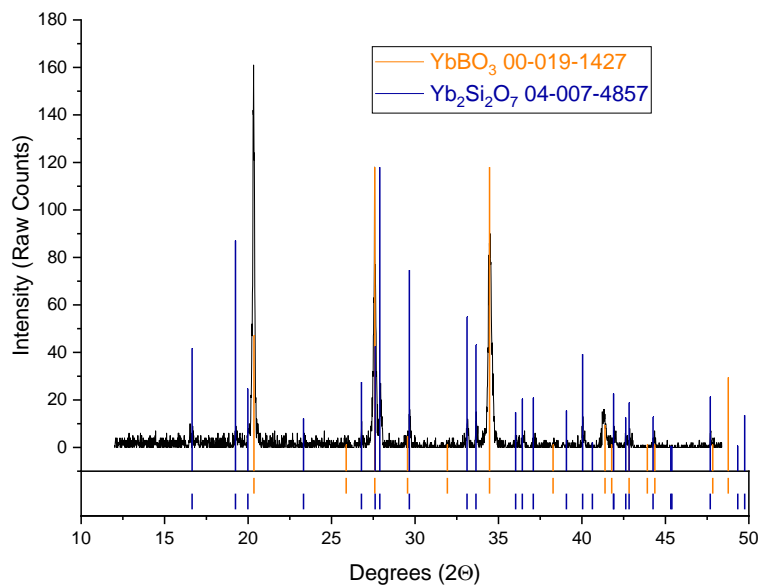


Figure 2.8: Micro-XRD data taken from the surface of $\text{Yb}_2\text{Si}_2\text{O}_7 + \text{B}_2\text{O}_3$ after exposure for 24 h at 1000°C and post-soak in 80°C DI water for 48 hours.

2.3.1.2 ICP-OES

ICP-OES analysis of the water soak solutions indicated that, for all cases, less than 4 ppm of Yb was present in the solution. Baseline soaks of $\text{Yb}_2\text{Si}_2\text{O}_7$ in DI water showed 0.0336 ppm Yb, less than the standard error for ICP (± 0.05 ppm) indicating that the measured ytterbium signal for the well tests is due to dissolution of the ytterbia in the borosilicate glass. This ICP-OES result is consistent with the high-contrast dendrites observed in the borosilicate glass on the surface of the pre-soaked samples (Figure 2.4). In all cases, Yb showed the lowest cation concentration in the solutions, indicating that very little Yb_2O_3 dissolves either into soluble glass or the water soak itself. Table 2-4 and Figure 2.9 compare the ratio of silicon to boron determined through ICP-OES to examine the time and temperature dependent compositional change of the water-soluble glass. Graphed errors are based on propagation of error calculations (8), which scale with the magnitude of the average measured value. This leads to the large errors for the 1200°C data, and errors smaller than the size of the data point marker for 800°C and 1000°C. A maximum in the Si:B ratio is observed after three hours at 800°C and at 1200°C. These results will be examined further in the discussion section.

Table 2-4: Ratio values and Calculated errors for ICP measurements of the Si:B ratio in the glass removed during the soak.

	800°C				1000°C				1200°C			
Time	1	3	8	24	1	3	8	24	1	3	8	24
B:Si ratio	0.031	0.624	0.303	0.398	0.193	0.088	0.682	0.757	0.832	7.292	4.079	1.691
Error Value	0.001	0.042	0.010	0.022	0.008	0.007	0.030	0.116	0.053	3.174	2.008	0.875

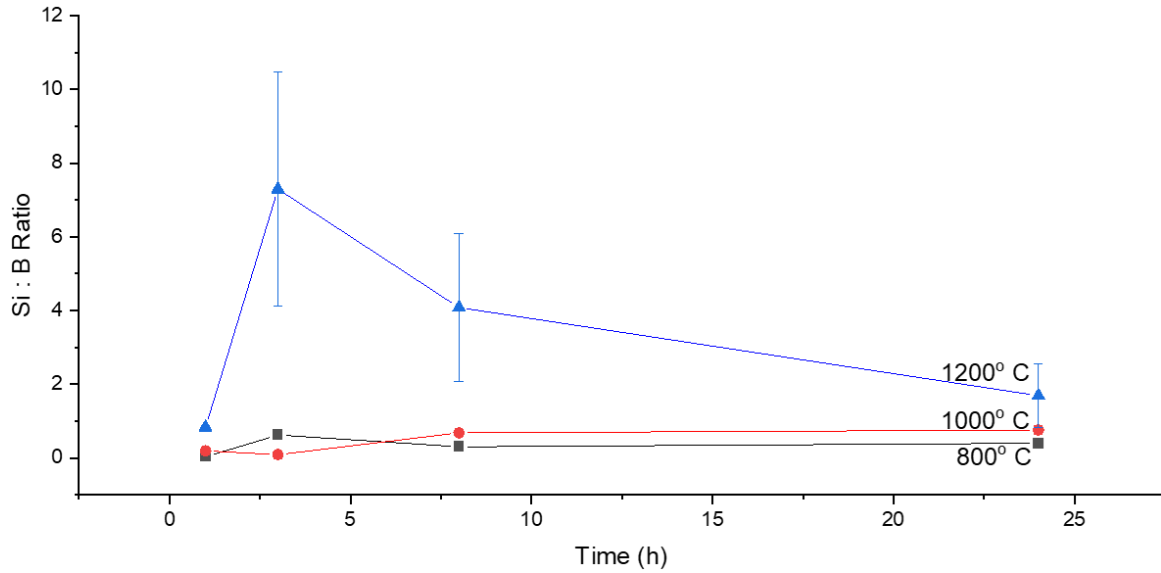


Figure 2.9: Silicon to boron ratio (Si: B) as a function of time and temperature from ICP-OES analysis of water-soluble glasses/reaction products dissolved from $\text{Yb}_2\text{Si}_2\text{O}_7$ sample surfaces after exposure to B_2O_3 . Note the error bars for the data at 800 and 1000 °C are smaller than the symbols.

2.3.1.3 Cross-Section Characterization

Polished cross-sections of $\text{Yb}_2\text{Si}_2\text{O}_7$ samples after B_2O_3 exposure show reaction layers present between the remaining glass and the edges of the $\text{Yb}_2\text{Si}_2\text{O}_7$ well. In addition, cracks attributed to SPS processing or the well drilling are filled with glass and show similar reaction layers to those seen on the well sides as illustrated in Figure 2.10 and observed in Figure 2.11 below.

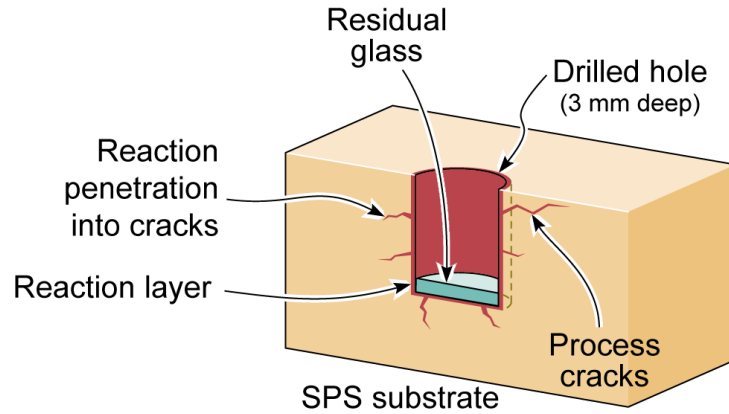


Figure 2.10: Diagram of a cross-sectioned well test sample (not soaked in DI H₂O) showing well, residual glass, and reaction layers penetrating the cracks remaining from SPS processing.

Further inspection of the reaction layers shows two morphologies (Figure 2.11). Immediately adjacent to the Yb₂Si₂O₇ substrate are columnar grains that are also seen in the reaction layer found in branching cracks. Additionally, bright contrast (by BSE SEM), porous clusters of equiaxed grains are seen trapped in remaining glass which are ytterbia-containing phases.

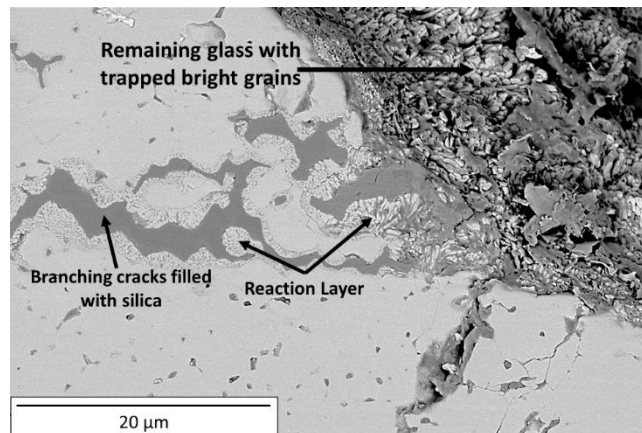


Figure 2.11 Cross-section BSE SEM image showing the YbBO₃ reaction layers (B₂O₃ exposure, 1000°C, 24 hours) along the edge of the Yb₂Si₂O₇ well (Top right) and in processing cracks leading away from the well. Reaction layers show a columnar structure at the interface with porous clusters of glass overtop in the well. Glass has filled the processing cracks leading away from the well.

The columnar grain reaction layer is clearly observed in the glass-filled branching cracks, as shown in Figure 2.12. Qualitative EDS mapping and semi-quantitative EDS point analysis show that the glass that has filled the cracks is rich in silicon, lean in boron, and shows no quantifiable trace of ytterbium. The reaction layers show an increase in boron signal, and very little silicon signal, indicating depletion of silicon from those areas and an enrichment of boron, consistent with the presence of the Yb-borate phase observed in the surface reaction layers via the μ -XRD testing. EDS of the unaffected substrate remains consistent with that of the disilicate starting phase.

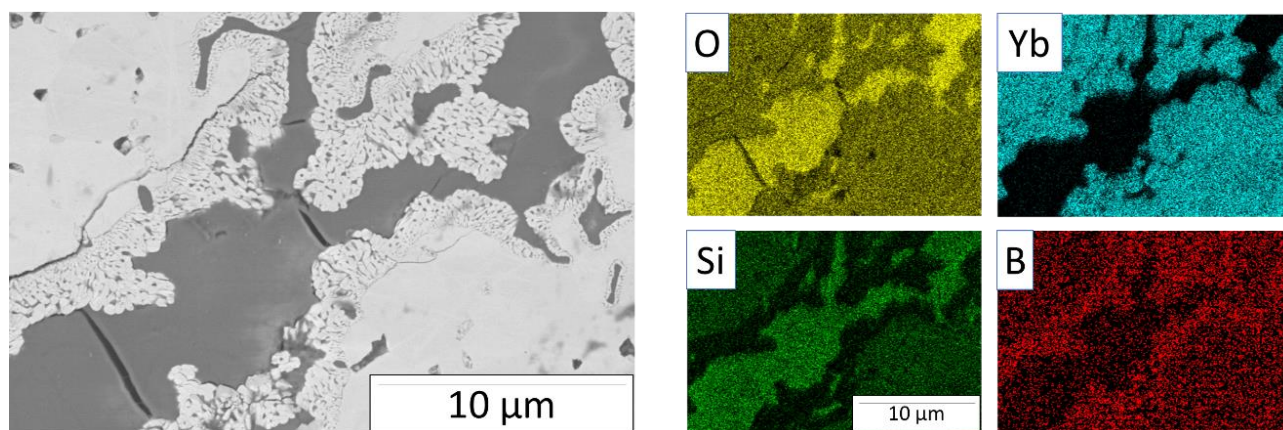


Figure 2.12: 1000°C, 24-hour Exposure. Higher magnification cross-section BSE SEM image of a glass-filled crack. Elemental mapping shows that remaining glass is silicon-rich and that reaction layers are depleted in silicon and enriched in boron.

FIB milling was used to remove a thin section across one of these glass-filled branching cracks and surrounding reaction layers to further investigate the crystal structure of the reaction layers through TEM diffraction analysis (Figure 2.13). Analysis via TEM selected area electron diffraction (SAED) confirms that material in the cracks is amorphous and the unaffected substrate is composed of polycrystalline ytterbium disilicate.

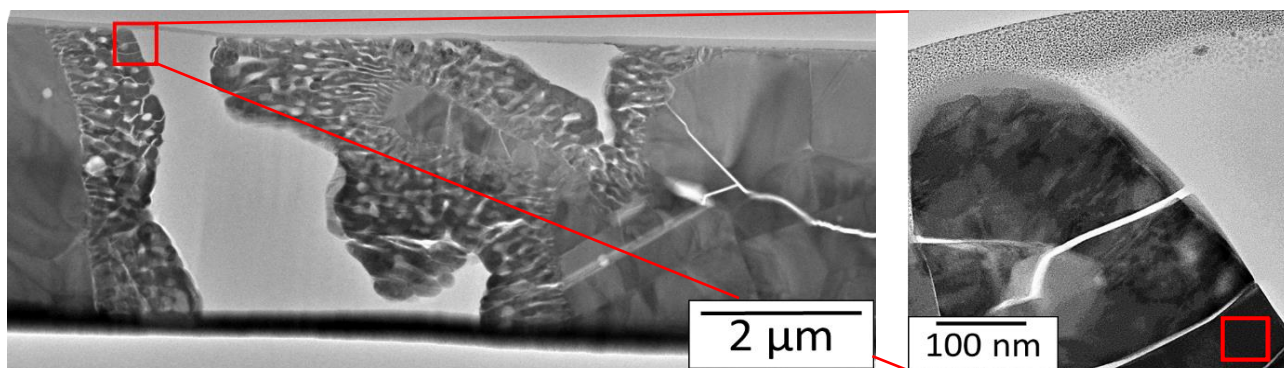


Figure 2.13 (Left) 1000°C, 24h $\text{Yb}_2\text{Si}_2\text{O}_7 - \text{B}_2\text{O}_3$ sample exposure. FIB Section taken across the glass-filled branching crack/ reaction layer interface. (Right) Higher magnification micrograph highlighting the area in which SAED was conducted.

Two TEM diffraction patterns were obtained. Analysis of the TEM SAED pattern in Figure 2.14a reveals a 6-fold symmetry zone axis and reciprocal lattice spacings of 1.79 nm^{-1} for the first order reflections. Table 2-5 lists the phases considered in identifying the reaction product. This combination of both symmetry and g-spacings for the first order reflections matched $\{11\bar{1}0\}$ for hexagonal YbBO_3 with a P-6c2 space group as shown in Table 2-5 (9,10).

Table 2-5: Possible Yb-borate phase candidates for SAED analysis including space groups and g-spacings for comparison. Potential as a match and associated reasoning shown in the right two columns.

Reference Pattern	Space Group	g-spacing	Match?	Reasoning
Yb_2O_3	P1	$<1.7 \text{ nm}^{-1}$	No	No 3-fold symmetry
Yb_2SiO_5	P21/c	1.71 nm^{-1}	No	No 3-fold symmetry
$\text{Yb}_2\text{Si}_2\text{O}_7$	A2/m	1.88 nm^{-1}	No	No 3-fold symmetry
YbBO_3 (rhombohedral)	R-3c	4.05 nm^{-1}	No	g-spacing does not match
$\text{Yb}_{26}\text{B}_{12}\text{O}_{57}$	C12/m1	-	No	No 3-fold or 6-fold symmetry
YbBO_3	P-6c2	1.77 nm^{-1}	Yes	g-spacings match & 6-fold
YbBO_3	P63/mmc	2.29 nm^{-1}	No	First g-spacing is too large
$\text{Yb}_3\text{B}_5\text{O}_{12}$	Pnma	-	No	No 3-fold symmetry

The first diffraction pattern (Figure 2.14 a) matches the simulated pattern for the hexagonal YbBO_3 $\langle 0001 \rangle$ zone axis. The second diffraction pattern (Figure 2.14 c) matches the $\langle 2\bar{2}43 \rangle$ zone axis for YbBO_3 , confirming this phase identification. A comparison of the experimentally obtained SAED diffraction patterns (a, c) with the simulated patterns (b, d) for this YbBO_3 phase is shown in Figure 2.14. (9–11)

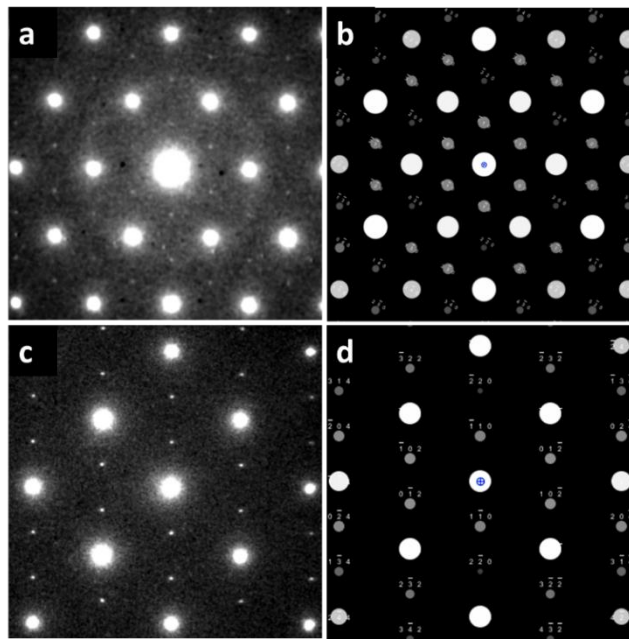


Figure 2.14: TEM SAED patterns of a reaction layer from $\text{Yb}_2\text{Si}_2\text{O}_7$ sample exposed to B_2O_3 at 1000°C for 24 hours. (a&c) The pattern obtained from boxed area in Figure 2.13 (Right) of the reaction layer adjacent to the glass-filled branching cracks. (b&d) Simulated patterns of hexagonal YbBO_3 . (Top) $\langle 0001 \rangle$ zone axis. (Bottom) $\langle 2\bar{2}43 \rangle$ zone axis. (9–11)

2.3.2 Yb_2SiO_5 & Yb_2O_3 Substrates

2.3.2.1 Plan View Characterization

Yb_2SiO_5 and Yb_2O_3 substrates were also exposed to B_2O_3 at 1000°C for 24 hours for comparison to the $\text{Yb}_2\text{Si}_2\text{O}_7$ substrate tests. This time and temperature were chosen as these conditions showed the most obvious signs of reactions for the B_2O_3 on the $\text{Yb}_2\text{Si}_2\text{O}_7$ substrates. Pre- DI H_2O soak imaging of the Yb_2SiO_5 substrates, shown below in Figure 2.15 exhibits similar behavior to the $\text{Yb}_2\text{Si}_2\text{O}_7$ substrates with the boria wicking out of the well along the surface of the substrate with a thicker glass ring immediately surrounding the well. This ring is less evident for the Yb_2O_3 substrate.

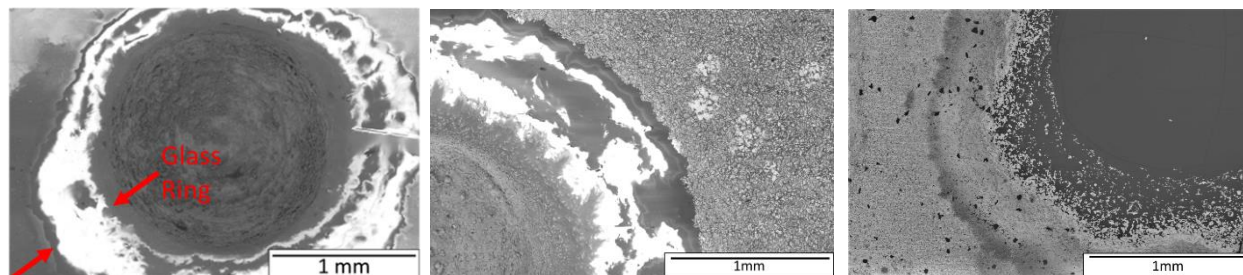


Figure 2.15: Comparison of $\text{Yb}_2\text{Si}_2\text{O}_7$, Yb_2SiO_5 , and Yb_2O_3 (Left-Right) substrates in plan view pre-soak showing the well and the ring of boria-rich glass surrounding it after exposure at 1000°C for 24 hours in the stagnant air box furnace.

Figure 2.16 shows images of the substrates after DI H_2O soak at 80°C for 48 hours. For the monosilicate samples, remaining glass is present further from the well out to the edges of the substrate, however this glass is not present on the Yb_2O_3 substrates as expected due to the lack of silica in that system.

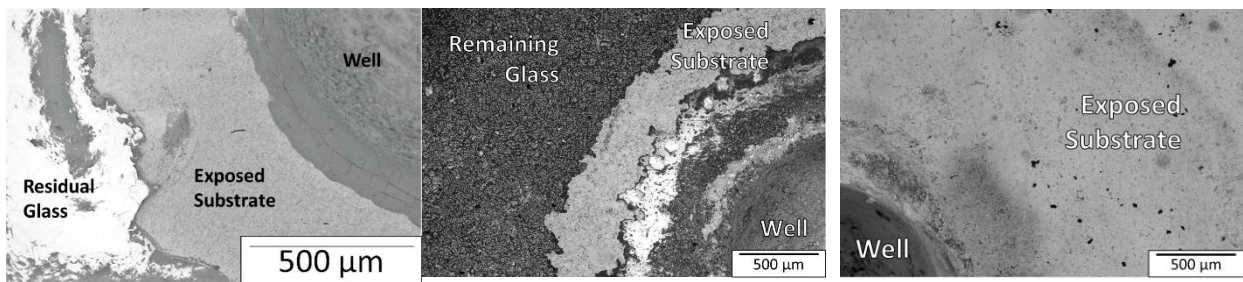


Figure 2.16: Comparison of outer edges of wells in plan view post-soak of the $\text{Yb}_2\text{Si}_2\text{O}_7$, Yb_2SiO_5 , and Yb_2O_3 substrates (Left – Right) show the reaction layers and exposed substrate rings after the water-soluble products were removed. No glass remains on the surface of the Yb_2O_3 substrate due to a lack of silica in the system.

Looking more closely at the exposed, reacted regions, a porous grain structure is visible on both the monosilicate and ytterbia surfaces where the substrate had been in contact with the glass indicating that they did react similarly to the $\text{Yb}_2\text{Si}_2\text{O}_7$ substrates as shown below in Figure 2.17.

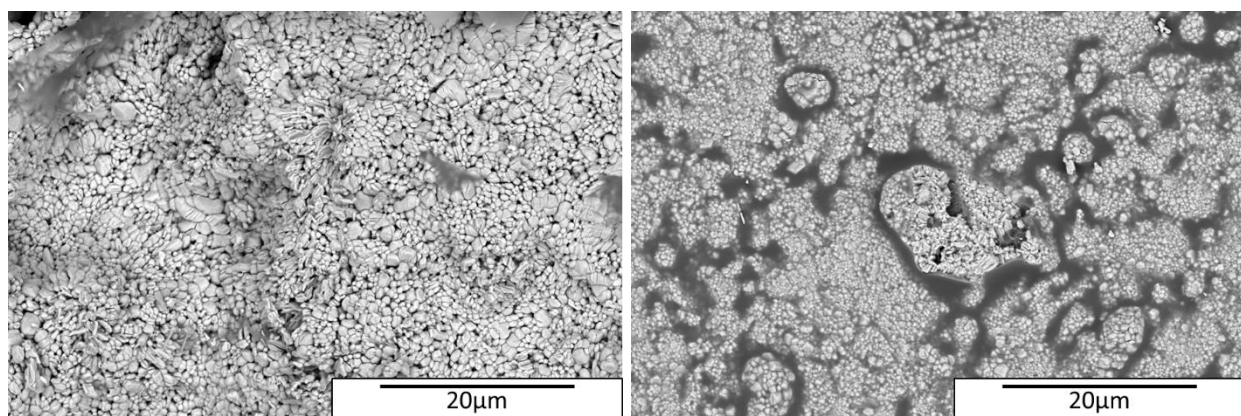


Figure 2.17: Close ups of the well test top surfaces (L: Yb_2SiO_5 , R: Yb_2O_3) post-soak in 80°C DI H_2O for 48 hours showing a small, granulated grain structure with residual borate & glassy phases.

2.3.2.2 ICP-OES:

Because silica is present in only half the amount for the monosilicate substrate relative to the disilicate and is not present at all in the ytterbia substrate, comparing the boron to silicon ratios for these substrates does not offer insight to the reaction as observed for the disilicate.

However, the ICP measurements of the removed glass and reaction product does lend insight

to the solubility of Yb_2O_3 in B_2O_3 . Shown below in Figure 2.18 and Figure 2.19 are the concentrations removed during the soak. For the Yb_2SiO_5 (or YbMS) substrate tests, the amount of material measured has no discernable trends with time. For the Yb_2O_3 substrate tests, the amount of boron decreases significantly when the 24h tests are compared to the 8h tests indicating that more boria is lost to atmospheric volatilization as it is not reacting with the silica to form the borosilicate glass on the substrate surface.

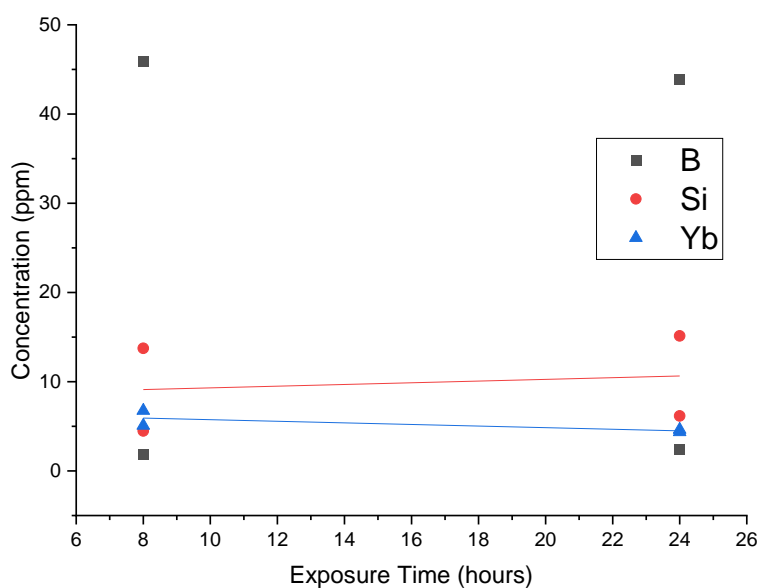


Figure 2.18: Amount of material measured in ICP for two Yb_2SiO_5 substrates exposed at each 8h and 24h with B_2O_3 at 1000°C . Linear fits shown to guide the eyes.

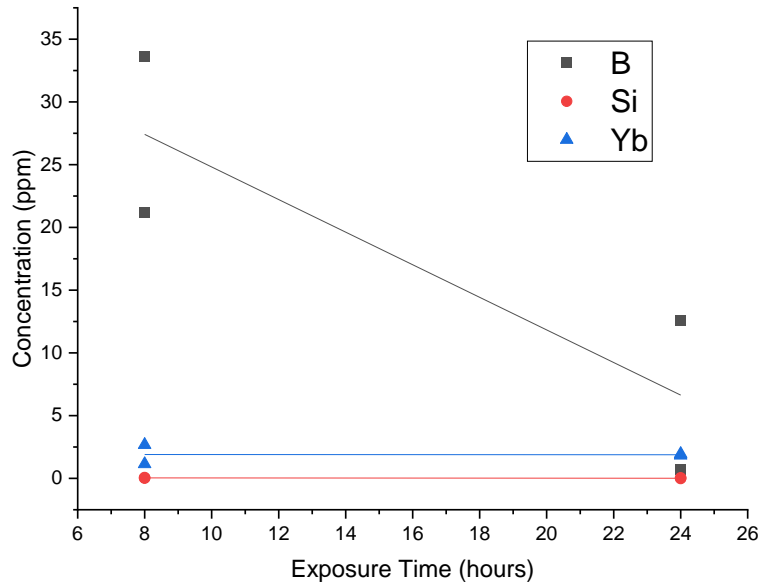


Figure 2.19: Amount of material measured in ICP for two Yb_2O_3 substrates exposed at each 8h and 24h with B_2O_3 at 1000°C . Linear fits shown to guide the eyes.

2.3.2.3 Cross-Section Characterization

Processing cracks observed in both the $\text{Yb}_2\text{Si}_2\text{O}_7$ and the Yb_2O_3 well test cross sections were lined with a porous reaction layer. These cracks were filled with glass in the monosilicate as shown in Figure 2.20. The reaction layer was confirmed to be YbBO_3 using micro-focus XRD as shown in Figure 2.21. The Yb_2O_3 substrate cracks have not filled with glass and instead filled with epoxy from the mounting process as shown in Figure 2.22. This is attributed to the lack of silica in the substrate to exchange with the boria and is consistent with the lack of glass remaining on the surface of the Yb_2O_3 well test substrates after the soak for ICP-OES. The presence of the borate product phase has also been confirmed with micro-focus XRD for the Yb_2O_3 substrates as shown in Figure 2.23.

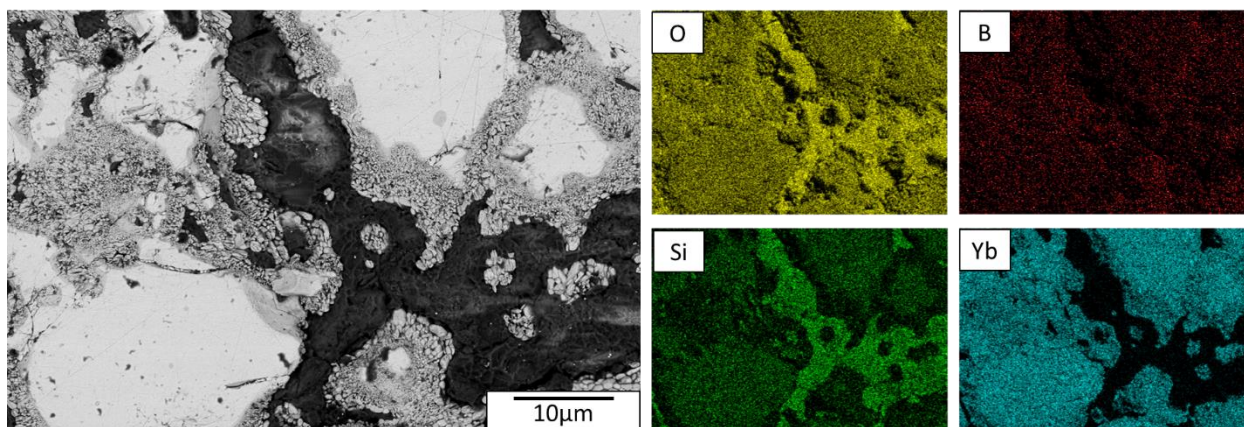


Figure 2.20: Reaction layers in cracks for Yb_2SiO_5 substrate exposed to B_2O_3 at 1000°C for 24 hours with EDS maps showing depletion of silica from reaction layers and into the glass-filled crack.

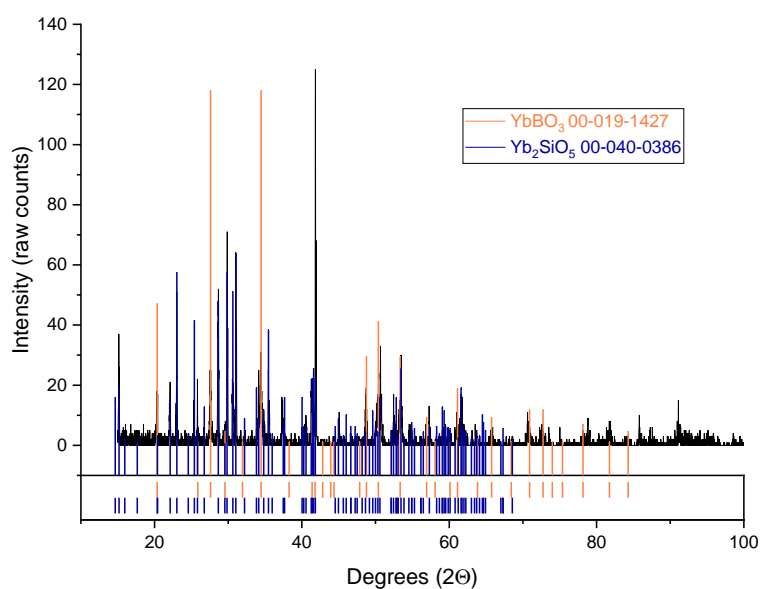


Figure 2.21: Micro-focus XRD results showing presence of YbBO_3 phase in the Yb_2SiO_5 reaction layers after substrate was exposed to B_2O_3 for 24h at 1000°C .

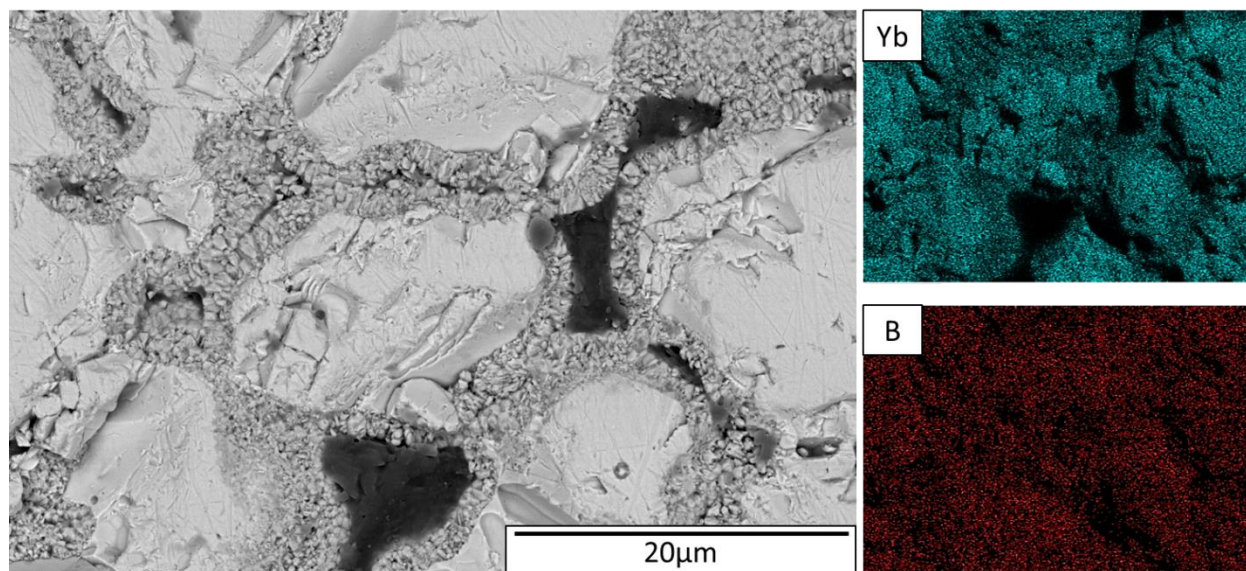


Figure 2.22: Yb_2O_3 substrate in cross section showing reaction layer with EDS after 24h to B_2O_3 at 1000°C .

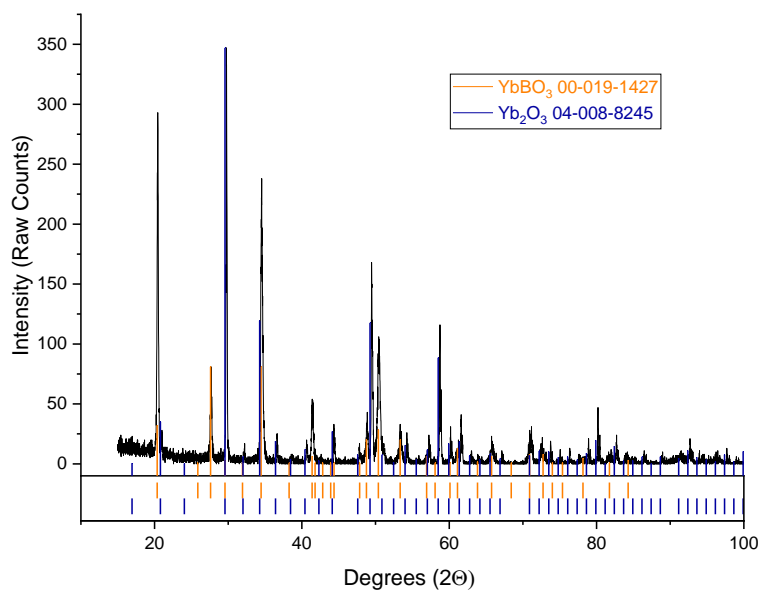
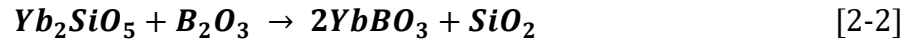
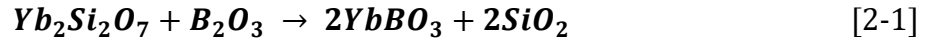


Figure 2.23: Micro-focus XRD results showing presence of YbBO_3 phase in the Yb_2O_3 reaction layers after substrate exposure to B_2O_3 for 24h at 1000°C .

2.4 Discussion

The glass remaining on the surface of the silicate samples post-soak combined with the presence of YbBO₃ suggest a newly identified reactions that occur when Yb₂Si₂O₇, Yb₂SiO₅, and Yb₂O₃ are in contact with B₂O₃. The proposed displacement reactions for the silicates, shown in Equations [2-3] and [2-4], indicate that the boria selectively leeches the silica from the silicate substrate and reacts with the remaining ytterbia to form the hexagonal YbBO₃ phase, and leaving behind the silica-rich glass. In the case of the Yb₂O₃ substrate, there is no silica to displace in the substrate, so the reaction consists solely of the formation of YbBO₃ from Yb₂O₃ and B₂O₃ as shown in Equation [2-5] below.



These reactions are supported by SAED for the Yb₂Si₂O₇ exposure and micro-XRD of all three substrates, which show YbBO₃ as a stable reaction product for all three systems. The glass in the branching cracks and the increasing amounts on the surface of the samples post-soak with both time and temperature indicate an increase in silica content in the glass. The only silica in the system before exposure is that in the disilicate substrate, indicating that it is selectively exchanged from the substrate during the exposure. The YbBO₃ phase unit cell (compared for 2 Yb cations) is smaller than that of Yb₂Si₂O₇ by ~19%, Yb₂SiO₅ by ~1.5%, and Yb₂O₃ by ~44% leading to the porous grains as observed in Figure 2.7 and Figure 2.17. These changes in volume

as the borate forms will be discussed more extensively in Chapter 4: “Investigation of YbBO_3 Properties”.

The silica and boria concentrations in the ICP-OES measurements change with the exposure time and temperature. ICP-OES measurements were only possible for water-soluble products, so this changing B:Si ratio is explained by the amount of boria remaining in the glass after exposure. Ytterbium exhibits limited solubility in the boria as evidenced by precipitation out of the glass as dendrites and the low ICP-OES concentration measurements for all exposure conditions.

There are three different reaction mechanisms that account for the increase of silicon in the glass, the first being the volatility of the boria. As tests were conducted in lab air, boria volatilized during the test. A plot of the $\text{B}_2\text{O}_3(\text{g})$ pressure with temperature can be seen below in Figure 2.24 showing the high activity of $\text{B}_2\text{O}_3(\text{g})$.

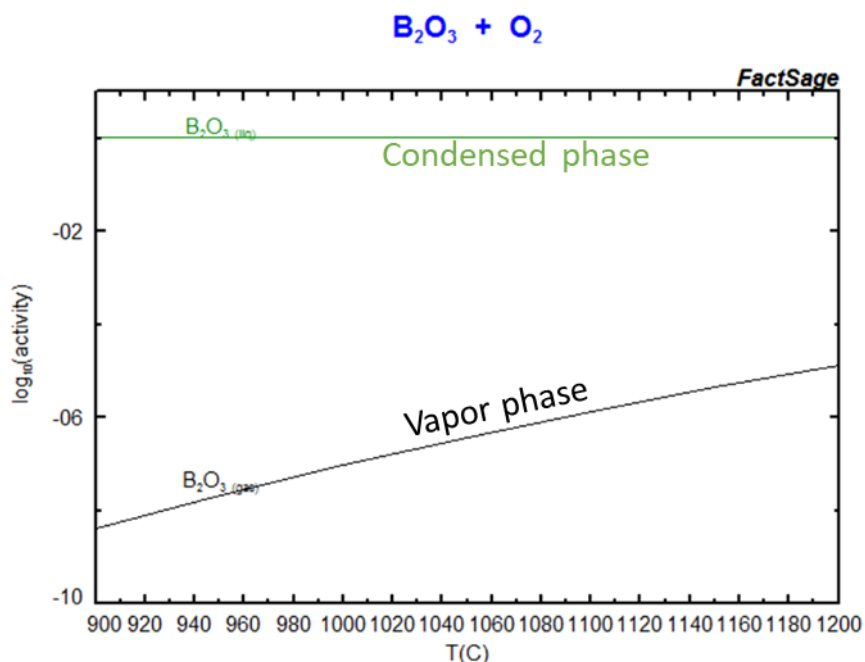


Figure 2.24: FactSage Simulation of $\log(\text{activity})$ vs. temperature for B_2O_3 in O_2

Concurrently, the selective production of silica paired with the consumption of boria to form YbBO_3 also increased the Si:B ratio in the glass. These reactions both lower the water solubility of the glass by raising the silica to boria ratio, the first by increasing the silica content directly, and the second by depleting the glass of boria. The increasing SiO_2 content in the glass is counteracted by the decreasing water solubility of the glass resulting in a maximum in the Si to B ratio after 3 hours at 1200°C .

The extent of the effects of YbBO_3 formation on the life of CMC/ EBC systems is currently unknown but may be detrimental. The YbBO_3 phase has a eutectic at 1446°C according to the partial diagram from Levin (shown in Figure 1-4 of the introduction), substantially lower than any of the eutectics associated with the $\text{Yb}_2\text{O}_3 - \text{SiO}_2$ system (12–14). The YbBO_3 phase is forming at temperatures as low as 1000°C after only a few hours, this could drastically reduce the life of these CMC/ EBC systems in the turbine environment. CTE mismatch can result in interfacial stress development and coating spallation. The thermal expansion of the YbBO_3 phase will be investigated in Chapter 4 of this work. Characterizing and understanding the physical properties of YbBO_3 will be crucial to determining its effect on CMC/ EBC systems. Additionally, the formation of silica as a reaction product in the EBC will lead to issues like those observed previously with TGO growth and the $\beta \rightarrow \alpha$ cristobalite transition from crystallization and thermal cycling at the Si bond coat interface (15).

2.5 Summary and Conclusions

Interfacial reaction testing was conducted on SPS-prepared $\text{Yb}_2\text{Si}_2\text{O}_7$, Yb_2SiO_5 , and Yb_2O_3 substrates. Wells were drilled in the substrates and filled with boria glass plugs to explore the reactions between boria and ytterbium-containing substrates. The reaction of the boria and the ytterbium silicates resulted in the formation of a rare earth borate phase, YbBO_3 , and a silica rich glass. It was found for the disilicate and monosilicate substrates that with increasing time and temperature, remaining glass in the samples became less water-soluble, indicating that boria was being removed both via volatility and reaction with the substrates. For the Yb_2O_3 substrate, YbBO_3 was formed from the reaction with the B_2O_3 glass, but no glass remained on the surface of the samples post-soak in water, and no silicate glass of any kind formed due to the lack of silica in the system. These results in total suggest that boria formed during the oxidation of the SiC/ BN/ SiC composite may be detrimental to rare earth silicate environmental barrier coatings through degradation of the EBC and formation of silica and the YbBO_3 phase.

2.6 References

1. Parker CG. Effect of the Air Plasma Spray Process on Rare Earth Silicate Coating Life by. 2020;(May).
2. Stolzenburg F, Johnson MT, Lee KN, Jacobson NS, Faber KT. The interaction of calcium-magnesium-aluminosilicate with ytterbium silicate environmental barrier materials. *Surface and Coatings Technology* [Internet]. 2015; 284:44–50. Available from: <http://dx.doi.org/10.1016/j.surfcoat.2015.08.069>
3. McFarland B, Angelici Avincola V, Morales M, Opila E. Identification of a new oxidation/dissolution mechanism for boron-accelerated SiC oxidation. *Journal of the American Ceramic Society*. 2020;103(9):5214–31.
4. Granneman SJC, Shahidzadeh N, Lubelli B, van Hees RPJ. Effect of borax on the wetting properties and crystallization behavior of sodium sulfate. *CrystEngComm* [Internet]. 2017 Feb 13 [cited 2021 Jun 3];19(7):1106–14. Available from: <https://pubs.rsc.org/en/content/articlehtml/2017/ce/c6ce02163h>
5. Saunders T, Tatarko P, Grasso S, Reece MJ. Effectiveness of boron welding flux in improving the wettability of ZrB₂ in contact with molten Cu. *Journal of the European Ceramic Society*. 2018 Sep 1;38(12):4198–202.
6. Peterson EI. Mold flux crystallization and mold thermal behavior [Internet]. [cited 2021 Jun 3]. Available from: https://scholarsmine.mst.edu/masters_theses/https://scholarsmine.mst.edu/masters_theses/7656
7. Brückner R, Navarro JF. Physikalisch-chemische untersuchungen im system B₂O₃-SiO₂. *Glastech. Ber.* 1966;39(6):283-94.
8. Taylor JR, Taylor SLLJR. Introduction To Error Analysis: The Study of Uncertainties in Physical Measurements [Internet]. University Science Books; 1997. (ASMSU/Spartans.4.Spartans Textbook). Available from: <https://books.google.com/books?id=giFQcZub80oC>
9. Generated using SingleCrystal (TM): a single-crystal diffraction program for Mac and Windows [Internet]. Oxford, England; Available from: www.crystallmaker.com
10. Newnham RE, Redman MJ, Santoro RP. Crystal Structure of Yttrium and Other Rare-Earth Borates. *Journal of the American Ceramic Society*. 1963;46(6):253–6.
11. Bradley WF, Graf DL, Roth RS. The vaterite-type ABO₃ rare-earth borates. *Acta Crystallographica*. 1966;20(2):283–7.
12. Levin EM, Roth RS, Martin JB. Polymorphism of ABO₃ Type Rare Earth Borates. the *American Mineralogist* [Internet]. 1961;46(1954):1030–55. Available from: http://www.minsocam.org/ammin/AM46/AM46_1030.pdf

13. Levin EM. Structural Interpretation of Immiscibility in Oxide Systems: IV, Occurrence, Extent, and Temperature of the Monotectic. *Journal of the American Ceramic Society*. 1967;50(1):29–38.
14. Levin EM, Robbins CR, Waring JL. Immiscibility and the System Lanthanum Oxide–Boric Oxide. *Journal of the American Ceramic Society*. 1961;44(2):87–91.
15. Richards BT, Begley MR, Wadley HNG. Mechanisms of Ytterbium Monosilicate/ Mullite/ Silicon Coating Failure during Thermal Cycling in Water Vapor. *Journal of the American Ceramic Society*. 2015 Dec 1;98(12):4066–75.

3 Phase Diagram Determination for the $\text{Yb}_2\text{O}_3 - \text{B}_2\text{O}_3$ and $\text{Yb}_2\text{O}_3 - \text{SiO}_2 - \text{B}_2\text{O}_3$ systems.

3.1 Introduction

The goal of this research is to determine the phase relations between boria and the $\text{Yb}_2\text{Si}_2\text{O}_7$ EBC material. Minimal thermodynamic data are available for the $\text{Yb}_2\text{O}_3 - \text{SiO}_2 - \text{B}_2\text{O}_3$ pseudo-ternary system that would provide insight to the interactions between boria and the $\text{Yb}_2\text{Si}_2\text{O}_7$ EBC that is currently used for SiC CMCs.

The $\text{SiO}_2 - \text{B}_2\text{O}_3$ system was studied extensively by Rockett and Foster in the 1960s, and their phase diagram is generally accepted to be the most accurate for the borosilicate system (1). At this same time, the rare earth silicates, including the $\text{Yb}_2\text{O}_3 - \text{SiO}_2$ system, were also explored by Toropov and Bondar (2). Phase equilibrium diagrams for these two systems are shown below in Figure 3.1, but phase equilibria data on the rare earth borates remain scarce.

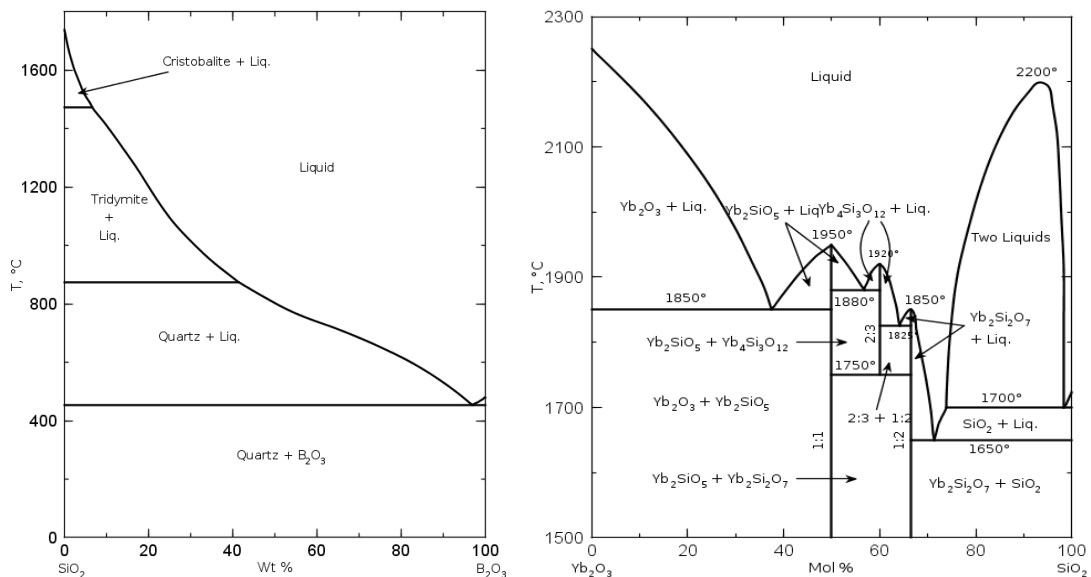


Figure 3.1: (Left) $\text{SiO}_2 - \text{B}_2\text{O}_3$ phase diagram from Rockett & Foster (1). (Right) $\text{Yb}_2\text{O}_3 - \text{SiO}_2$ phase diagram from Toropov & Bondar (2). Diagrams # 2353, 2391 from ACERS-NIST database (29)

Some initial research was conducted on the rare earth borate systems by Newnham, Roth, and Levin in the late 1950s and early 60s. This work focused on liquid immiscibility, borate crystal structures, and polymorphism (3–7). Levin’s incomplete phase diagram for the $\text{Yb}_2\text{O}_3 - \text{B}_2\text{O}_3$ system, shown in Figure 3.2, indicates a suspected phase transition from a low-temperature polymorph to a high-temperature polymorph at 1040°C . It also implies liquid immiscibility on the boria-rich side of the diagram, with limited information as the composition approaches 100% boria. B_2O_3 has a melting temperature of only 450°C , well below the lowest temperature on the published diagram.

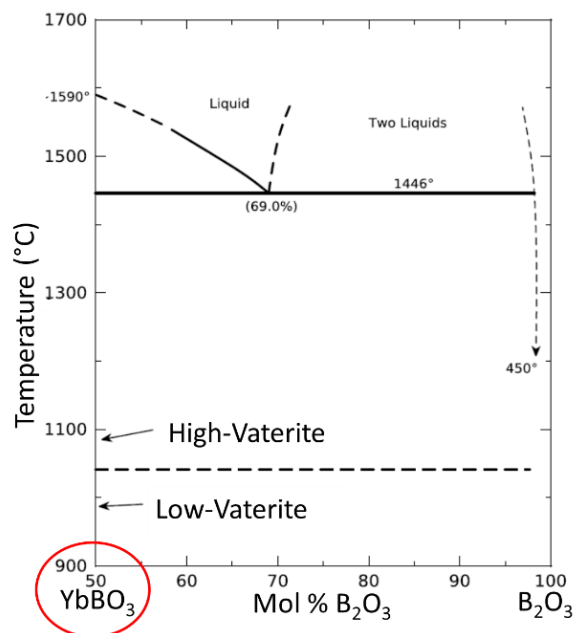


Figure 3.2: Boria rich half of the $\text{Yb}_2\text{O}_3 - \text{B}_2\text{O}_3$ system phase diagram from Levin (7)

More recently, extensive studies were conducted on the structure of gadolinium borate by Ren in 1999 (8) and the $\text{La}_2\text{O}_3 - \text{B}_2\text{O}_3$ system by Dmitruk in 2008 as shown below in Figure 3.3 (9). Despite this interest in rare earth borates however, there is still no complete phase diagram or any thermodynamic data available on the $\text{Yb}_2\text{O}_3 - \text{B}_2\text{O}_3$ pseudo-binary system.

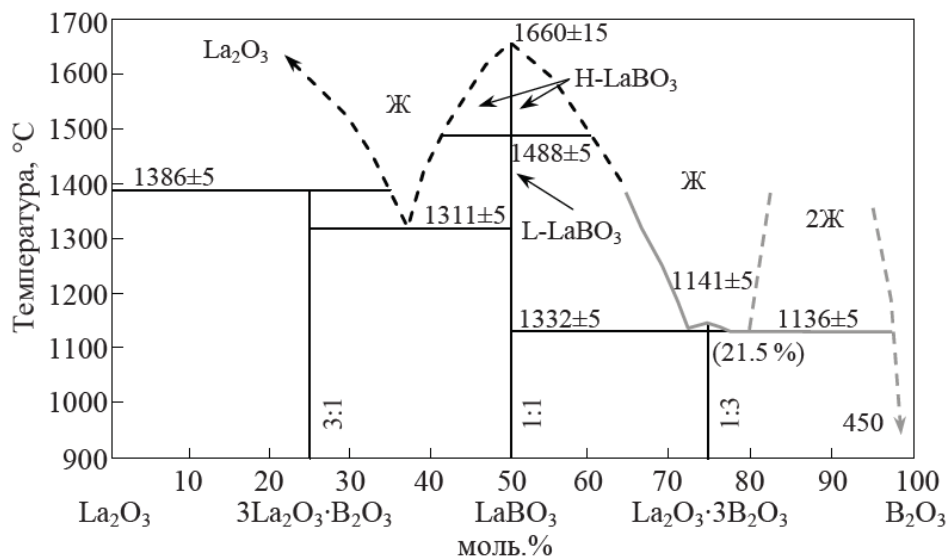


Figure 3.3 La_2O_3 – B_2O_3 phase diagram from Dmitruk (9)

The only phase recorded in the Yb_2O_3 - B_2O_3 system at standard pressures and temperatures is YbBO_3 . Some high-pressure (10 GPa) crystalline phases such as $\text{Yb}_3\text{B}_5\text{O}_{12}$ have been reported in studies on rare earth borate glasses for optical applications (10), however it is unlikely that such phases would form in the CMC/ EBC systems of interest due to the high formation pressures required.

As discussed by Levin and Newnham, YbBO_3 forms in a hexagonal structure analog to vaterite which is most recognized as a metastable polymorph of CaCO_3 . Despite being a metastable phase in the CaCO_3 system, this structure is known to be stable for rare earth borates as shown by Bradley, Graf, and Roth (5). However, there is still great debate as to the exact sub-structure of these vaterite-type borates (11–17). Vaterite is a layered structure, alternating between the two oxide groups as shown in Figure 3.4 below for the CaCO_3 structure. The CO_3 groups, being planar, can take several different orientations as shown in the figure. The debate in the case of the rare earth borate analogs arises from the both the bonding of the borate groups within the

crystal structure as well as uncertainty in the orientation of these groups and therefore the superlattice of the boroxyl ring symmetry (18).

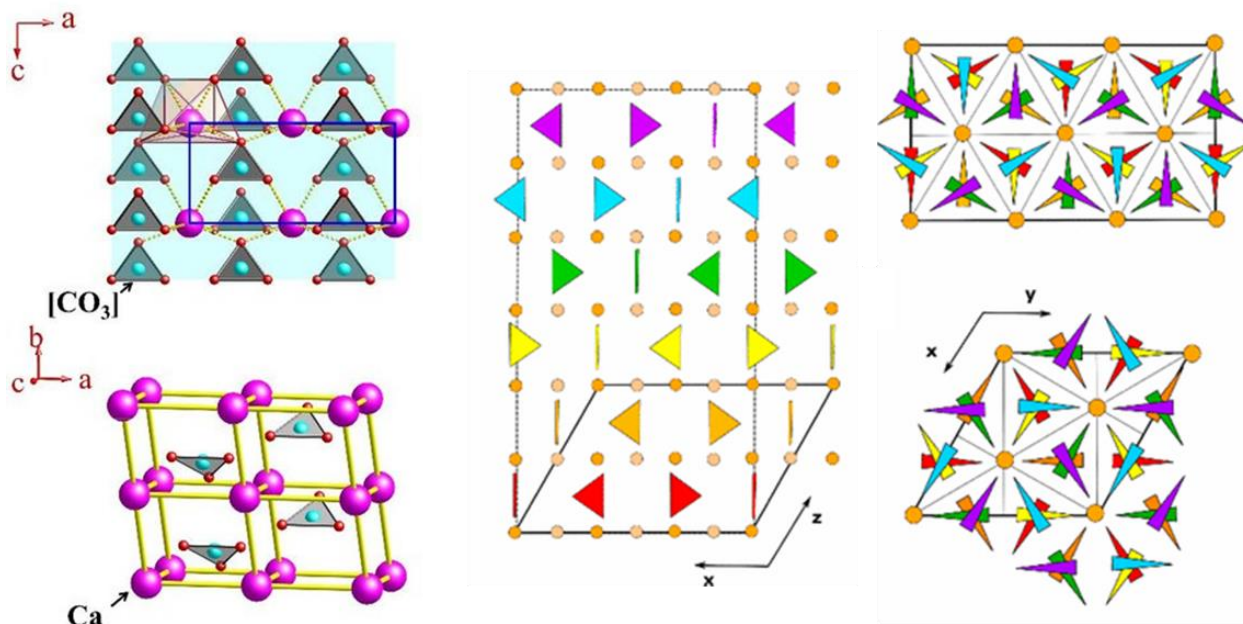


Figure 3.4: (Left) ball and stick model of vaterite showing the CO_3 triangular groups. (19)
 (Center) Side view of vaterite CaCO_3 showing the layering between oxide groups and varied orientations of the CO_3 groups (colored triangles). (Right) top-down views of CaCO_3 vaterite showing the number of different orientation that the CO_3 groups can take within the unit cell. (16)

3.1.1 Computational Predictions for the $\text{Yb}_2\text{O}_3 - \text{SiO}_2 - \text{B}_2\text{O}_3$ System

Given the lack of experimental data on this ternary oxide system, computational databases were surveyed for stable phases for the pseudo-ternary. The two databases discussed here are the OQMD and the Materials Project websites (20,21). These predictive databases can be powerful tools for new systems of materials, though there are some drawbacks. Both OQMD and that Materials Project use DFT (density functional theory) and convex hull theory in their predictions, meaning that all calculations assume a temperature of 0K. As a result, no entropy or temperature effects are considered in looking at phase stability. An example of this is that

Yb_2SiO_5 and B_2O_3 register as “unstable” according to the databases, despite being stable phases at STP conditions. Materials Project relies mostly on experimental data, where OQMD utilizes more predictive phases generated via machine learning. As a result, the two databases often deliver slightly different results when given the same query. An example of this is shown below for the Yb_2O_3 - SiO_2 - B_2O_3 system in Figure 3.5.

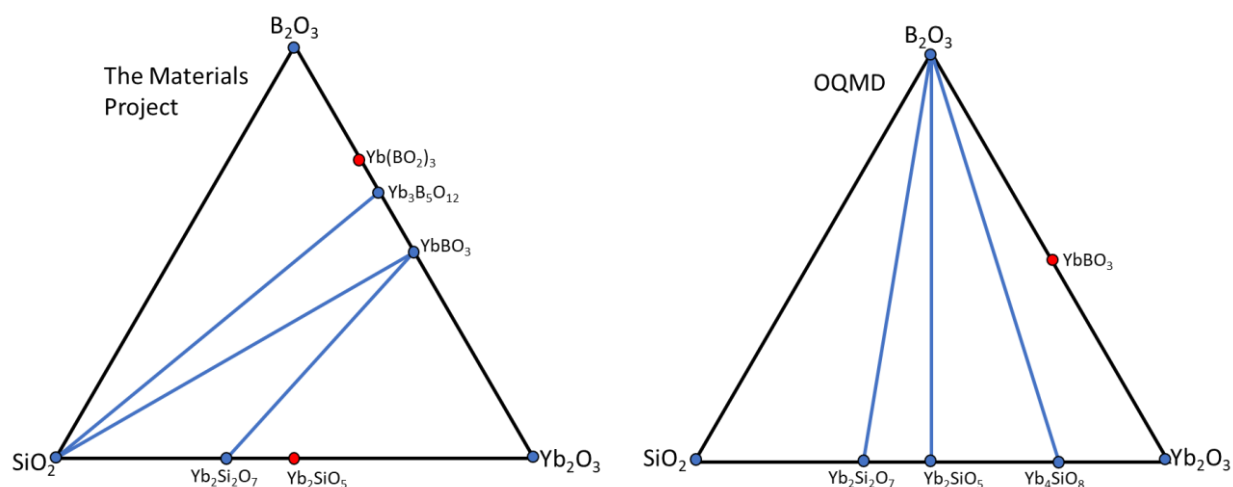


Figure 3.5: Predicted phase diagrams via convex hull theory at 0K for the Yb_2O_3 – SiO_2 – B_2O_3 ternary system. Blue points indicate stable phases, and red dots indicate metastable phases according to convex hull predictions for 0K. The blue lines are Alkemade lines indicating equilibrium between phases.

As shown in the phase diagrams above, the Materials Project and OQMD show different phase stabilities for a given system at 0K, however they still provide useful information for comparison to experimental observations.

3.1.2 Phase Equilibria Testing Methods

Determination of phase equilibria for a given system has traditionally been done using static methods such as those described by Rockett and Foster (1), which utilizes a Pt encapsulation procedure first described by George Morey in 1923 (22). The technique is still in use in the field

of geosciences (23), and will be discussed in Chapter 4 of this work when properties of YbBO_3 are addressed. However, with dynamic testing methods, it is possible to rapidly obtain large phase equilibria data sets. The two methods used in this study are differential scanning calorimetry (DSC) and high-energy X-ray diffraction (HE-XRD). The DSC testing was conducted at UVA, and the high energy diffraction was conducted at The Argonne National Laboratory Advanced Photon Source in Lemont, IL. Both the DSC and high-energy XRD take *in situ* measurements as a function of temperature. The DSC measures heat flux while the XRD measures crystal structure with changing temperature.

3.2 Experimental Methods

For this phase equilibria investigation, compositions of interest were chosen from both the pseudo-binary B_2O_3 - Yb_2O_3 system, as well as compositions from the Yb_2O_3 - SiO_2 - B_2O_3 pseudo-ternary system. Given that boria is known to be reactive and volatile, it is unlikely that more than 30% B_2O_3 would be present in a CMC/ EBC system (24,25). Therefore, compositions were chosen to be ≤ 30 mol B_2O_3 . For the binary system, compositions were chosen to fill out the boria-lean side of the diagram as shown in Table 3.1 below. Compositions start at 10 mol% B_2O_3 and increase in B_2O_3 content by 10% intervals up to 50 mol% B_2O_3 , with the balance being Yb_2O_3 . An additional composition of 75% B_2O_3 – 25% Yb_2O_3 was also selected to verify the portion of the phase diagram published by Levin.

Table 3.1: Binary $\text{Yb}_2\text{O}_3 - \text{B}_2\text{O}_3$ compositions of interest in both molar and weight percent

Sample	mol% B_2O_3	mol% Yb_2O_3	wt% B_2O_3	wt% Yb_2O_3
B1	10	90	1.93	98.07
B2	20	80	4.23	95.77
B3	30	70	7.04	92.96
B4	40	60	10.54	89.46
B5	50	50	15.01	84.99
B6	75	25	34.64	65.36

For the ternary system, the amount of boria was limited to ≤ 30 mol%. Again, compositions were varied in 10 mol% intervals, resulting in testing of the 21 compositions illustrated below on the ternary diagram (Figure 3.6) along with Alkemade lines indicating phase equilibria between the Yb-silicates and Yb-borate. The ternary compositions of interest are also laid out by both atomic and weight percent in Table 3.2. All 27 compositions, both binary and ternary, were probed using both DSC and HE-XRD up to temperatures of 1500°C.

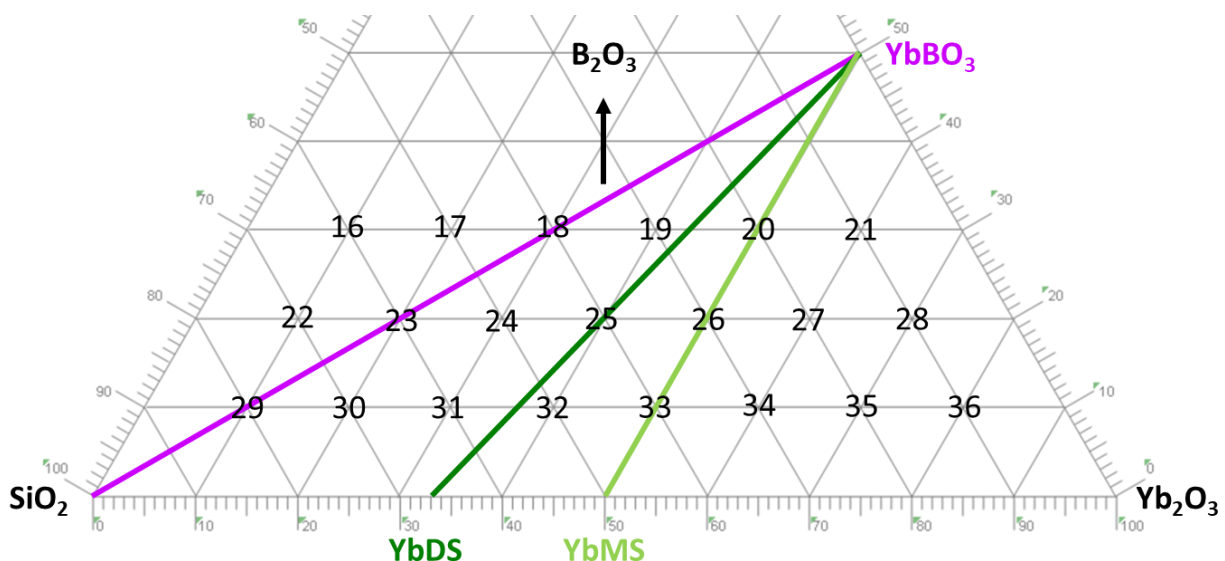


Figure 3.6 $\text{B}_2\text{O}_3 - \text{SiO}_2 - \text{Yb}_2\text{O}_3$ ternary compositions of interest overlaid on a partial ternary phase diagram showing tie Alkemade lines of equilibrium reactions identified with idealized interfacial reaction tests (Chapter 2).

Table 3.2: Ternary sample compositions of interest by both molar and weight percent

Sample	mol% B_2O_3	mol% SiO_2	mol% Yb_2O_3	wt% B_2O_3	wt% SiO_2	wt% Yb_2O_3
T16	30	60	10	21.68	37.42	40.90
T17	30	50	20	16.10	23.15	60.75
T18	30	40	30	12.80	14.73	72.47
T19	30	30	40	10.63	9.17	80.21
T20	30	20	50	9.08	5.23	85.69
T21	30	10	60	7.93	2.28	89.79
T22	20	70	10	14.60	44.09	41.31
T23	20	60	20	10.81	27.99	61.20
T24	20	50	30	8.58	18.52	72.89
T25	20	40	40	7.12	12.29	80.59
T26	20	30	50	6.08	7.87	86.05
T27	20	20	60	5.31	4.58	90.11
T28	20	10	70	4.71	2.03	93.26
T29	10	80	10	7.37	50.90	41.73
T30	10	70	20	5.45	32.90	61.65
T31	10	60	30	4.32	22.36	73.32
T32	10	50	40	3.58	15.43	80.99
T33	10	40	50	3.05	10.54	86.41
T34	10	30	60	2.66	6.89	90.44
T35	10	20	70	2.36	4.08	93.56
T36	10	10	80	2.12	1.83	96.05

3.2.1 Materials and Sample Preparation Methods

All samples were prepared from powders in the ratios in the tables above via mechanical mixing with a borosilicate stir rod in HDPE snap-top containers. Table 3.3 below shows the powder information. PVA was added to DI water and heated to 80°C to make a 2 wt% solution. This PVA solution was added dropwise to the mechanically mixed powders and further mechanically mixed until they formed a viscous paste that could be shaped like clay. For DSC, these pastes were pressed into 6.35mm pellets on a Carver press (unheated benchtop manual press; model no. 3851; Carver Inc. Wabash, IN). For testing at the beamline, the pastes were rolled by hand

into small spherical beads approximately 3mm in diameter. They were then stored in a desiccator to prevent hydration or volatility of boria from the system.

Table 3.3: Powder information for oxides used in phase diagram experiments.

<i>Oxide:</i>	<i>Source:</i>	<i>Purity:</i>	<i>Particle Size:</i>
B_2O_3	Sigma Aldrich	99.98%	Unknown
SiO_2		99.9%	0.2-0.7mm, granular
Yb_2O_3		99.9%	Unknown

3.2.2 Differential Scanning Calorimetry

Pellets of desired compositions (Table 3.1 and Table 3.2) were placed in a platinum pan which sits on a 0.25mm thick sapphire spacer in the DSC (Netzsch Pegasus 404, SiC furnace). Samples were heated to 1500°C in flowing argon at 10 K/min, then cooled at the same rate back to room temperature. The heat needed to keep the sample and empty reference pan at the same temperature is recorded. Any peaks in the heat flow indicate a phase change or chemical reaction at that temperature and allow for further identification of the thermodynamic events occurring in the system.

3.2.3 High Energy X-ray Diffraction

High energy X-ray diffraction (HE-XRD) was also used for phase identification and characterization of the powder mixtures. The 6-ID-D beamline at Argonne National Laboratory Advanced Photon Source was used for this work. The experimental setup allows for rapid X-ray scans of levitated samples over a range of temperatures. As shown below in Figure 3.7, samples in the form of small beads were levitated above a nozzle using a flowing argon gas stream. The levitation of the beads prevents any potential interactions between the samples

and containers at high temperatures. The beads were then heated using a laser, and the X-ray beam passed through the sample. Each individual scan lasts 30 seconds.

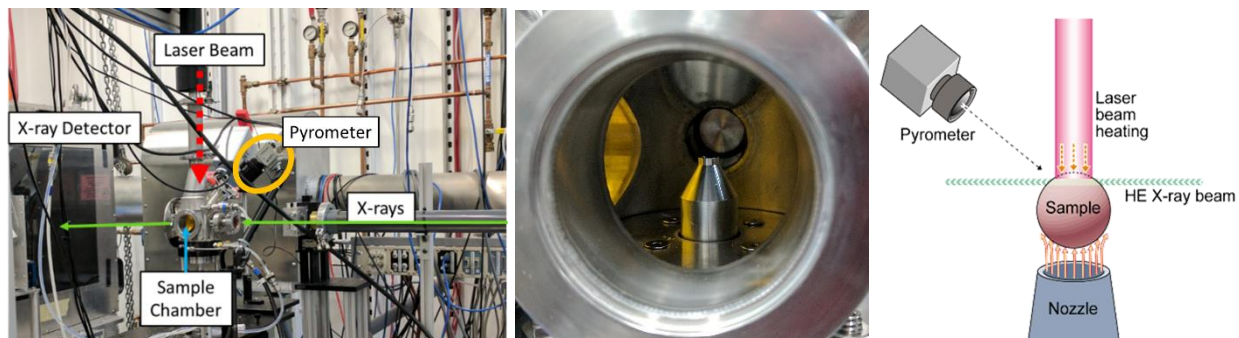


Figure 3.7: Pictures of the 6-ID-D Beamline at Argonne National Lab showing (from left to right) the beamline setup, inside of the sample chamber, and diagram of the sample during the experiment.

Samples were levitated and XRD spectra were obtained at room temperature, then every 100 degrees from 900° to 1500°C. Five individual scans of 30 seconds each were taken at every temperature. Two beads of each composition were characterized.

The resultant data from these scans was stored as a .TIF file of the detected diffraction rings as shown below in Figure 3.8. Before analysis, the patterns were integrated from the raw TIF files to get the powder diffraction spectra using GSAS-II, a program developed at Argonne National Lab (26). Once integrated, the five scans taken at every temperature for each sample were averaged together and then exported as one file for analysis in HighScore Plus (Panalytical) using the ICDD (International Center for Diffraction Data) database for phase identification. The beamline wavelength varies slightly depending on current operating conditions. During the first visit to the beamline, the X-ray wavelength was $\lambda=0.123654\text{\AA}$. During the second visit, the wavelength was $\lambda= 0.123637\text{\AA}$. The wavelength that the data was collected at can be set in

HighScore Plus which automatically adjusts reference patterns in the database for analysis of the experimental data.

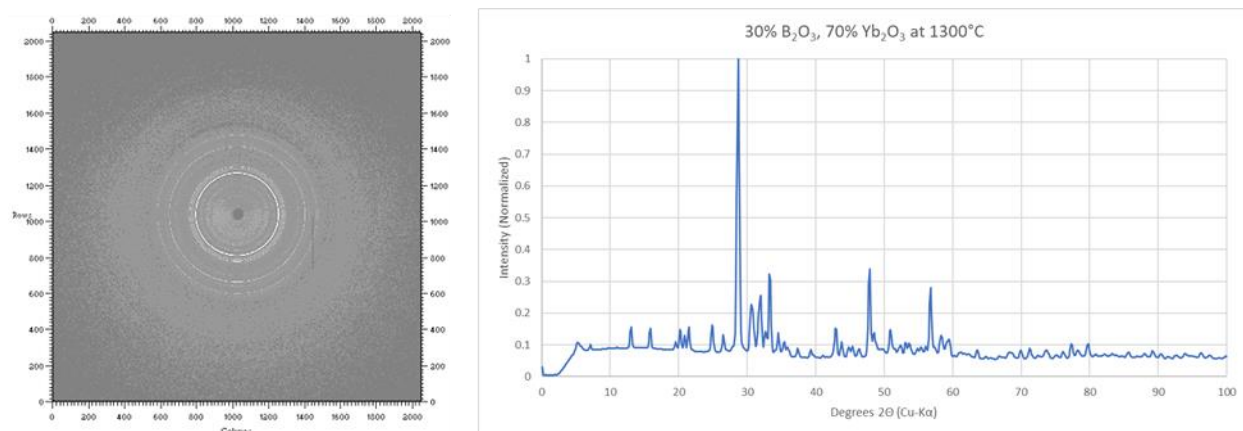


Figure 3.8: Raw .tif File of composition B3 taken at 1300°C and resultant integrated XRD pattern for analysis in HighScore Plus.

3.3 Results

3.3.1 Binary Phase Studies

DSC of the binary phases showed two thermal events upon heating: the first, endothermic and occurring at roughly 200°C while the second is exothermic and occurs around 730°C. These peaks become more pronounced with increasing boria content. The 200°C peak is attributed to the burnout of the PVA *in situ*. Upon cooling there is an exothermic event that occurs between 500°C and 600°C that, in addition to becoming more pronounced, also occurs at increasing temperatures with increasing boria content. The DSC scan for composition B5 (50 mol% B₂O₃, 50 mol% Yb₂O₃) is shown below in Figure 3.9. All remaining DSC scans can be found in Appendix A (Section 7).

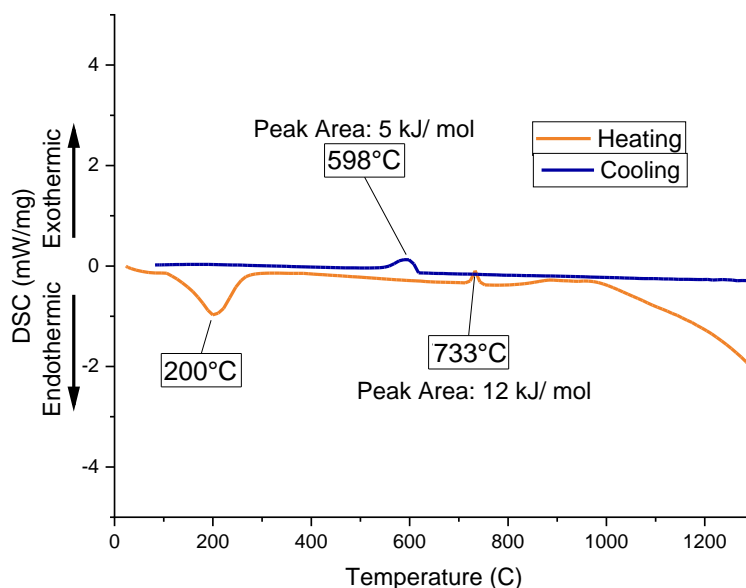


Figure 3.9: DSC scan of composition B5, 50 mol% B_2O_3 and 50 mol% Yb_2O_3 showing PVA burnout at $\sim 200^\circ C$ on heating, an exothermic event at $733^\circ C$ on heating, and an exothermic event at $598^\circ C$ on cooling.

The beamline results for the binary compositions show Yb_2O_3 and $YbBO_3$ as the main phases at all elevated temperatures. The borate content increases with increasing boria concentration. No other phases were identified with these binary compositions. An example of the binary HE-XRD is shown as a function of temperature below in Figure 3.10. The shown composition is B5, which is 50 mol% B_2O_3 and 50 mol% Yb_2O_3 . All other scans can be found in Appendix B.

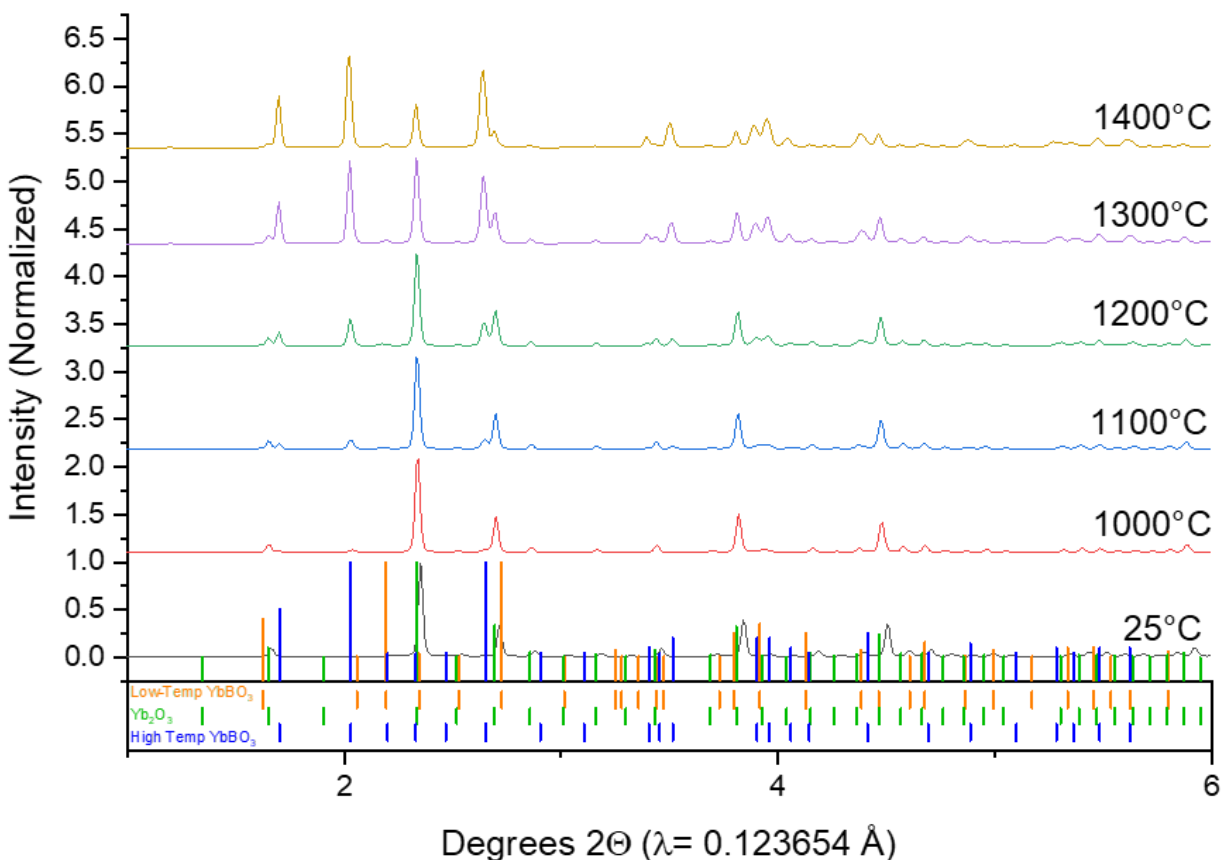


Figure 3.10: Stacked XRD scans of composition B5- 50 mol% B_2O_3 and 50 mol% Yb_2O_3 with reference patterns for Yb_2O_3 and the two polymorphs of $YbBO_3$

3.3.2 Ternary Phase Studies

The ternary DSC showed the water and PVA burnout below 200°C. The other exothermic events on heating at ~730°C and between 500°C and 600°C on cooling were also present for each of the 21 compositions explored. Additionally, some compositions showed clear peaks indicative of melting between 1425°C and 1450°C. Shown below in Figure 3.11 is a scan of composition T19 which has the composition of 40 mol% Yb_2O_3 , 30 mol% SiO_2 , and 30 mol% B_2O_3 . This DSC scan shows all five thermal events discussed. The DSC scans of the other compositions can be found in Appendix B.

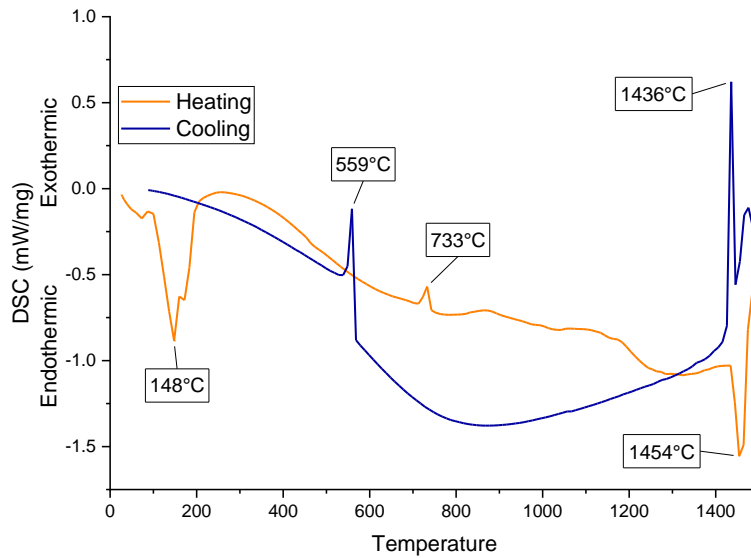


Figure 3.11: DSC Scan of T19 (40 mol% Yb_2O_3 , 30 mol% SiO_2 , and 30 mol% B_2O_3) showing PVA burnout below 200°C on heating, an exothermic event at 733°C on heating, melting at 1454°C on heating, solidification at 1436°C on cooling, and a phase transition at 559°C on cooling.

The ytterbium borate phase was identified in nearly every scan of the ternary compositions, along with ytterbia. Samples with higher silica and boria content showed melting at much lower temperatures than ytterbia-rich mixtures. Some ytterbium silicates were also recorded at compositions where the molar ratio of silica to ytterbia was close to 1:1. Figure 3.12 shows the expected phase equilibria fields for the regions of the ternary phase diagram investigated. These phase fields are based on the Alkemade lines and equilibrium reactions explored in Chapter 2 (*Idealized Interfacial Reactions Between B_2O_3 and $\text{Yb}_2\text{Si}_2\text{O}_7$*) of this document. Isothermal slices of the ternary phase diagram are shown below (Figure 3.13, Figure 3.14, Figure 3.15, Figure 3.16, and Figure 3.17) with the tested compositions numerically marked and the phases present at that temperature and composition marked with colored symbols surrounding the composition marker. Each phase in the system is denoted by a different color and symbol as shown in the legend in Figure 3.13. Compositions that showed a large

amorphous hump, indicative of either amorphous phases or liquids, have their numerical text markers colored orange.

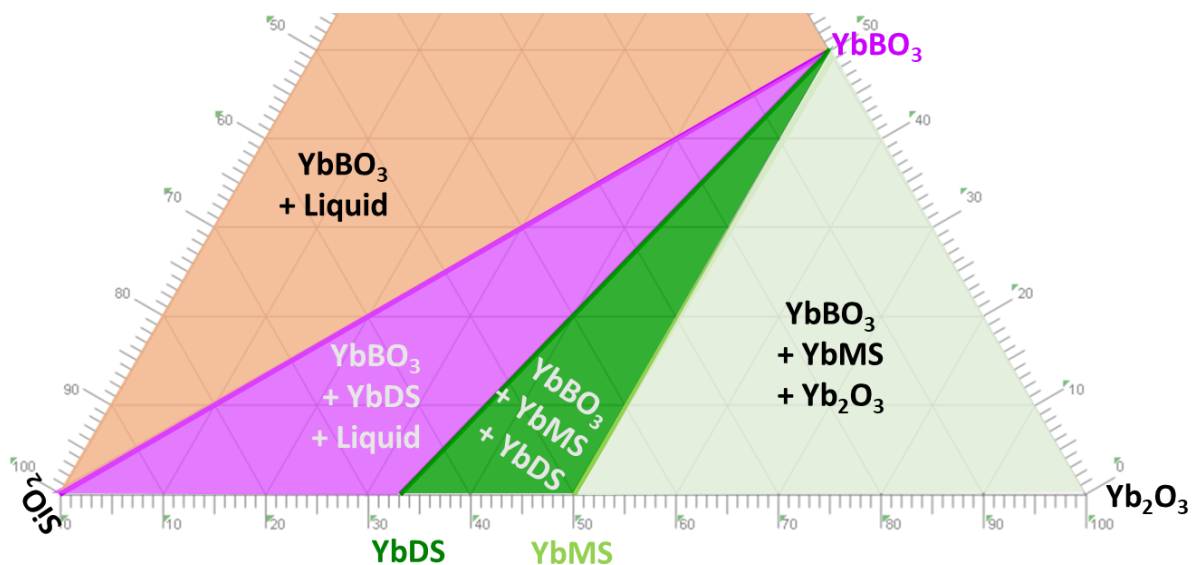


Figure 3.12: Expected equilibrium phase fields for the $\text{Yb}_2\text{O}_3 - \text{SiO}_2 - \text{B}_2\text{O}_3$ ternary system based on Alkemade lines from the equilibrium reactions discussed in the idealized interfacial reactions studies in Chapter 2. $\text{YbDS} = \text{Yb}_2\text{Si}_2\text{O}_7$ and $\text{YbMS} = \text{Yb}_2\text{SiO}_5$.

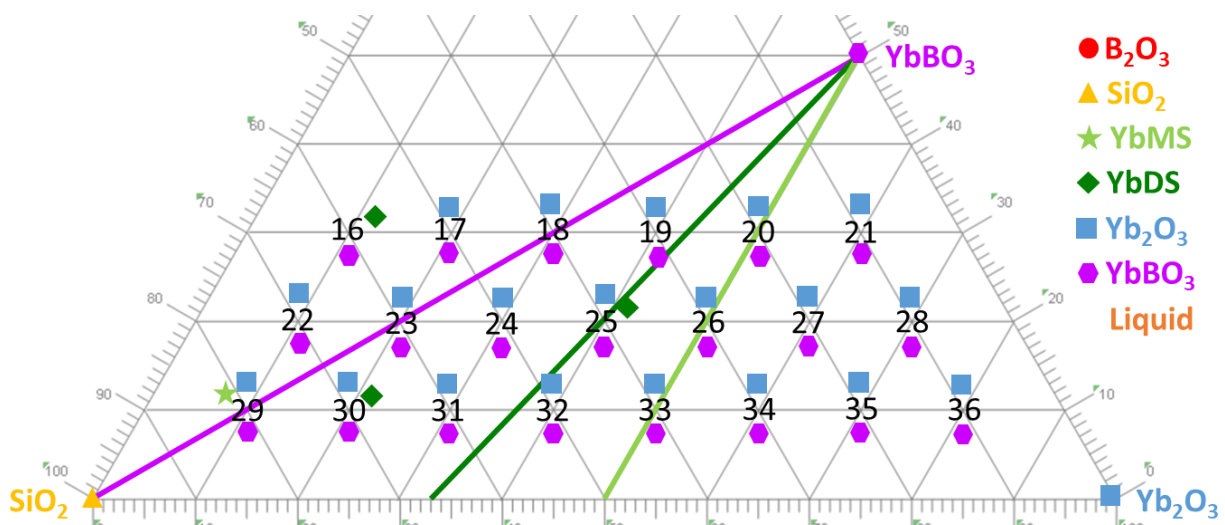


Figure 3.13: Phase identification results for the $\text{Yb}_2\text{O}_3 - \text{SiO}_2 - \text{B}_2\text{O}_3$ ternary system from HE-XRD scans taken at 1100°C .

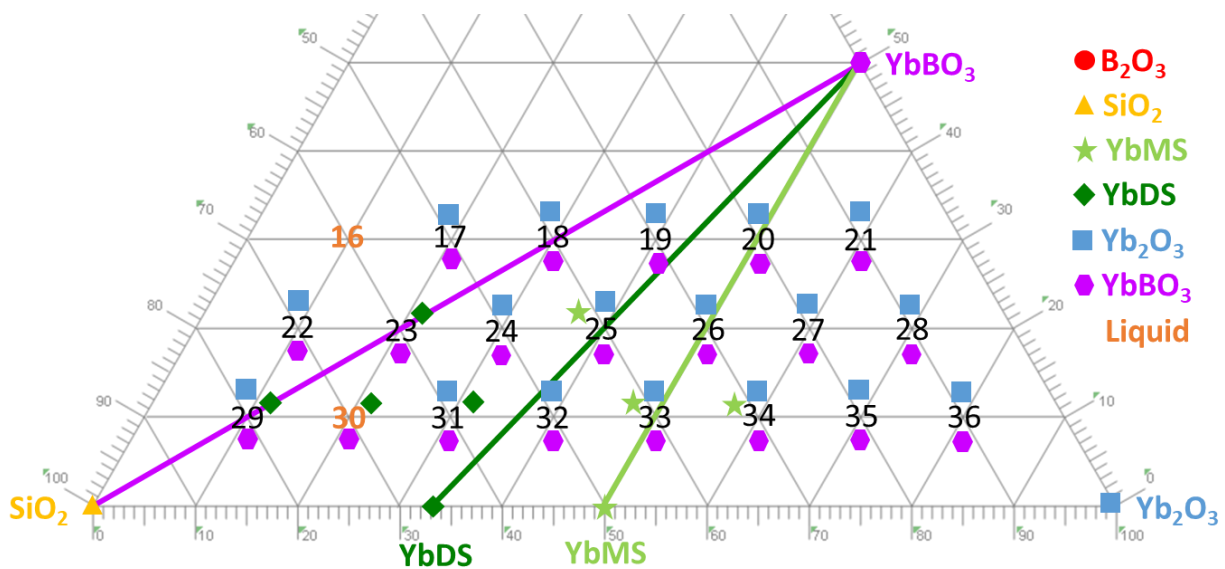


Figure 3.14: Phase identification results for the $\text{Yb}_2\text{O}_3 - \text{SiO}_2 - \text{B}_2\text{O}_3$ ternary system from HE-XRD scans taken at 1200°C.

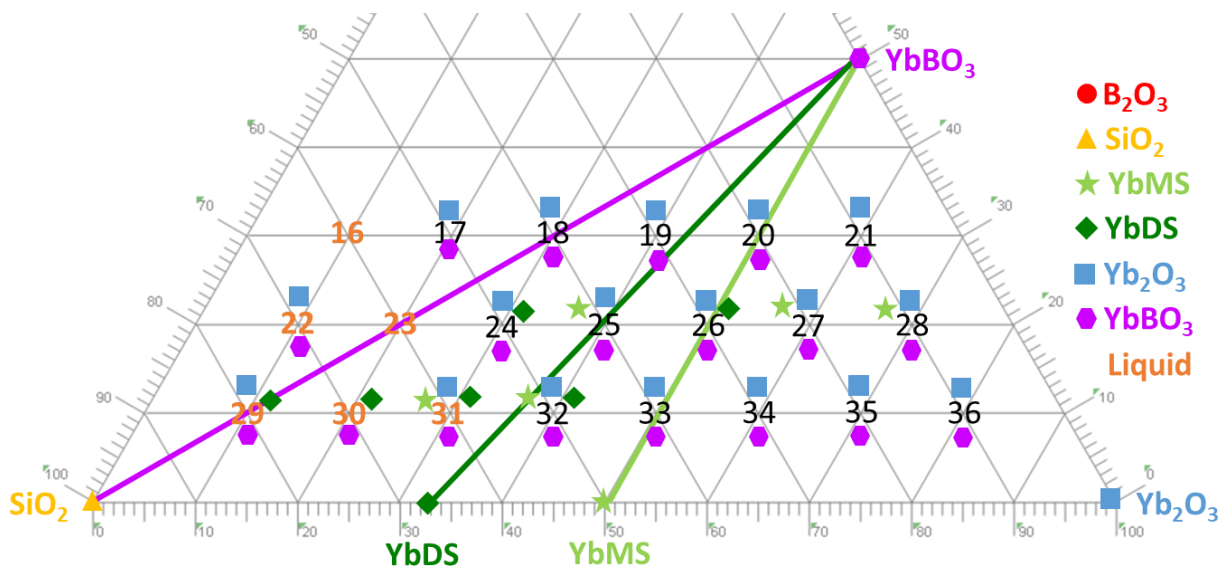


Figure 3.15: Phase identification results for the $\text{Yb}_2\text{O}_3 - \text{SiO}_2 - \text{B}_2\text{O}_3$ ternary system from HE-XRD scans taken at 1300°C.

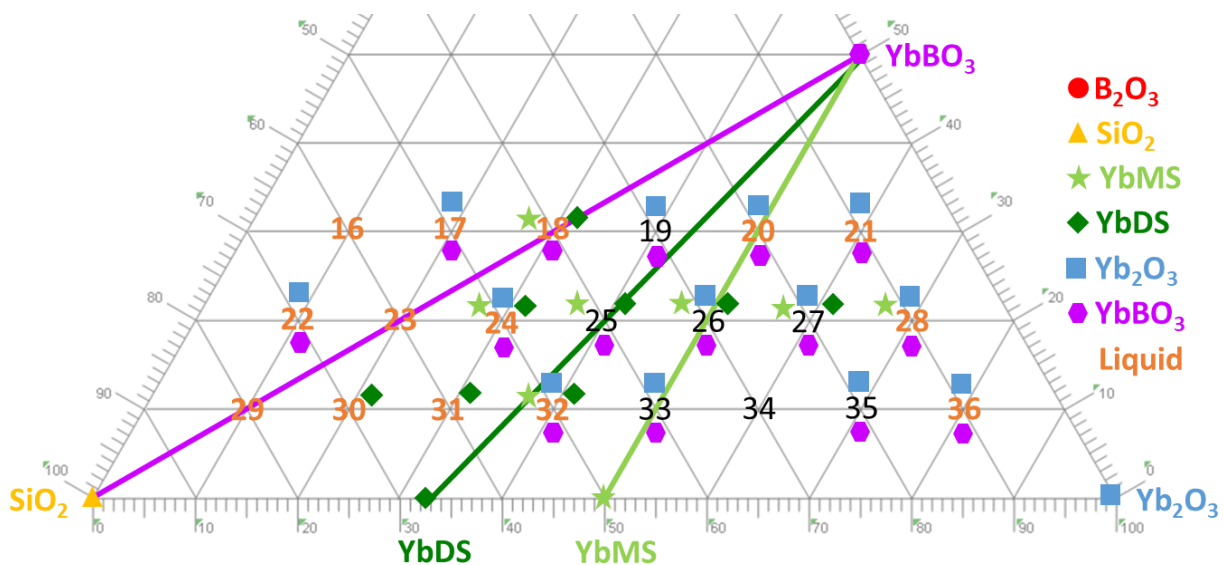


Figure 3.16 Phase identification results for the $\text{Yb}_2\text{O}_3 - \text{SiO}_2 - \text{B}_2\text{O}_3$ ternary system from HE-XRD scans taken at 1400°C .

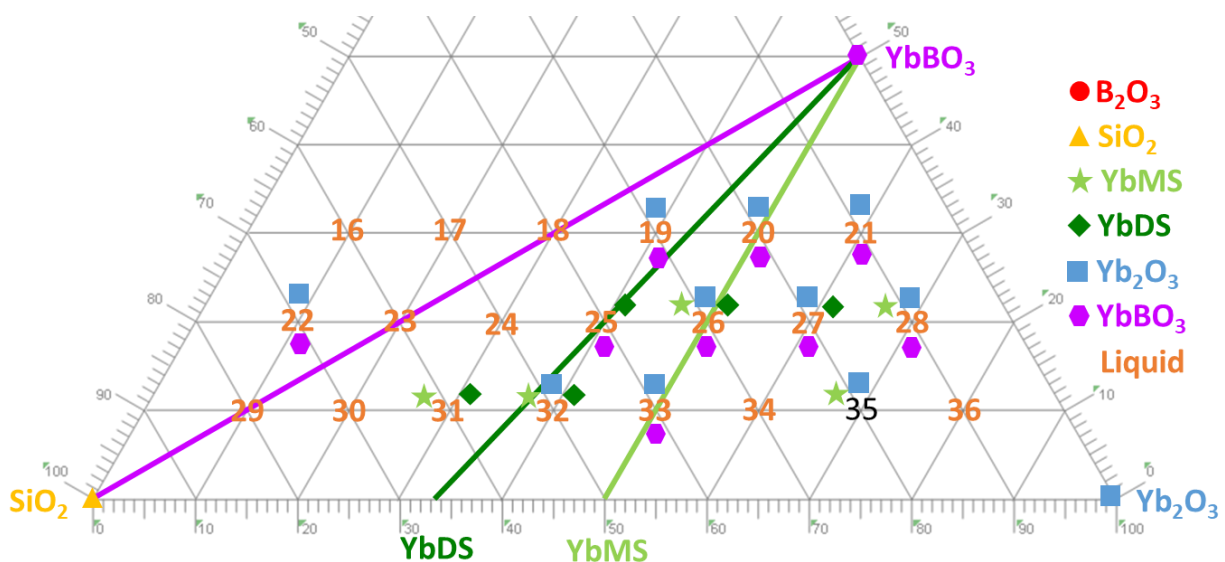


Figure 3.17: Phase identification results for the $\text{Yb}_2\text{O}_3 - \text{SiO}_2 - \text{B}_2\text{O}_3$ ternary system from HE-XRD scans taken at 1500°C .

It is important to note that these isothermal sections may not indicate true equilibrium at the recorded compositions and temperatures. Each data acquisition condition was held for approximately 2.5 minutes. A comparison of sequential scans taken of a single sample

(composition T25) can be seen below in Figure 3.18 showing very little difference between scans with increasing time held at temperature. The presence of monosilicate and disilicate phases recorded outside the bounds of their predicted equilibrium phase fields is attributed to this lack of true equilibrium.

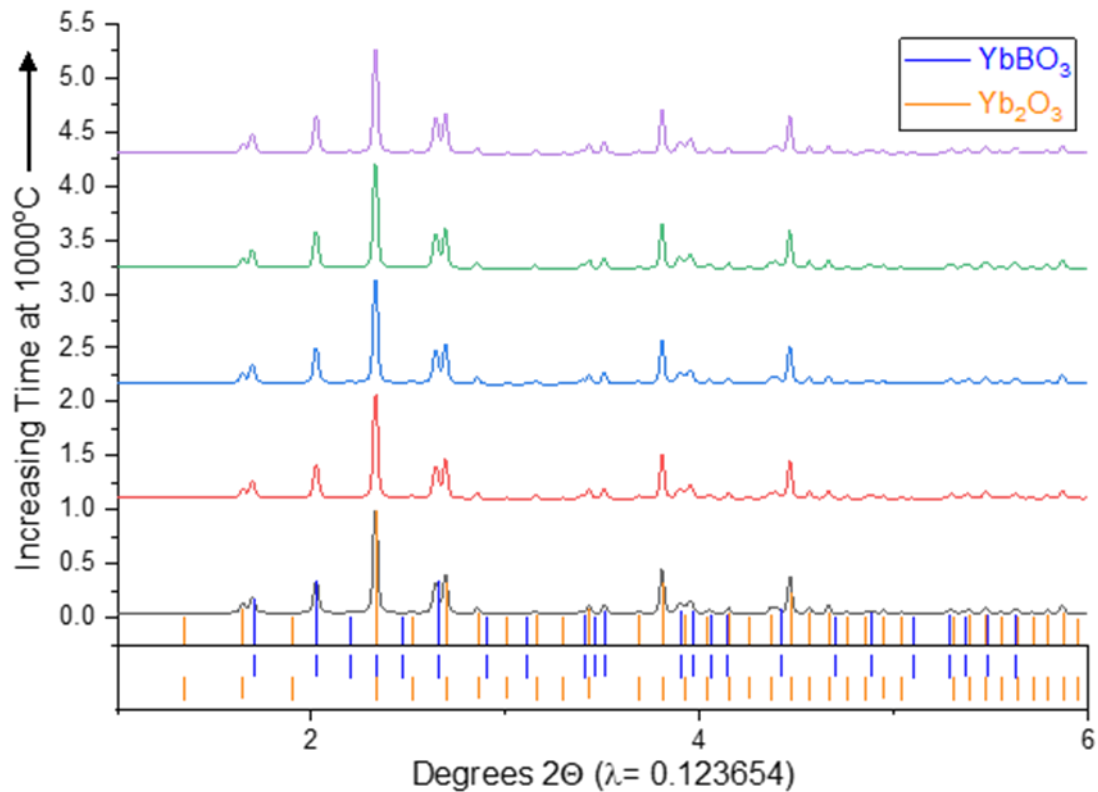


Figure 3.18: Composition T25 (40% Yb₂O₃ 40% SiO₂ and 20% B₂O₃) individual HE-XRD scans stacked according to increasing time held at 1000°C with reference patterns for YbBO₃ and Yb₂O₃.

3.4 Discussion

3.4.1 Binary Compositions

For all tested compositions of the binary $\text{Yb}_2\text{O}_3 - \text{B}_2\text{O}_3$ system, the only phases detected in the XRD scans are YbBO_3 and Yb_2O_3 . This suggests that, unlike the lanthanum borate system, the only line compound in the ytterbium borate system is YbBO_3 . This suggests the thermal event recorded in the DSC at 730°C on heating (Figure 3.9) is the formation of YbBO_3 from the Yb_2O_3 and B_2O_3 constituent oxides in accordance with the formation reaction (Equation [3-1]) discussed in the previous chapter.



Given that the 730°C thermal event is the formation of YbBO_3 , the event that occurs between 500°C and 600°C on cooling is attributed to the transition of the high temperature YbBO_3 polymorph transitioning to the low temperature polymorph. This also implies that when the YbBO_3 initially forms from the constituent oxides it forms in the high temperature polymorph. The recorded formation temperature of 733°C is lower than the low to high polymorphic transition temperature noted in the Levin diagram (1040°C). The high to low transition temperature, recorded in the DSC cooling curve as occurring between 500°C and 600°C , is nearly 500° lower than the transition marked in the Levin diagram (Figure 3.2). The formation reaction has a low enthalpy of only 12 kJ/mol , indicating that the borate phase is not much more stable than its constituent oxides. The discrepancies in these phase changes were further investigated as described in Chapter 4.

3.4.2 Ternary Compositions

The addition of silica to the system complicates phase studies via the addition of three rare earth silicate phases (Yb_2SiO_5 , $\text{Yb}_4\text{Si}_3\text{O}_{12}$, and $\text{Yb}_2\text{Si}_2\text{O}_7$) as well as through the formation of amorphous glassy borosilicate phases. Note that the apatite phase $\text{Yb}_4\text{Si}_3\text{O}_{12}$ was not observed in this study and is not shown in the following ternary diagrams.

The $\text{P}_2\text{O}_5 - \text{SiO}_2 - \text{B}_2\text{O}_3$ phase diagram was used as a reference system for the expected phase fields and liquidus lines since there is a complete lack of thermodynamic and phase data for the $\text{Yb}_2\text{O}_3 - \text{SiO}_2 - \text{B}_2\text{O}_3$ ternary system. The phosphate-based system shown in Figure 3.19 includes both phospho-silicates with cation ratios comparable to that of the ytterbium mono- and disilicates (α and β in the diagram below) as well as a single phospho-borate phase with a 1:1 cation ratio (γ in the diagram below) equivalent to YbBO_3 (27). Additionally, a $\text{P}_2\text{O}_5 - \text{B}_2\text{O}_3$ partial binary (boria rich) is shown with more confirmed phase equilibria fields than the $\text{Yb}_2\text{O}_3 - \text{B}_2\text{O}_3$ phase diagram developed by Levin. This $\text{P}_2\text{O}_5 - \text{SiO}_2 - \text{B}_2\text{O}_3$ phase diagrams was utilized to help guide predictions of phase equilibria fields and liquidus lines in the $\text{Yb}_2\text{O}_3 - \text{SiO}_2 - \text{B}_2\text{O}_3$ ternary phase diagram.

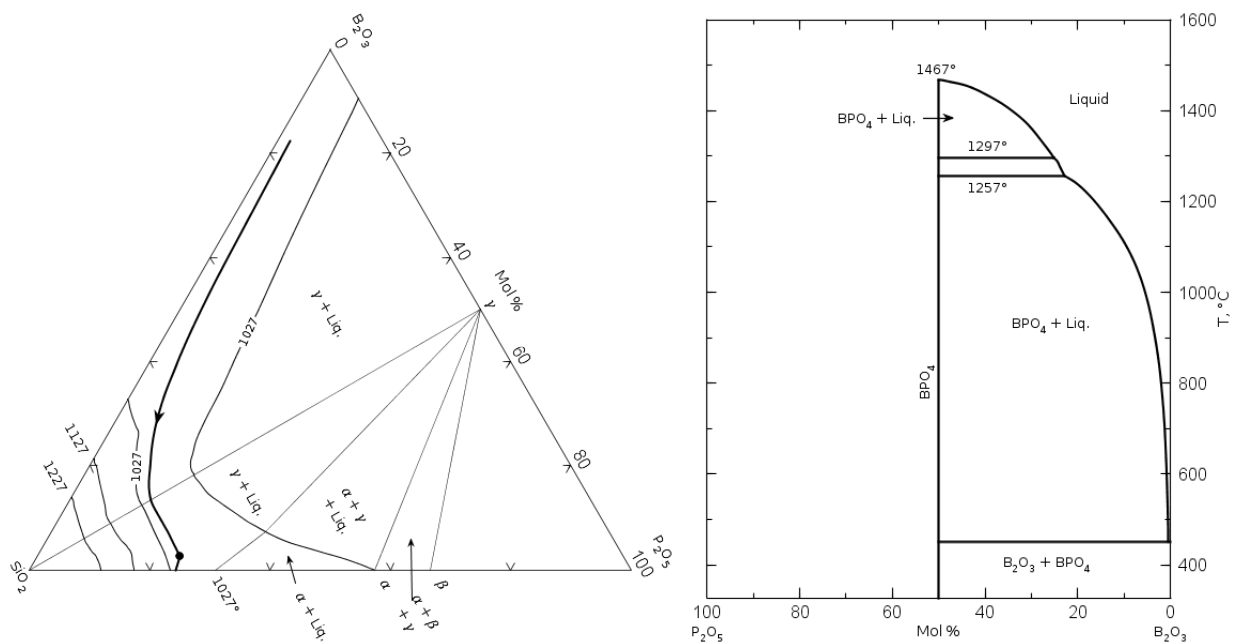


Figure 3.19: $P_2O_5 - SiO_2 - B_2O_3$ and $P_2O_5 - B_2O_3$ phase diagrams used for reference due to equilibrium phase similarities to the $Yb_2O_3 - SiO_2 - B_2O_3$ system.(28)

As predicted by the phase equilibrium fields shown above in Figure 3.12, the $YbBO_3$ phase is present across the compositional phase space explored. Additionally, a low-melting eutectic is observed running through compositions 16 and 30 at 1200°C (Figure 3.21) similarly to that observed in the reference $P_2O_5 - SiO_2 - B_2O_3$ phase diagram. The melt front, shown in dashed lines in Figure 3.21 and Figure 3.22, was determined for 1200°C - 1400°C. This determination was made using both the development of the amorphous hump in the HE-XRD scans with composition and temperature, as well as the melting temperatures measured in DSC.

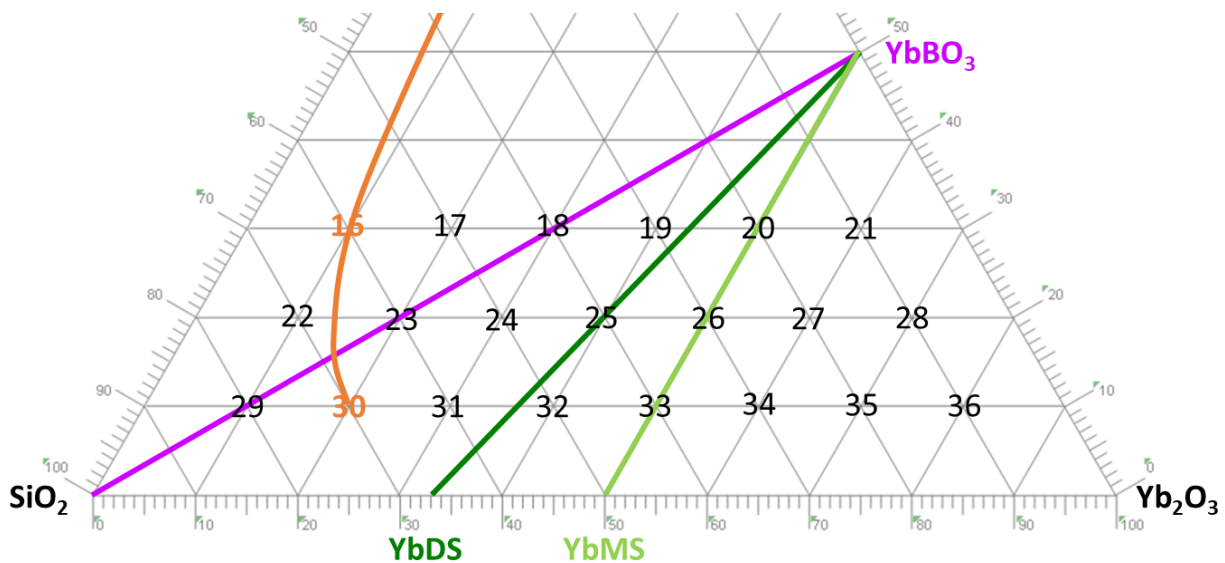


Figure 3.20: Predicted liquidus boundary (orange line) at 1200°C based on HE-XRD scans showing melting in compositions T16 and T30.

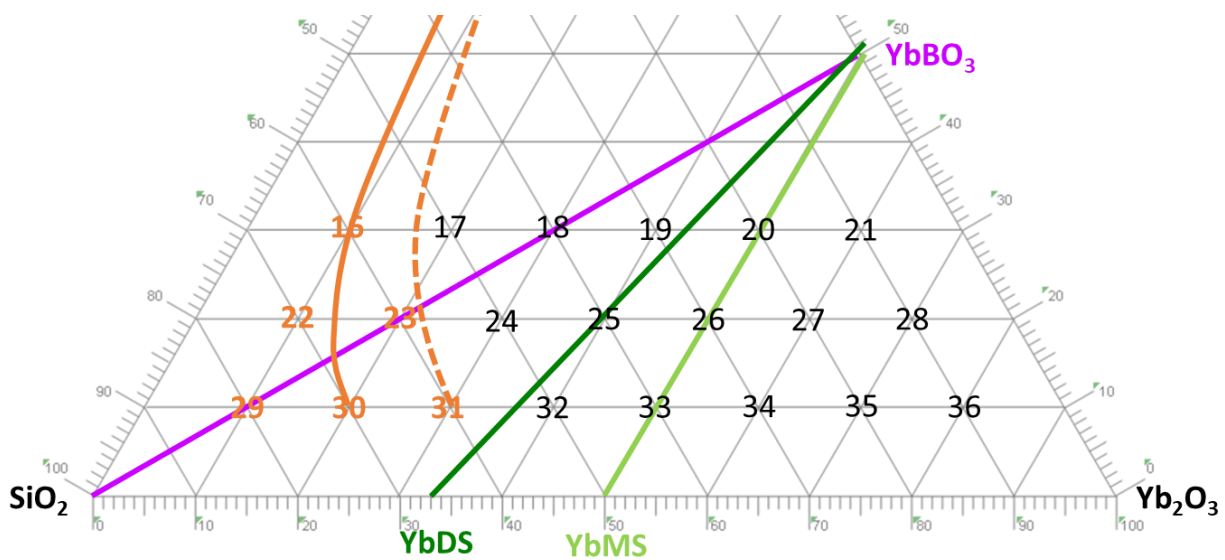


Figure 3.21: Predicted liquidus boundary (dashed orange line) at 1300°C based on HE-XRD scans showing melting in compositions T25 and T31.

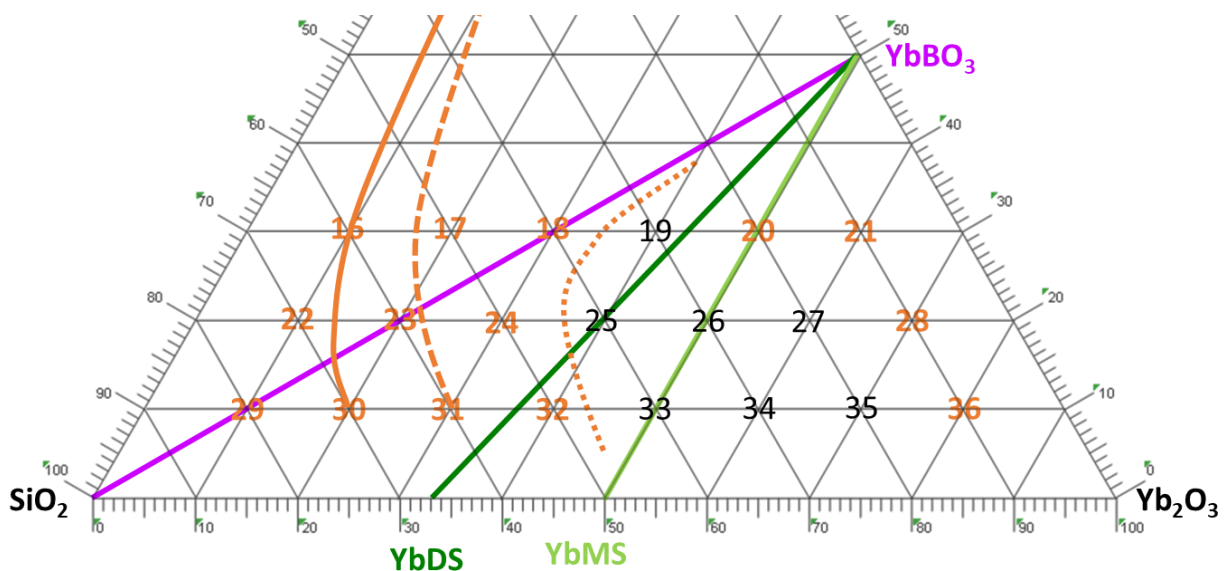


Figure 3.22: Predicted liquidus boundary (dotted orange line) at 1400°C based on HE-XRD scans showing melting in compositions T18, T24, and T32. Some melting was also seen in compositions T20, T21, T28, and T36.

Based on the melt temperatures recorded at the compositions that were investigated, it is likely that there is a local eutectic point on the Yb_2O_3 - YbBO_3 join of the Yb_2O_3 – B_2O_3 binary phase diagram. This is consistent with the observed melting of T20, T21, T28, and T36, despite Yb_2O_3 having the highest melting temperature ($T_m = 2355^\circ\text{C}$) of the ternary oxide end members. In addition to this eutectic in the binary system, it is likely that there is a localized ternary eutectic near composition T30, similarly to the one marked on the B_2O_3 – SiO_2 – P_2O_5 ternary phase diagram. Both of these eutectic points are marked with blue stars. Additional local eutectic points are necessary based on phase rules. The predicted locations for these are marked in blue pentagons. The known liquid phase boundaries are shown in thick solid lines, and the predicted phase boundaries are shown in the dotted thick lines. All liquidus surfaces drop off rapidly as the compositions approach B_2O_3 with a melting temperature of only 450°C . This is more consistent with the P_2O_5 – B_2O_3 binary phase diagram shown in Figure 3.19 than the Levin diagram. There are also implied regions of liquid immiscibility in both the SiO_2 – B_2O_3 system as

well as the $\text{Yb}_2\text{O}_3 - \text{B}_2\text{O}_3$ system. Given these predictions, the liquidus surface for the ternary phase diagram is illustrated below in Figure 3.23 with the grey dotted lines showing where regions of liquid immiscibility might be located. The phase Alkemade lines are again shown in the same colors as the diagrams above. The thin orange lines show estimated liquidus temperature isotherms at approximately 100°C intervals.

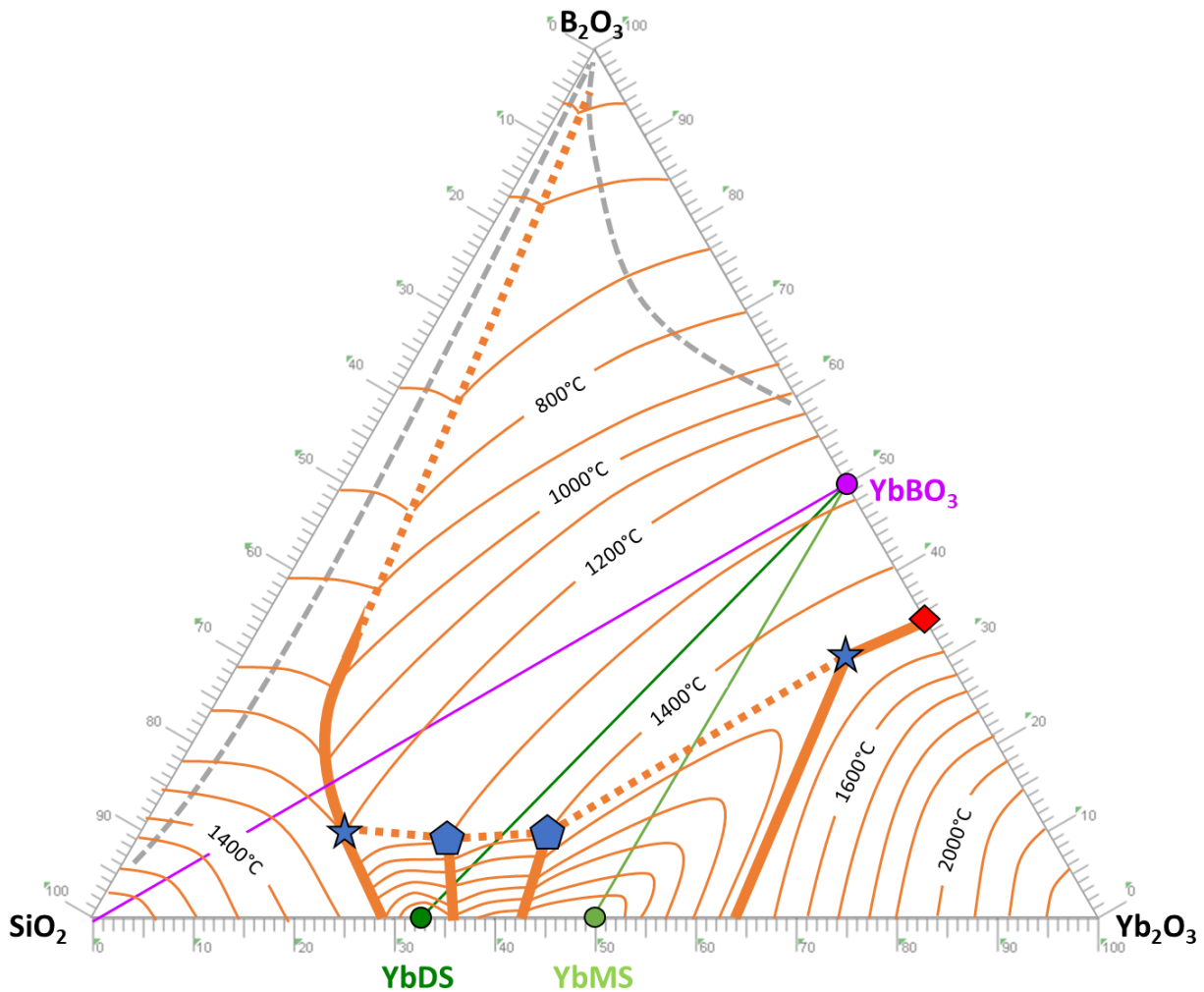


Figure 3.23: Predicted liquidus surface of $\text{Yb}_2\text{O}_3 - \text{SiO}_2 - \text{B}_2\text{O}_3$ phase diagram with boundary lines shown in thick orange, ternary eutectic points shown in blue, and regions of possible liquid immiscibility shown in grey. Alkemade lines for equilibrium reactions are shown in purple and green.

3.5 Conclusions

Six binary compositions from the $\text{Yb}_2\text{O}_3 - \text{B}_2\text{O}_3$ system and 21 ternary compositions from the $\text{Yb}_2\text{O}_3 - \text{SiO}_2 - \text{B}_2\text{O}_3$ system were prepared from the constituent oxide powders. The resulting phase assemblage after high temperature exposure was explored using a combination of DSC and high-energy X-ray diffraction at The Argonne National Laboratory Advanced Photon Source, beamline 6ID-D. The data collected from the DSC and XRD tests were used to confirm the phases present at a range of temperatures up to 1500°C and the melting temperatures of each composition of interest. These results were used to predict phase fields, boundary lines, and eutectic points for the ternary phase diagram. The $\text{P}_2\text{O}_5 - \text{SiO}_2 - \text{B}_2\text{O}_3$ was used for guidance in predicting the $\text{Yb}_2\text{O}_3 - \text{SiO}_2 - \text{B}_2\text{O}_3$ ternary diagram due to similarities in Alkemade lines and equilibrium phases. The $\text{Yb}_2\text{O}_3 - \text{SiO}_2 - \text{B}_2\text{O}_3$ liquidus surface was constructed based on all available data.

3.6 References

1. Rockett TJ, Foster WR. Phase Relations in the System Boron Oxide–Silica. *Journal of the American Ceramic Society*. 1965;48(2):75–80.
2. Toropov NA, Bondar' IA. Silicates of the rare earth elements. *Bulletin of the Academy of Sciences of the USSR Division of Chemical Science*. 1961;10(8):1278–85.
3. Newnham RE, Redman MJ, Santoro RP. Crystal Structure of Yttrium and Other Rare-Earth Borates. *Journal of the American Ceramic Society*. 1963;46(6):253–6.
4. Levin EM, Roth RS, Martin JB. Polymorphism OF ABO₃ Type Rare Earth Borates. the *American Mineralogist* [Internet]. 1961;46(1954):1030–55. Available from: http://www.minsocam.org/ammin/AM46/AM46_1030.pdf
5. Bradley WF, Graf DL, Roth RS. The Vaterite-type ABO₃ Rare-earth Borates. *Acta Crystallographica*. 1966;20(2):283–7.
6. Levin EM, Robbins CR, Waring JL. Immiscibility and the System Lanthanum Oxide–Boric Oxide. *Journal of the American Ceramic Society*. 1961;44(2):87–91.
7. Levin EM. Liquid immiscibility in oxide systems. *Phase Diagrams Materials Science and Technology*. 2012; 3:143–236.
8. Ren M, Lin JH, Dong Y, Yang LQ, Su MZ, You LP. Structure and phase transition of GdBO₃. *Chemistry of materials*. 1999 Jun 14;11(6):1576–80.
9. Dmitruk LN, Petrova OB, Popov AV, Shukshin VE. Synthesis and investigation of transparent rare earth borate glassceramics. *Bulletin of RAS, Proceedings of the Institute of General Physics*. 2008; 64:49.
10. Emme H, Valldor M, Pöttgen R, Huppertz H. Associating Borate and Silicate Chemistry by Extreme Conditions: High-Pressure Synthesis, Crystal Structure, and Properties of the New Borates RE₃B₅O₁₂ (RE = Er–Lu). *Chemistry of Materials*. 2005;17(10):2707–15.
11. Jacob DE, Wehrmeister U, Soldati AL, Hofmeister W. Spectroscopic Characterisation of biological vaterite: relations to synthetic and geological vaterites. *Geophysical Research Abstracts*. 2009; 11:2006–7.
12. Lin J, Sheptyakov D, Wang Y, Allenspach P. Structures and phase transition of vaterite-type rare earth orthoborates: A neutron diffraction study. *Chemistry of Materials*. 2004;16(12):2418–24.
13. Turnbull AG. A thermochemical study of vaterite. *Geochimica et Cosmochimica Acta*. 1973;37(6):1593–601.
14. Demichelis R, Raiteri P, Gale JD, Dovesi R. The multiple structures of vaterite. *Crystal Growth and Design*. 2013;13(6):2247–51.
15. Makovicky E. Vaterite: Interpretation in terms of OD theory and its next of kin. *American Mineralogist*. 2016;101(7):1636–41.

16. Christy AG. A Review of the Structures of Vaterite: The Impossible, the Possible, and the Likely. *Crystal Growth and Design*. 2017;17(6):3567–78.
17. Weir CE, Lippincott ER. Infrared studies of aragonite, calcite, and vaterite type structures in the borates, carbonates, and nitrates. *Journal of Research of the National Bureau of Standards Section A: Physics and Chemistry*. 1961;65A (3):173.
18. Hudon P, Baker DR. The nature of phase separation in binary oxide melts and glasses. I. Silicate systems. *Journal of Non-Crystalline Solids*. 2002;303(3):299–345.
19. Podder J, Lin J, Sun W, Pan Y, Botis SM, Tse J, et al. Uptake and speciation of iodine in calcium carbonates. *Canadian Nuclear Society - 35th Annual Conference of the Canadian Nuclear Society and 38th CNS/CNA Student Conference 2015*. 2015;2(May):1334–9.
20. OQMD | The Open Quantum Materials Database [Internet]. [cited 2021 Jan 10]. Available from: http://oqmd.org/analysis/phase_diagram/
21. Materials Project [Internet]. [cited 2021 Jan 10]. Available from: <https://materialsproject.org/#apps/phasediagram/%7B%22chemsys%22%3A%5B%22B%22%2C%22O%22%2C%22Yb%22%5D%2C%22projel%22%3A%22%22%7D>
22. Academy W, Academy W. A comparison of the heating-curve and quenching methods of melting-point determinations Author (s): George W . Morey Source: *Journal of the Washington Academy of Sciences* , August 19 , 1923 , Vol . 13, No . Published by: Washington Academy of Science. 1923;13(14):326–9.
23. Hudon P, Baker DR. The nature of phase separation in binary oxide melts and glasses. I. Silicate systems. *Journal of Non-Crystalline Solids*. 2002;303(3):299–345.
24. Zhang Z, Hirao K, Soga N. Water corrosion behavior of densified glass. II. Borate glasses. *Journal of Non-Crystalline Solids*. 1991;135(1):62–6.
25. Amietszajew T, Seetharaman S, Bhagat R. The Solubility of Specific Metal Oxides in Molten Borate Glass. *Journal of the American Ceramic Society*. 2015 Oct 1;98(10):2984–7.
26. Toby BH, von Dreele RB. GSAS-II: The genesis of a modern open-source all-purpose crystallography software package. *Journal of Applied Crystallography*. 2013 Apr;46(2):544–9.
27. Experimental I, Phase C, Martin S, Bernard C. Silica-Based Oxide Systems I t \ V,. o. 1991;138(9):2830–5.
28. Baret G, Madar R, Bernard C. Silica-Based Oxide Systems: I. Experimental and Calculated Phase Equilibria in Silicon, Boron, Phosphorus, Germanium, and Arsenic Oxide Mixtures. *Journal of The Electrochemical Society*. 1991;138(9):2830–5.
29. Phase Equilibria Diagrams Online Database (NIST Standard Reference Database 31), The American Ceramic Society and the National Institute of Standards and Technology, 2021. Figure Numbers 2353, 2391; www.nist.gov/srd/nist31.cfm

4 Thermal and Physical Properties of YbBO₃

4.1 Introduction

Ytterbium borate was found to be the main product phase in reactions between B₂O₃ and Yb-containing silicates and oxides in all previous studies. YbBO₃ formed in idealized interfacial tests where boria was in contact with the ytterbia and ytterbium silicate substrates, as well as in both the binary and ternary phase diagram studies. The rare earth borate phases have not been well studied. Initial studies on rare earth borates were conducted by Levin, Newnham, and Roth in the 1960s and 70s(1–3) focusing on liquid immiscibility and crystal structure. Interest in these phases has only recently developed as rare earths have been identified as important for optical applications. However, most contemporary studies are concerned with glass properties with rare earths additives. As such, little data exist on the thermal and physical properties of the crystalline rare earth borate phases.

The rare earth borates take a crystal structure (Figure 4.1) analog to that of vaterite, a metastable CaCO₃ phase(1). The superlattice of the vaterite structure is highly debated as the phase is metastable in the CaCO₃ system (Chapter 3), and readily transforms to either calcite or aragonite depending on the temperature and presence of water vapor. The structure for this phase has been a topic of debate for over half a century, with most crystallographers agreeing that the structure is either hexagonal or rhombohedral, however the exact space group and bonding is still unknown(4–13). The CaCO₃ vaterite structure does not include a high temperature and a low temperature polymorph as is observed in rare earth borate analogs. Both polymorphs observed in the ytterbium borate system for this study are hexagonal crystal

structures with space groups that have been considered the “correct” structure for CaCO_3 vaterite(1). Both crystal structures, shown below in Figure 4.1 for the borate analog, consist of a hexagonal unit cell with the same number of formula units, however the dimensions of the unit cells are different(1). In addition to differences in the cell dimensions, the bonding of the boron atoms to the oxygen atoms is different in each structure. For the low temperature polymorph, the boron atoms are tetrahedrally coordinated to the surrounding oxygen atoms, where in the high temperature polymorph, the boron has trigonal coordination with oxygen. Differences between the two structures are also detailed in Table 4-1 below (2,3). The phase transition between these two polymorphs is also observed in the GdBO_3 system(14).

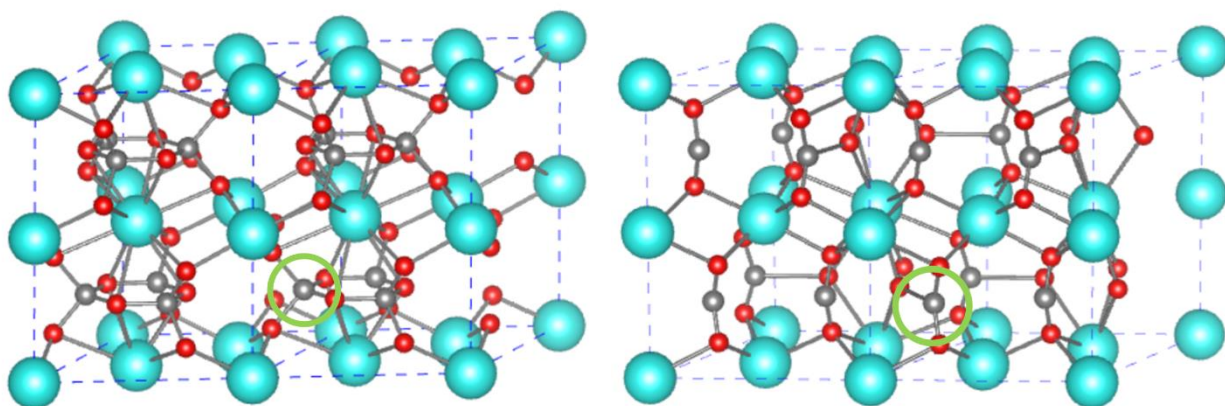


Figure 4.1: Comparison of the two YbBO_3 structures generated in CrystalMaker. Two unit cells shown for each structure. (Left) Low temperature polymorph. (Right) High temperature polymorph. Yb = Blue, O=Red, B=grey. Note the differences in the bonding state of the B to the O as circled in green.

Table 4-1: Comparison of YbBO_3 polymorph crystal structures from HighScore PDF cards 00-019-1426 and 00-019-1427(2,3)

	Low-temperature polymorph	High-temperature polymorph
Crystal System	Hexagonal	Hexagonal
Space Group	P6c2	P6 ₃ /mmc
Basal plane dimension “a”	6.47 Å	6.99 Å
“c” dimension	8.74 Å	8.34 Å
Unit cell volume	315.87 Å ³	352.9 Å ³

The work discussed in this chapter explores the physical and thermal properties of the YbBO_3 phase to determine how the formation of this phase will affect CMC/ EBC systems. Differential scanning calorimetry (DSC) was used to validate the formation of the YbBO_3 phase from the constituent oxides. It was also used to investigate the transition temperatures for pre-reacted borate to further probe the polymorphic phase change between the high temperature and low temperature polymorphs. This DSC study enabled determination of the enthalpies of formation and transition for the borate. Hot Stage XRD was used to measure the lattice parameters and coefficient of thermal expansion (CTE) of the borate and record the changes in the crystal structure with temperature. This method is complementary to the *in situ* HE-XRD beamline testing discussed previously in Chapter 3, but allows for testing from room temperature up to 1200°C while the beamline temperature range 900°C to 2000°C. The lower temperature range allows for XRD observation of polymorphic phase changes as recorded by the DSC.

Further investigation of the borate phase transitions was be conducted using the platinum packet encapsulations for static equilibrium testing. These tests, used by Morey in 1923 (15), were used by both Rockett and Toropov for their phase studies of the borosilicate and ytterbium silicate systems respectively(16,17), and are still used today by many in the field of geosciences (18,19). Small capsules made from a platinum tube are filled with the oxides of interest, equilibrated at the desired temperatures, followed by quenching and phase analysis with SEM and XRD. Additionally, bulk borate was prepared for further physical and thermal testing.

4.2 Experimental Procedures

4.2.1 DSC and Pt encapsulation

Samples used for the encapsulation and DSC were prepared from B_2O_3 and Yb_2O_3 powder mixtures. Information on the powders used can be found in Table 4-2. Powders were weighed in a 50 mol% B_2O_3 and 50 mol% Yb_2O_3 ratio for the static equilibration and DSC tests. They were then mechanically mixed in a HDPE storage container by stirring with a borosilicate stir rod before being used to fill the platinum packets or pressed into ¼ inch pellets for DSC.

Table 4-2: Powders used for preparation of $YbBO_3$ bulk samples and Pt encapsulation samples.

Oxide:	Source:	Purity:	Particle Size:
B_2O_3	Sigma Aldrich	99.98%	Unknown
Yb_2O_3		99.9%	Unknown

DSC scans of the equimolar borate mixture were run in argon, twice in succession without changing the sample. The first scan allowed for measurement of the formation temperature of the high temperature polymorph on heating, expected to be $\sim 730^\circ\text{C}$ from the binary phase studies; and then transition from the high temperature polymorph to the low temperature polymorph on cooling, expected to be between 500°C and 600°C from the binary phase studies. The scans were conducted from room temperature up to 1200°C at 10k/min , then back down to room temperature at the same rate. After the initial scan, it was assumed that the borate phase had fully formed from the constituent oxides. The second scan followed immediately and allowed for measurement of the transition from the low temperature polymorph to the high temperature polymorph, melting on heating, and then back to the low temperature polymorph on cooling.

Equilibrium studies were conducted by encapsulating 50 mol% B_2O_3 / 50 mol% Yb_2O_3 in a 3mm OD/ 2.8mm ID platinum tube (Purity 99.95%, Goodfellow USA, Coraopolis PA). These tubes were cut into 10mm lengths and annealed using a Bunsen burner and lab gas. When red-hot, they were removed from the flame and allowed to air quench on a ceramic plate. One end of the tube was then crimped shut with standard flat-nose jewelry pliers in a 3-fold geometry as illustrated in Figure 4.2 below. The three-fold geometry ensures more structural stability in the packet welds. This crimped bottom end was sealed shut using a Puk 5.1 (Lampert Werktechnik GmbH, Werneck Germany) arc welder with a tungsten tip and argon gas flow. Packets were then filled approximately halfway with the prepared powder mixture. The empty top of the packet was then crimped shut in a flat geometry, closing off any empty space in the packet to prevent air pockets in the final encapsulation. The flat crimp at the top of the packet was then sealed again using the Puk arc welder. Packets were then set upright in a sample holder shaped from refractory ceramic for exposure in the stagnant air box furnace. Samples were both inserted and removed from the furnace at temperature. Each sample was equilibrated for 24 hours. Upon removal from the furnace, samples were quenched in ethylene glycol to avoid loss of any volatile boron to aqueous quenching mediums. As these packets were used to examine the high temperature to low temperature phase transition, the packets were first exposed at 800°C for 24 hours for borate formation and equilibration. Some packets were then quickly moved to a 600°C furnace while others were moved to a 500°C furnace for 24 hours to equilibrate at those temperatures before quenching. These temperatures were selected as the upper and lower bounds of the temperature range at which this transition was observed in the DSC scans of the binary compositions during the phase equilibrium testing.

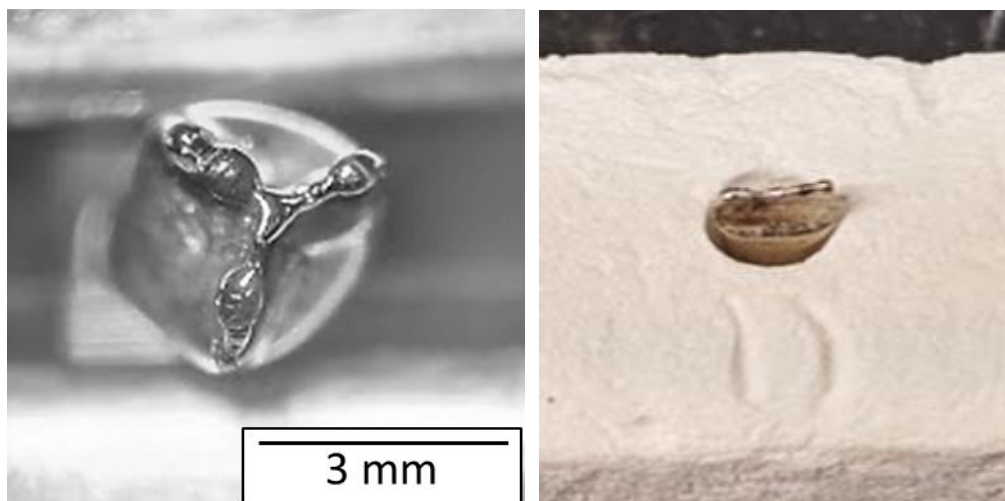


Figure 4.2: (Left) three-fold crimp & welds on the bottom of the platinum equilibration packet. (Right) Filled & sealed platinum packet in drilled alumina holder for exposure in stagnant air box furnace.

Packets were mounted in epoxy for characterization, then cut open using a low speed saw to expose the ceramic sample inside. They were then characterized using a combination of SEM and micro-focus XRD for phase identification. Micro-focus XRD uses an alignment microscope and beam optics that allow for a beam width of $430\mu\text{m}$ to be focused on a specific area of the sample. As the platinum packets are only three mm in diameter, this instrument configuration is vital to ensure that the beam is aligned with the sample.

4.2.2 Bulk Borate Tests- CTE & Physical Properties

Bulk YbBO_3 was prepared from powders mixed in a 60 mol% B_2O_3 to 40 mol% Yb_2O_3 ratios. This ratio of the oxides, as discussed in the Rockett & Foster study of the borosilicate system, accounts for the boria volatility during processing in air which they found to be between 7% and 10% depending on the conditions of the exposure (16). These powders were weighed and mechanically mixed in HDPE storage containers with a borosilicate stir rod, then placed in a platinum crucible. The mixture was placed in a stagnant air box furnace (RapidTemp Furnace,

CM Furnaces) at 800°C for 24 hours to react and equilibrate. It was then removed from the furnace at temperature and allowed to air quench. The resultant borate was a white, porous ceramic and confirmed to be phase pure via XRD as shown below in Figure 4.3.

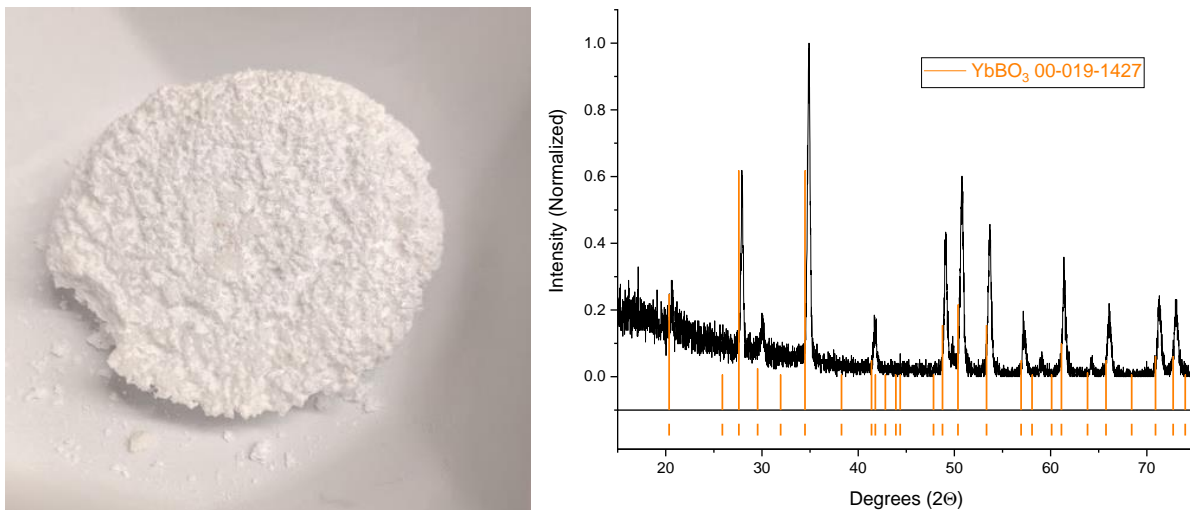


Figure 4.3: (left) YbBO_3 formed after 24-hour exposure of mechanically mixed 40 mol% Yb_2O_3 and 60 mol% B_2O_3 powders at 800°C in a stagnant air box furnace. (Right) XRD of the bulk YbBO_3 showing that it is phase pure YbBO_3 .

The borate was then crushed to a powder for further testing. Hot-stage XRD (Anton Parr), was conducted using powder that was leveled with the surface of an alumina sample dish with a 0.8 mm lip that was lined with platinum foil. The sample was inserted into the furnace and measurements were taken at 25°C, then 100°C and every hundred degrees up to 1200°C, the maximum temperature of the hot stage furnace. A second run of the borate powder for lattice parameter and CTE determination was also done starting at 900°C up to 1000°C in 25°C increments. The sample was next heated to 1200°C and lowered to 600°C in 100°C increments at which point the increments were again changed to 25°C until 450°C. The purpose of this second run was to observe the transition from the low temperature polymorph to the high

temperature polymorph and then back again, collecting additional lattice parameter and CTE data in those ranges.

Solid samples were also pressed from the borate powders in a 1-inch die using a Carver manual hydraulic press (unheated benchtop manual press; model no. 3851; Carver Inc. Wabash, IN).

The pucks were pressed from the crushed YbBO_3 powders with a few drops of DI H_2O to act as a plasticizer. They were pressed up to 7 metric tons and held at that pressure for 20 minutes.

Once pressed, they were dried for 24 hours in a convection oven at 150°C to remove any water from the samples. These samples were approximately 2 grams each and were intended for cutting into coupons for thermogravimetric analysis, high temperature, high-velocity steam exposures, and time domain thermal reflectance testing, however meaningful results were not obtained as will be discussed further in the results section.

4.3 Results

4.3.1 DSC

The first DSC scan obtained of the equimolar oxide mixture mirrors that of the prior scan from the binary phase studies with the first thermal event occurring at 733°C and then the cooling event at $\sim 600^\circ\text{C}$ as shown below in Figure 4.4. The second DSC scan of the same sample no longer shows an event at 733°C and now exhibits an endothermic event at 995°C and the exothermic event on cooling at 540°C as already observed. These peaks are labeled in Figure 4.5 along with the associated enthalpies. The melting of B_2O_3 at 450°C is not observed in these DSC scans, however it is also not observed in the baseline scan of just the B_2O_3 powder as is shown in the Appendix (7.1.1).

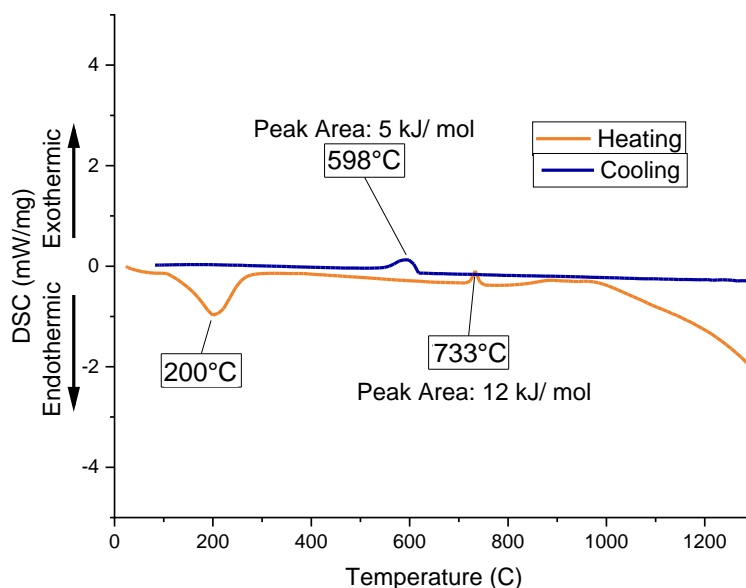


Figure 4.4: 1st DSC results of Yb_2O_3 and B_2O_3 equimolar mixture showing PVA burnout at 200°C on heating, exothermic formation reaction at 733°C on heating, and exothermic phase transition at 599°C on cooling.

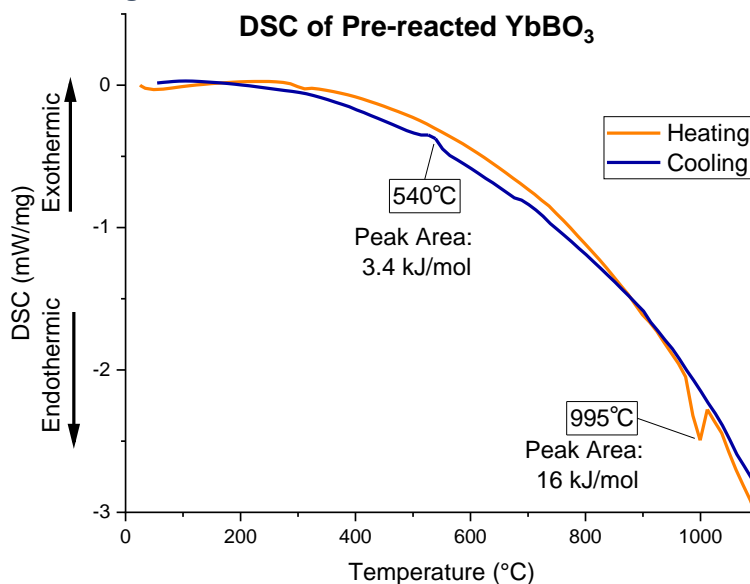


Figure 4.5: Repeat of DSC run from sample in Figure 4.4 above, now YbBO_3 , showing endothermic phase change at 995°C on heating and exothermic phase change at 540°C on cooling.

These results (Figure 4.4 and Figure 4.5) confirm that the 733°C thermal event is the formation of the high-temperature polymorph of YbBO_3 from the constituent oxides, and that the transition from the low temperature to the high temperature polymorph occurs at ~1000°C,

consistent with the existing phase diagram. The transition back from the high temperature polymorph to the low temperature polymorph shows a much lower temperature that ranges between 500°C and 600°C. The large hysteresis in this transition is unusual for most crystalline materials, however it was confirmed via hot stage XRD where both polymorphs were recorded in a scan taken at 500°C on cooling as shown in Figure 4.6 below. The measured enthalpies for this polymorphic transition, 16 kJ/mol YbBO_3 on heating and approximately 4 kJ/mol YbBO_3 on cooling, is of a similar magnitude for the quartz to tridymite transitions which are approximately 10 kJ/mol for $\text{quartz}_{(l)} \rightarrow \text{tridymite}_{(l)}$ and 2 kJ/mol for $\text{quartz}_{(h)} \rightarrow \text{tridymite}_{(h)}$ (25).

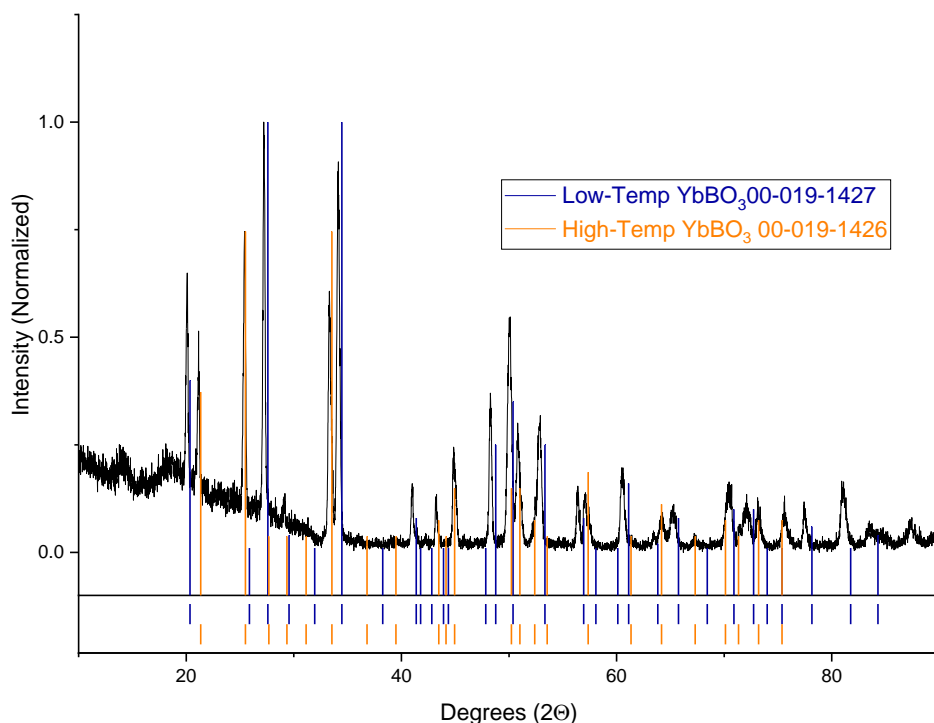


Figure 4.6: Hot Stage XRD scan showing both YbBO_3 polymorphs at 500°C on cooling.

4.3.2 Hot Stage Lattice Parameter and CTE Results

Lattice parameter and CTE data were obtained for the borates from both hot stage XRD runs.

Some ytterbia did appear in the scans, allowing for comparison of the data to literature values

and validation of the accuracy of the technique. As shown below in Figure 4.7, the hot stage lattice parameter results obtained for cubic Yb_2O_3 match well with previously recorded data for ytterbia taken by Sectura (20,21).

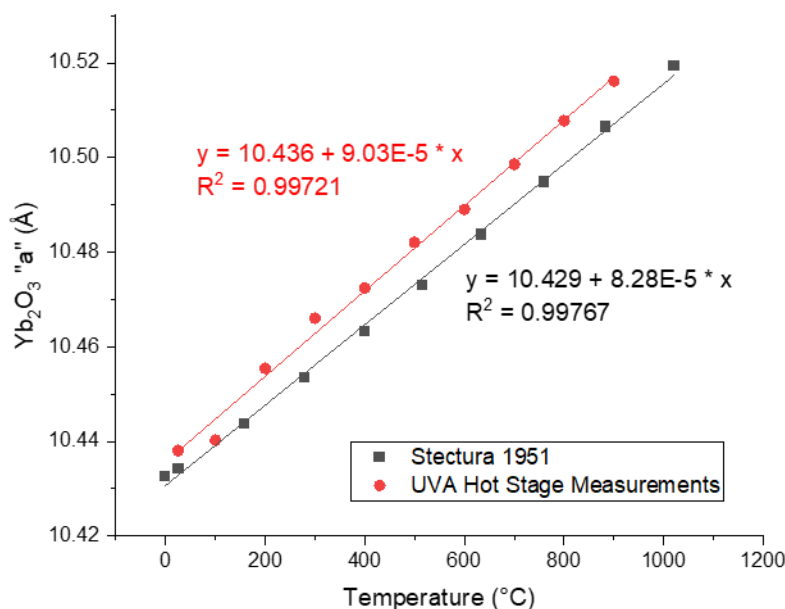


Figure 4.7 : Cubic Yb_2O_3 lattice parameters taken from hot-stage XRD on heating compared to Sectura data for Yb_2O_3 CTE taken in 1961 (20)

Unit cell measurements for YbBO_3 were taken from both hot stage XRD heating runs and graphed to show the expansion of the unit cell dimensions in the basal “a” and normal “c” directions, shown below in Figure 4.8. As illustrated from the jumps in cell dimensions, the basal “a” direction expands and the “c” direction contracts during the transition from the low temperature polymorph to the high temperature polymorph. Thermal expansion coefficients were calculated from these unit cell dimensions and are reported in Table 4-3 below along with the CTEs of other CMC components for comparison (21–24). CTEs were found to be significantly larger in both directions for the high-temperature polymorph than for the low temperature polymorph.

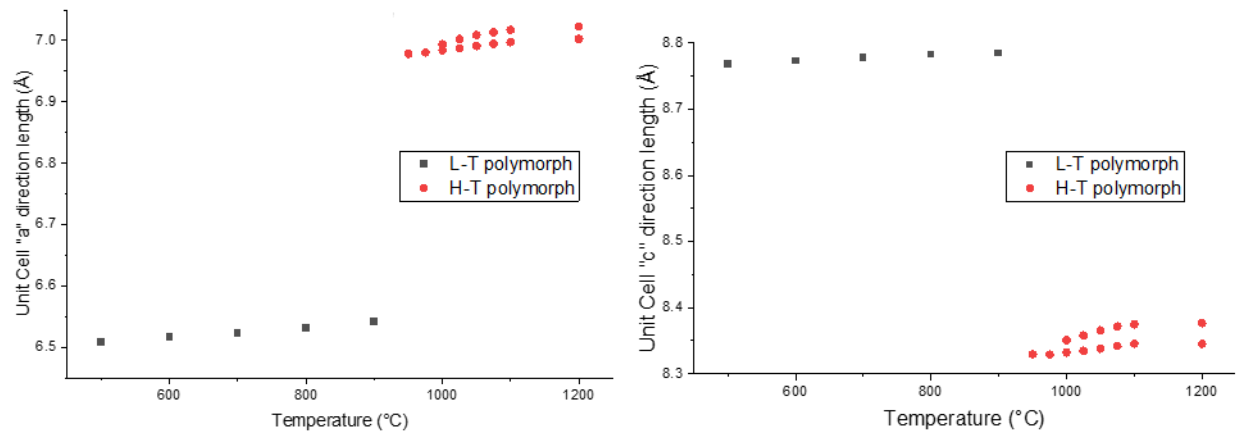


Figure 4.8: Unit cell expansion data for both YbBO_3 vaterite polymorphs. (Left) Unit cell expansion in “a” basal plane direction. (Right) expansion in “c” direction. High temperature polymorph data taken in two separate runs shown in red. Low temperature polymorph data shown in black.

Table 4-3: Calculated CTEs for YbBO_3 and material components of EBC/ CMC systems. CTE for individual lattice directions are reported for the YbBO_3 polymorphs while data reported for other constituents are the average linear CTE for the phase. (21,23,24)

Component	Crystal Structure	Isotropic?	Linear CTE ($\ast 10^{-6} \text{ }^\circ\text{C}^{-1}$)
Low-Temp YbBO_3	Hexagonal	No	a: 10.37, c: 5.69
High Temp YbBO_3	Hexagonal	No	a: 26.8, c:22.7
Yb_2O_3 ⁽²¹⁾	Cubic	Yes	6.8-8.4
$\text{Yb}_2\text{Si}_2\text{O}_7$ ⁽²³⁾	Monoclinic	No	4-6
Yb_2SiO_5 ⁽²³⁾	Monoclinic	No	4-8
Si ⁽²⁴⁾	Cubic	Yes	3.5-5.5
SiC ⁽²⁴⁾	Hexagonal (α)	Yes	4.5-5.5

In addition to determining the CTE, the unit cell dimensions of both the low temperature and the high temperature polymorphs were used to calculate the change in volume that occurs during the phase transition as well as the change in volume that would occur when the borate forms as a result of boria reacting with the silicates in the EBC. All the phases of interest are listed in Table 4-4 below. The change in volume during a transition from the phase of interest to the low-temperature polymorph of YbBO_3 is calculated using Equation [4-1] below where the

starting phase (V_0) is the phase of interest, and the final phase is the low temperature polymorph (V_i). The reaction of the $\text{Yb}_2\text{Si}_2\text{O}_7$, Yb_2SiO_5 , and Yb_2O_3 starting phases with B_2O_3 results in two units of YbBO_3 formed as accounted for in Equation [4-1] below. The factor of two is not needed in the calculation for the change in volume between the two borate polymorphs.

$$\% \text{ Change in Volume} = \frac{V_0 - 2V_i}{V_0} \quad [4-1]$$

Table 4-4: Calculated volumes for assorted phases of interest and difference in volumes relative to low-temperature YbBO_3 polymorph

Phase	Formula units in Unit Cell	UC volume (\AA^3)	Unit volume	ΔV to Low Temperature YbBO_3 Polymorph
Yb_2O_3	16	1165	72.8	44.3% increase
Yb_2SiO_5	8	829	103	1.4% increase
$\text{Yb}_2\text{Si}_2\text{O}_7$	4.0	518	129	18.9% decrease
YbBO_3 (L-T)	6	315	52	N/A
YbBO_3 (H-T)	6	353	58	10.7% decrease

4.3.3 Static Equilibrium Testing

The phases present in the platinum packets were characterized using a combination of SEM and micro-focus XRD. The packets were filled with an equimolar mixture of B_2O_3 and Yb_2O_3 powders before exposure, first at 800°C for 24h to allow formation of the borate phase, and then at either 500°C or 600°C for 24h to allow equilibration at those temperatures. The SEM images of the packet cross sections show porous samples with agglomerations of a bright phase, likely Yb_2O_3 , suspended in a darker matrix, likely YbBO_3 and B_2O_3 . This is the case for samples equilibrated at both 500°C and 600°C , though as shown in the micrographs below (Figure 4.9), the bright phases are more prevalent in the 600°C sample. Packets annealed at

800°C for 24 hours showed only YbBO_3 in the micro-focus XRD scans as shown below in Figure 4.10, so this suggests that the YbBO_3 experiences some phase separation after the initial formation reaction. Also, of note in the image of the 500°C sample is the stringing of sample across a crack that has formed, likely during quenching of the samples.

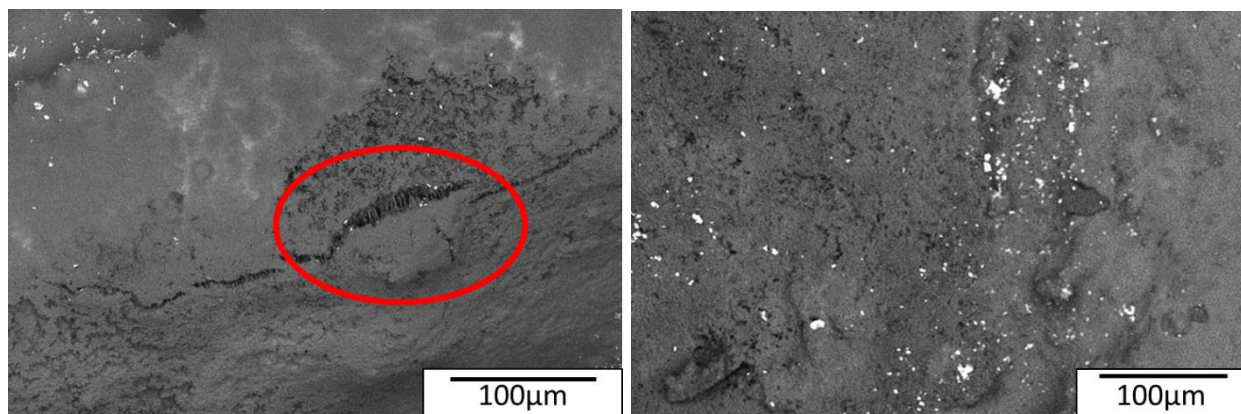


Figure 4.9: Backscatter electron micrographs of the YbBO_3 samples inside the platinum packets. Equimolar mixtures of Yb_2O_3 and B_2O_3 were first equilibrated at 800°C for 24 hours before a secondary 24h equilibration at the temperatures of interest. (Left) 500°C, note the stringing in the crack. (Right)- 600°C, note the bright phase is more prevalent after equilibration at the higher temperature.

When scanned with the micro-focus XRD, both encapsulated specimens showed both Yb_2O_3 and the low temperature polymorph of YbBO_3 as product phases (Figure 4.10). The presence of Yb_2O_3 after these exposures verifies the SEM results that either the powders did not fully react or experienced some phase separation during the exposure.

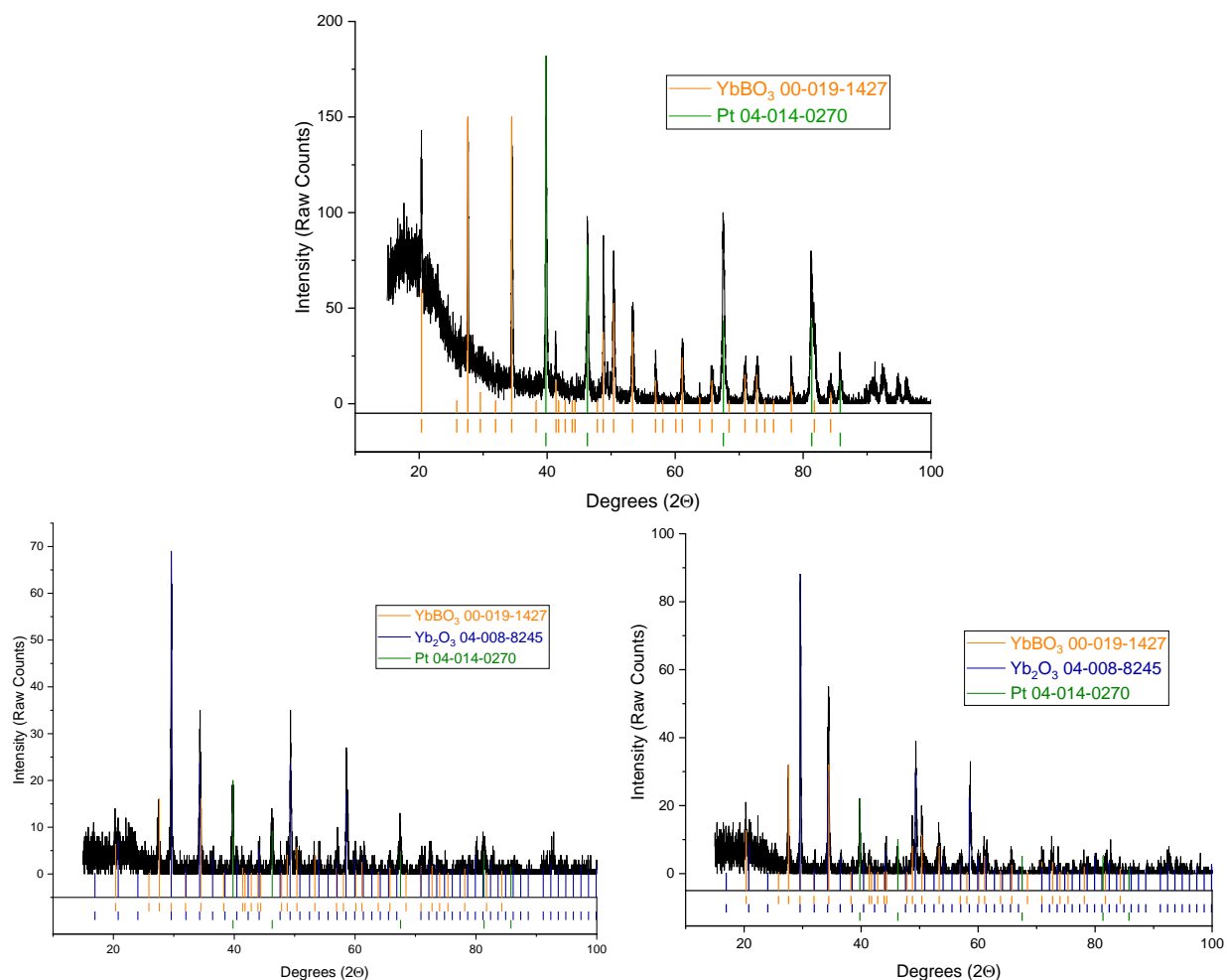


Figure 4.10: Micro focus XRD scans of static equilibration of equimolar Yb_2O_3 and B_2O_3 mixtures after reaction at 800°C (Top) and 24h equilibrations. Note the presence of YbBO_3 in the 800°C exposure and the presence of both YbBO_3 and Yb_2O_3 in the 500°C (Left) and 600°C (Right) exposures.

4.3.4 Solid YbBO_3 Samples

Solid samples for environmental stability testing were produced via reaction of 60% B_2O_3 and 40% Yb_2O_3 powders at 800°C for 24 hours as shown in Figure 4.3. The resultant YbBO_3 solid was crushed into powder, then pressed in the Carver press with DI H_2O as a plasticizer. After pressing the YbBO_3 powder into pellets, the pellets were dried to remove the DI H_2O that had been used as a pressing aid. These pellets were then placed in the box furnace to anneal and

sinter at 500°C, just above the melting temperature of boria, and well below the phase transformation temperature or melting temperature of the borate. However, at this temperature the borate pucks swelled. This would indicate some expansion and out-gassing of trapped volatile species in the sample, though there was no significant weight change after swelling and cooling of the samples. This rapid expansion and slumping behavior could also be attributed to phase separation and B_2O_3 melting. Figure 4.11 below shows the swelling of the pucks after 1200°C exposure for 10 minutes.



Figure 4.11: Pressed, polished, and sectioned YbBO₃ puck piece (Left) swelling after 10 min exposure at 1200°C in stagnant air box furnace (Right).

This swelling was found to occur at temperatures as low as 475°C and for times as short as 15 minutes at this temperature. The swelling was more pronounced at 1200°C for 10 minutes, and at longer exposure times (1h) at 800°C, the pucks showed apparent melting, running off the edges of the platinum foil-lined plate that was being used for the annealing. Additionally, while still hot from exposure, the borate samples were extremely malleable, able to be easily deformed with tweezers as shown below in Figure 4.12.

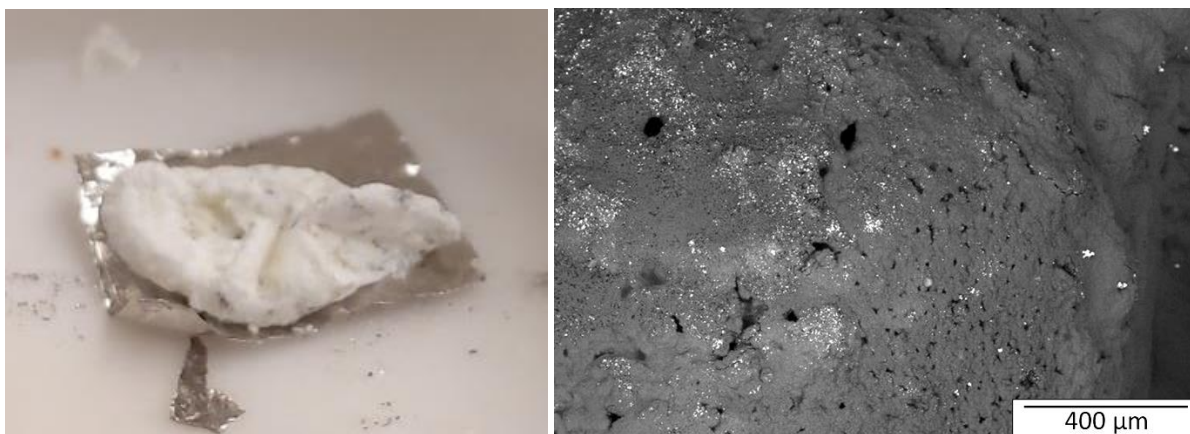


Figure 4.12: YbBO_3 ceramic puck sample after manipulation with tweezers while hot (30 minutes at 1200°C) and backscatter electron micrograph of sample surface.

As the ceramics cooled, they did harden, but exhibited this swelling behavior upon both re-exposure to elevated temperatures as well as crushing and re-pressing the samples into new pucks. Pucks were characterized using SEM and XRD after the heat treatments at 475°C , 500°C , and 1200°C . While the 1200°C sample showed 98.2% YbBO_3 via Rietveld refinement (Figure 4.14), both Yb_2O_3 and YbBO_3 were found in the 475° and 500° samples (Figure 4.13), indicating that there was some degree of either phase separation or incomplete reaction for those samples. Given the XRD phase measurements, it is assumed the dark matrix phase observed in the SEM micrographs is YbBO_3 and the agglomerated bright phase is residual or phase separated Yb_2O_3 .

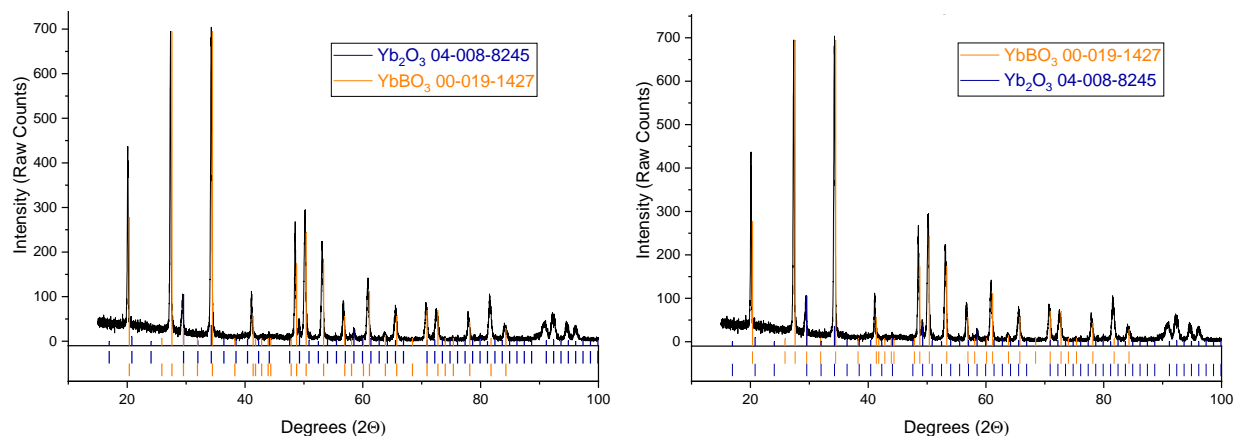


Figure 4.13: XRD scans of YbBO_3 pucks from the pre-reacted YbBO_3 powder reacted post-anneal for 1 hour at 475°C (left) and 500°C (right) showing both YbBO_3 and Yb_2O_3 present in the samples.

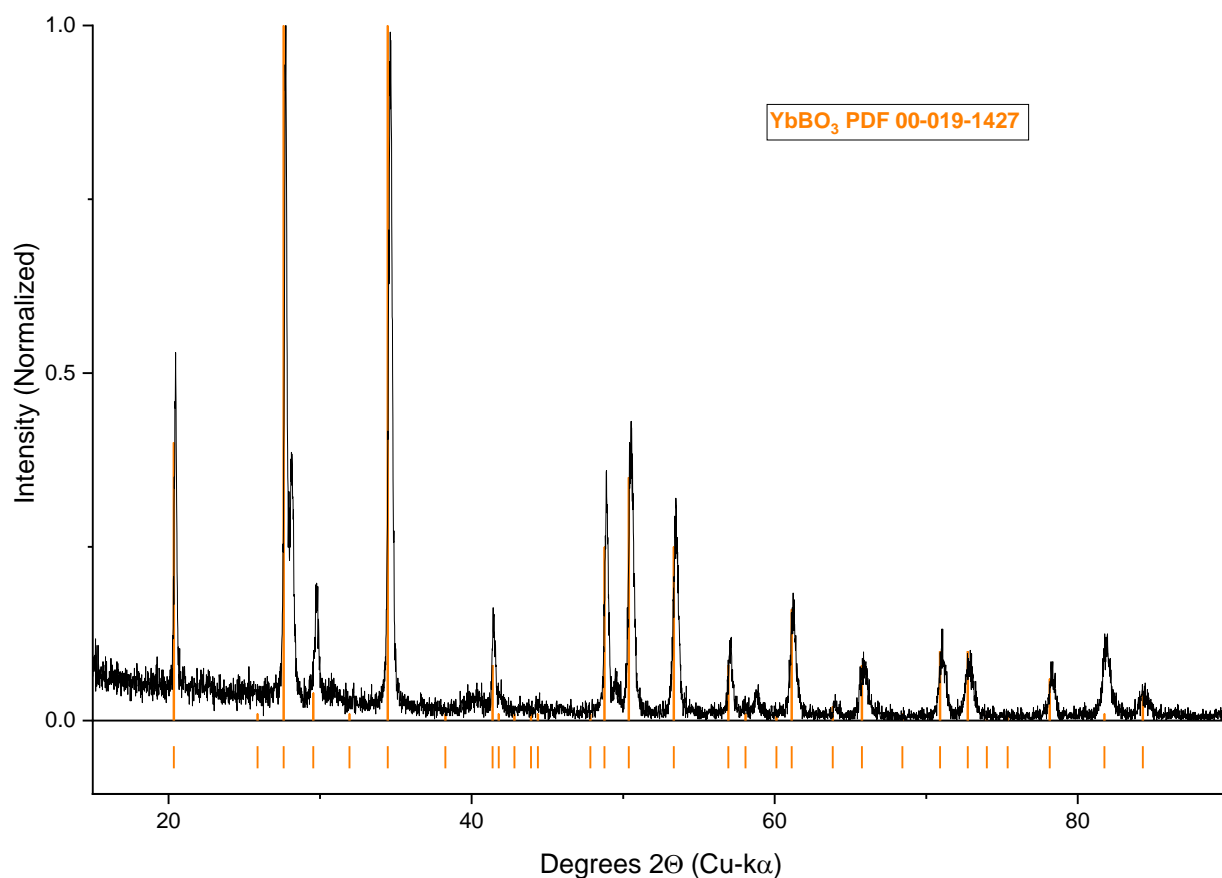


Figure 4.14: XRD scan of YbBO_3 puck from the pre-reacted YbBO_3 powder after annealing at 1200°C for 10 minutes showing only the YbBO_3 phase present.

4.4 Discussion

The formation of YbBO_3 from its constituent oxides, Yb_2O_3 and B_2O_3 was characterized through DSC and found to occur at 733°C with an enthalpy of formation of 12 kJ/mol . This small ΔH for the borate formation is consistent with a relatively low stability when compared to the constituent oxides Yb_2O_3 and B_2O_3 . DSC of pre-reacted YbBO_3 showed that the transition from the low temperature polymorph to the high temperature polymorph occurs at 1000°C on heating with an enthalpy of 16 kJ/mol . The transition back to the low temperature polymorph occurs between 500°C and 600°C upon cooling with an enthalpy of 3.4 kJ/mol . These ΔH values for the YbBO_3 reconstructive polymorphic transformation are similar in magnitude to the reconstructive phase transformation for quartz to tridymite for SiO_2 which has an enthalpy of approximately 10 kJ/mol .

The borate phase exhibited several unusual phenomena that are not generally seen in ceramic materials, though several of these behaviors can be explained by the structure and bonding within the structure of this vaterite analog. As shown in work done by Ren (14), gadolinium borate exhibits a similar hysteresis in the transitions of approximately 300°C between the high temperature and the low temperature polymorph; 836°C on heating and 546°C on cooling. Ren et al. attribute this to the fact that the phase transition is a reconstructive transition where the boron in the structure changes its number of oxygen bonds, switching between tetrahedral coordination and trigonal planar coordination as shown in Figure 4.1. The transition as observed in this study is kinetically limited, leading to both the lag in transition temperature as well as the range of temperatures between 500°C and 600°C at which the transition was recorded in DSC.

This phase transition also results in a sudden change in both the unit cell dimensions of the borate, and a change in volume of $\sim 11\%$. This change in bonding and unit cell dimensions is also accompanied by a sudden jump in the CTE of the YbBO_3 phase. The CTE of both YbBO_3 polymorphs is significantly higher than that of the other constituents of the CMC/ EBC system as shown in Table 4-3. This large CTE observed for YbBO_3 is similar to that of CaCO_3 vaterite which exhibits a volumetric CTE ranging between 35 and 105 ($\times 10^{-6} \text{ K}^{-1}$) from room temperature up to 600°C (5,7). The CO_3 groups in CaCO_3 vaterite take the trigonal planar coordination as is seen in the borate groups in the high-temperature polymorph of YbBO_3 . These trigonal planar groups have a lower network connectivity between unit cells and can take multiple orientations within the cell. They will also expand in a more anisotropic manner than the tetragonally bonded B-O groups in the low temperature polymorph, all of which contribute to a larger and more anisotropic CTE for the high temperature polymorph. The rapid change in unit cell size as well as the jump in CTE during the polymorphic transitions, combined with the large, anisotropic CTE for the YbBO_3 phase will be detrimental to the CMC/EBC system as it undergoes thermal cycling.

The swelling and melting behavior observed in the bulk YbBO_3 samples will also be highly detrimental to the CMC/ EBC system stability and lifetime if found to occur during use. This behavior was observed at temperatures as low as 450°C for exposure times as short as 15 minutes. Shown below in Figure 4.15 are XRD scans of the YbBO_3 samples discussed above in various stages of processing to form the pucks. Yb_2O_3 content was calculated via Rietveld refinement of the scans, and the measured weight percent of Yb_2O_3 is listed to the right of the scans under the sample name. The bulk sample, as-reacted in the box furnace shows less than

5% Yb_2O_3 . This increases to between 13 & 15% once the solid sample is crushed into a powder, indicating that the Yb_2O_3 may not have reacted as fully with the B_2O_3 during the furnace exposure as was observed on the surface of the solid sample. The powders were then pressed into pucks and re-exposed in the box furnace for sintering. At 475°C only 6% Yb_2O_3 was measured on the surface of the puck. This increased to 58% at 500°C indicating some phase separation during the exposure. When subsequently exposed again at 1200°C, the measured amount of Yb_2O_3 dropped down to only 0.2%. It is possible that once exposed at temperatures greater than the formation temperature of YbBO_3 , the phase separated oxides reacted to form the borate phase again or residual boria volatilized.

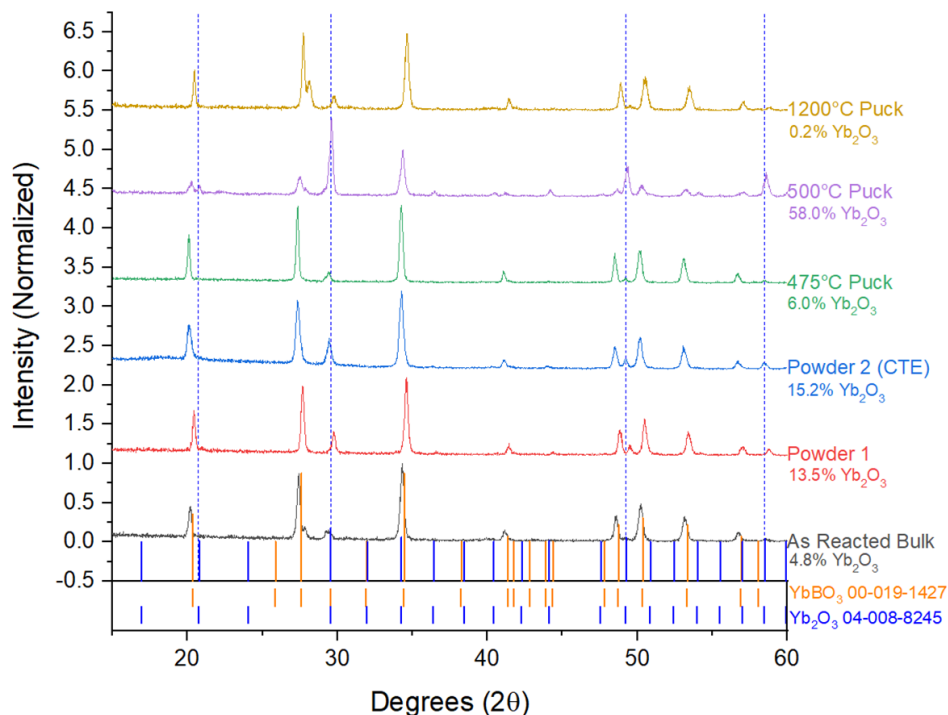


Figure 4.15: Stacked XRD patterns of the YbBO_3 samples in various stages of processing and testing. Yb_2O_3 -specific peaks are highlighted with vertical blue lines and the measured Yb_2O_3 content via Rietveld refinement is shown under the sample identification to the right of each scan.

XRD results, both in bulk and in the platinum encapsulation packets, show that after 24h at 800°C, the Yb_2O_3 and B_2O_3 powders had almost fully reacted on the surface, however crushing showed an excess of Yb_2O_3 throughout the bulk of the sample. Characterization after the secondary exposures both in the platinum packets and the heat treatments for the pressed pucks indicated that there was a degree of phase separation of the YbBO_3 back into its constituent oxides of Yb_2O_3 and B_2O_3 . Either excess boria from unreacted constituent oxides or phase separation of YbBO_3 would explain the rapid expansion and melting behavior observed at low temperatures. Boria has a melting point of 450°C, and the expansion as it melted into the liquid phase would account for some of the swelling as well as the slumping behavior observed.

4.5 Conclusions

The reaction to form YbBO_3 from the constituent Yb_2O_3 and B_2O_3 was confirmed via DSC and found to occur at 733°C with an associated enthalpy of 12 kJ/mol. The reconstructive phase transition between the high temperature and the low temperature polymorphs of YbBO_3 was found to occur at approximately 1000°C upon heating with an associated enthalpy of 16 kJ/mol and 540°C on cooling with an associated enthalpy of approximately 4 kJ/mol. This hysteresis in the transition temperatures is unusual but has also been observed in GdBO_3 . This polymorphic transition is a reconstructive transition where the B-O polyhedra bonding within the unit cell changes between tetragonal and trigonal planar. This bond reconstruction suggests that the transition is kinetically limited on cooling, leading to the large hysteresis in transition temperatures.

Coefficients of thermal expansion were also measured for both the high temperature and the low temperature polymorphs of YbBO_3 . It was found that the unit cell experiences a rapid

change in both dimension and CTE during the polymorphic transition. The CTE was found to be much larger in both the “a” and “c” directions for the high-temperature polymorph than the low-temperature polymorph as expected with the trigonal planar rather than the tetrahedral B-O bonding. The measured CTEs for YbBO₃ are also significantly larger than those of other components of the CMC/EBC system which will be detrimental to the system as it undergoes thermal cycling due to the expansion mismatch.

Bulk, nearly phase pure YbBO₃ was produced via furnace reaction. The powder was then pressed into pellets for further testing, but annealing procedures resulted in unexpected behavior. The pellets expanded rapidly and became very malleable, easily deformed while hot, and would melt after longer exposure times. The mechanism for this rapid expansion behavior is attributed to either excess unreacted boria and/or phase separation of the YbBO₃ into B₂O₃ and Yb₂O₃ with melting and liquid expansion of the B₂O₃.

The formation of the YbBO₃ phase would be detrimental to the stability of the CMC/EBC due to the large, anisotropic CTE for both polymorphs, and the CTE mismatch of YbBO₃ relative to other CMC/EBC system components, as well as the rapid change in volume during the polymorphic phase change. Phase separation will cause further issues as the B₂O₃ phase forms a low viscosity melt with rapid expansion at temperatures as low as 450°C.

4.5.1 Future Work

The unusual behavior of the YbBO_3 phase and its long-term stability warrant further study. The extent of the rapid expansion and slumping behavior as a result of the potential phase separation is still unknown. Longer-term phase separation studies are recommended as well as long term stability testing of the phase in combustion environments. H_2O soaks and ICP analysis after heat treatments would be useful for quantifying free boria content. The stability of this phase in the presence of high pressures, temperatures, and steam-containing environments has not yet been investigated and will be vital to determine the impact of YbBO_3 formation on the CMC/ EBC system.

4.6 References

1. Bradley WF, Graf DL, Roth RS. The vaterite-type ABO₃ rare-earth borates. *Acta Crystallographica*. 1966;20(2):283–7.
2. Levin EM, Roth RS, Martin JB. Polymorphism of ABO₃ Type Rare Earth Borates. *the American Mineralogist* [Internet]. 1961;46(1954):1030–55. Available from: http://www.minsocam.org/ammin/AM46/AM46_1030.pdf
3. Newnham RE, Redman MJ, Santoro RP. Crystal Structure of Yttrium and Other Rare-Earth Borates. *Journal of the American Ceramic Society*. 1963;46(6):253–6.
4. Jacob DE, Wehrmeister U, Soldati AL, Hofmeister W. Spectroscopic characterisation of biological vaterite: relations to synthetic and geological vaterites. *Geophysical Research Abstracts*. 2009; 11:2006–7.
5. Turnbull AG. A thermochemical study of vaterite. *Geochimica et Cosmochimica Acta*. 1973;37(6):1593–601.
6. Demichelis R, Raiteri P, Gale JD, Dovesi R. The multiple structures of vaterite. *Crystal Growth and Design*. 2013;13(6):2247–51.
7. Ševčík R, Šašek P, Viani A. Physical and nanomechanical properties of the synthetic anhydrous crystalline CaCO₃ polymorphs: vaterite, aragonite and calcite. *Journal of Materials Science*. 2018;53(6):4022–33.
8. Day SJ, Thompson SP, Parker JE, Evans A. Non-aqueous formation of the calcium carbonate polymorph vaterite: Astrophysical implications. *Astronomy and Astrophysics*. 2013; 553:1–10.
9. Makovicky E. Vaterite: Interpretation in terms of OD theory and its next of kin. *American Mineralogist*. 2016;101(7):1636–41.
10. Tang CC, Thompson SP, Parker JE, Lennie AR, Azough F, Kato K. The ikaite-to-vaterite transformation: new evidence from diffraction and imaging. *Journal of Applied Crystallography*. 2009;42(2):225–33.
11. Christy AG. A Review of the Structures of Vaterite: The Impossible, the Possible, and the Likely. *Crystal Growth and Design*. 2017;17(6):3567–78.
12. Weir CE, Lippincott ER. Infrared studies of aragonite, calcite, and vaterite type structures in the borates, carbonates, and nitrates. *Journal of Research of the National Bureau of Standards Section A: Physics and Chemistry*. 1961;65A (3):173.
13. Burgess KMN, Bryce DL. On the crystal structure of the vaterite polymorph of CaCO₃: A calcium-43 solid-state NMR and computational assessment. *Solid State Nuclear Magnetic Resonance* [Internet]. 2015; 65:75–83. Available from: <http://dx.doi.org/10.1016/j.ssnmr.2014.08.003>

14. Ren M, Lin JH, Dong Y, Yang LQ, Su MZ, You LP. Structure and phase transition of GdBO₃. *Chemistry of Materials*. 1999;11(6):1576–80.
15. Academy W, Academy W. A comparison of the heating-curve and quenching methods of melting-point determinations Author (s): George W . Morey Source: *Journal of the Washington Academy of Sciences* , August 19 , 1923 , Vol . 13, No . Published by: Washington Academy of Science. 1923;13(14):326–9.
16. Rockett TJ, Foster WR. Phase Relations in the System Boron Oxide–Silica. *Journal of the American Ceramic Society*. 1965;48(2):75–80.
17. Toropov NA, Bondar' IA. Silicates of the rare earth elements. *Bulletin of the Academy of Sciences of the USSR Division of Chemical Science*. 1961;10(8):1278–85.
18. Hudon P, Baker DR. The nature of phase separation in binary oxide melts and glasses. I. Silicate systems. *Journal of Non-Crystalline Solids*. 2002;303(3):299–345.
19. Konar B, Hudon P, Jung IH. Experimental investigation of the LiAlSi₂O₆-MgSiO₃ and LiAlSi₂O₆-CaMgSi₂O₆ isopleths at 1 atm. *Journal of the American Ceramic Society*. 2017;100(7):3269–82.
20. Grain CF, Campbell WJ. Thermal Expansion and Phase Inversion of Six Refractory Oxides. *US Bur Mines Rep Invest*. 1962;(5982):21.
21. Stecura S, Campbell WJ, Udall SL, Ankeny MJ. Thermal Expansion and Phase inversion of Rare Earth Oxides. *Report of Investigations 5847 United States Department of the Interior*.
22. Richards BT, Begley MR, Wadley HNG. Mechanisms of Ytterbium Monosilicate/Mullite/Silicon Coating Failure during Thermal Cycling in Water Vapor. *Journal of the American Ceramic Society*. 2015 Dec 1;98(12):4066–75.
23. Lee KN. Current status of environmental barrier coatings for Si-based ceramics. *Surface and Coatings Technology*. 2000;133–134:1–7.
24. Richards, Bradley, and Wadley, Haydn (advisor). Ytterbium Silicate Environmental Barrier Coatings. University of Virginia, Materials Science - School of Engineering and Applied Science, PHD (Doctor of Philosophy), 2015, 2015, doi.org/10.18130/V3C259.
25. C. W. Bale, E. Bélisle, P. Chartrand, S. A. Deckerov, G. Eriksson, A.E. Gheribi, K. Hack, I. H. Jung, Y. B. Kang, J. Melançon, A. D. Pelton, S. Petersen, C. Robelin, J. Sangster, P. Spencer and M-A. Van Ende, *FactSage Thermochemical Software and Databases - 2010 - 2016*, Calphad, vol. 54, pp 35-53, 2016 <www.factsage.com>

5 Effects of Boria on the Si Bond Coat Oxidation and $\text{Yb}_2\text{Si}_2\text{O}_7$ EBCs

5.1 Introduction

The studies discussed up to this point have all focused on pure materials and ideal interphases to determine what reactions are occurring in the $\text{Yb}_2\text{O}_3 - \text{SiO}_2 - \text{B}_2\text{O}_3$ system and to what extent, however, these studies have used significantly more boria than is present in real CMC/EBC systems. This final chapter aims to determine the effects of the boria on the SiC CMC/ Si/EBC interfaces in a real CMC system.

The focus of these studies is first on the thermally grown oxide (TGO) that forms when CMC/EBC systems are subjected to oxidizing environments. The TGO develops in the interface between the Si bond coat and the EBC as oxygen diffuses through the EBC. The silica bond coat is a vital layer between the EBC and the CMC as it acts as a getter to the ingress of oxygen to the system, significantly inhibiting the oxygen from reaching the CMC and oxidizing the SiC and BN, both of which would be detrimental to the system's performance(1–9). The main way that the Si bond coat prevents this oxidation is through the growth of silica in the EBC/ bond coat interface, or the formation of the thermally grown oxide (TGO). Si oxidation is preferable to SiC oxidation since no $\text{CO}_{(\text{g})}$ or $\text{CO}_{2(\text{g})}$ forms during oxidation rendering the EBC/TGO interface more adherent (1). However, the SiO_2 TGOs are prone to volatilization in the presence of water vapor, necessitating the use of the rare earth silicate EBCs (2,10).

Previous studies show that both Si and SiC oxidize to form SiO_2 as shown in Equations [5-1] and [5-2] below. Their oxidation is described by the Deal & Grove model for oxide thicknesses greater than 20 nm (11–13).



At lower temperatures ($\leq 800^\circ\text{C}$), the oxidation is dominated by surface reaction kinetics where the oxide thickness grows linearly with time at a rate given by k_l . However, at longer times and higher temperatures such as those used in this study, the oxidation kinetics are diffusion controlled where the rate limiting step for the oxidation is the diffusion of molecular oxygen (D_{eff}) through the silica scale and is described by a parabolic rate constant (k_p) as shown in Equation [5-3] (13).

$$k'_p = \frac{2D_{eff}C^*}{N} \quad [5-3]$$

C^* is the equilibrium concentration of O_2 molecules in SiO_2 and N is the number of O_2 molecules per unit volume SiO_2 . Given the parabolic oxidation kinetics, it is expected that the oxidation of the Si bond coat to form the TGO will increase proportionally with increased time, temperature, and partial pressure (P_{O_2}) according to the following dependencies:

$$K_p \propto t^{1/2}$$

$$K_p \propto \exp(-\Delta H/RT) \text{ where } \Delta H \text{ is the activation energy for oxygen transport in } SiO_2$$

$$K_p \propto P_{O_2}^n \text{ where } n=1 \text{ for molecular oxygen}$$

These Si bond coats and RE-EBC topcoats are both applied to the CMC substrates via atmospheric plasma spray (APS) processes. This process, illustrated below in Figure 5.1 employs the use of a plasma torch and powder feedstock to apply the coatings. The torch liquefies the powder feedstock and accelerates it towards the target, in this case CMC substrates. The molten coating material then impinges or “splats” onto the substrate surface

where it solidifies. This process results in non-equilibrium coatings that are prone to microcracking, and porosity (14,15) as shown in Figure 5.2.

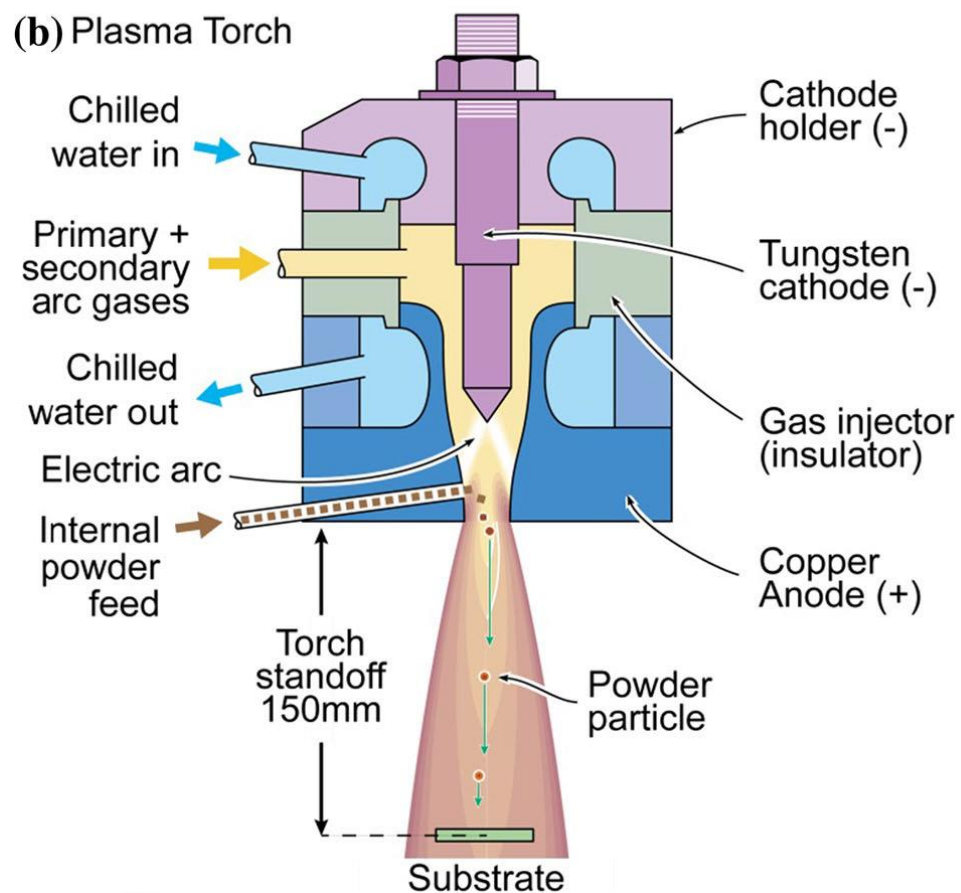


Figure 5.1: Diagram of APS process illustrating torch & powder feeds (14)

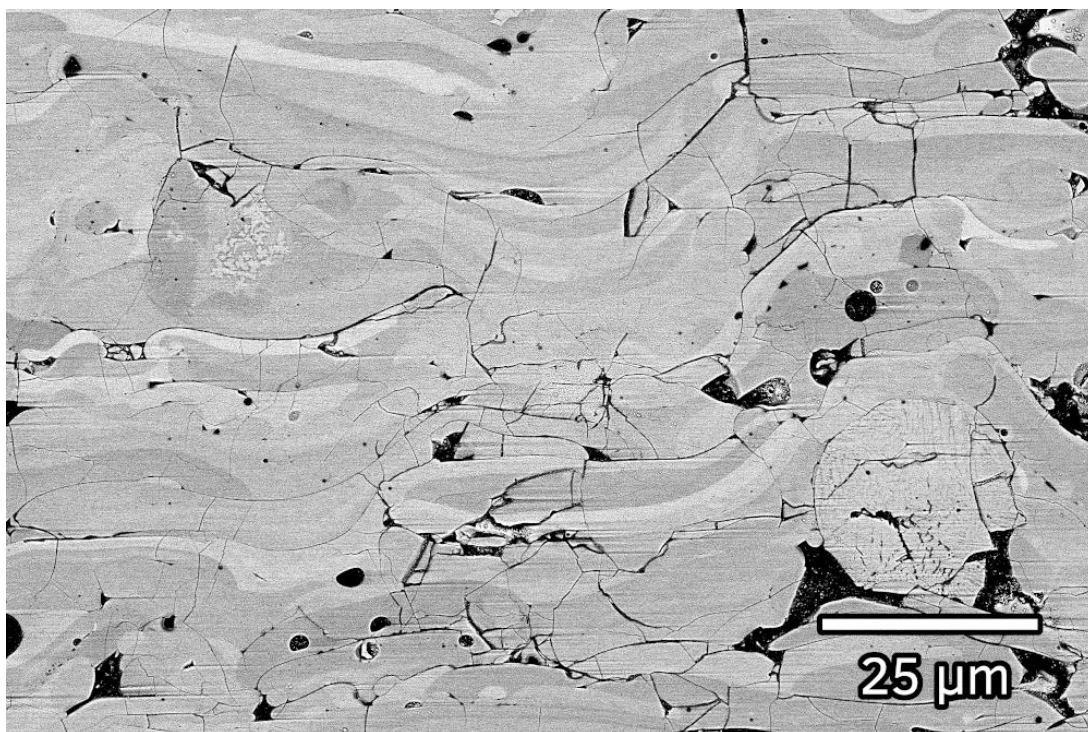


Figure 5.2: $\text{Yb}_2\text{Si}_2\text{O}_7$ coatings fabricated via APS processes showing pores, microcracking, and multiple Yb-silicate phases with varying SiO_2 content (16).

Boron can be found in the CMC/ EBC system both in the BN interphase surrounding the fibers and as phases within the matrix phase where it is used as an additive to assist with the melt infiltration process. Boria readily forms wherever boron-containing phases from the CMC are exposed to oxygen, whether on an edge of the CMC article or via microcracking. The resultant boria is known to reduce the melting temperature of silica when a borosilicate glass is formed as shown in the Rockett-Foster Phase diagram (Chapter 3 Figure 3.1) (17). It is then expected that growth of the silica TGO will be affected by any boron phases that oxidize in the system.

Additionally, boria has also been found to accelerate the oxidation of SiC. The mechanisms for this have been discussed in previous studies(11,18), though most recently, McFarland proposed that the accelerated oxidation rates in the presence of boria was due to increased surface reaction kinetics. This was found to be most readily observed at lower temperatures (800°C) as

the volatility of boria at 1200°C combined with the rapid formation of a protective silica scale prevented the etching of the SiC surface by the boria. The presence of B_2O_3 in the TGO and transport through the TGO is important to assess its contact with the $Yb_2Si_2O_7$ topcoat.

The studies discussed here aim first to determine the TGO formation kinetics in the CMC/ EBC systems as well as determine any time, temperature, and pressure effects on the oxidation. Second, the TGO amount and distribution through the bond coat will be measured, and finally the effects of boria on the EBC itself will be examined. These data will be gathered through exposure of coated CMC and reaction bonded (RB) SiC coupons for a range of times, temperatures, and pressures, followed by characterization of the samples in cross section.

5.2 Experimental Procedure

5.2.1 Materials and Test Matrix

For this study, two kinds of coupons were studied. The first are reaction-bonded SiC, referred to as RBSiC. These machined coupons were provided by Rolls-Royce with varying boron concentrations up to 4 wt%. CMC coupons were also provided by Rolls-Royce. Both the RBSiC and the CMC coupons were atmospheric plasma spray (APS) coated with a Si bond coat and $Yb_2Si_2O_7$ EBC on the majority of the front and back faces of the coupon. The sides, top, and bottom faces were left exposed as shown in Figure 5.3 of the coupons below.

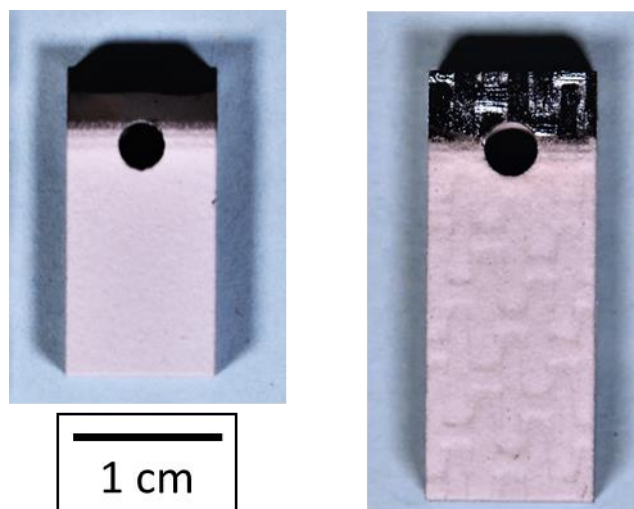


Figure 5.3: (Left) RBSiC and (Right) CMC coupons with Si bond coat and $\text{Yb}_2\text{Si}_2\text{O}_7$ topcoat.

The RBSiC and CMC coupons were exposed for 24, 100, and 500 hours at 900°, 1050°, and 1200°C, at pressures of 1 atm and 4.4 atm in the Keiser Rig at Oak Ridge National Lab. The benchtop weight changess from these samples were compared with 100h thermogravimetric analysis (TGA) tests at the same temperatures to compare oxidation of these coupons. Test conditions are listed below in Table 5-1. Additionally, the oxidation behavior of these coupons was compared to both literature standards as well as uncoated samples of the same substrates.

Table 5-1: TGA and Keiser Rig (ORNL) testing conditions for characterized RBSiC & CMC samples

Test Rig	Gas	Times	Temperatures	Pressure	Samples tested
TGA	O ₂	100h	900°C, 1050°C, 1200°C	1 atm	0%B, 4%B, CMC (1200°C only)
Keiser Rig	O ₂	24, 100, 500h		1 atm and 4.4 atm	0%B, 1%B, 2%B, 4%B, CMC

5.2.2 Sample Testing and Characterization

Benchtop weights were taken for all samples both before and after exposure. Coupon dimensions were also recorded prior to exposure. The Keiser Rig consists of two Hexoloy™ SiC chambers that can be pressurized with different oxidative environments. This setup allows for

the testing of many samples at varying times, temperatures, pressures, and oxidation environments to see how each of these variables affects the TGO formation and boron formation in the CMC/ EBC system.

For the Keiser rig (KR) exposures, samples were hung on horizontal alumina rods that sat in holes drilled through an alumina tube as shown below in Figure 5.4. The alumina tube was then lowered into the Hexoloy™ SiC chambers of the Keiser rig. The entire rig is sealed and brought to temperature with flowing O₂. The Keiser Rig has two chambers, enabling testing at both pressures, 1 atm and 4.4 atm simultaneously for each of the times and temperatures listed in the test matrix above (Table 5-1).

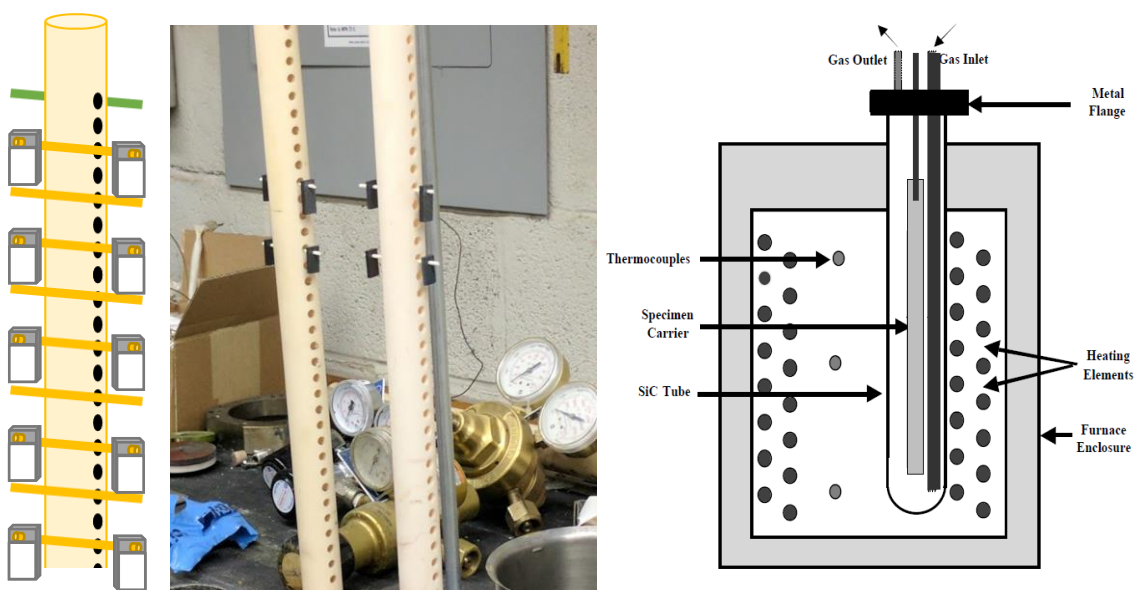


Figure 5.4: Keiser Rig Sample setup showing the hanging coupons and furnace setup of the coupon hangers inserted into Hexoloy™ SiC chambers.

TGA samples were hung from a single alumina hook (99.5 wt.% purity, Coorstek, Golden, CO) in a 22mm ID fused quartz tube (99.995% purity, 22 mm inner diameter, Quartz Scientific, Inc. Fairport Harbor, OH) that acts as the controlled atmosphere chamber in a custom-built

apparatus(19). The furnace (Lab-Temp Furnace Model LSL-2.5-0-6-1M-J11214/1A, Thermcraft Winston-Salem, NC) fits around this tube and is brought to temperature before being raised so the coupon hangs within the hot zone of the furnace tube at a lower gas velocity of 0.4 cm/sec. Dry O₂ (99.5% purity, Praxair Danbury, CT) flows at 1 atm through a MKS 247 Four Channel Readout flow controller (MKS Instruments Andover, MA) set to 100sccm, then through the fused quartz tube for the length of the 100h test. Weight changes are continuously measured by a Setaram B SETSYS 100g Microbalance (Setaram, Inc., Hillsborough, NJ) located well above the furnace to minimize signal disturbances from furnace operation. An images of the TGA setup and a detailed drawing of the coupon in the test are shown below in Figure 5.5.

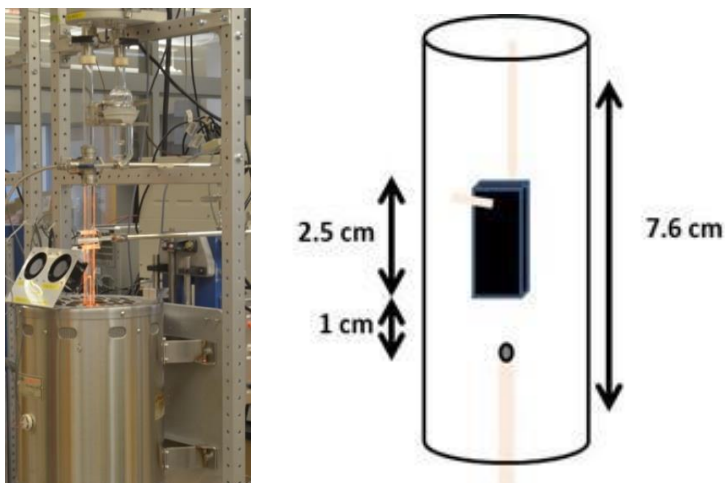


Figure 5.5: Photograph and hot zone schematic of a SiC coupon in the TGA

After exposure, oxidation kinetics for the samples were derived from the TGA data and the benchtop weight changes for the coated samples. Weight change was normalized to the calculated surface area based on the sample dimensions taken before the exposures. The specific weight changes were then graphed vs. time or square root of time to determine the oxidation mechanism for the sample and calculate the rate constants. These oxidation kinetics

were compared to the uncoated RBSiC and CMC samples that were also tested in the Keiser Rig, for which the data can be found in the McFarland Dissertation (20).

For characterization of the TGOs in the CMC samples, coupons were cut in half lengthwise before being mounted in epoxy. Samples were the polished to a 0.25 μm finish in glycol to limit dissolution of any exposed, water-soluble boron-rich phases in the system. The CMCs were cross-sectioned lengthwise down the center of the sample and imaged using SEM (FEI Quanta 650, Hillsboro, Oregon) to avoid edge oxidation effects from uncoated faces along both coated sides of the sample, avoiding the ends of the coated area where the TGO growth is likely affected by diffusion of oxygen from the uncoated regions.

Due to the number of variables being considered (Table 5-1), a machine learning-based imaging program called Dragonfly (ORS; Montreal, Quebec) was used to quantify the TGO growth in the CMC samples. The Dragonfly software is intended for rapid analysis of many images of multiple samples by teaching the artificial intelligence in the program to quantifiably identify the microstructural features such as area fraction of phases. In the case of TGO analysis for these CMCs, Dragonfly's AI was taught to distinguish the TGO from the Si bond coat based on phase contrast.

The bond coat/ TGO micrographs were imported to the Dragonfly imaging program for analysis. The process of masking, shown below in Figure 5.6, limits the area of the image to the bond coat and TGO to utilize for phase segmentation.

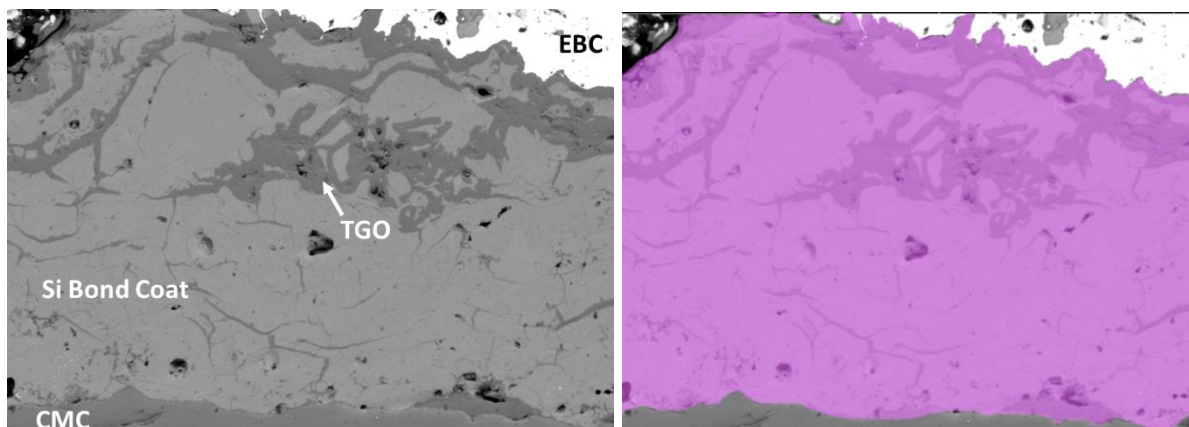


Figure 5.6: Masked image for Dragonfly (L: starting image- CMC with Si bond coat and EBC exposed in 4.4 atm O₂ at 900°C for 500h, R: Masked image showing that only the TGO and bond coat have been selected for segmentation)

Segmentation is the process of differentiating the TGO from the bond coat and porosity based on phase contrast. This segmentation process utilizes machine learning and artificial intelligence. These methodologies require training first to identify phases properly. This is done with a set of test images and an iterative learning process. Initially, multiple machine learning and deep learning models were trained on the image set. The first few images were segmented manually, then the AI is tested. Phase segmentations were corrected manually, and this process of AI learning to identify phases and being corrected manually repeated until the accuracy on the segmentation models was at an acceptable level. In this case, five separate models were trained- two classical machine learning models and three artificial intelligence “Deep learning” models. After training, all five models had over 99% accuracy according to Dragonfly’s internal metrics. It was found, however, that the deep learning models were more accurate with the segmentations than the classical machine learning models when applied to new images that were not in the original training set. An example of an image after segmentation in Dragonfly can be seen in Figure 5.7 below.

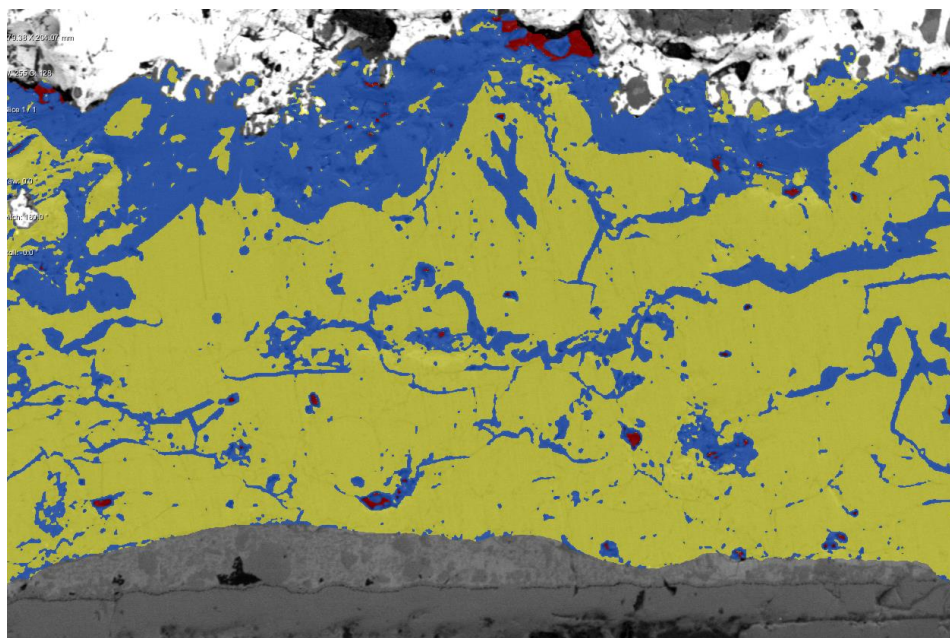


Figure 5.7: Si bond coat in CMC/ EBC coupon exposed in 4.4 atm O_2 at 900°C for 500h. Segmented in Dragonfly. Yellow is the Si bond coat, blue is the TGO, and red is the pores.

Once the images were segmented, manual correction and touch-ups of the segmentation was carried out to remove extra voxels that have been labeled as the wrong phase as shown below in Figure 5.8. Dragonfly then provided output of the number of voxels attributed to each region of interest, in this case the TGO, pores, and bond coat. These voxel counts were then used to calculate the area fraction of each phase in the image. This process was repeated with three images for each sample, and the voxel counts were averaged together to get the area fraction of TGO in the bond coat for the entire sample.

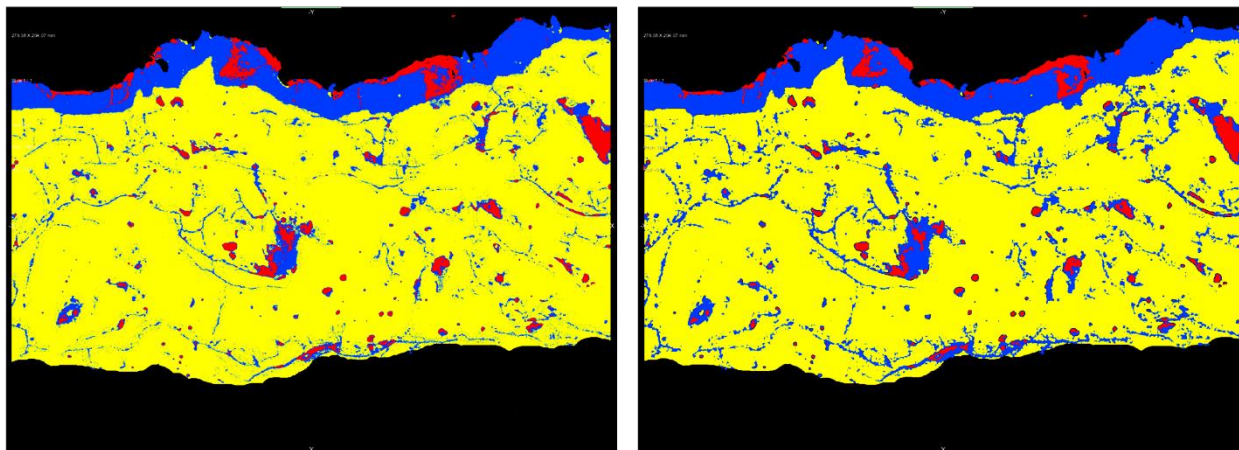


Figure 5.8: Segmentation of Si bond coat (yellow) TGO (blue) and pores (red) before and after manual touch-ups, micrograph layer hidden.

In addition to area fractions, depth concentrations of the TGO were calculated based on the amount of TGO present at a given depth from the topcoat/ bond coat interface. This was done using the segmented images by utilizing a MATLAB code [Dominic Pinnisi, UVA] developed for use with the Dragonfly output images. The code breaks the segmentations into vertical slices and then quantifies the amount of TGO and its relative depth in the bond coat. These results are displayed in the form of a histogram showing the depth penetration and distribution of TGO into the Si bond coat.

5.3 Results

5.3.1 RBSiC and CMC Oxidation: TGA Data

Both benchtop weight change and TGA results indicated that the RBSiC coupons oxidation results were consistent with parabolic oxidation kinetics rather than linear kinetics at all temperatures tested. This in turn means that the oxidation of these samples is diffusion limited. Results are shown below for the 0%B and the 4%B at 900°C and 1050°C, and the CMC as well at 1200°C. They are shown graphed in mg/cm^2 vs $\text{time}^{1/2}$. It can be seen from the TGA data that

there are two oxidation regimes, the first transient regime (shown in magenta) which occurs in the first 15-30 minutes of testing, followed by a more steady-state regime through the end of the test. The initial transient region data was removed from the calculations and forced linear fits (dashed lines) were then applied to the steady-state portion of the data to determine the oxidation rate constants as shown in Figure 5.9, Figure 5.10, and Figure 5.11. The parabolic rate constant is determined from the square of the slope taken from the specific weight vs. root(time) plot. The 0%B RBSiC tested at 1050°C shows a high amount of curvature in the TGA run, indicating deviation from ideal parabolic kinetics.

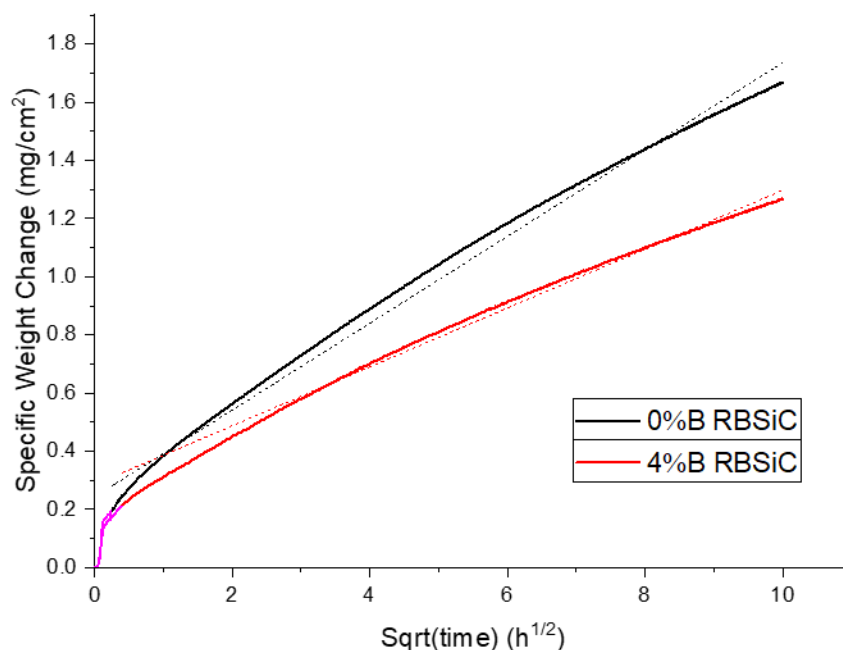


Figure 5.9: 100h TGA data of coated 0%B and 4%B RBSiC coupons at 900°C in O₂ shown with forced linear fits for parabolic rate constants.

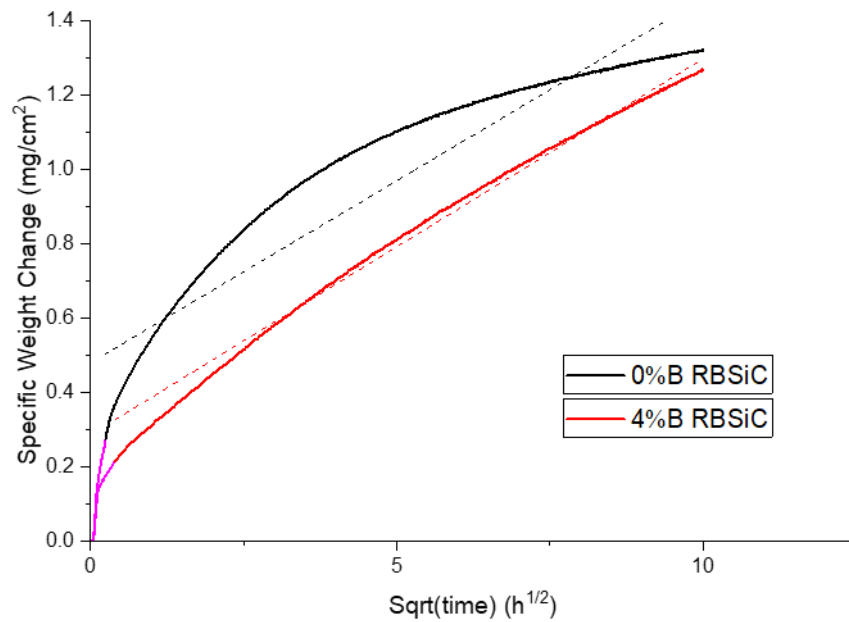


Figure 5.10: 100h TGA data of coated 0%B and 4%B RBSiC coupons at 1050°C in O₂ shown with forced linear fits for parabolic rate constants.

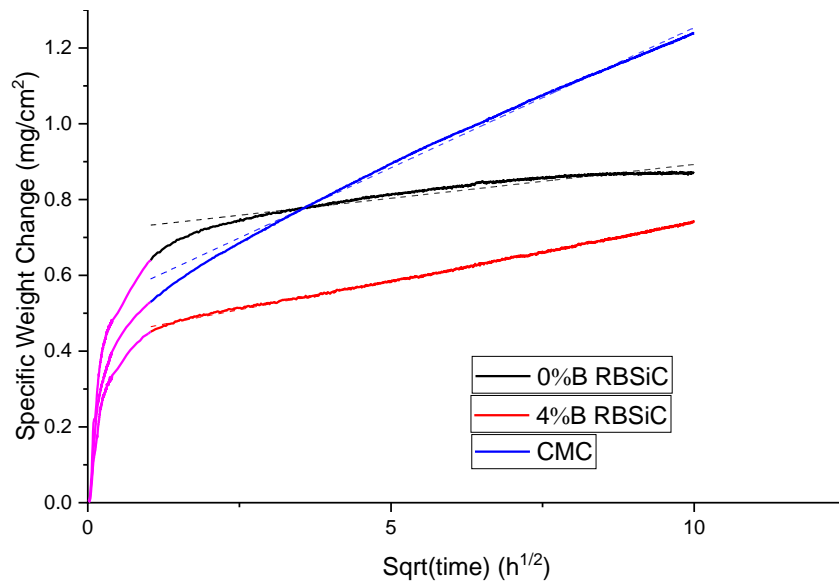


Figure 5.11: 100h TGA data of coated 0%B and 4%B RBSiC coupons and CMC coupons at 1200°C in O₂ with forced linear fits for parabolic rate constants.

These TGA results were compared to TGA results of the uncoated RBSiC and CMC samples that were tested under the same conditions. It was found that in every case, the coated samples showed both much higher net weight gain as well as much higher rate constants than the uncoated samples. As the coated samples include an APS layer of Si, this is expected for comparison to the SiC of the uncoated samples. All data for uncoated specimens are from the McFarland dissertation (20).

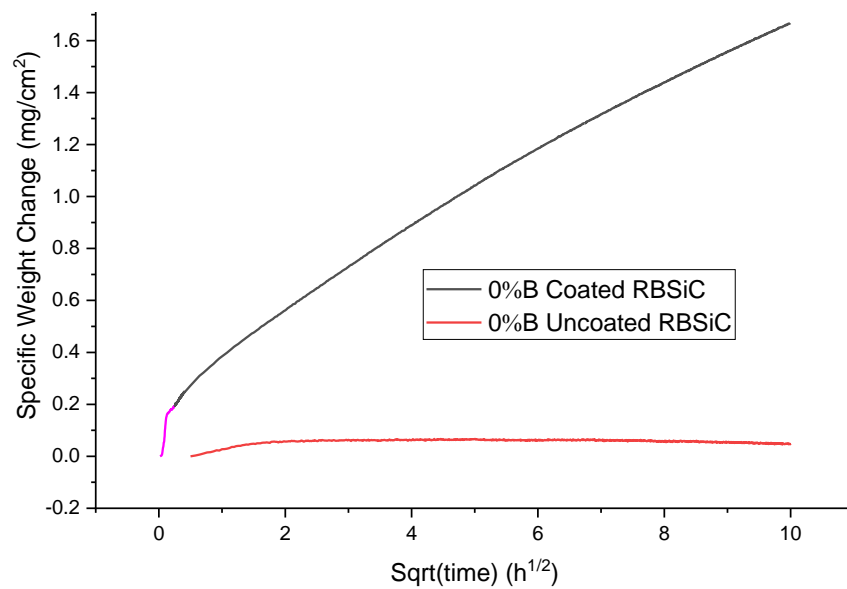


Figure 5.12: TGA data comparing 0%B coated RBSiC samples to uncoated samples exposed at 900°C for 100h in O₂.

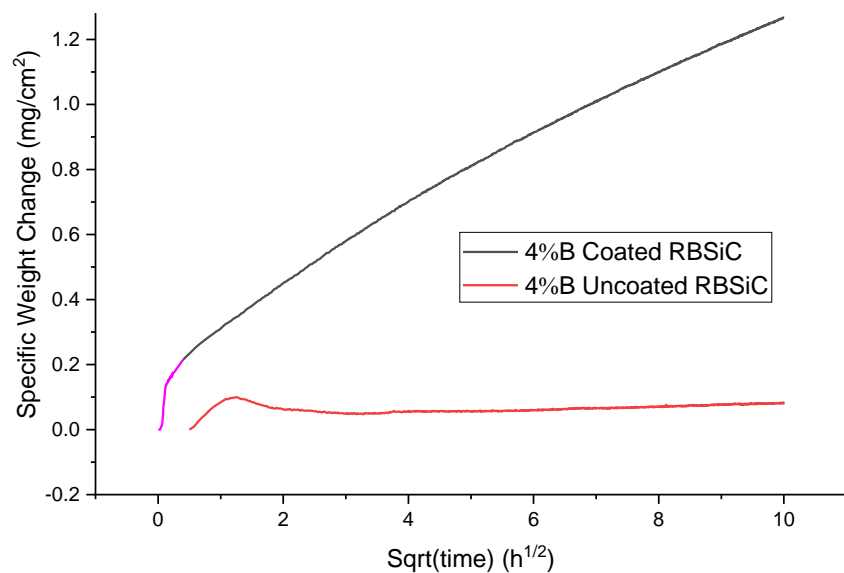


Figure 5.13: TGA data comparing 4%B coated RBSiC samples to uncoated samples exposed at 900°C for 100h in O₂.

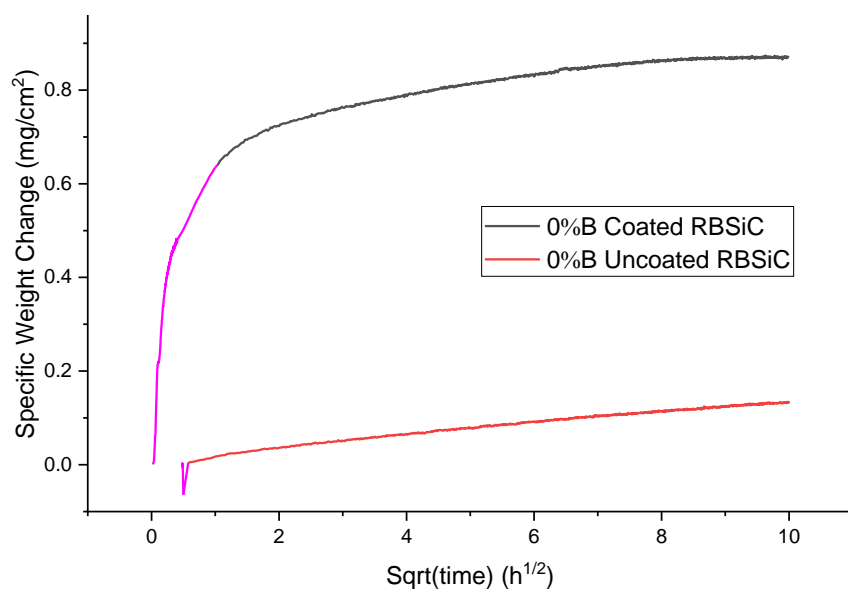


Figure 5.14: TGA data comparing 0%B coated RBSiC samples to uncoated samples exposed at 1200°C for 100h in O₂.

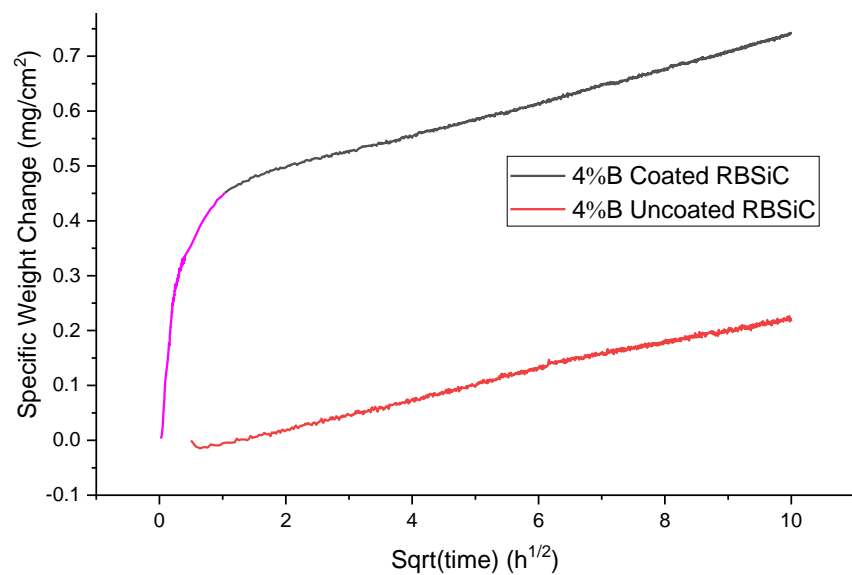


Figure 5.15: TGA data comparing 4%B coated RBSiC samples to uncoated samples exposed at 1200°C for 100h in O₂.

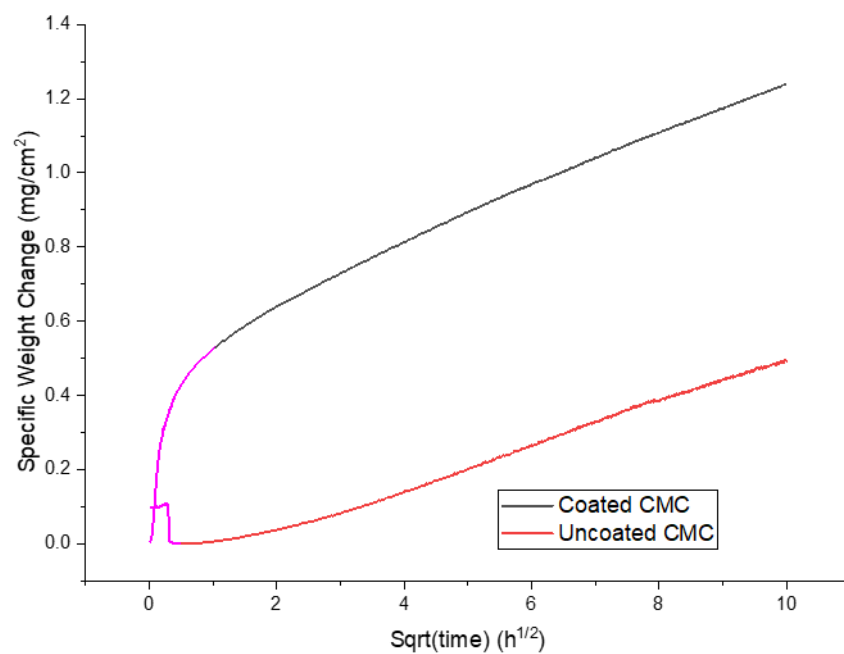


Figure 5.16: TGA data comparing CMC coated RBSiC samples to uncoated samples exposed at 1200°C for 100h in O₂.

Rate constants for parabolic oxidation kinetics were calculated for all the samples that were tested in the TGA. The results are shown below in Table 5-2 for both the coated and uncoated samples.

Table 5-2: Parabolic Oxidation rates ($\text{mg}^2/\text{cm}^4\cdot\text{h}$) calculated from TGA exposures.

	<i>0%B coated</i>	<i>4%B coated</i>	<i>CMC coated</i>	<i>0%B uncoated</i>	<i>4%B uncoated</i>	<i>CMC uncoated</i>
<i>900°</i>	2.23E-2	1.02E-2		5.00E-7	9.80E-6	
<i>1050°</i>	9.60E-3	1.02E-2		-	-	-
<i>1200°</i>	3.20E-4	9.33E-4	5.48E-3	1.49E-4	6.48E-2	3.42E-3

5.3.2 Complexities in Experimental Setup

Though the intent of this study is to determine the effects of boria on TGO growth kinetics of the Si bond coat, it is important to note that there are significant differences from ideal oxidation conditions in this study. First, the RBSiC and CMC coupons used here are only partially coated on 2 faces so that weight changes of the samples cannot be correlated directly to the amount of growth of the TGOs (measured as oxide thickness) observed under the coatings. Additionally, the coatings were applied by an APS process, resulting in non-equilibrium phases. Third, the Si bond coat and YbDS topcoat splat geometry and interfaces between splats in the APS coating have significant impact on oxidation kinetics. Fourth, the Keiser Rig does not provide for a pristine environment because it uses SiC and alumina tubes and furnace ware. Additionally, many samples are tested simultaneously with potential for cross-contamination. Finally, due to a limited number of samples, not all the coupon compositions were tested at every condition, limiting the comparisons made between TGA and Keiser Rig data as well as limiting the quantification of oxidation kinetics for these samples.

5.3.3 RBSiC and CMC Oxidation: Benchtop Weight Changes

For every sample composition that had data for three tested times in the Keiser rig, the benchtop weight changes were graphed vs time^{1/2} to quantify the parabolic oxidation rate constant. In many cases, there were duplicates of the sample in the 500h test, so forced linear fits were applied to the data for each of the duplicated samples. Only two times were tested in the Keiser Rig at 900°C, so the data in this section are only for the 1050°C and the 1200°C Keiser Rig exposures. Graphs of these data can be found in Figure 5.17 and Figure 5.18

In cases like the 1%B at 1050°C, there was a large difference in the linear fit depending on which 500h point was used, while for the 0%B there was almost no difference. There were no duplicates for the 1050°C test at 500h for the 2%B or the CMC. Similarly to the 0%B coupon tested at 1050°C in the TGA, the 0%B at 1 atm here shows a 100h weight change significantly higher than the forced linear fit. The TGA values in this case are slightly higher than those from the Keiser Rig-exposed samples but do seem to follow a similar trend. Many of the samples do not exhibit a good fit to the linear trendlines, indicating again that there are likely some mixed oxidation mechanisms occurring at this temperature.

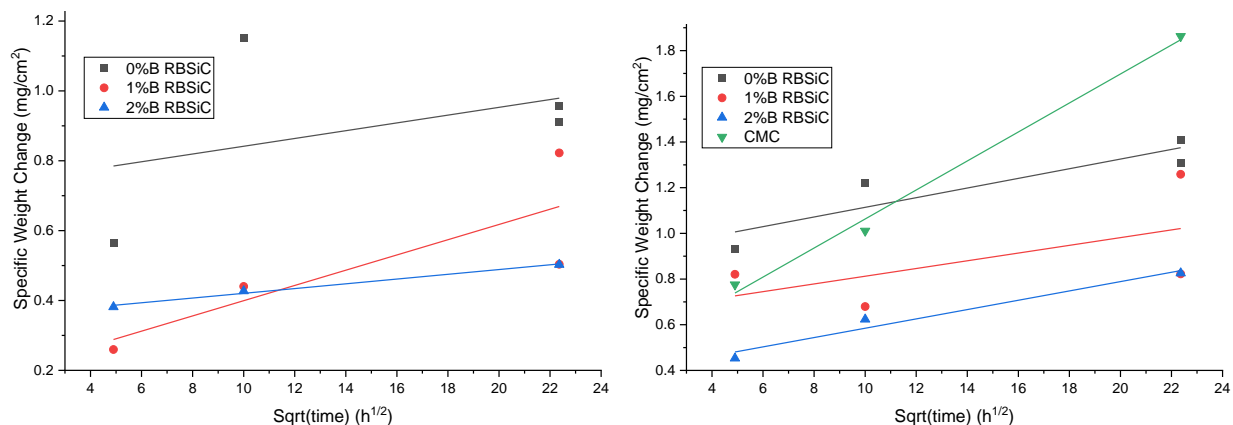


Figure 5.17: 1050°C dry O₂ benchtop weight changes for samples exposed in the Keiser Rig with forced linear fits to parabolic kinetics. (Left) 1 atm exposure. (Right) 4.4 atm exposure

Looking at the 1200°C results from the Keiser rig in Figure 5.18, the linear trendlines show a much better fit to the data indicating that the oxidation kinetics at this temperature are more closely parabolic than at 1050°C. Additionally, there is less spread overall between the linear fits with the duplicate 500h samples. For samples that had TGA runs for comparison, the data are included as grey points. In all cases the TGA data were higher in specific weight change than for the samples exposed in the Keiser Rig.

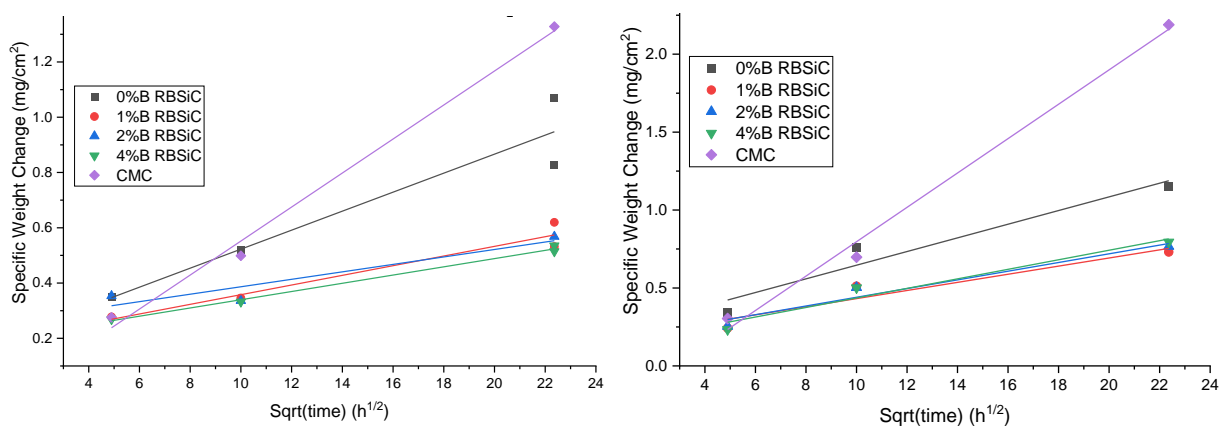


Figure 5.18: 1200°C dry O₂ benchtop weight changes for samples exposed in the Keiser Rig with forced linear fits. (Left) 1 atm exposure. (Right) 4.4 atm exposure

Parabolic oxidation rate constants were derived from the forced linear fits for each of the compositions for both 1050°C and 1200°C as shown in Table 5-3. It should be noted that many

of the 1050°C samples did not show a good linear fit. Ideally these data would be used to determine the temperature dependence of the rate constants for each composition, however without a third temperature data set in combination with the poor fits at 1050°C, these calculations cannot be done with any statistical significance. However, the pressure dependence was calculated as a ratio of the rate constants of samples exposed at 4.4 atm relative to those exposed at 1 atm. Though there is an increase in the rate constant with pressure as expected, the 1050°C data do not display any discernable trends with B content. The 1200°C data show the expected increase based on pressure for the 2%B and 4%B samples, but the other compositions show a lower ratio than the expected 4.4. For comparison, Table 5-4 from McFarland has also been included to compare the pressure effects on the oxidation of the uncoated coupons.

Table 5-3: Calculated parabolic rate constants ($\text{mg}^2/\text{cm}^4\cdot\text{h}$) and pressure dependence.

	1050°C			1200°C		
	1 atm	4.4 atm	Kp4:Kp1	1 atm	4.4 atm	Kp4:Kp1
0%B	1.24E-4	4.46E-4	3.59738	1.18E-3	1.92E-3	1.62361
1%B	4.75E-4	2.85E-4	0.59956	3.05E-4	6.78E-4	2.22175
2%B	4.61E-5	4.16E-4	9.02653	1.82E-4	7.78E-4	4.27111
4%B	-	-		2.22E-4	9.37E-4	4.2204
CMC	-	4.03E-3		3.79E-3	1.22E-2	3.21349

Table 5-4: Calculated parabolic rate constants and pressure effects on uncoated RBSiC coupons. (20)

	TGA	KR 1 atm	KR 4.4 atm	4.4:1
0%B	1.26E-04	1.38E-04	4.73E-04	3.43
4%B	2.28E-04	2.34E-04	8.98E-04	3.85

5.3.4 Dragonfly Segmentation and TGO Morphology

Only the CMC samples were cross sectioned for analysis of the TGO morphology. Samples exposed at 900°C, 500h, 4.4 atm O₂ showed the most tortuous TGO growth of any samples listed. These samples had TGO present throughout the entire thickness of the bond coat as shown in the oxygen map in Figure 5.19. Also seen in the micrograph is a large, glassy inclusion centered in the bond coat that shows a higher concentration of Yb than the surrounding bond coat phase or TGO. It is possible that this phase contains YbBO₃, though the boron signal is very weak throughout the EDS map save areas where the B-rich phase is exposed.

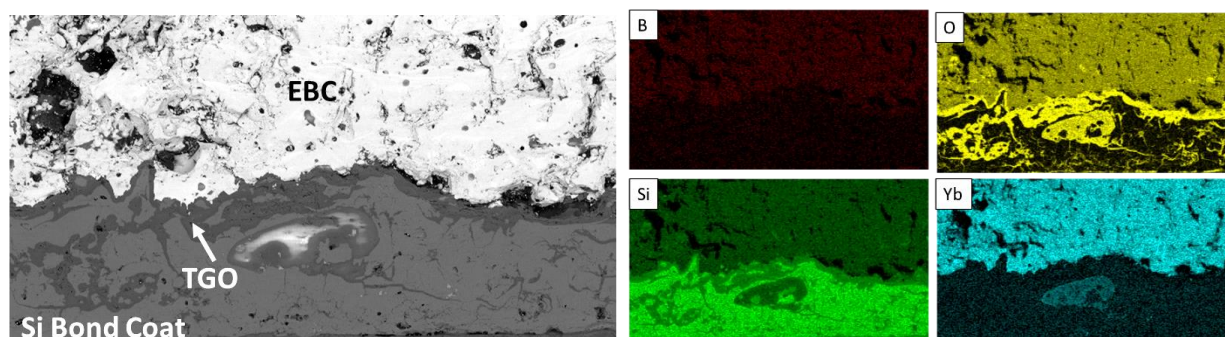


Figure 5.19: Backscatter electron and elemental maps of a tortuous TGO and glassy inclusion in coated CMC sample exposed at 900°C for 500 h at 4.4 atm O₂.

For comparison, the 1200°C, 500h, 4.4 atm CMC sample shows a more regular growth of the TGO along the bond coat/ EBC interface as shown in Figure 5.20 below. There is still some penetration of TGO growth into the bond coat, though it appears significantly less severe than in the 900°C CMC sample.

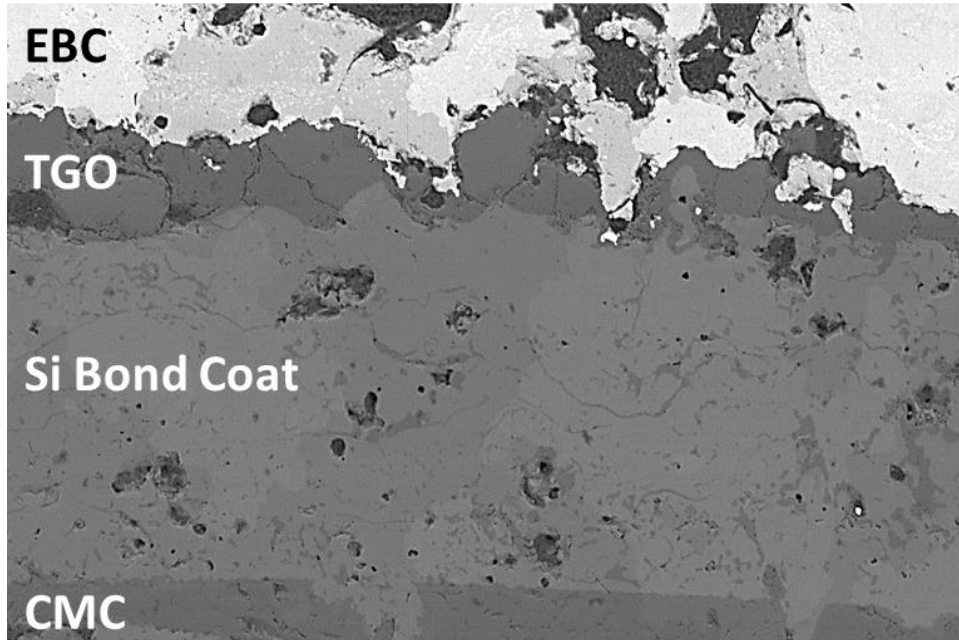


Figure 5.20: Backscatter electron micrograph of the TGO in a coated CMC exposed at 1200°C in 4.4 atm O₂ for 500h in the Keiser rig.

As the CMC samples exposed at 4.4 atm for 500h showed the most extreme growth of TGO as well as the widest range of TGO morphologies between the extremely tortuous and amorphous TGOs seen in the 900°C sample, and the thick, regular TGOs seen in the 1200°C samples, this combination of time and pressure was chosen to be further analyzed using Dragonfly.

Three micrographs from each of the three CMC samples were segmented using Dragonfly. The area fractions, listed below in Table 5-5, were determined from the dragonfly segmentations.

900°C showed the highest TGO area fraction at 30%, consistent with being the least protective.

1050°C showed the least amount of TGO at 12% TGO, and 1200°C showed an intermediate amount of 19% TGO. The sample segmentations are shown below for each of the CMC coupons.

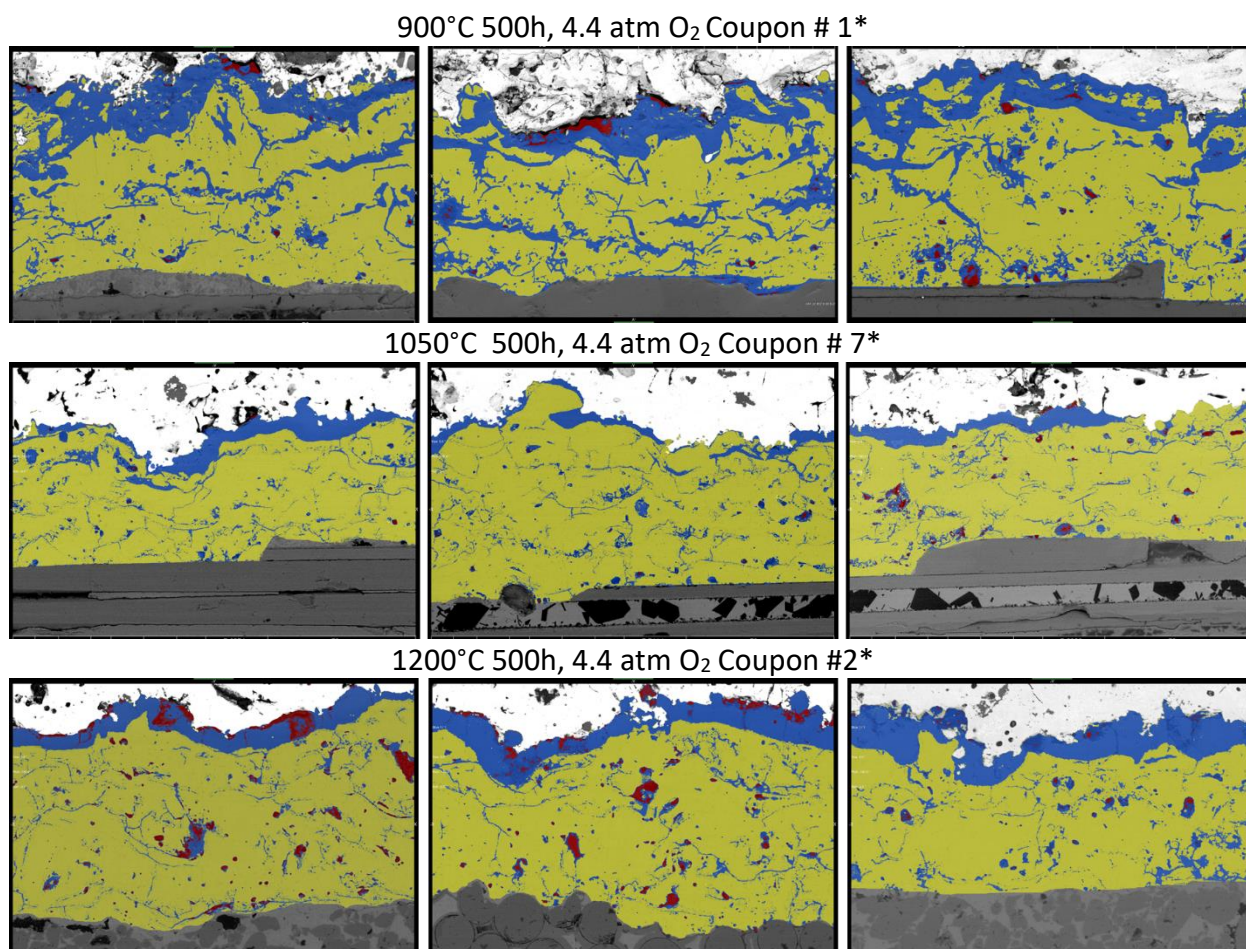


Figure 5.21: Backscatter electron micrograph of Si/EBC coated CMC coupons with segmented overlay of the bond coat (yellow), TGO (blue), and pores (red).

Table 5-5: TGO Area Fractions from Dragonfly Segmentations of the micrographs in Figure 5.23

Temperature	Area Fraction TGO (%)			
	Image 1	Image 2	Image 3	Average
900°C	28	32	30	30
1050°C	16	9	11	12
1200°C	12	18	26	19

After phase segmentation, the colored ROIs (regions of interest), in this case the bond coat, TGO and pores were exported as .tif image files for depth penetration and distribution measurements using the MATLAB code. One of the extracted segmentations is shown with its histogram in Figure 5.22, and Figure 5.23 shows all the histograms for the segmentations in Figure 5.21, arranged in the same order as above but rotated by 90°. Note that the vertical scales for each of the histograms is set to the maximum number of counts, so the vertical scale varies for each graph. The left of the graph is set to the bond coat/ EBC interface and the right is set at the bond coat/ CMC interface.

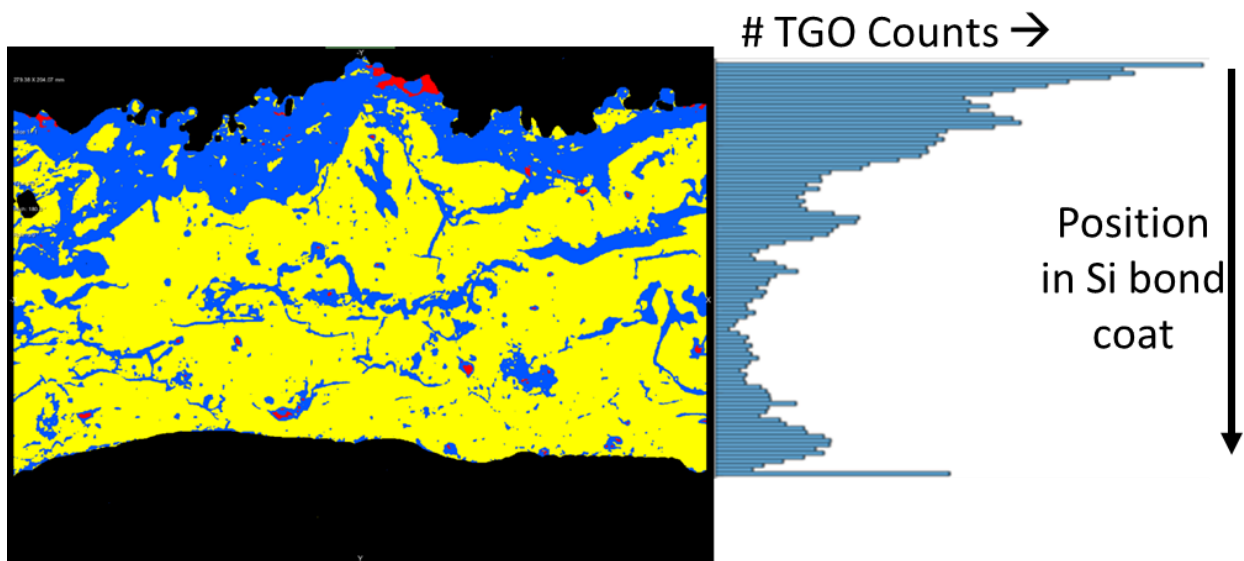


Figure 5.22: 900°C 500h 4.4 atm O₂ segmentation of the bond coat (yellow), TGO (blue), and pores (red) with resultant histogram of TGO distribution through the depth of the bond coat

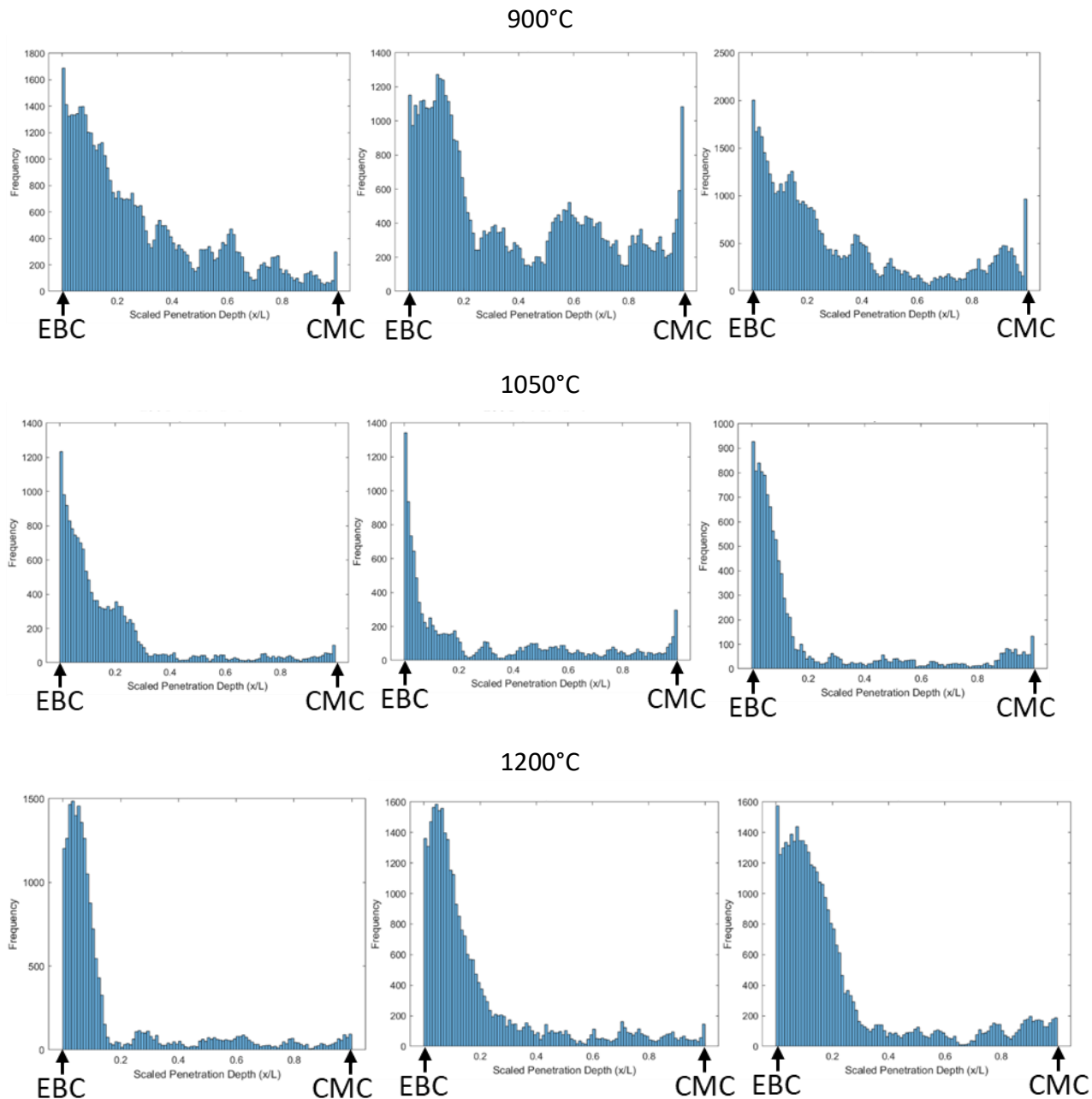


Figure 5.23: Histograms of TGO distribution in the Si bond coat for EBC coated CMCs tested in the Keiser Rig at 4.4 atm O₂ for 500h. They have been rotated 90° for ease of reading with the bond coat/ EBC interface on the left and bond coat/ CMC interface on the right. They are presented in the same order as their corresponding segmentations in Figure 5.21.

From the histograms, it can be clearly seen that the 900°C TGO has the most penetration throughout the depth of the bond coat. At 1050°C, the TGO becomes more defined along the Si/EBC interface, and at 1200°C it is very clearly defined along the Si/EBC interface and thicker than at 1050°C. There is still TGO throughout the entire depth of the bond coat in all cases, though there is significantly less inter-splat TGO with increasing temperatures. The data from the histograms were summed and normalized to the bond coat depth to get a TGO concentration curve. The metric of 80% of the total with respect to depth in the bond coat was chosen to compare the penetration depth concentrations. The concentration gradients for these CMC samples can be seen below in Figure 5.24. The marked points denoting 80% of the total TGO are labeled.

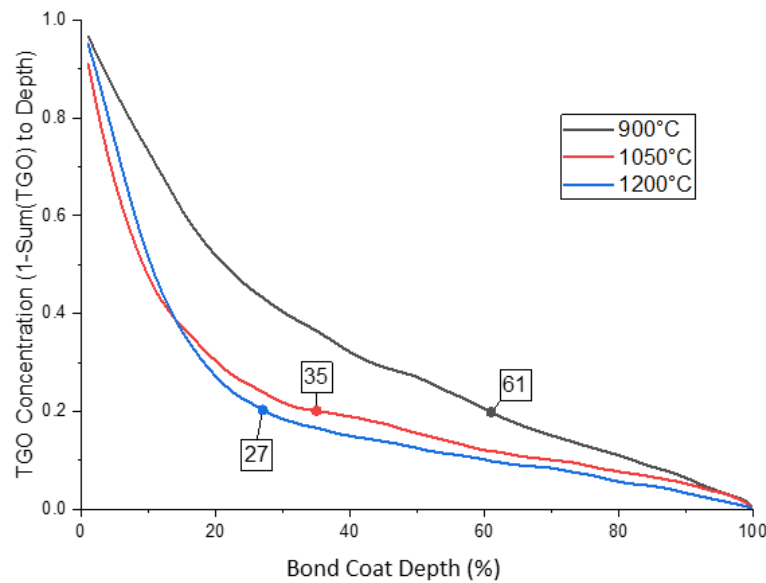


Figure 5.24: Comparison of TGO depth penetration concentrations for the CMC samples exposed in the Keiser Rig for 500h in 4.4 atm dry O₂. Numbers refer to % depth of Si bond coat at which 80% of the TGO is formed.

5.3.5 TGA & Keiser Rig Exposure Comparison

Cross sectional characterization and Dragonfly segmentation was also performed on the 14 samples, discussed above for weight changes and oxidation kinetics, from comparable exposures in the Keiser Rig and TGA. All these exposures were 100 hours in length at 1 atm of Dry O₂. These samples were coated 0%B and 4%B RBSiC coupons exposed at 900°C, 1050°C and 1200°C with additional coated CMC samples also exposed at 1200°C.

There were many discrepancies in the microstructure of the bond coats themselves. As shown below in Figure 5.25, the bond coats exhibited large pores (left), many EBC inclusions (bottom right), and crumbly microstructures (top right). This variation in the bond coat structure complicated both sample preparation and segmentation and analysis of the TGO in Dragonfly.

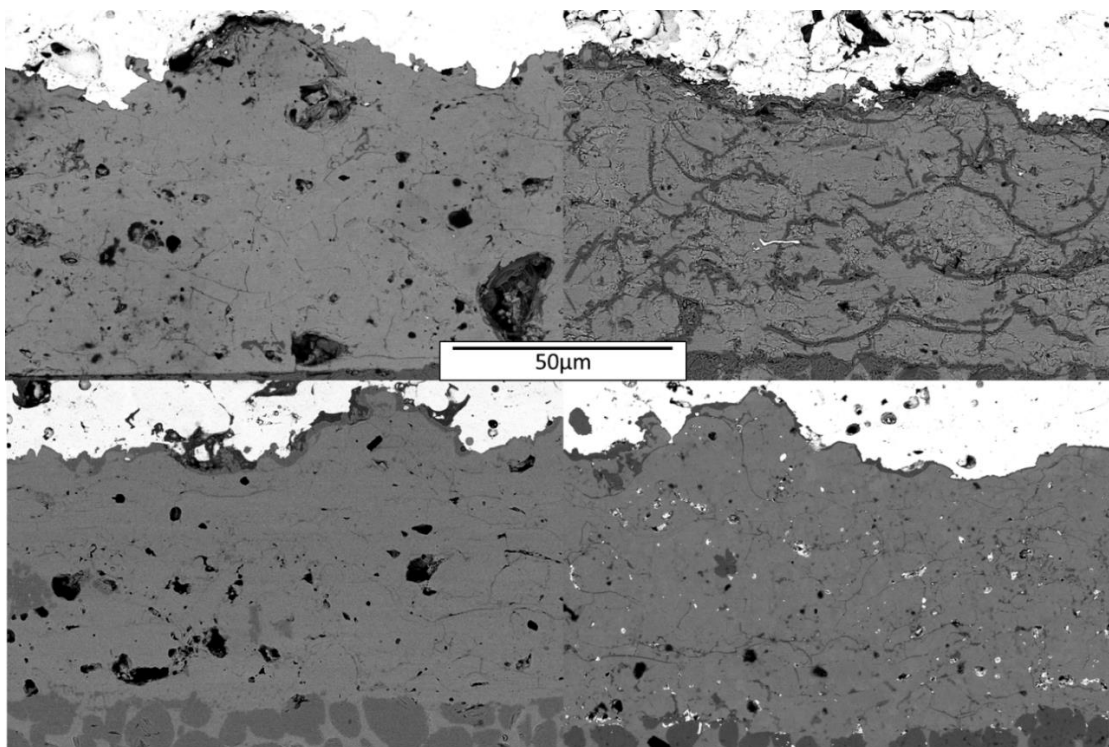


Figure 5.25: Defect variations observed in the silicon bond coats of CMC and RBSiC samples that were characterized for segmentation in Dragonfly. (Left) Large and numerous pores in the bond coat of the CMC (top) and RBSiC sample (bottom). (Top Right) crumbly microstructure of the bond coat and small EBC inclusions. (Bottom Right) Numerous EBC inclusions.

The micrographs and segmentations for these samples and exposures can be found in Appendix cC, however the TGO depth concentration graphs have been included below. All the samples in this case showed a much more linear concentration gradient than the CMCs that had been exposed for 500h at 4.4 atm with 80% of the TGO being located in roughly the top 80% of the bond coat depth as shown below in Figure 5.26, Figure 5.27, and Figure 5.28. Area fractions for the TGO in these samples are listed in Table 5-6 below.

Table 5-6: Area fraction comparisons for RBSiC and CMC samples exposed in the Keiser Rig & TGA for 100h in dry O₂

Temperature	0%B KR	0%B TGA	4%B KR	4%B TGA	CMC KR	CMC TGA
900°C	29	22	24	27		
1050°C	15	34	13	14		
1200°C	10	17	12	23	14	12

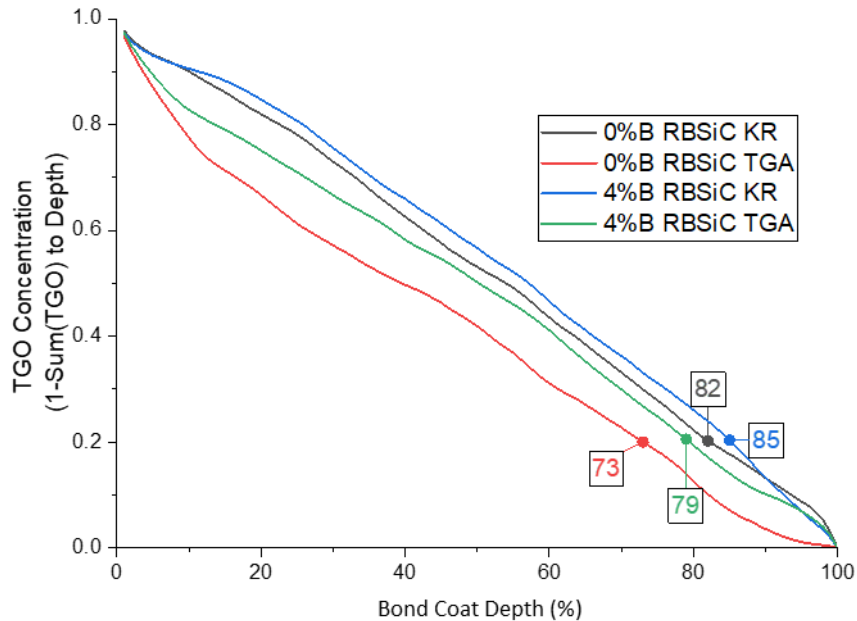


Figure 5.26: TGO depth concentration curves for EBC/Si coated 0%B and 4%B RBSiC coupons exposed in the Keiser Rig and TGA at 900°C for 100h in 1 atm O₂. Numbers refer to % depth of Si bond coat at which 80% of the TGO is formed.

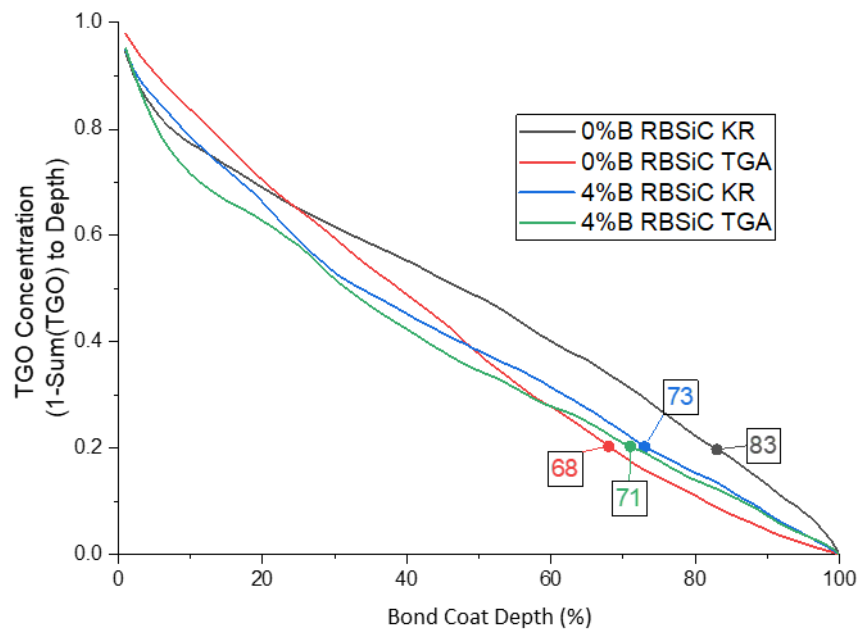


Figure 5.27: TGO depth concentration curves for EBC/Si coated 0%B and 4%B RBSiC coupons exposed in the Keiser Rig and TGA at 1050°C for 100h in 1 atm O₂. Numbers refer to % depth of Si bond coat at which 80% of the TGO is formed.

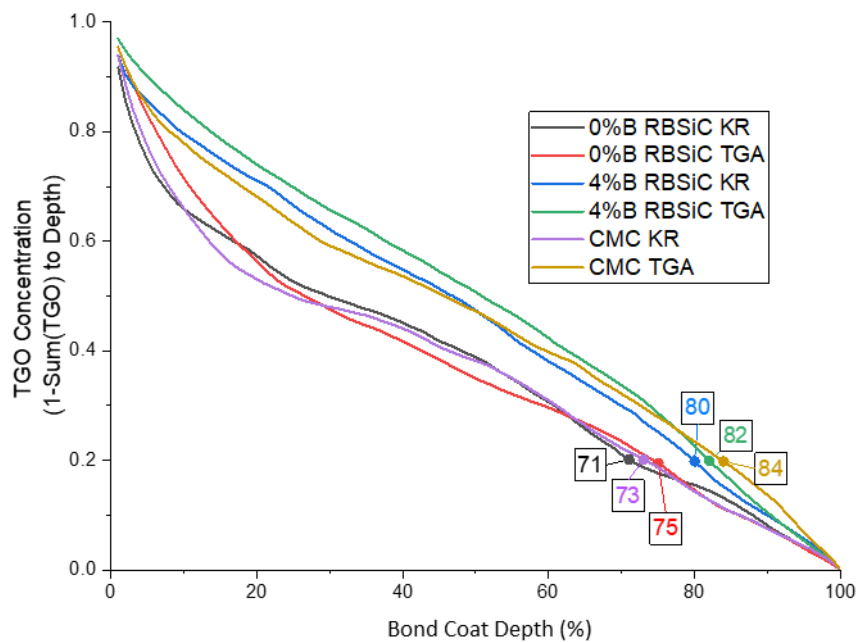


Figure 5.28: TGO depth concentration curves for EBC/Si coated 0%B and 4%B RBSiC coupons exposed in the Keiser Rig and TGA at 1200°C for 100h in 1 atm O₂. Numbers refer to % depth of Si bond coat at which 80% of the TGO is formed.

5.3.6 B Effects on $\text{Yb}_2\text{Si}_2\text{O}_7$ EBC

A 4%B RBSiC coupon exposed at 1200°C for 500h and 4.4 atm in the Keiser Rig was cross-sectioned and examined using both SEM and TEM/ SAED to look for the formation of the YbBO_3 phase in the EBC. Though the SEM micrographs (Figure 5.29) show a similar microstructure to that of the reaction layers observed in the well tests, SAED of the region (Figure 5.30) showed only $\text{Yb}_2\text{Si}_2\text{O}_7$ as shown below. No correlation was found between these features and proximity to B-rich phases in the matrix.

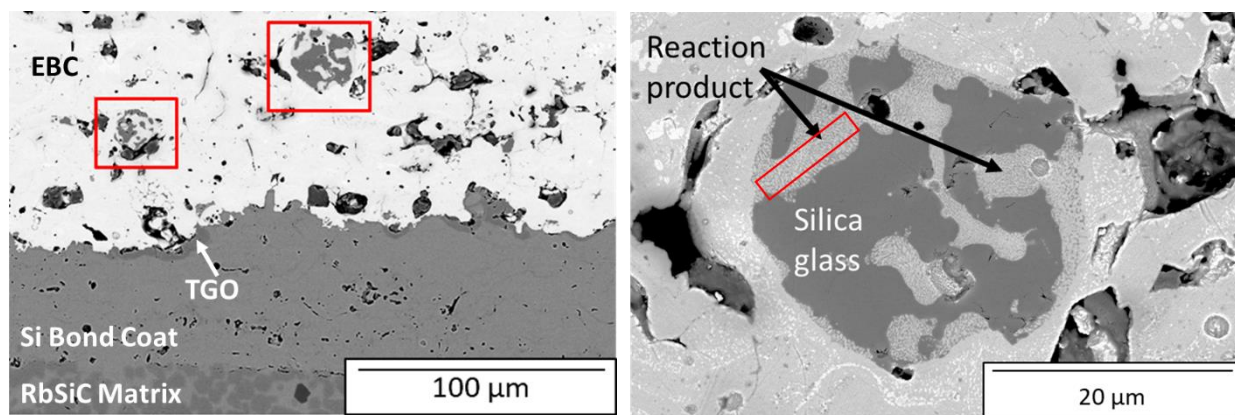


Figure 5.29: 4%B RBSiC cross section of the EBC showing features similar to the reaction layers seen in the well tests.

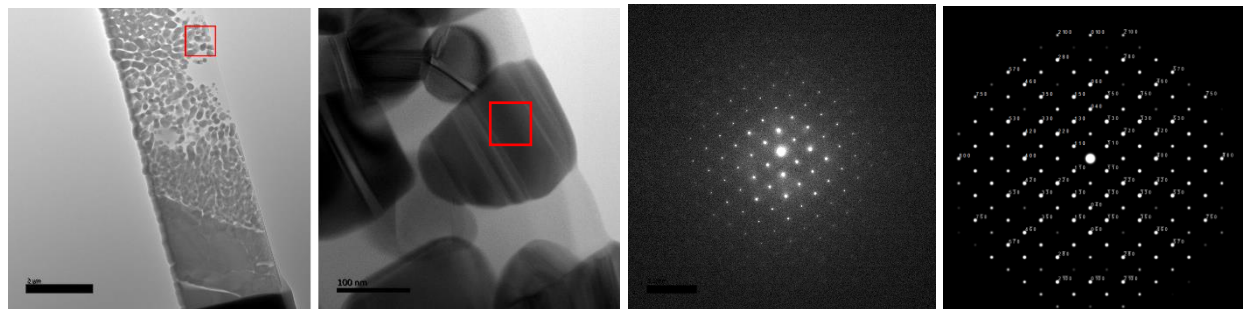


Figure 5.30: FIB section of porous reaction phase taken from the red rectangle in Figure 19 right, SAED pattern, and reference diffraction pattern showing that the grains are $\text{Yb}_2\text{Si}_2\text{O}_7$.

Every sample characterized, including the 0%B RBSiC coupons, showed multiple instances of the silica pool/ “reaction layer” microstructural features in the EBC as shown below in Figure 5.31. The presence of this feature in every composition and both type of tests indicates that this microstructure is not a result of boria in the system or the testing apparatus used.

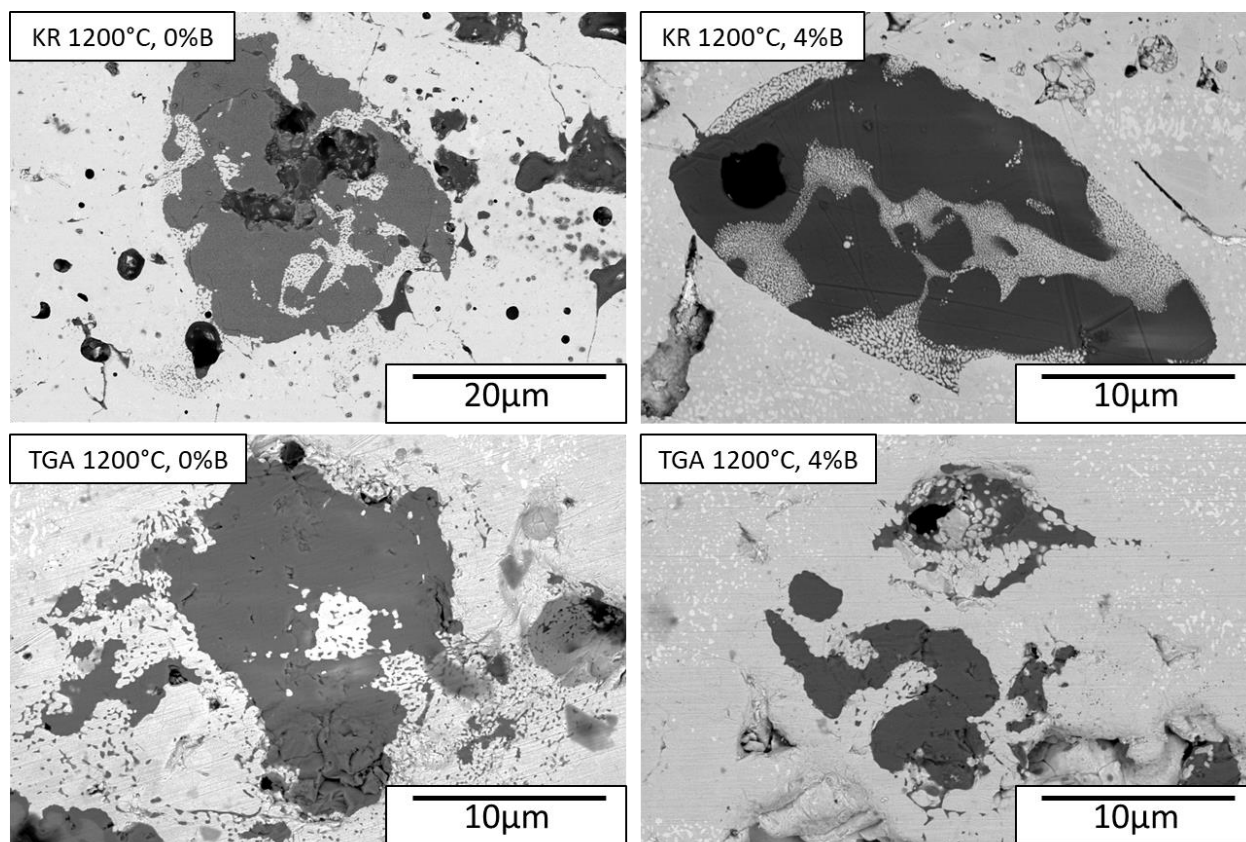


Figure 5.31: Silica pools and porous EBC grain structure features reminiscent of YbBO_3 from well tests was found in samples of all characterized boron contents and both exposure apparatuses. These RBSiC samples are from 1200°C, 100h, 1 atm dry O_2 exposures. (Top) Samples exposed in Keiser Rig. (Bottom) Sample exposed in TGA. (Left) 0%B RBSiC Samples. (Right) 4%B RBSiC Samples.

5.4 Discussion

5.4.1 Oxidation Kinetics and Experimental Discrepancies

There are several complexities in this study that prevent it from being a rigorous, quantitative oxidation kinetics study including the lack of coating on all sides of the samples, the lack of samples for all test conditions, and the limits of the Keiser Rig. Since all the samples are in the same test chamber, cross-contamination between samples is a potential issue for any volatile species such as boria. The weight changes cannot be correlated to the TGO growth due to the edge effects of the samples not being coated on all sides, and the surface area measurements taken from the sample dimensions do not account for the additional surface area of the APS splat interfaces. The increased surface area of the APS Si splats explains the significantly higher weight gain in the coated samples than the uncoated ones.

Parabolic rate constants were calculated from the TGA runs and the sample compositions that have three time-points from the Keiser Rig tests, but the samples at 1050°C, notably the 0%B RBSiC showed a large deviation from the parabolic rate constant fits. This is likely due to the variations observed in the bond coats and EBCs for these coupons. It can be seen in the micrograph of the sample below (Figure 5.32) that the EBC is crumbly and porous in this sample, which also shows thick, tortuous TGO formation as well as a porous and crumbly bond coat microstructure. This particular sample also had a significantly larger area fraction of TGO by over a factor of two compared to other samples exposed at 1050°C.

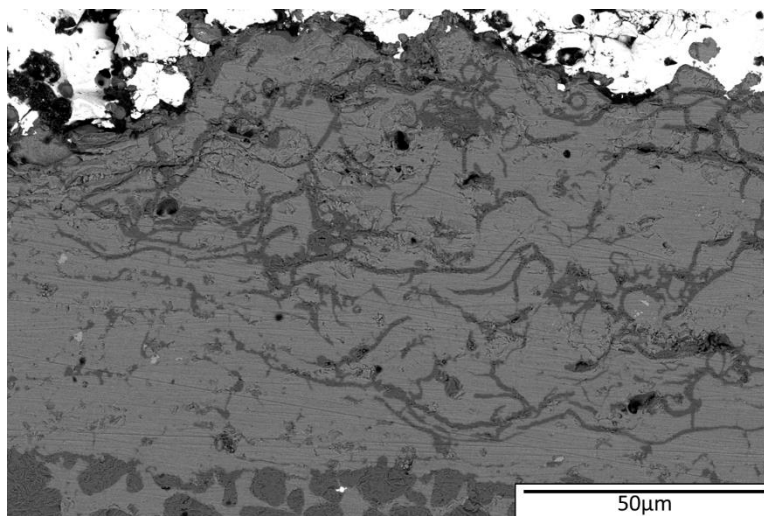


Figure 5.32: Micrograph of 0%B RBSiC coupon exposed in the TGA at 1050°C for 100h in dry O₂

It was not possible to calculate temperature dependencies on the rate constants with any significance due to the lack of a third temperature point for most of the compositions tested in the Keiser Rig. Pressure effects were calculated for samples that were tested at both 1 atm and 4.4 atm. The 1050°C samples the behavior does not match the expected proportional increase with increased pressure, but the 1200°C samples show a better correlation to the expected 4-fold increase of the rate constant with increased pressure.

Cross sections of the samples did not show any formation of the Yb-borate phase in the EBC either in the CMC samples used for Dragonfly or for the 4%B RBSiC coupon which was specifically investigated for the presence of YbBO₃ formation in the EBC. The features of interest were observed in the EBCs of many of the tested samples as shown in Figure 5.31, regardless of initial boron content, exposure temperature, or test apparatus used. This indicated that this feature is not a result of the presence of boron in the samples. It is likely that the lack of borate phase formation is due to rapid oxidation of any exposed boron-rich phases during the testing, and rapid loss of B₂O₃ to the environment once it has formed. As

shown in the plot calculated from the Factsage thermodynamic database below, the volatility of B_2O_3 increases with increasing temperature in 1atm O_2 , so it is likely that any boria volatilized before it was able to react with the EBC at this temperature and pressure.

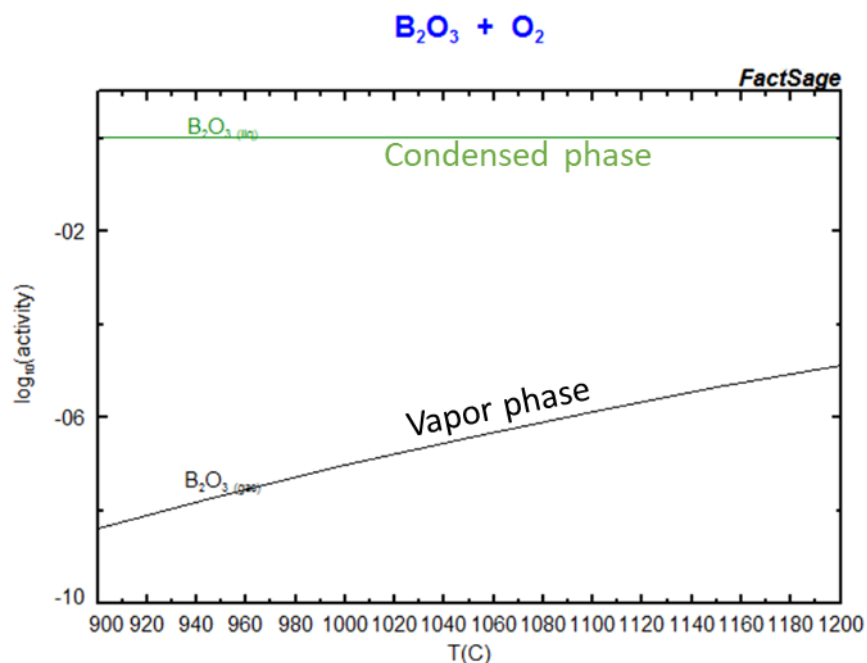


Figure 5.33: FactSage Simulation of $\log(\text{activity})$ vs. temperature for B_2O_3 in O_2

5.4.2 Dragonfly Application to TGO analysis

The masking protocols in Dragonfly made the segmentation of the bond coat region of the micrographs much easier to use than in ImageJ. The AI “segmentation wizard” protocols required 50-60 hours of training with 5 models on 20 images. Manual correction was still required to achieve accurate segmentations. The automatic segmentation was less reliable if there were significant differences between the training micrographs and the new micrographs being segmented. One of the common issues was that any inclusion of the brighter EBC phase in the masked area resulted in the bond coat and TGO phases both being identified as the TGO and the EBC being identified as the bond coat phase. This issue could be rectified by including

the EBC as a fourth region of interest in the segmentation routine but would require re-training the program. Another issue was that the bottom of the mask for the bond coat would often include regions of the CMC matrix due to similar contrast between the bond coat and TGO phases. These regions had to be removed manually from the mask. Finally, when segmenting, small polishing scratches in the image of the sample surface would be identified as TGO, and when thresholding to correct the segmented areas, random pixels would register as TGO rather than bond coat, necessitating the manual cleaning of the images as illustrated above in Figure 5.8. Careful polishing and consistent high-contrast SEM micrographs of the bond coat were necessary for the segmentation protocols to work.

The Dragonfly program also lacked routines for calculating the area fractions, though it could output the voxel numbers of each segmented regions of interest. A custom MATLAB code was written to plot the depth penetration and distributions of the TGO in the bond coat. A method to obtain this information in Dragonfly was not identified. The segmentations from the dragonfly program were used for those calculations, exported separately from the program as a .tif file.

Overall, the Dragonfly program was used to segment and measure the amount of TGO in the bond coat based on the micrographs including the thin, inter-splat TGOs. However, the time required for both the users and the AI in the program was long, suggesting this approach is best utilized for ongoing studies rather than one-time projects.

The quantitative TGO area fraction data from these segmentations could not be correlated to the weight gain due to the edge oxidation effects of the uncoated faces of the tested coupons.

However, as the micrographs were taken from a region meant to avoid any edge effects, qualitative conclusions can be drawn about the TGO growth in the APS coatings for those regions. The micrographs and histograms of TGO distribution show that the TGO growth is much more penetrating and larger in area at 900°C than at 1050°C or 1200°C. As the temperature increases, the TGO growth becomes more defined along the EBC interface with less penetration through the depth of the bond coat due to increased B_2O_3 volatility and rapid formation of a thick TGO at the surface. The TGO that does penetrate the bond coat appears to follow microcracking in the material and the splat interfaces from the APS process used to apply the coatings. Given that B_2O_3 becomes more volatile with increasing temperature, it is likely that enough B_2O_3 was present in the coupons exposed at 900°C to affect the oxygen permeation of the SiO_2 TGO and to increase the penetration of that TGO phase through the cracks and splat boundaries in the bond coat.

At higher temperatures and pressures, despite the appearance of a phase with similar morphology to that of the $YbBO_3$ reaction layers observed in the well tests, no $YbBO_3$ was found in the EBC indicating that there either was not enough B_2O_3 or that it volatilized too rapidly to react with the $Yb_2Si_2O_7$ and form $YbBO_3$.

5.5 Conclusions

Reaction-bonded SiC with varying B content and CMC samples, all with APS Si bond coats and YbDS EBCs were exposed in the TGA and Keiser Rig at ORNL. They were tested at 900°C, 1050°C, and 1200°C for 24, 100, and 50 hours in 1 atm and 4.4 atm O₂ to determine the effect of boria on the oxidation kinetics of these samples.

Parabolic rate constants were calculated from TGA data and benchtop weight changes. The samples mostly adhered to parabolic reaction kinetics, save for outliers caused by defects and inclusions in the bond coats of the samples.

The weight changes and TGO thickness could not be directly correlated as the sample coupons were only coated on two faces. Much of the oxidation was found to occur within the splat boundaries of the Si bond coat as rapid paths of oxygen ingress through the coating system. The coupons with the APS coatings systematically gained more weight than the uncoated coupons as the splat boundaries in the bond coat behave as additional surface area readily available for oxidation. The effects of boria on the TGO growth and weight change could not be distinguished from the effects of the excessive splat boundary oxidation.

Coupons were characterized in cross-section using the Dragonfly image analysis program for segmentation and a MATLAB program written by Dom Pinnisi (UVA) to calculate the bond coat penetration depth and distribution of the TGO growth through the bond coat. CMC coupons exposed in the Keiser Rig for 500h in 4.4 atm of dry O₂ showed important TGO trends. The sample exposed at 900°C showed the highest area fraction of TGO phase as well as the most linear distribution of the TGO phase throughout the depth of the bond coat. As temperature

increased, the TGO was found to form a thicker, more continuous oxide layer that showed significantly less distribution through the bond coat, indicating improved protective capability.

Additional coupons, tested for 100h in 1atm dry O₂ in both the TGA and Keiser Rig displayed very linear oxide depth concentration behavior in the Si bond coat. The TGO was distributed evenly throughout the depth of the bond coat for every sample composition and exposure condition. However, it was found that the coupons exposed at 900°C still showed a greater TGO area fraction than their higher-temperature counterparts. The bond coats in these 100h exposure samples displayed a wide range of defects such as pores and a crumbly microstructure as well as EBC inclusions. There was significant variation in the Si bond coat microstructure in these samples and based on the inconsistent TGA results for the 0%B RBSiC coupon exposed at 1050°C, these differences play a significant role in the extent of oxidation for these systems. Dense, uniform coatings free of these defects and inclusions will significantly reduce the oxidation rates of these samples by limiting the oxygen ingress through the coatings, especially at the lower temperature of 900°C.

5.5.1 Suggested Future Work

To date, no oxidation studies have been conducted on APS Si as is used for the bond coat of these CMC systems. An understanding of the oxidation kinetics in that structure and comparison to the oxidation of polycrystalline or single crystal Si is necessary to be able to distinguish between the surface oxidation effects of the APS splats and the B effects on the TGO growth in these specimens. Additional testing on fully-coated coupons to gather data on all times, temperatures, pressures, and compositions would also be recommended to understand the oxidation kinetics of these real CMC systems without complications presented by exposed CMC/ bond coat edges.

5.6 References

1. Lee KN, Opila EJ, Miller R. Oxidation and pore formation at the Mullite/SiC interface in air and water vapor. *Fundamental Aspects of High Temperature Corrosion*. 1996 Oct;124-38..
2. Lee KN. Current status of environmental barrier coatings for Si-based ceramics. *Surface and Coatings Technology*. 2000;133-134:1-7.
3. Lee KN, Zhu D, Lima RS. Perspectives on Environmental Barrier Coatings (EBCs) Manufactured via Air Plasma Spray (APS) on Ceramic Matrix Composites (CMCs): A Tutorial Paper. *Journal of Thermal Spray Technology* [Internet]. 2021;30(1-2):40-58. Available from: <https://doi.org/10.1007/s11666-021-01168-0>
4. Lee KN, Fox DS, Bansal NP. Rare earth silicate environmental barrier coatings for SiC/SiC composites and Si₃N₄ ceramics. *Journal of the European Ceramic Society*. 2005;25(10 SPEC. ISS.):1705-15.
5. Opila EJ, Hann RE. Parabolic oxidation of CVD SiC in water vapor. *Journal of the American Ceramic Society*. 1997;80(1):197-205.
6. Opila EJ, Boyd MK. Oxidation of SiC fiber-reinforced SiC matrix composites with a BN interphase. *Materials Science Forum*. 2011;696:342-7.
7. Opila EJ, Boyd MK. Oxidation of SiC Fiber-Reinforced SiC Matrix Composites With a BN Interphase [Internet]. [cited 2021 Feb 7]. Available from: <https://ntrs.nasa.gov/search.jsp?R=20100040692>
8. Opila EJ, Jacobson NS. Oxidation and Corrosion of Ceramics. *Ceramics Science and Technology, Applications*. 2013;4:1-93.
9. Ogbuji LUJT, Opila EJ. A Comparison of the Oxidation Kinetics of SiC and Si₃N₄. *Journal of The Electrochemical Society* [Internet]. 1995 Mar 1 [cited 2021 Feb 7];142(3):925-30. Available from: <https://iopscience.iop.org/article/10.1149/1.2048559>
10. Lee KN, Fox DS, Bansal NP. Rare earth silicate environmental barrier coatings for SiC/SiC composites and Si₃N₄ ceramics. *Journal of the European Ceramic Society*. 2005;25(10 SPEC. ISS.):1705-15.
11. McFarland B, Angelici Avincola V, Morales M, Opila E. Identification of a new oxidation/dissolution mechanism for boron-accelerated SiC oxidation. *Journal of the American Ceramic Society*. 2020;103(9):5214-31.
12. Ramberg CE, Cruciani G, Spear KE, Tressler RE, Ramberg Jr CF. Passive-oxidation kinetics of high-purity silicon carbide from 800° to 1100° C. *Journal of the American Ceramic Society*. 1996 Nov;79(11):2897-911.
13. Deal BE, Grove AS. General relationship for the thermal oxidation of silicon. *Journal of Applied Physics*. 1965;36(12):3770-8.

14. Richards BT, Zhao H, Wadley HNG. Structure, composition, and defect control during plasma spray deposition of ytterbium silicate coatings. *Journal of Materials Science*. 2015;50(24):7939–57.
15. Richards BT, Begley MR, Wadley HNG. Mechanisms of Ytterbium Monosilicate/Mullite/Silicon Coating Failure during Thermal Cycling in Water Vapor. *Journal of the American Ceramic Society*. 2015 Dec 1;98(12):4066–75.
16. Parker CG. Effect of the Air Plasma Spray Process on Rare Earth Silicate Coating Life by. 2020;(May).
17. ROCKETT TJ, FOSTER WR. Phase Relations in the System Boron Oxide–Silica. *Journal of the American Ceramic Society*. 1965;48(2):75–80.
18. Ogbuji LUJT. A Pervasive Mode of Oxidative Degradation in a SiC-SiC Composite. *Journal of the American Ceramic Society* [Internet]. 2005 Jan 20 [cited 2021 Feb 7];81(11):2777–84. Available from: <http://doi.wiley.com/10.1111/j.1151-2916.1998.tb02696.x>
19. Opila EJ, Nguyen QGN. Oxidation of chemically-vapor-deposited silicon carbide in carbon dioxide. *Journal of the American Ceramic Society*. 1998;81(7):1949–52.
20. McFarland B. Boria Effects on the High Temperature Oxidation of Silicon Carbide [Internet]. [Charlottesville, VA]; 2017 [cited 2021 Feb 7]. Available from: https://libraetd.lib.virginia.edu/public_view/1c18df86b

6 Summary and Conclusions

6.1 Objectives and Summary

The aim of this body of work was to elucidate the effects of boria on the $\text{Yb}_2\text{Si}_2\text{O}_7$ EBC and Si bond coat system for use with SiC/SiC CMCs. SiC/BN/SiC CMCs with rare earth oxide EBCs entered use in civilian turbine engines in 2016. The BN interphase used between the SiC fibers and the matrix is vital to the mechanical properties of the CMC, but has been found to readily oxidize and form B_2O_3 at temperatures above 400°C . B_2O_3 is a highly reactive glass-former with a low melting temperature of 450°C .

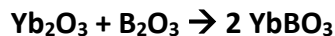
Previous studies of boron-containing systems had shown possible spinodal decomposition and dendritic structure formation in the EBC after exposure in a combustion rig at 1150°C for 100h. These microstructural effects were hypothesized to derive from thermally grown B_2O_3 . However, a lack of thermodynamic and detailed experimental information on the $\text{B}_2\text{O}_3 - \text{SiO}_2 - \text{Yb}_2\text{O}_3$ system prevented any definitive conclusions from being drawn.

Given the lack of information on the $\text{B}_2\text{O}_3 - \text{SiO}_2 - \text{Yb}_2\text{O}_3$ system, four objectives were laid out to investigate the effects of B_2O_3 on the $\text{Yb}_2\text{Si}_2\text{O}_7$ EBC and Si bond coat systems:

1. Understand the reactions & equilibrium phases that occur when B_2O_3 reacts with the phases found in the rare earth silicate EBC; $\text{Yb}_2\text{Si}_2\text{O}_7$, Yb_2SiO_5 , and Yb_2O_3 .
2. Develop a phase diagram for the $\text{Yb}_2\text{O}_3 - \text{SiO}_2 - \text{B}_2\text{O}_3$ ternary system.
3. Determine the properties of any reaction products & equilibrium phases that are found to form in the $\text{Yb}_2\text{O}_3 - \text{SiO}_2 - \text{B}_2\text{O}_3$ ternary system.

4. Determine the impact of the formation of these reaction products on the oxidation of SiC/BN/SiC CMC, Si bond coat, and Yb₂Si₂O₇ EBC systems.

For the first objective, idealized interfacial reaction tests between B₂O₃ and Yb₂Si₂O₇, Yb₂SiO₅, and Yb₂O₃, referred to as “well tests”, were used to investigate the reactions that occur between boria and the rare earth oxides and silicates of SiC/BN/SiC CMC, Si bond coat, and Yb₂Si₂O₇ EBC systems. From these exposures, it was found that YbBO₃ was the main product of the reaction between B₂O₃ and the Yb-containing oxides and silicates as shown in the three reaction pathways below.



For the second objective, development of a ternary phase diagram, these three reaction pathways were assumed to be the phases in equilibrium for the system. 31 different compositions were chosen to investigate the Yb₂O₃ – YbBO₃ region of the binary Yb₂O₃ – B₂O₃ phase diagram as well as the portion of the ternary system with compositions ≤30 mol% B₂O₃. Samples were characterized using differential scanning calorimetry to record thermodynamic events and high-energy X-ray diffraction at The Argonne National Lab Advanced Photon Source for *in situ* diffraction of samples at temperatures up to 1500°C. Phase equilibrium fields were laid out on the ternary using the reaction paths as Alkemade lines. Phase boundaries and the

liquidus surface were proposed based on melting temperatures determined from the DSC and HE-XRD scans. The proposed liquidus surface diagram can be seen below.

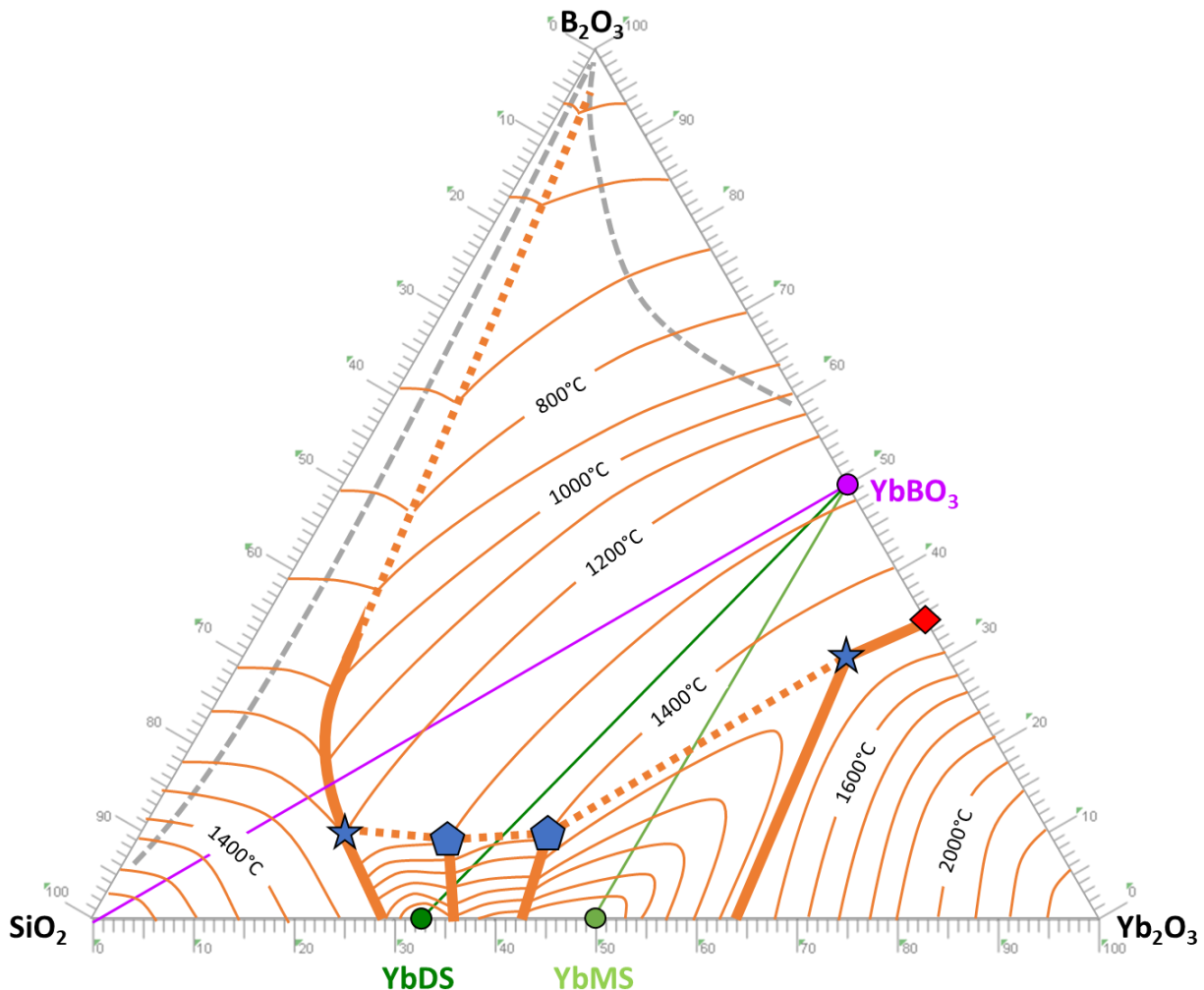


Figure 6.1: Predicted liquidus surface of $\text{Yb}_2\text{O}_3 - \text{SiO}_2 - \text{B}_2\text{O}_3$ phase diagram with boundary lines shown in thick orange, ternary eutectic shown in blue, and regions of possible liquid immiscibility shown in grey. Alkemade lines for equilibrium reactions are shown in purple and green.

The YbBO_3 reaction product phase was further studied using both static and dynamic phase equilibrium testing methods. DSC was used to determine the temperatures of formation and polymorphic phase transitions for YbBO_3 as well as to measure the enthalpy of those thermal events. It was found that the YbBO_3 phase forms from the constituent Yb_2O_3 and B_2O_3 at 733°C

with a 12 kJ/ mol enthalpy of formation. YbBO_3 initially forms in its high-temperature polymorphic structure (hexagonal ($P6c2$)) with the borate groups taking trigonal planar coordination between the B and O. The transformation to the low-temperature polymorph is reconstructive where the B-O bonding switched to tetrahedral coordination. This transition is kinetically limited and was found to occur between 500°C and 600°C on cooling. The transition back to the high temperature polymorph on heating was found to occur at approximately 1000°C, in agreement with the transition temperature reported by Levin et al. This phase transition on heating occurs suddenly and results in a sudden change in the lattice parameters of the YbBO_3 phase as well as a sudden jump in the CTE of the phase. The CTE for YbBO_3 was measured for both the low temperature and the high temperature polymorphs. It was found to be anisotropic and significantly larger than the other constituents of the CMC/EBC system. Additionally, bulk samples of YbBO_3 were found to expand rapidly, slumping and flowing at temperatures as low as 450°C for times as short as 15 minutes. This behavior is attributed to phase separation of the borate into Yb_2O_3 and B_2O_3 leading to liquid phase expansion and melting of the boria. This liquid-phase behavior combined with the large, anisotropic CTE and the rapid, polymorphic phase change will negatively impact the CMC/ EBC lifetime if the YbBO_3 forms. The stability of this YbBO_3 phase for longer times and in combustion environments remains unknown.

For the final objective, coated reaction-bonded SiC and CMC samples were exposed in both TGA and the high-temperature, high-pressure “Keiser Rig” at Oak Ridge National Lab. Weight changes were used to determine the oxidation kinetics for the samples. The coated coupons exhibited near-parabolic oxidation kinetics for all times, temperatures, and pressures tested.

The coated samples also exhibited much larger oxidation rates than uncoated RBSiC and CMC samples exposed at the same conditions. This difference in oxidation rates was attributed to the increased surface area in splat boundaries from the APS splat microstructure of the coatings. The samples were also cross sectioned for analysis of the TGO growth in the Si bond coat and to look for phase separation in the EBC. The Dragonfly image analysis program was used to segment the micrographs and then measure the area fraction of TGO in the bond coat of the cross-sectioned samples. A MATLAB program [Dom Pinnisi, UVA] was then used with the Dragonfly segmentations to calculate the TGO depth concentrations relative to the thickness of the Si bond coat. The 900°C exposures formed the least protective TGOs with the deepest Si bond coat penetrations, reaching all the way to the CMC substrate. The 1050°C TGOs were more continuous and concentrated near the bond coat/ EBC interface, but still showed some penetration into the bond coat. The 1200°C TGOs were the most protective, forming a thick, continuous oxide along the EBC interface. The weight change of the samples could not be correlated to TGO area fractions due to edge effects from the uncoated sides of the coupons. It was also not possible to distinguish any boron effects on the coatings from the effects of the excessive splat boundary oxidation. There was significant variation in the Si bond coat microstructure in these samples and based on the inconsistent TGA results, these differences play a significant role in the extent of oxidation for these systems. Dense, uniform coatings free of these defects and inclusions will significantly reduce the oxidation rates of these samples by limiting the oxygen ingress through the coatings, especially at the lower temperature of 900°C.

6.2 Impact

Though the work detailed here, it was found that YbBO_3 is the main product phase in reactions between B_2O_3 and Yb-containing silicates and oxides. Considerable progress was made in determining both the $\text{Yb}_2\text{O}_3 - \text{B}_2\text{O}_3$ and the $\text{Yb}_2\text{O}_3 - \text{SiO}_2 - \text{B}_2\text{O}_3$ phase diagrams, and the phase boundaries and liquidus were proposed for the ternary system. Properties of the YbBO_3 phase such as phase stability, CTE and the thermal behavior were investigated.

The YbBO_3 phase was found to undergo a polymorphic phase transformation at approximately 1000°C on heating. This reconstructive transformation results in a sudden jump in the unit cell dimensions of the phase as well as a sudden change of the CTE. The CTE for YbBO_3 was also found to be significantly larger than that of the other material components of the CMC/EBC system. Additionally, the YbBO_3 phase exhibits apparent decomposition and phase separation into its constituent oxides resulting in rapid expansion and melting of the B_2O_3 at temperatures as low as 450°C . These properties would be detrimental to the performance and lifetime of the CMC/ EBC system due to thermal mismatch, rapid changes in phase volume upon thermal cycling, and low temperature melting which could lead to cracking and spallation of the coatings.

Finally, it was found that the oxidation of the APS Si bond coat is highly dependent on the APS spray parameters and temperature. It was found that coatings exposed at lower temperatures oxidized rapidly, most notably along the APS splat boundaries, penetrating the depth of the bond coat to reach the CMC substrate. These coating oxidation behaviors play a critical role in the CMC/ EBC properties and lifetimes, determining whether or not the CMC will oxidize.

6.3 Suggestions for Future Work

Further study of interactions between B_2O_3 and APS coatings could help to determine whether $YbBO_3$ will form in the EBC coatings. Understanding the formation of the $YbBO_3$ phase and the effect of B_2O_3 on the TGO formation in the Si bond coat will be vital to determining how B_2O_3 will affect the CMC/EBC systems in service.

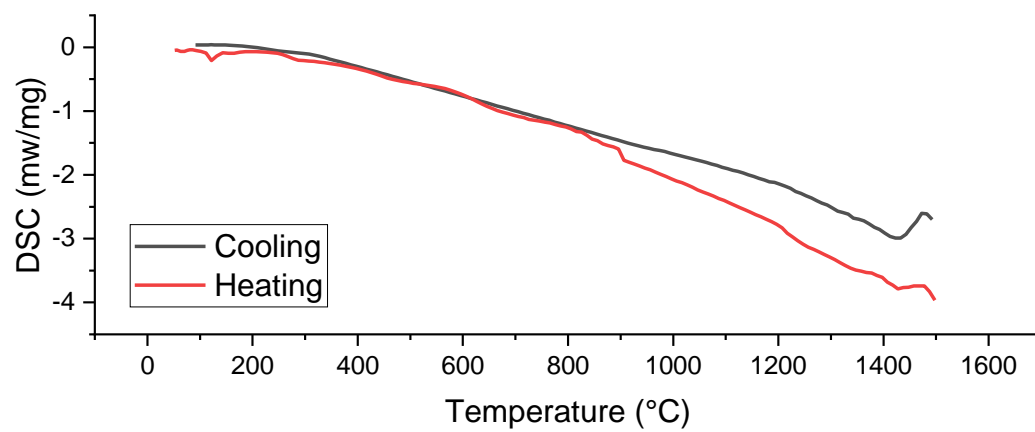
The unusual behavior of the $YbBO_3$ phase and its long-term stability warrant further study. The extent of the rapid expansion and slumping behavior as a result of the potential phase separation is still unknown. Longer-term phase separation studies are recommended as well as long term stability testing of the phase in combustion environments. The stability of this phase in the presence of high pressures, temperatures, and steam-containing environments has not yet been investigated and will be vital to determine the impact of $YbBO_3$ formation on the CMC/ EBC system.

To date, no oxidation studies have been conducted on APS Si as is used for the bond coat of these CMC systems. An understanding of the oxidation kinetics in that structure and comparison to the oxidation of polycrystalline or single crystal Si is necessary to be able to distinguish between the surface oxidation effects of the APS splats and the B effects on the TGO growth in these specimens. Additional testing on fully coated coupons to gather data on all times, temperatures, pressures, and compositions would also be recommended to understand the oxidation kinetics of these real CMC systems without complications presented by exposed CMC/ bond coat edges.

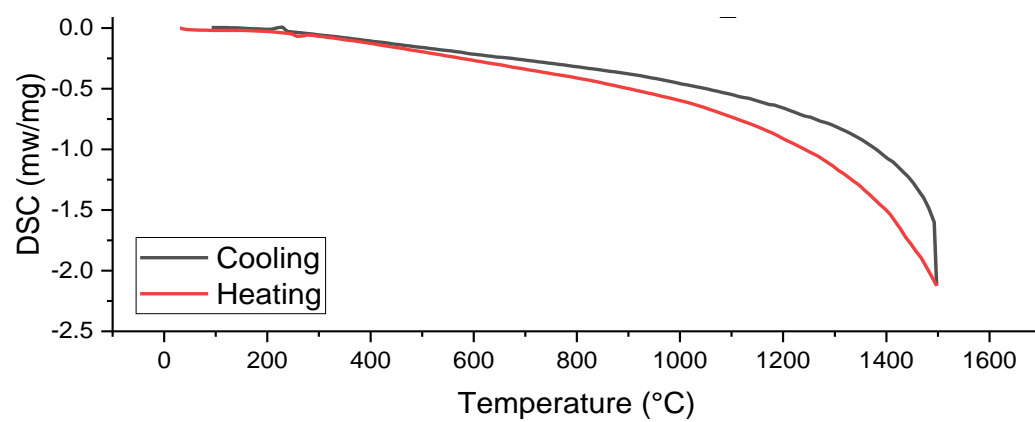
7 Appendix A: DSC Data

7.1 Baseline DSC Scans

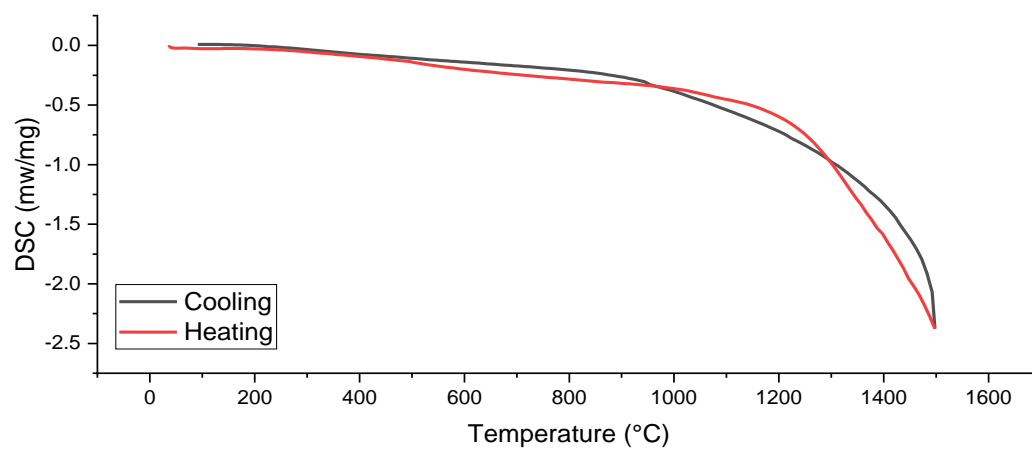
7.1.1 B_2O_3



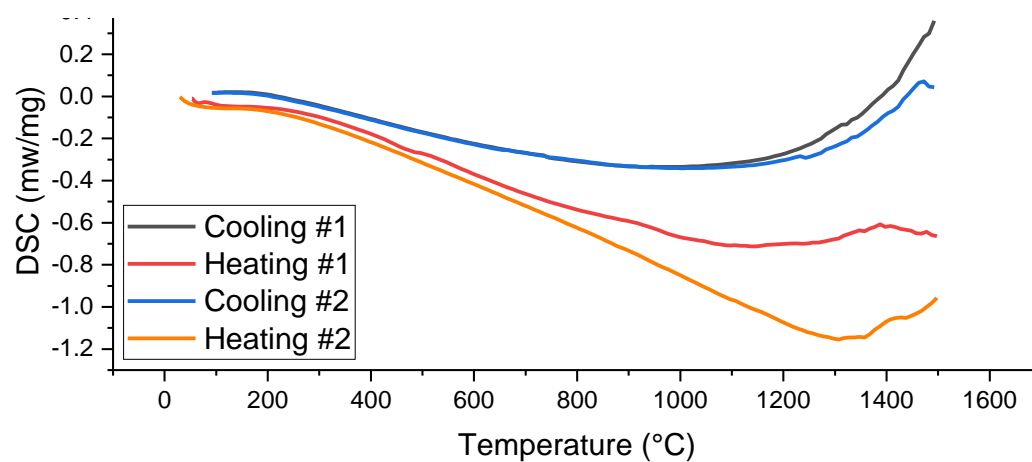
7.1.2 SiO_2



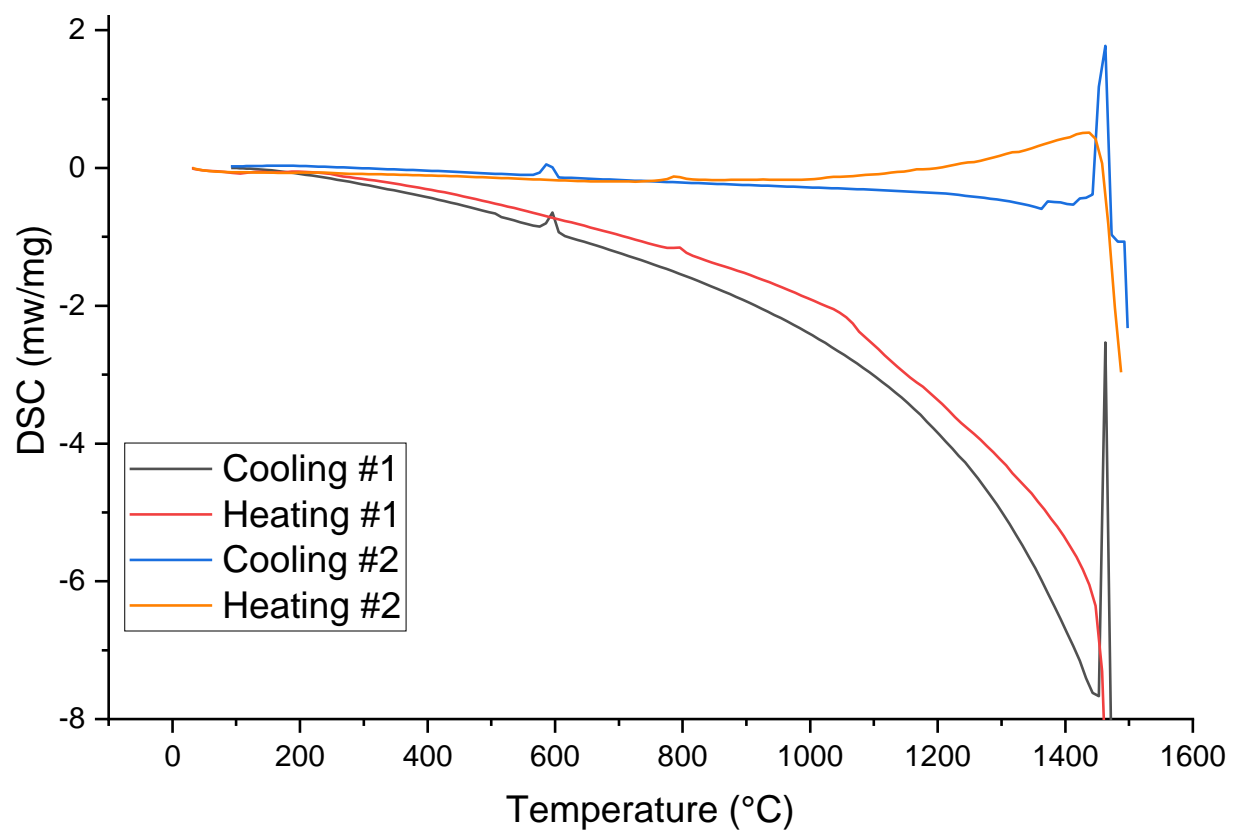
7.1.3 Yb_2O_3



7.1.4 $\text{Yb}_2\text{Si}_2\text{O}_7$ (YbDS)

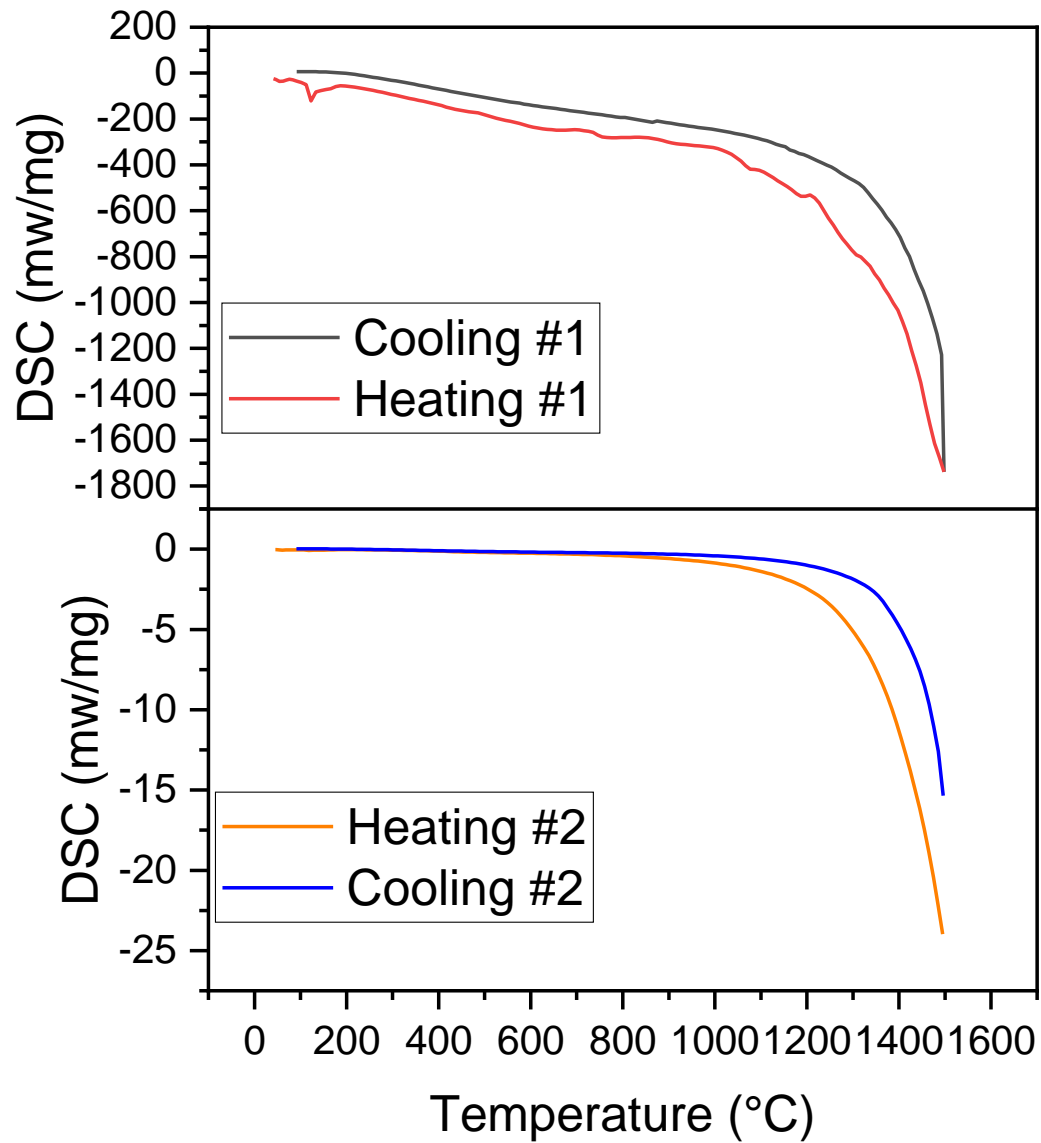


7.1.1.5 $\text{Yb}_2\text{Si}_2\text{O}_7 + \text{B}_2\text{O}_3$

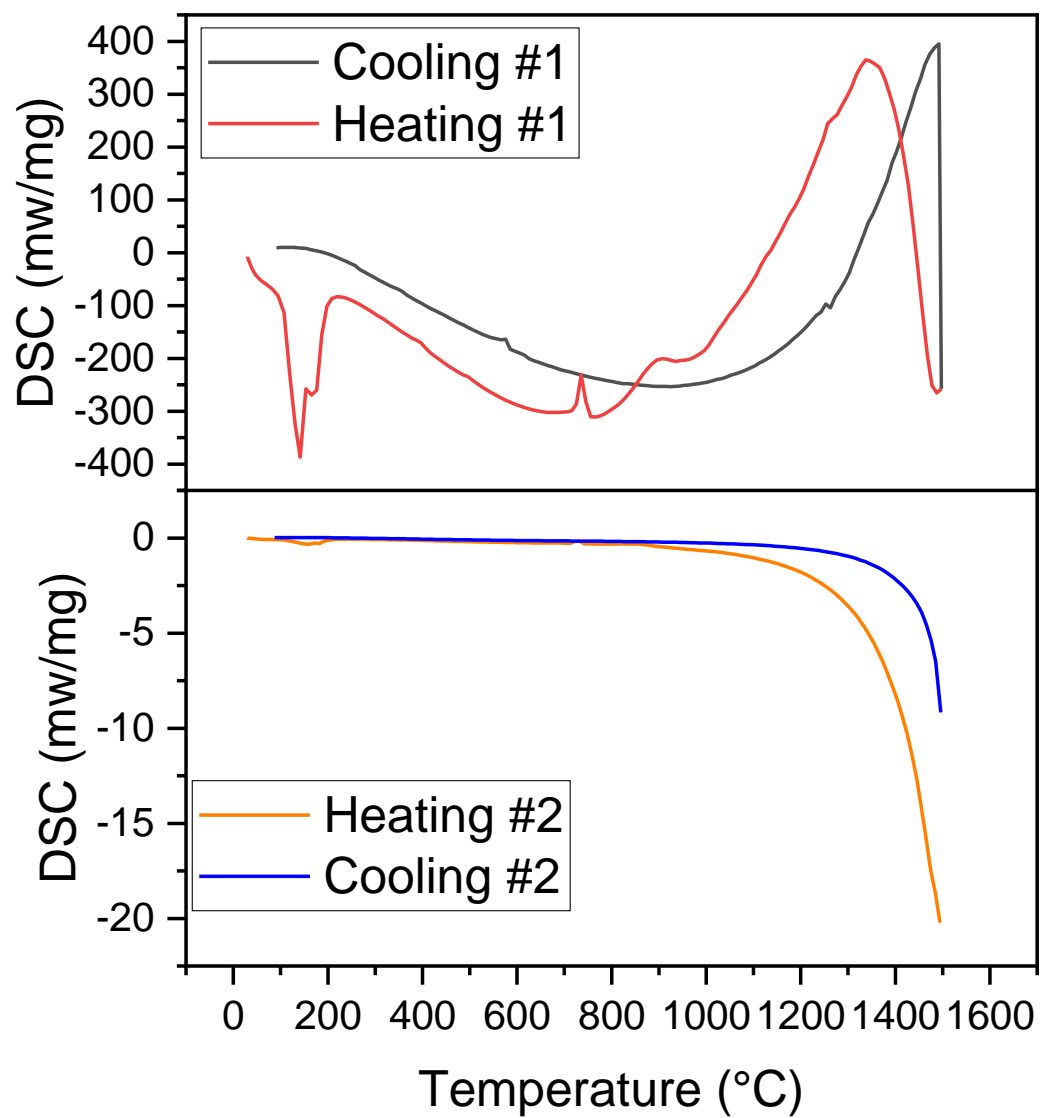


7.2 Binary Composition DSC Scans

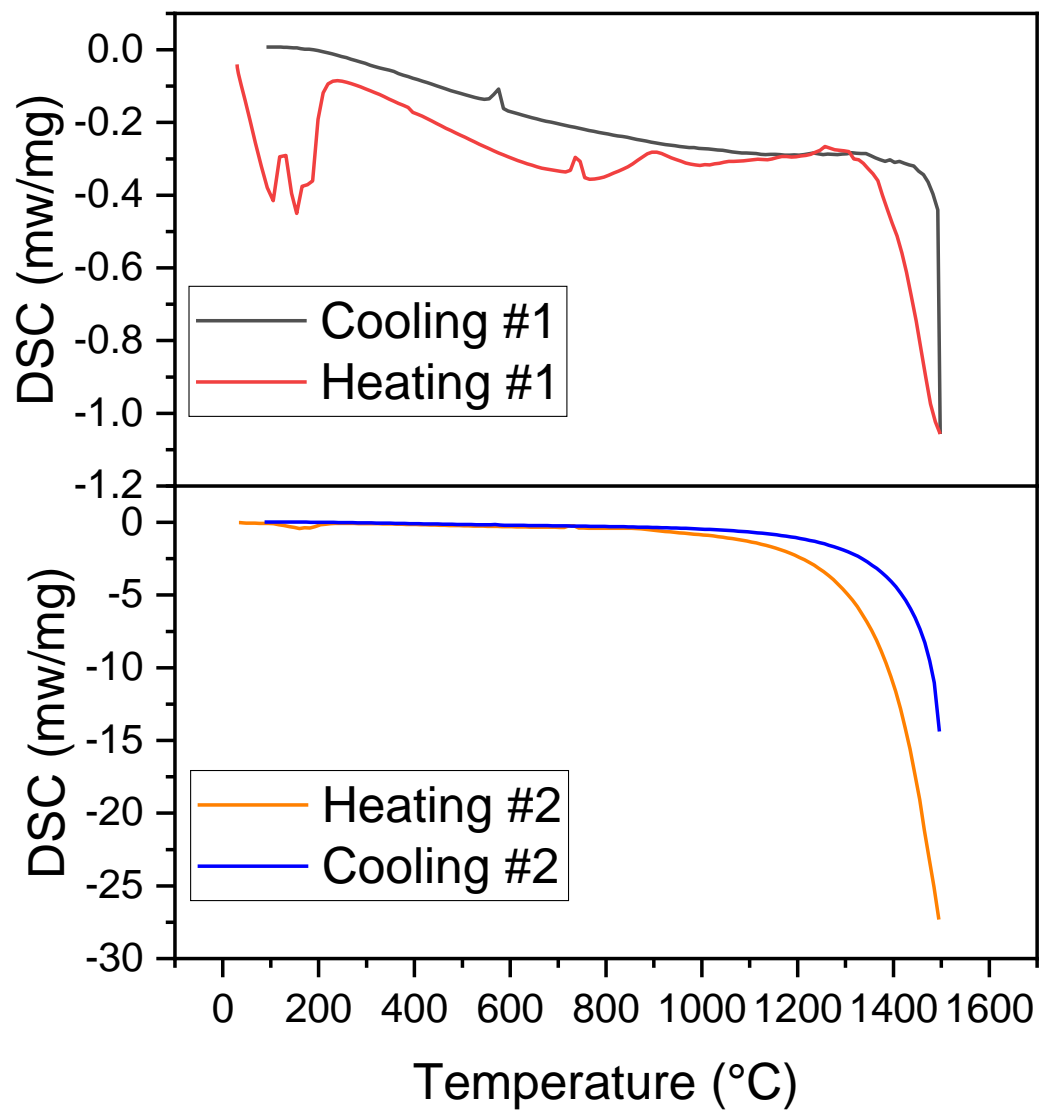
7.2.1 B1: 10 mol% B_2O_3 & 90 mol% Yb_2O_3



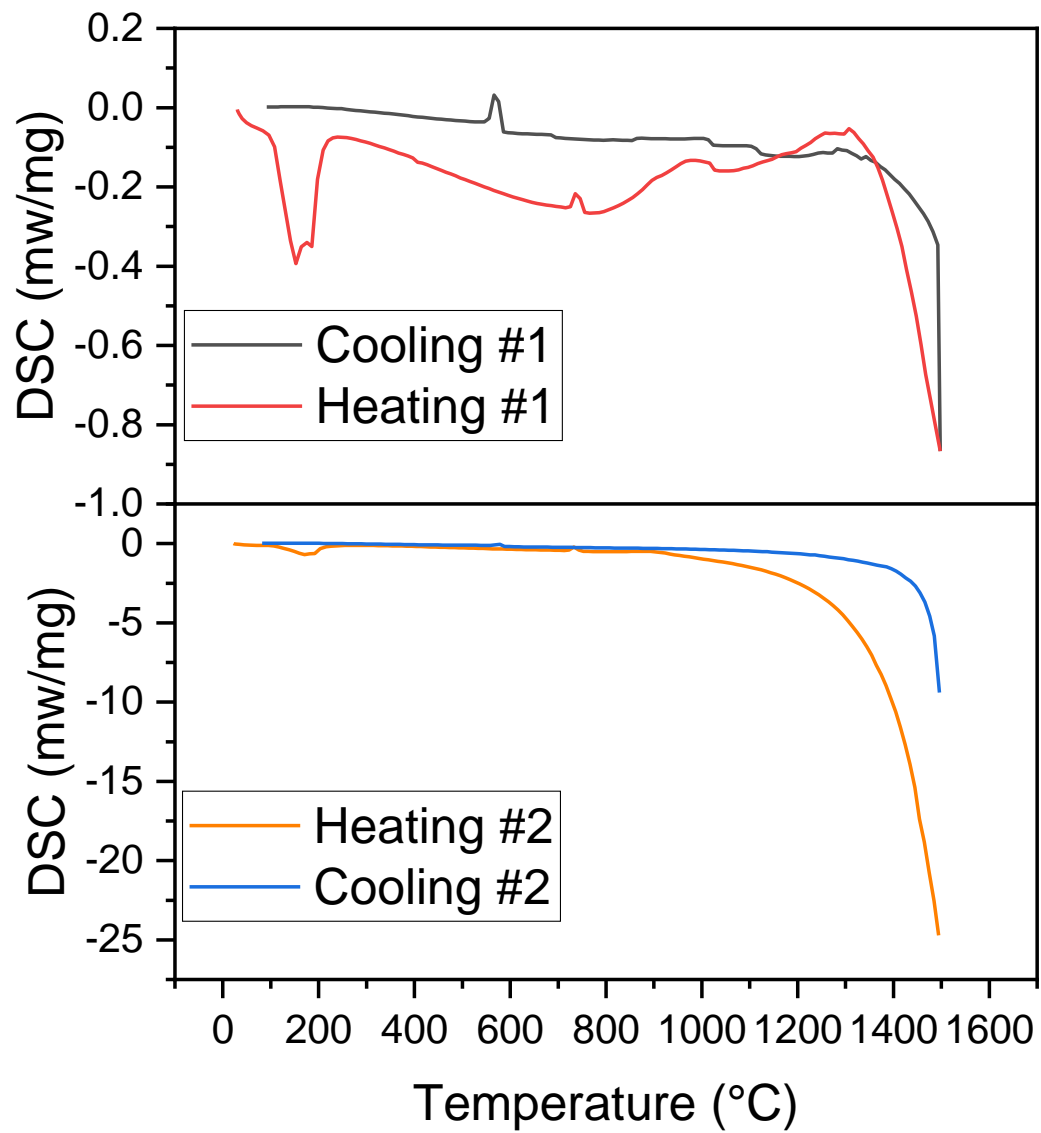
7.2.2 B2: 20 mol% B₂O₃ & 80 mol% Yb₂O₃



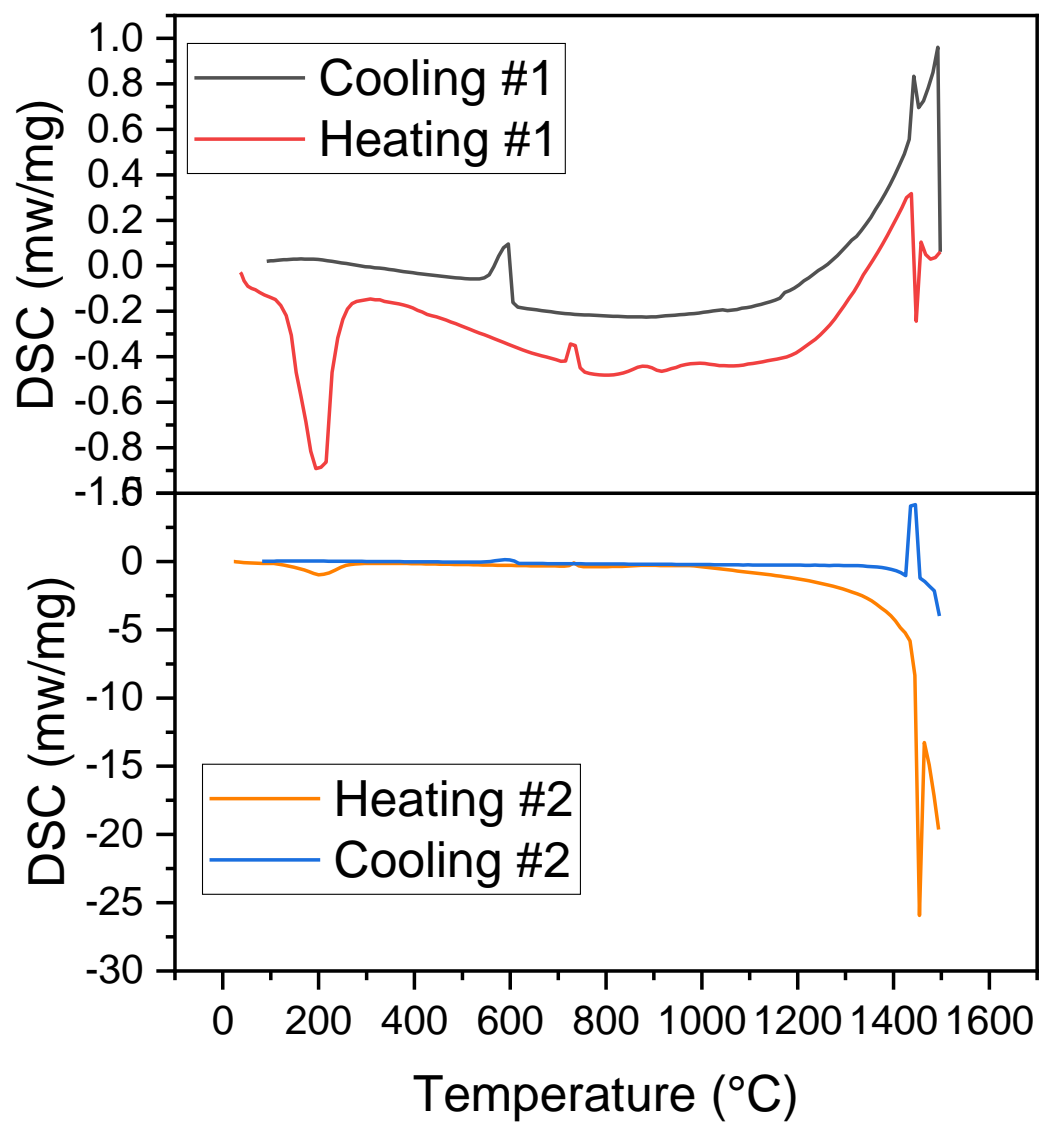
7.2.3 B3: 30 mol% B₂O₃ & 70 mol% Yb₂O₃



7.2.4 B4: 40 mol% B₂O₃ & 60 mol% Yb₂O₃

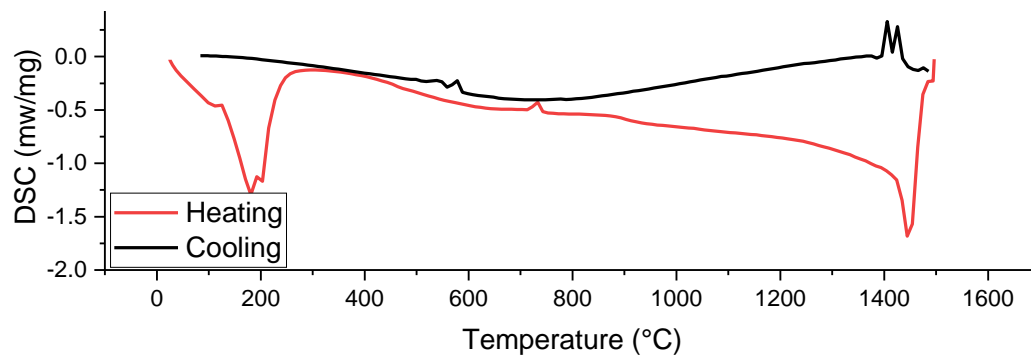


7.2.5 B5: 50 mol% B₂O₃ & 50 mol% Yb₂O₃

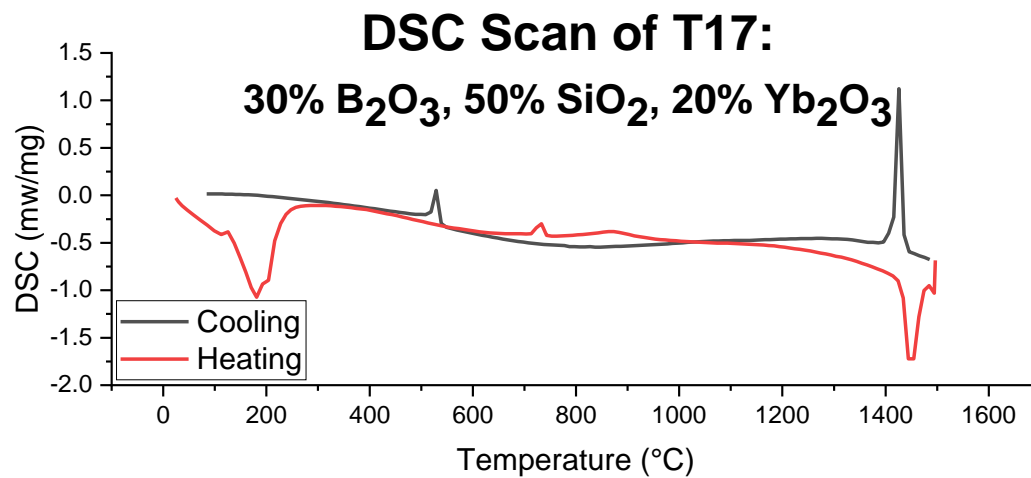


7.3 Ternary Composition DSC Scans

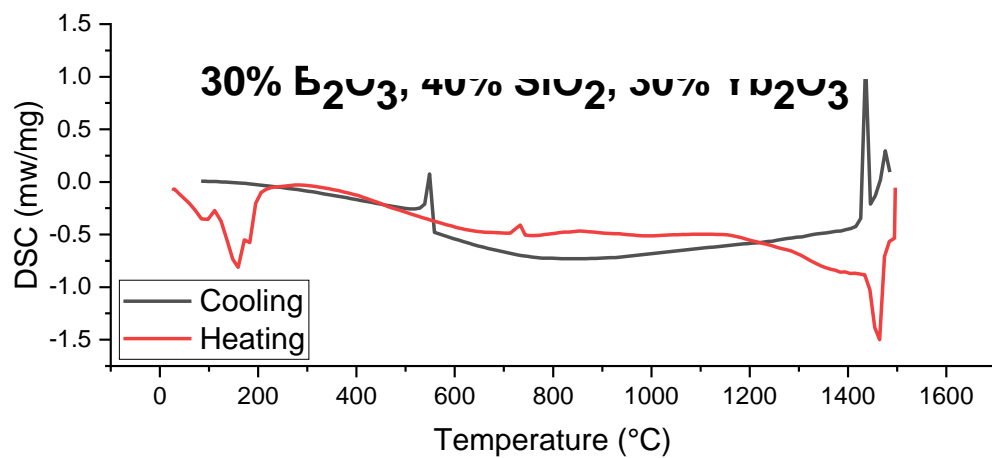
7.3.1 T16: 30% B₂O₃, 60% SiO₂, 10% Yb₂O₃



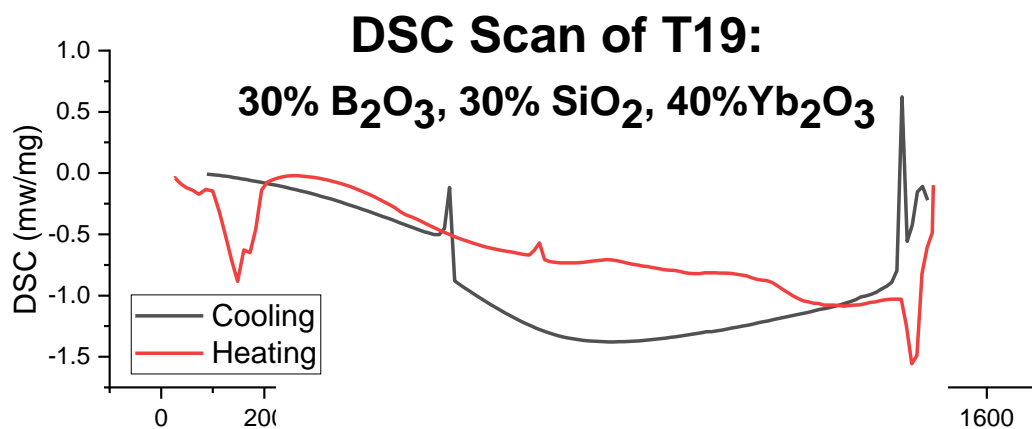
7.3.2 T17: 30% B₂O₃, 50% SiO₂, 20% Yb₂O₃



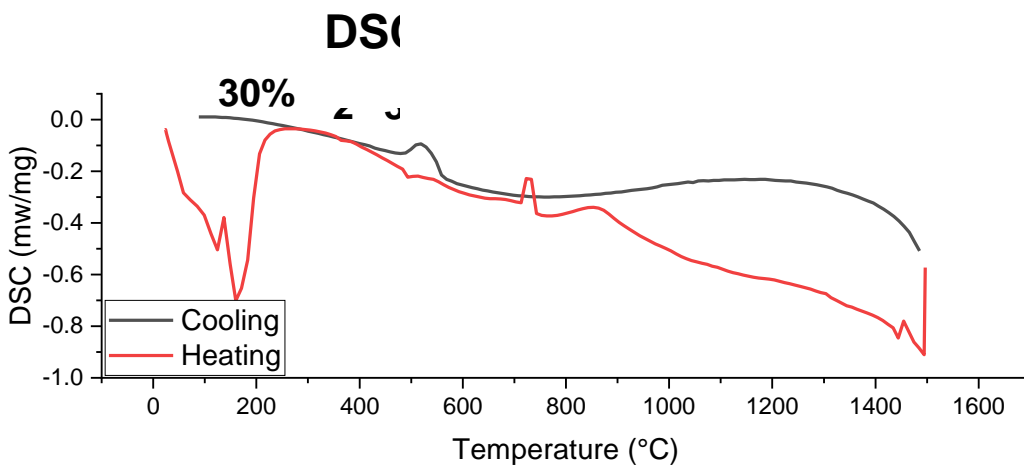
7.3.3 T18: 30% B₂O₃, 40% SiO₂, 30% Yb₂O₃



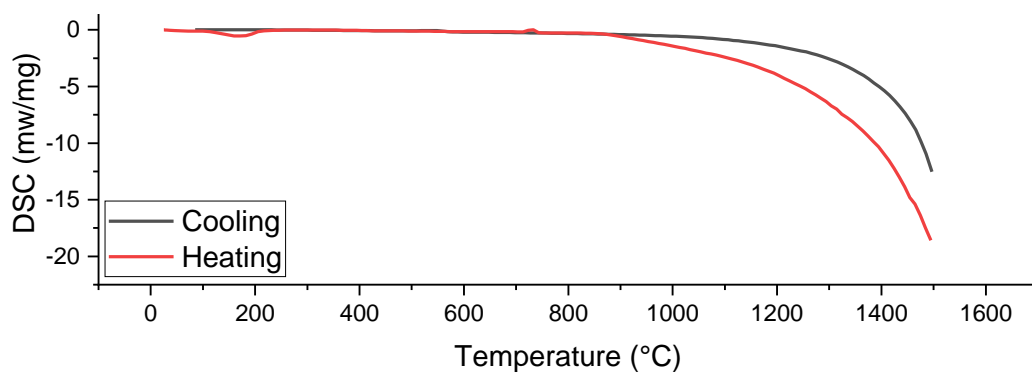
7.3.4 T19: 30% B₂O₃, 30% SiO₂, 40% Yb₂O₃



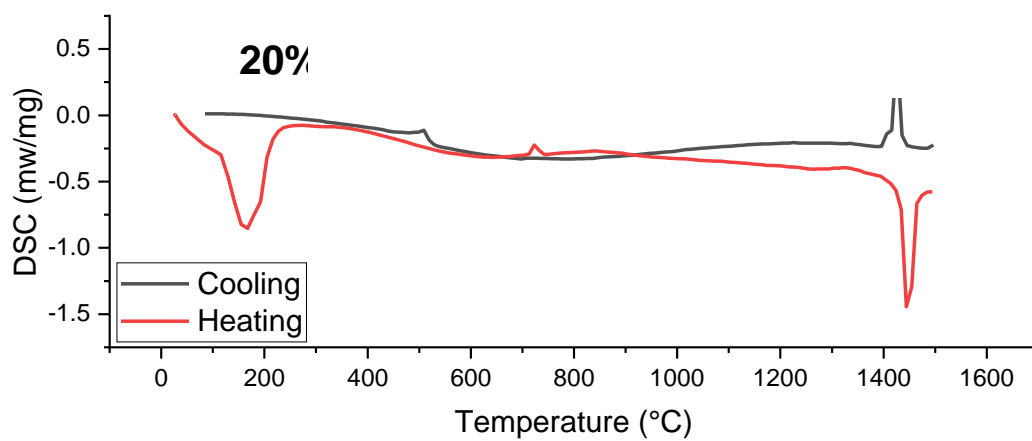
7.3.5 T20: 30% B₂O₃, 20% SiO₂, 50% Yb₂O₃



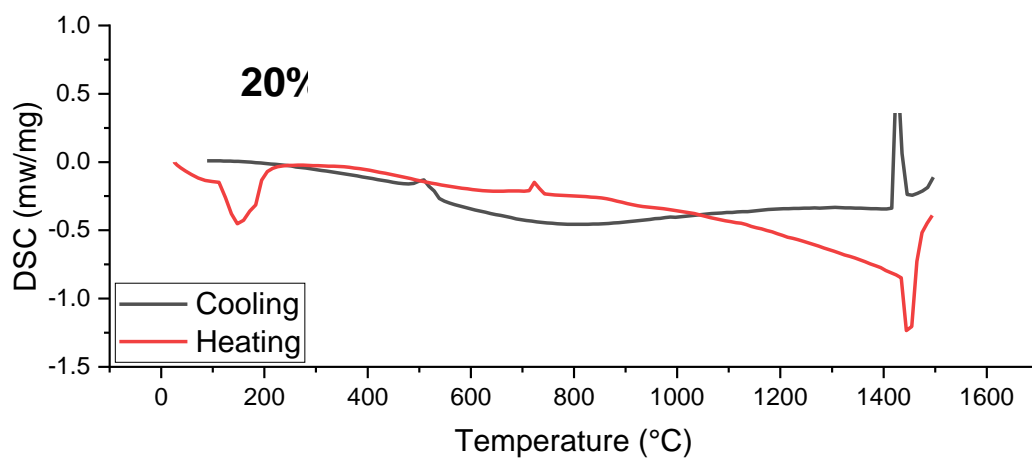
7.3.6 T21: 30% B₂O₃, 10% SiO₂, 60% Yb₂O₃



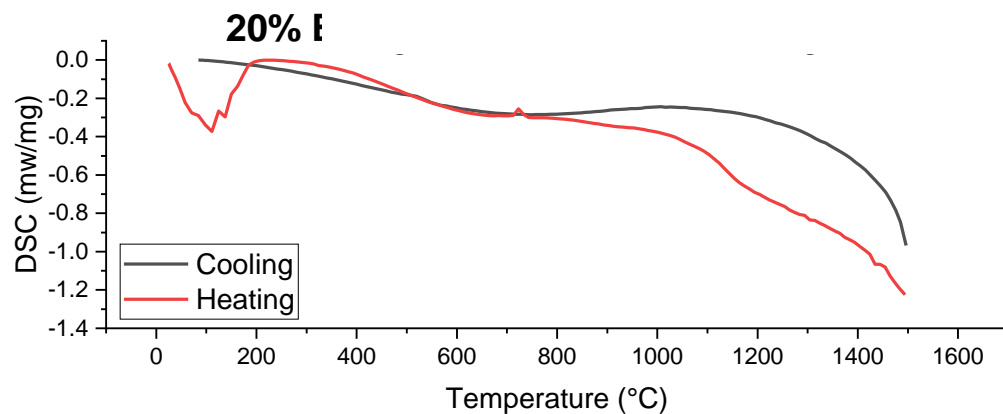
7.3.7 T22: 20% B₂O₃, 70% SiO₂, 10% Yb₂O₃



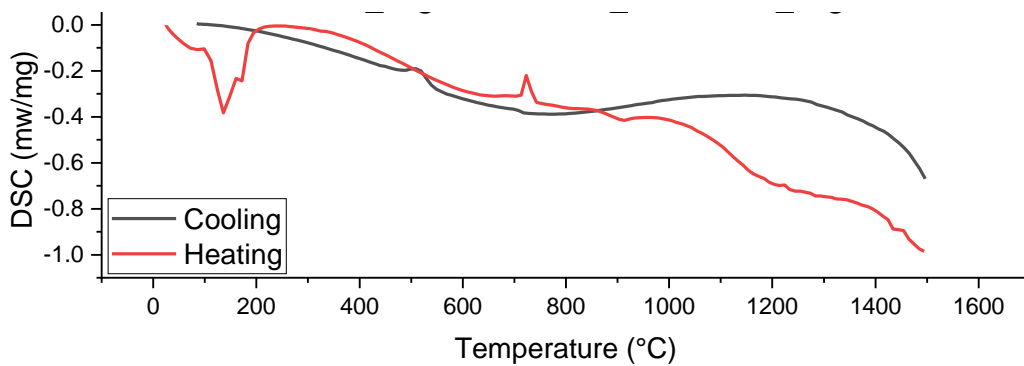
7.3.8 T23: 20% B₂O₃, 60% SiO₂, 20% Yb₂O₃



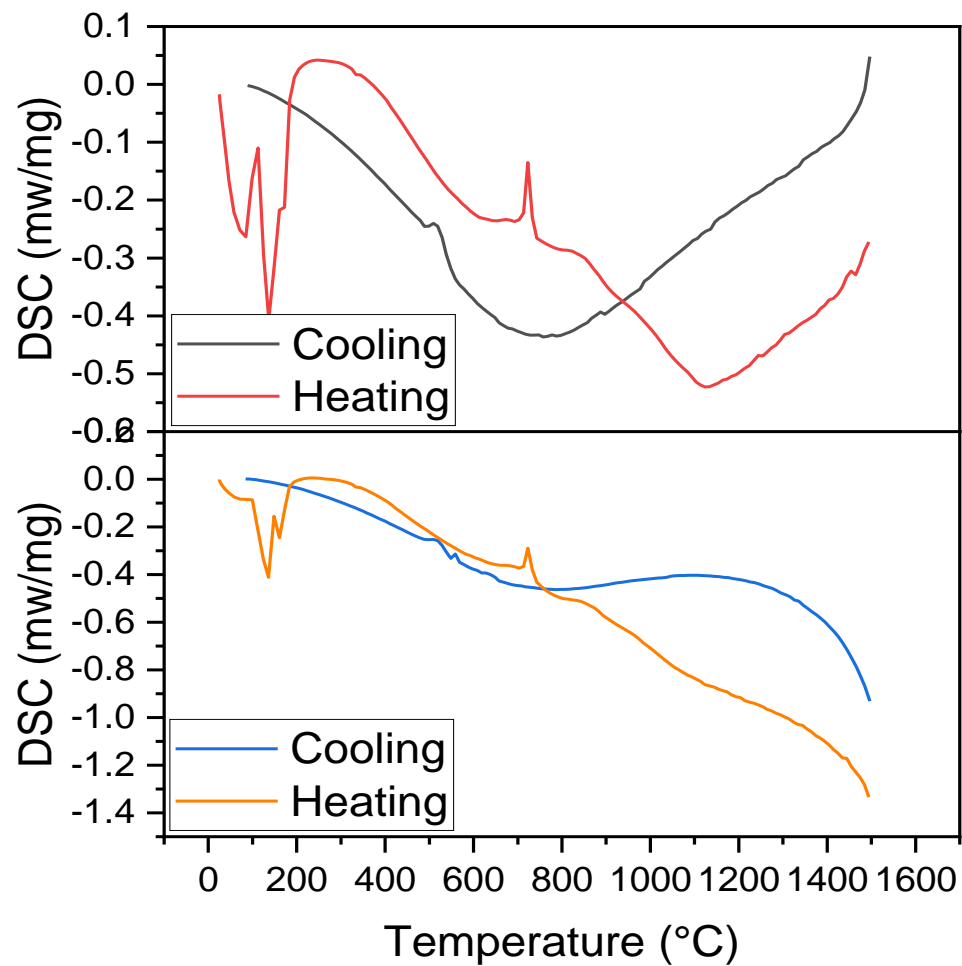
7.3.9 T24: 20% B₂O₃, 50% SiO₂, 30% Yb₂O₃



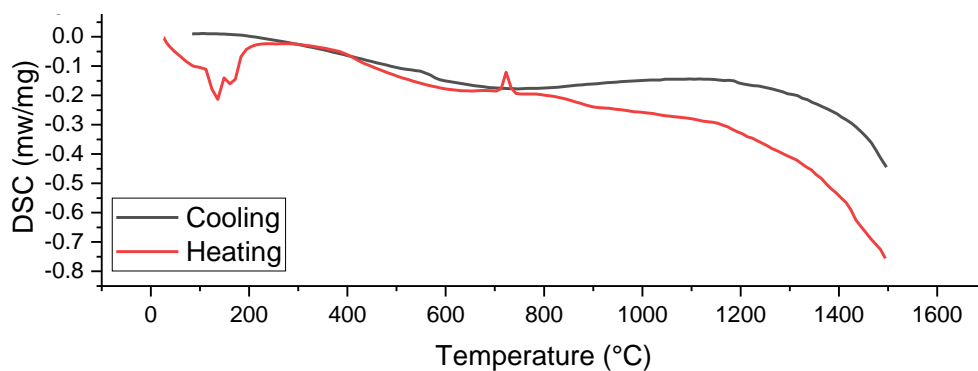
7.3.10 T25: 20% B₂O₃, 40% SiO₂, 40% Yb₂O₃



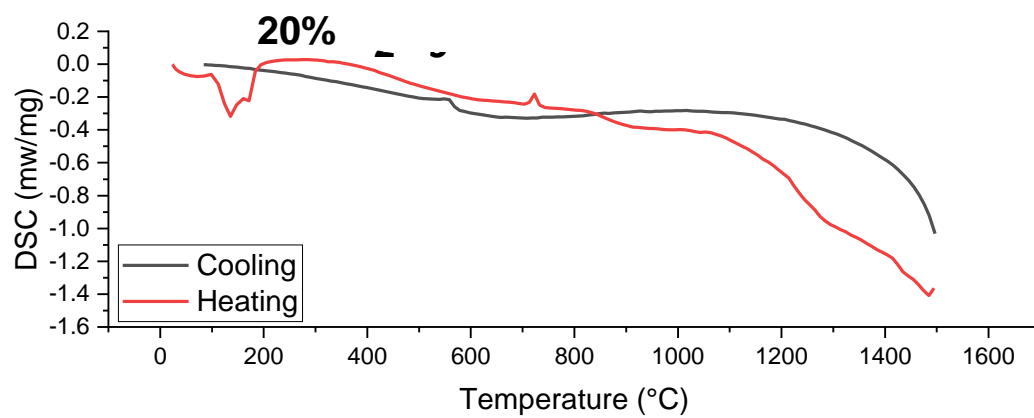
7.3.11 T26: 20% B₂O₃, 30% SiO₂, 50% Yb₂O₃



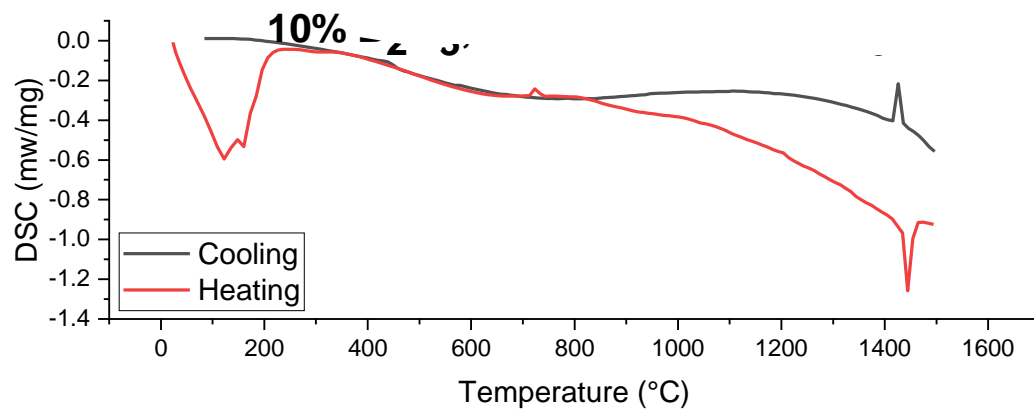
7.3.12 T27: 20% B₂O₃, 20% SiO₂, 60% Yb₂O₃



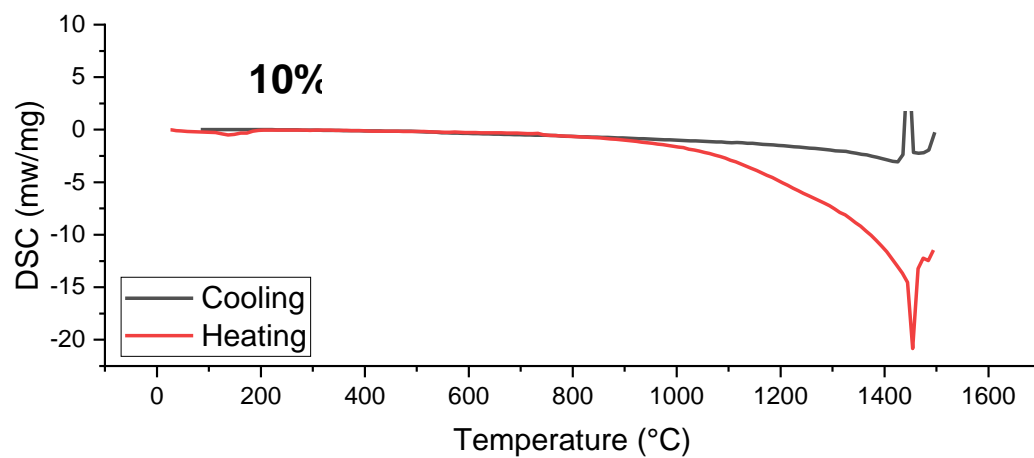
7.3.13 T28: 20% B₂O₃, 10% SiO₂, 70% Yb₂O₃



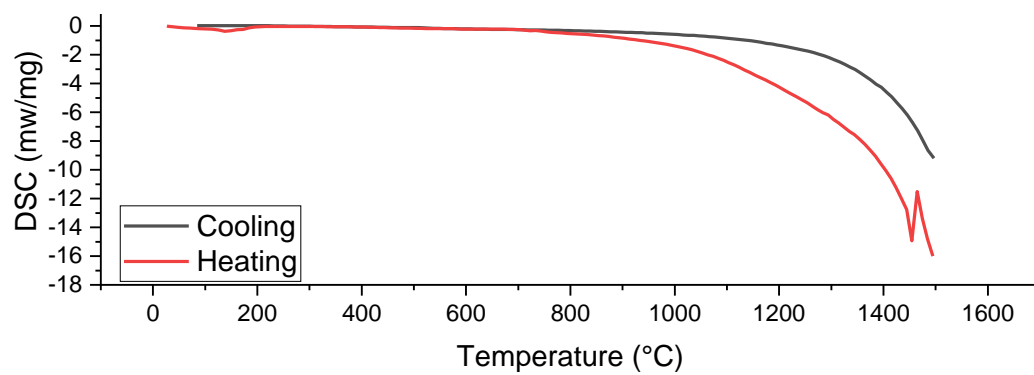
7.3.14 T29: 10% B₂O₃, 80% SiO₂, 10% Yb₂O₃



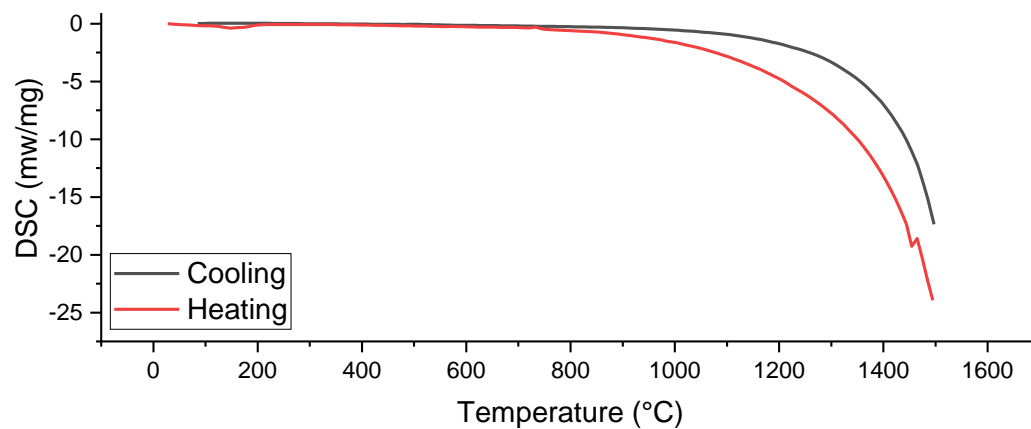
7.3.15 T30: 10% B₂O₃, 70% SiO₂, 20% Yb₂O₃



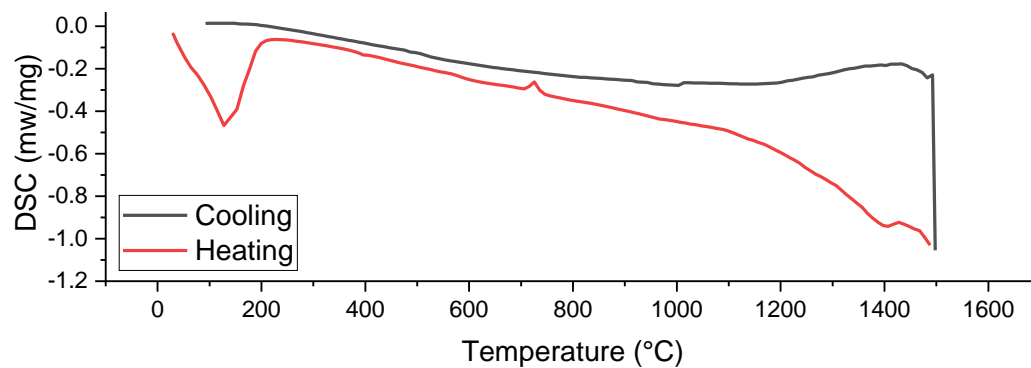
7.3.16 T31: 10% B₂O₃, 60% SiO₂, 30% Yb₂O₃



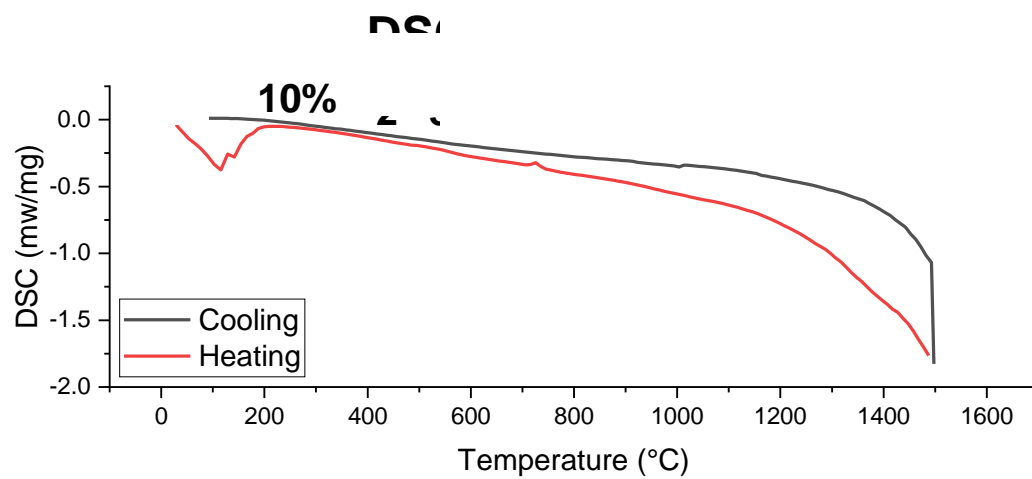
7.3.17 T32: 10% B₂O₃, 50% SiO₂, 40% Yb₂O₃



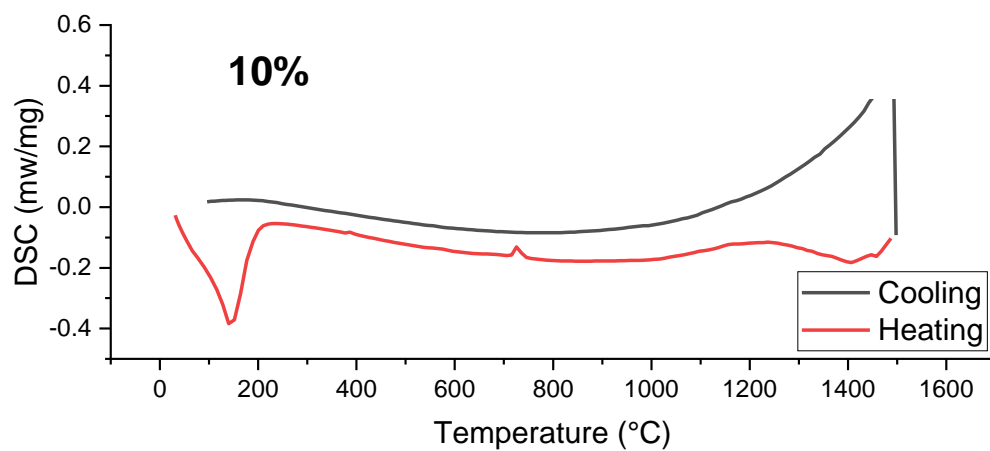
7.3.18 T33: 10% B₂O₃, 40% SiO₂, 50% Yb₂O₃



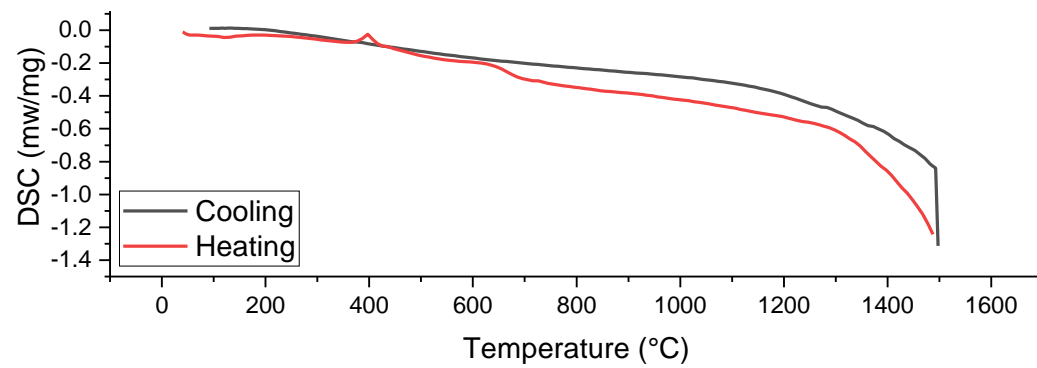
7.3.19 T34: 10% B₂O₃, 30% SiO₂, 60% Yb₂O₃



7.3.20 T35: 10% B₂O₃, 20% SiO₂, 70% Yb₂O₃



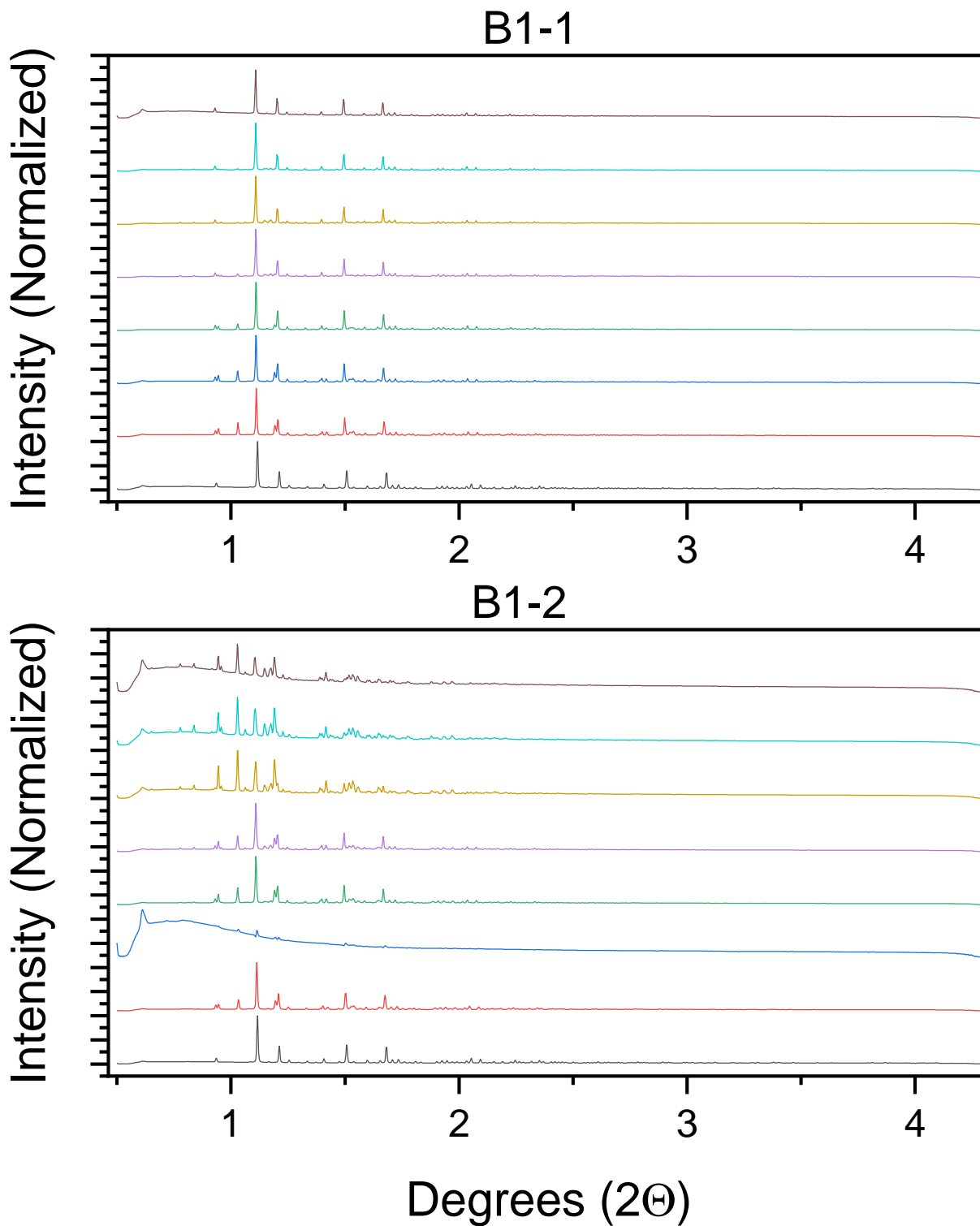
7.3.21 T36: 10% B₂O₃, 10% SiO₂, 80% Yb₂O₃

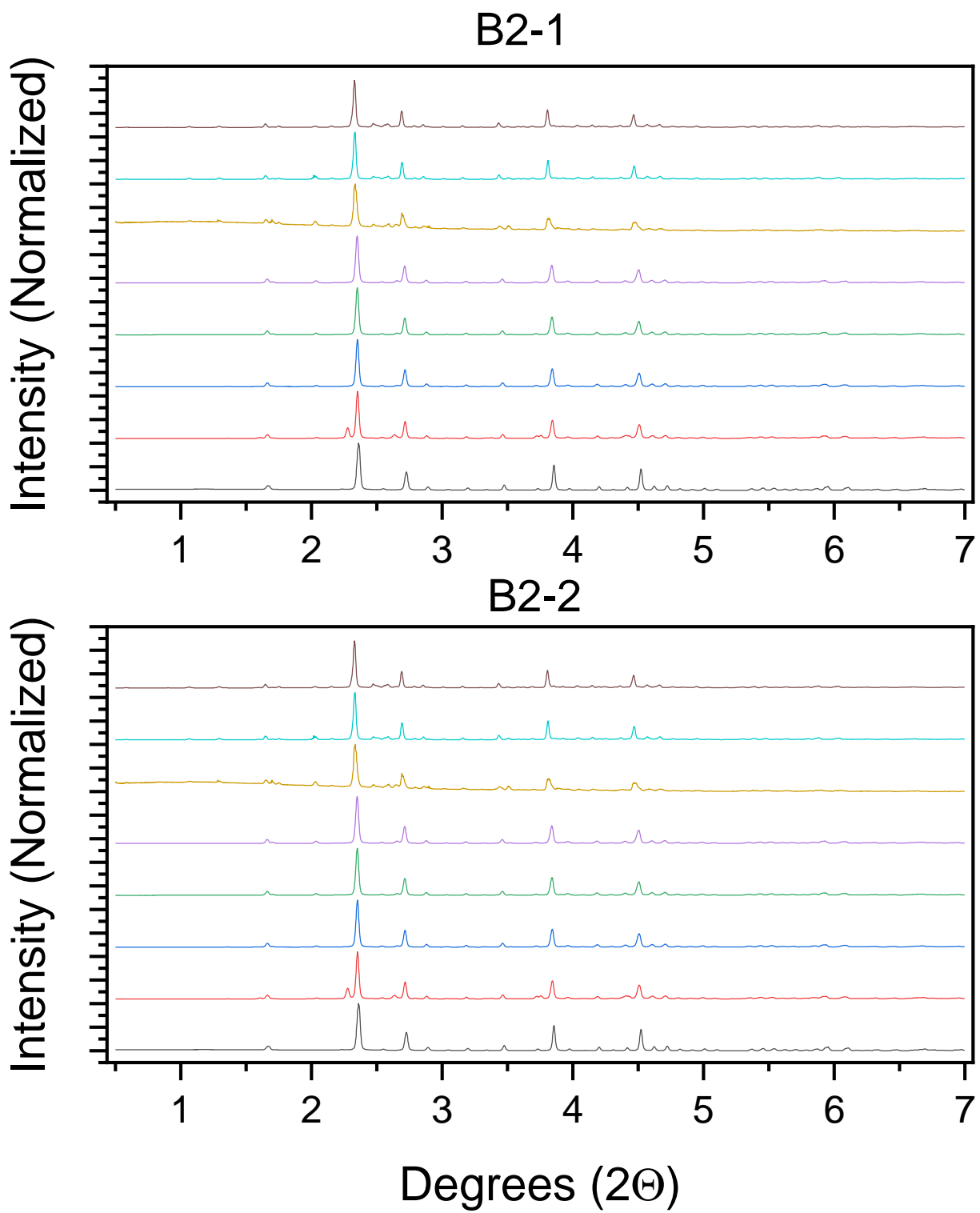


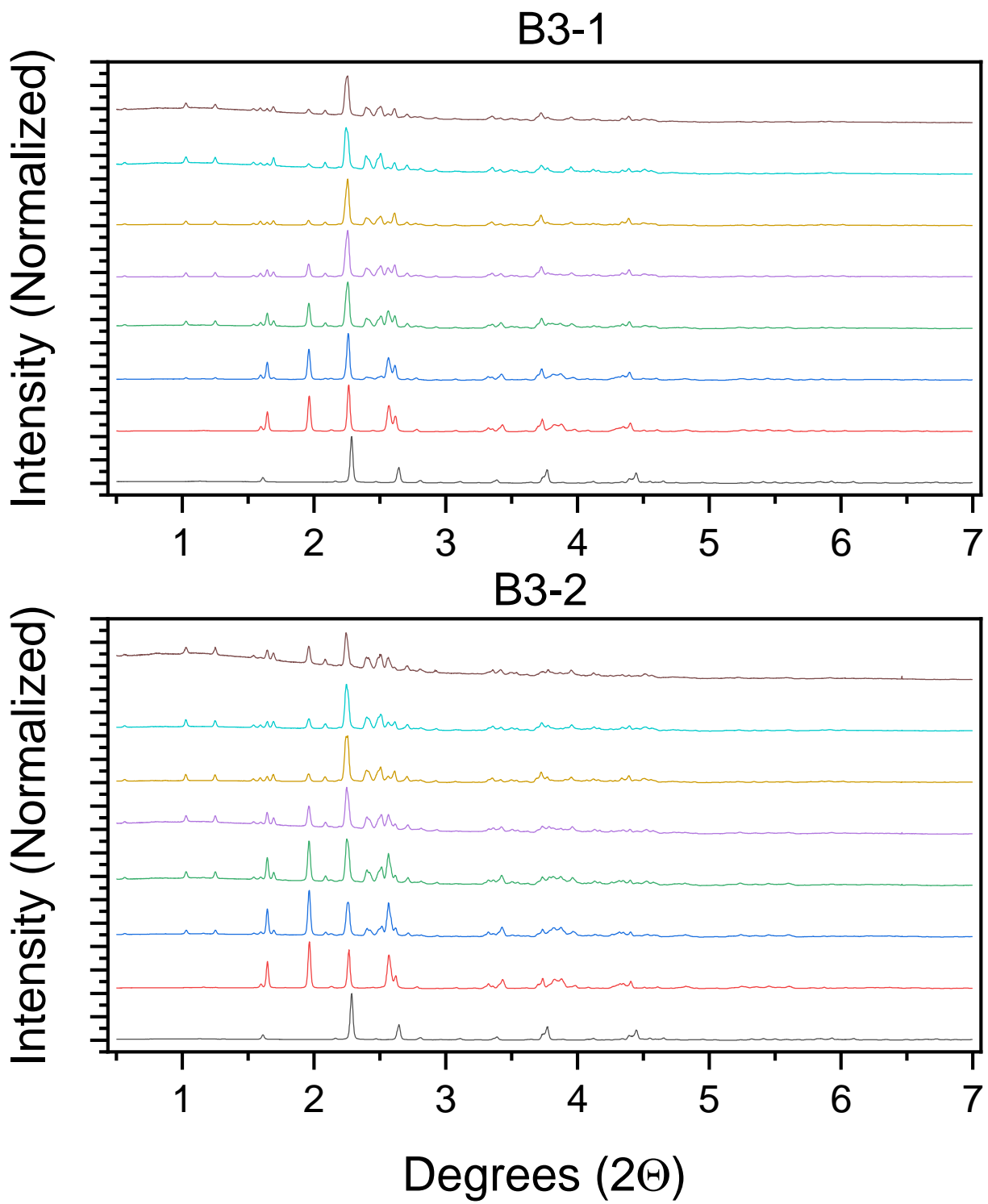
8 Appendix B: Beamline Scans

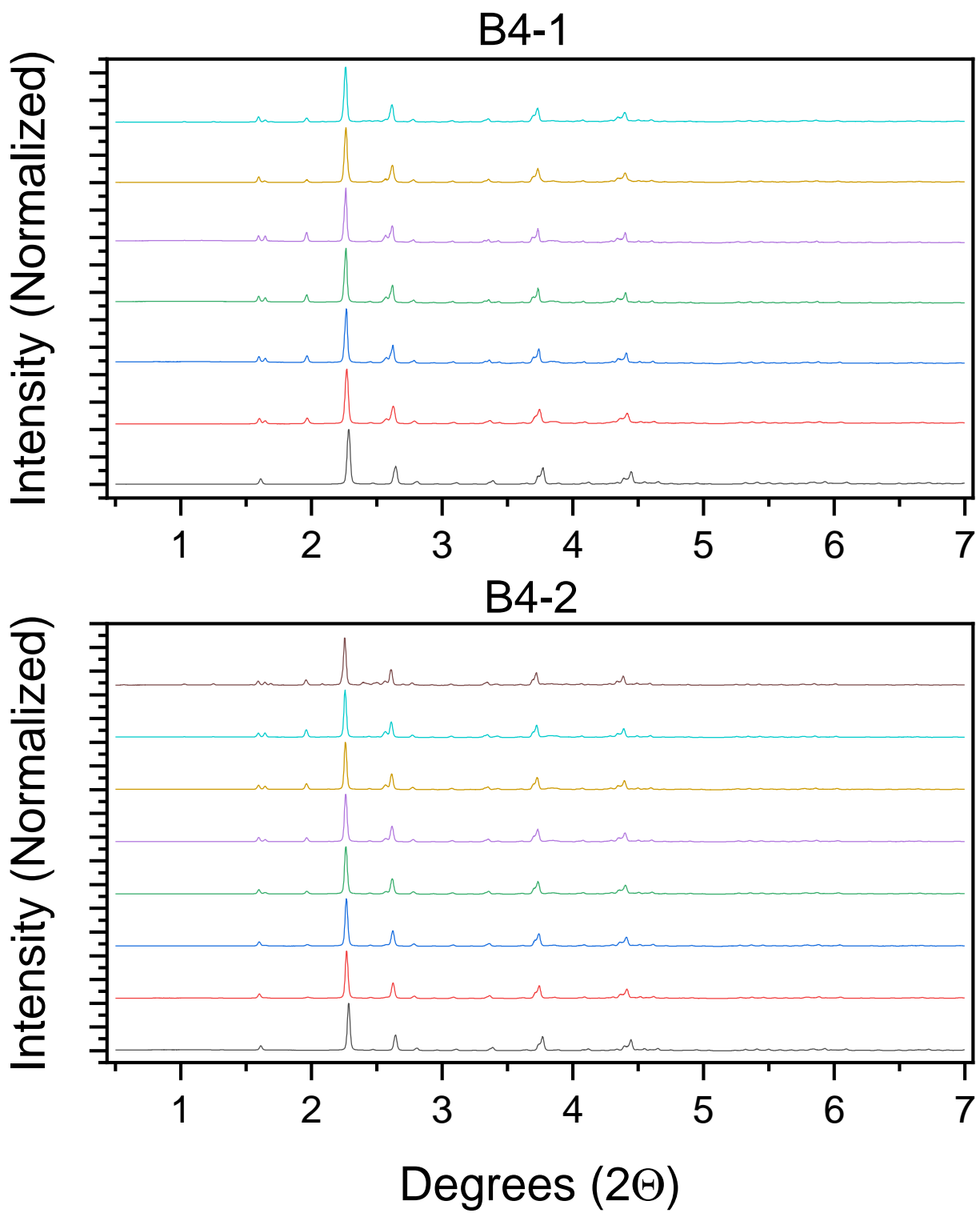
8.1 Binary Composition Scans

8.1.1 B1: 10 mol% B_2O_3 & 90 mol% Yb_2O_3

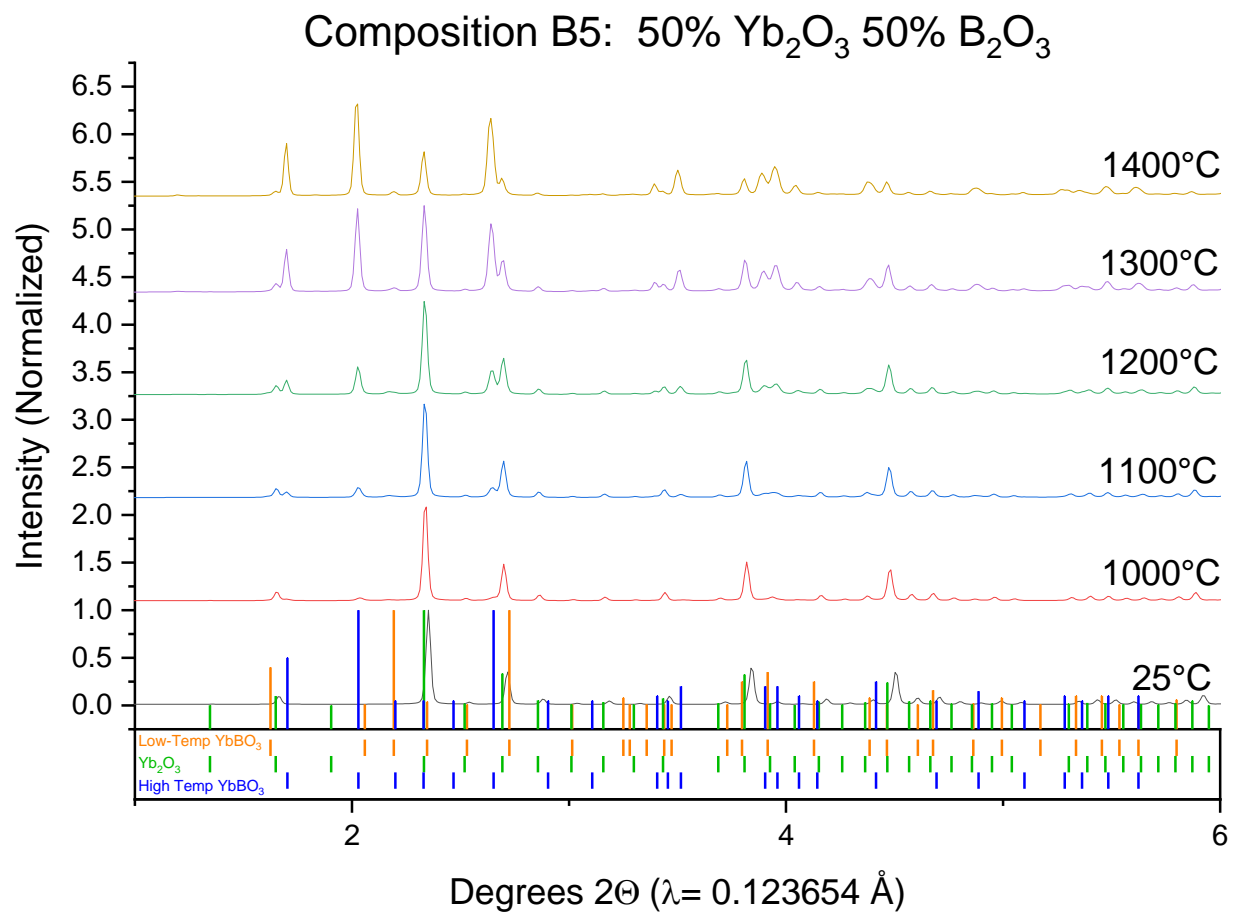






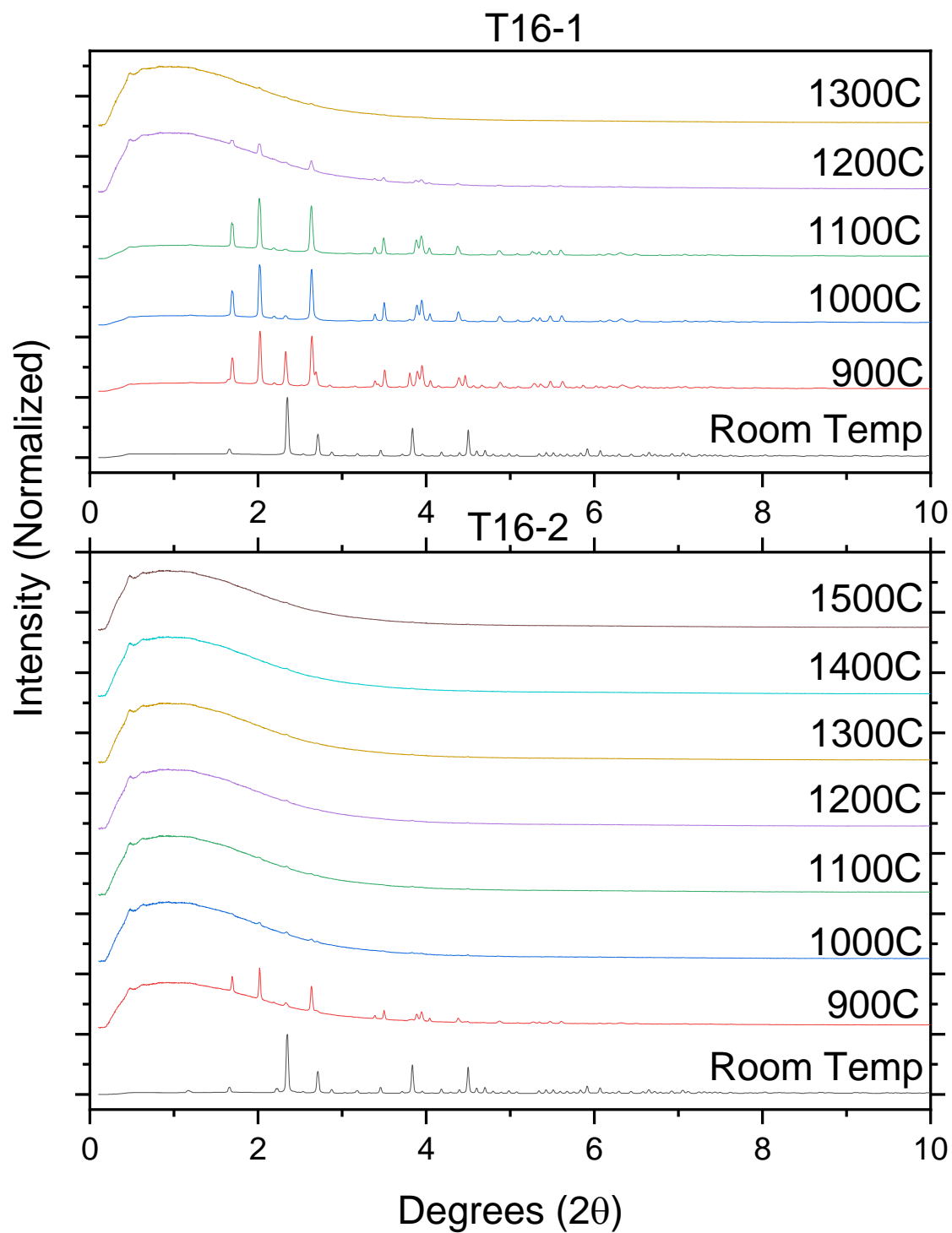


8.1.5 B5: 50 mol% B₂O₃ & 50 mol% Yb₂O₃

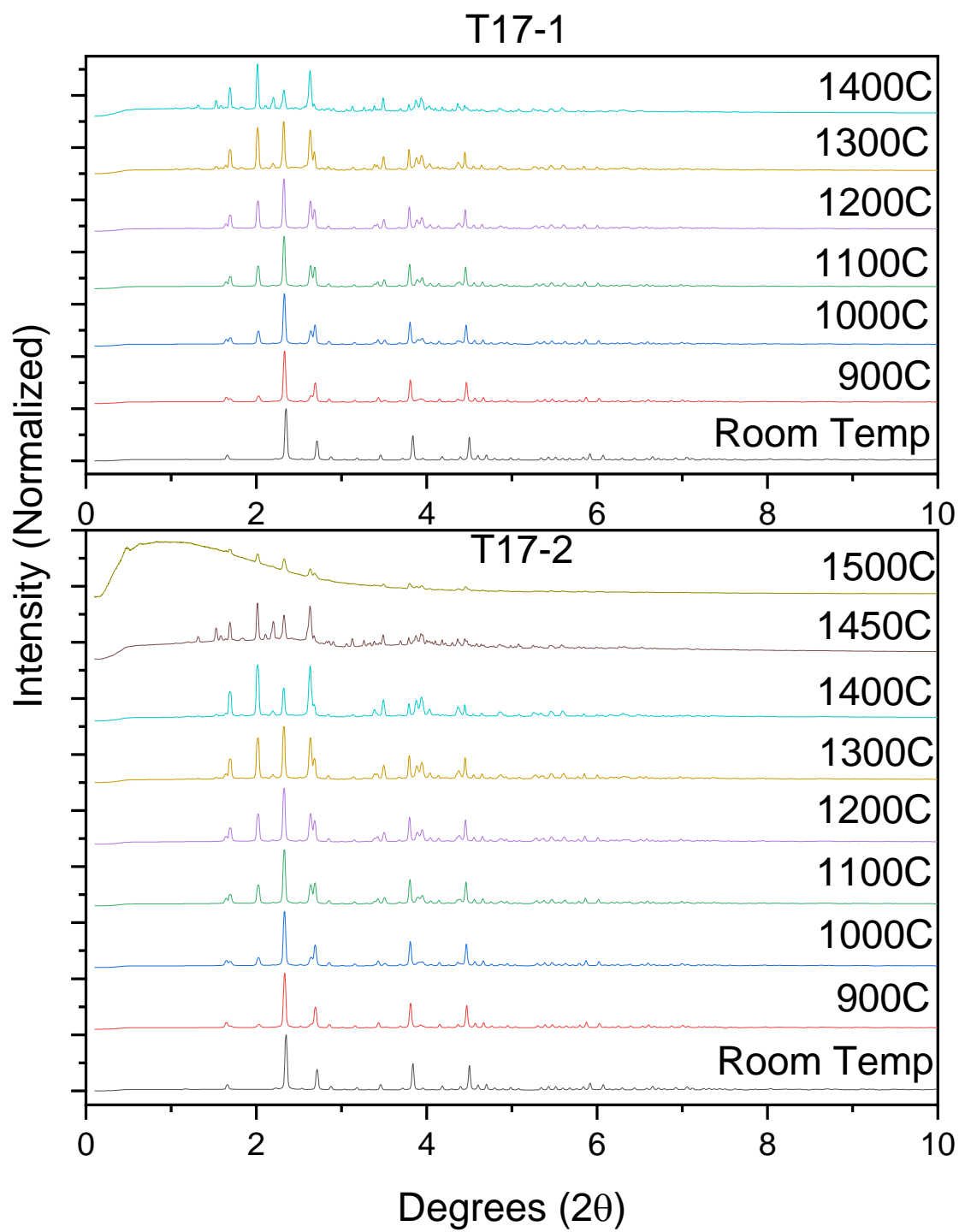


8.2 Ternary Composition Scans

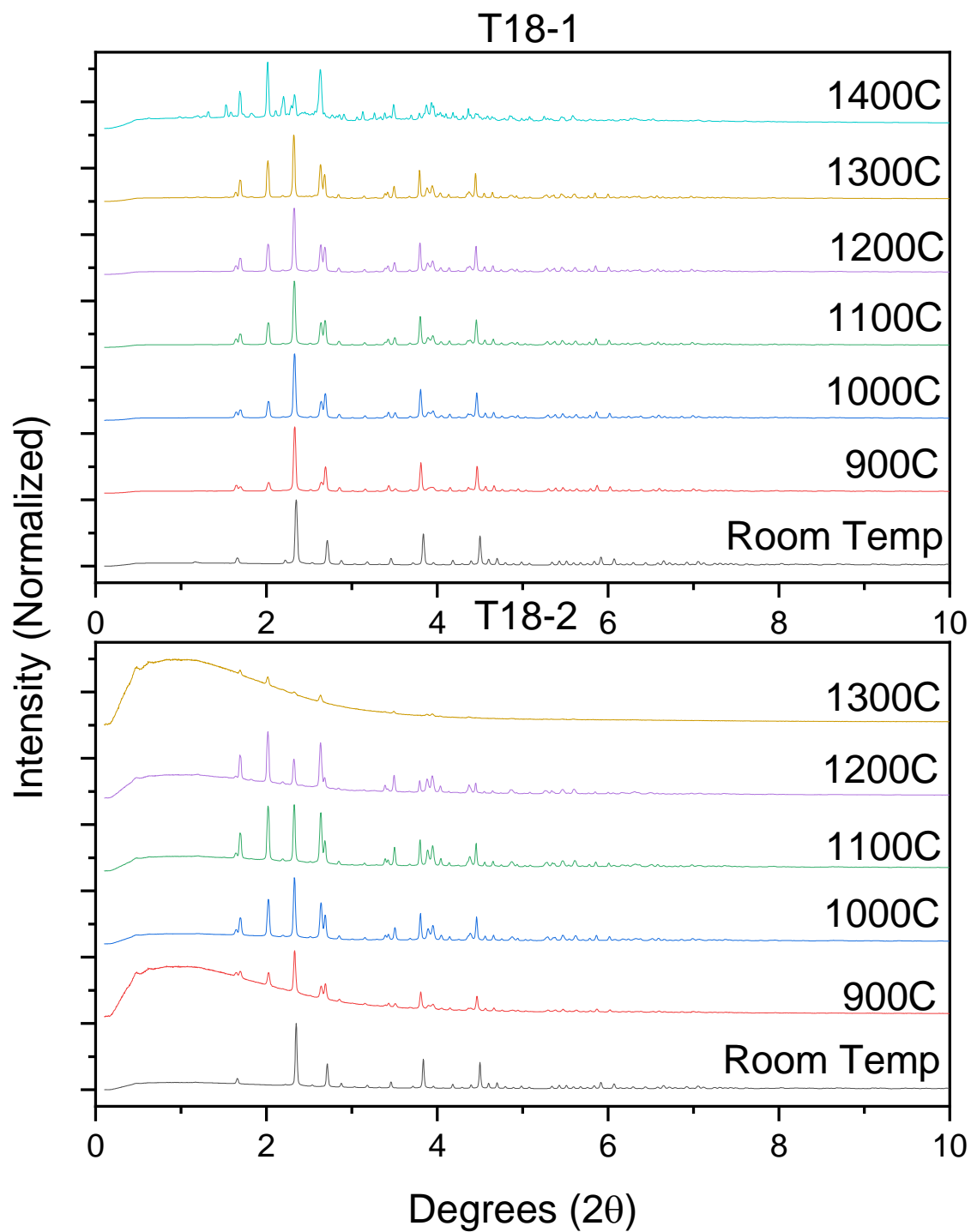
8.2.1 T16: 30% B₂O₃, 60% SiO₂, 10% Yb₂O₃



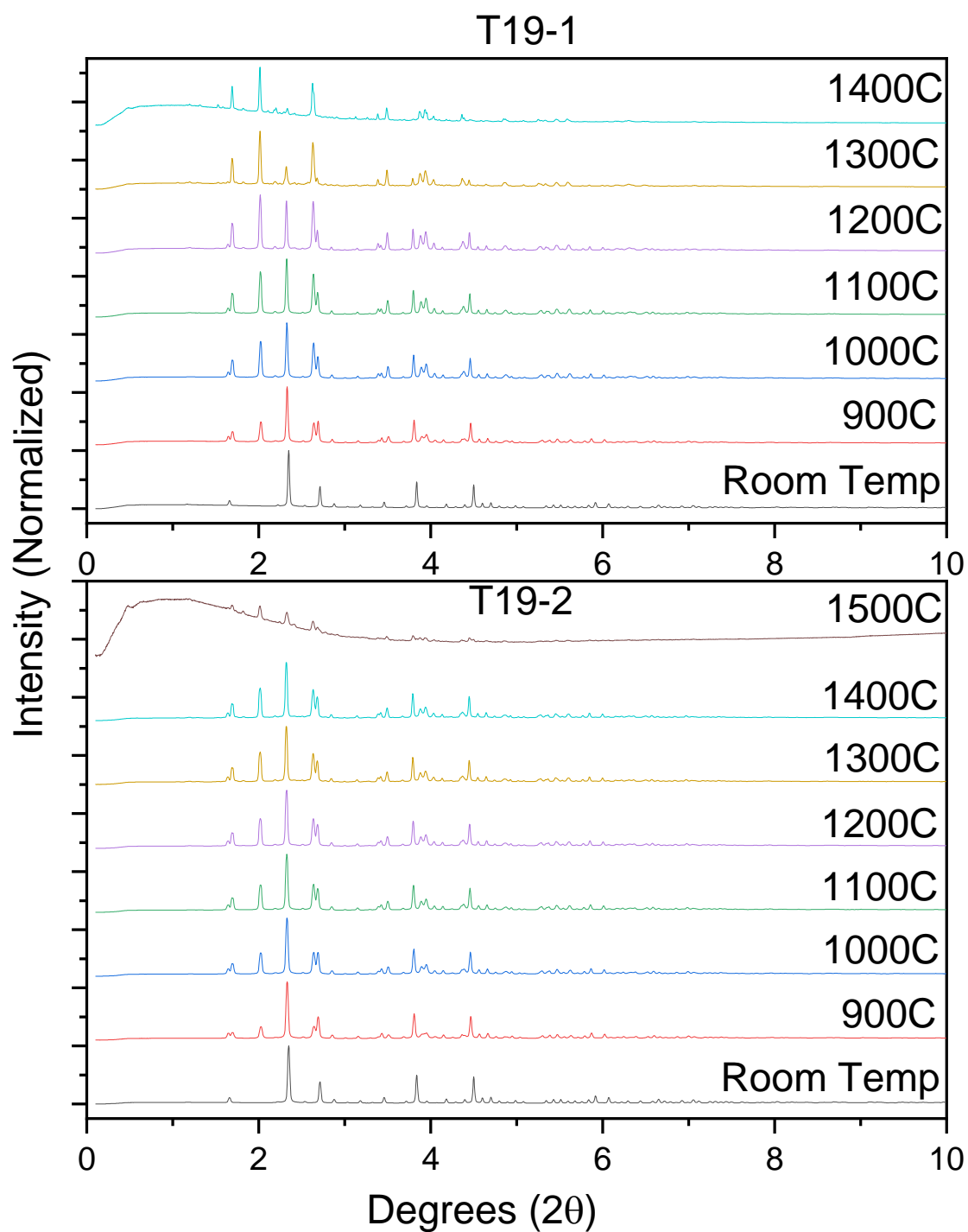
8.2.2 T17: 30% B₂O₃, 50% SiO₂, 20% Yb₂O₃



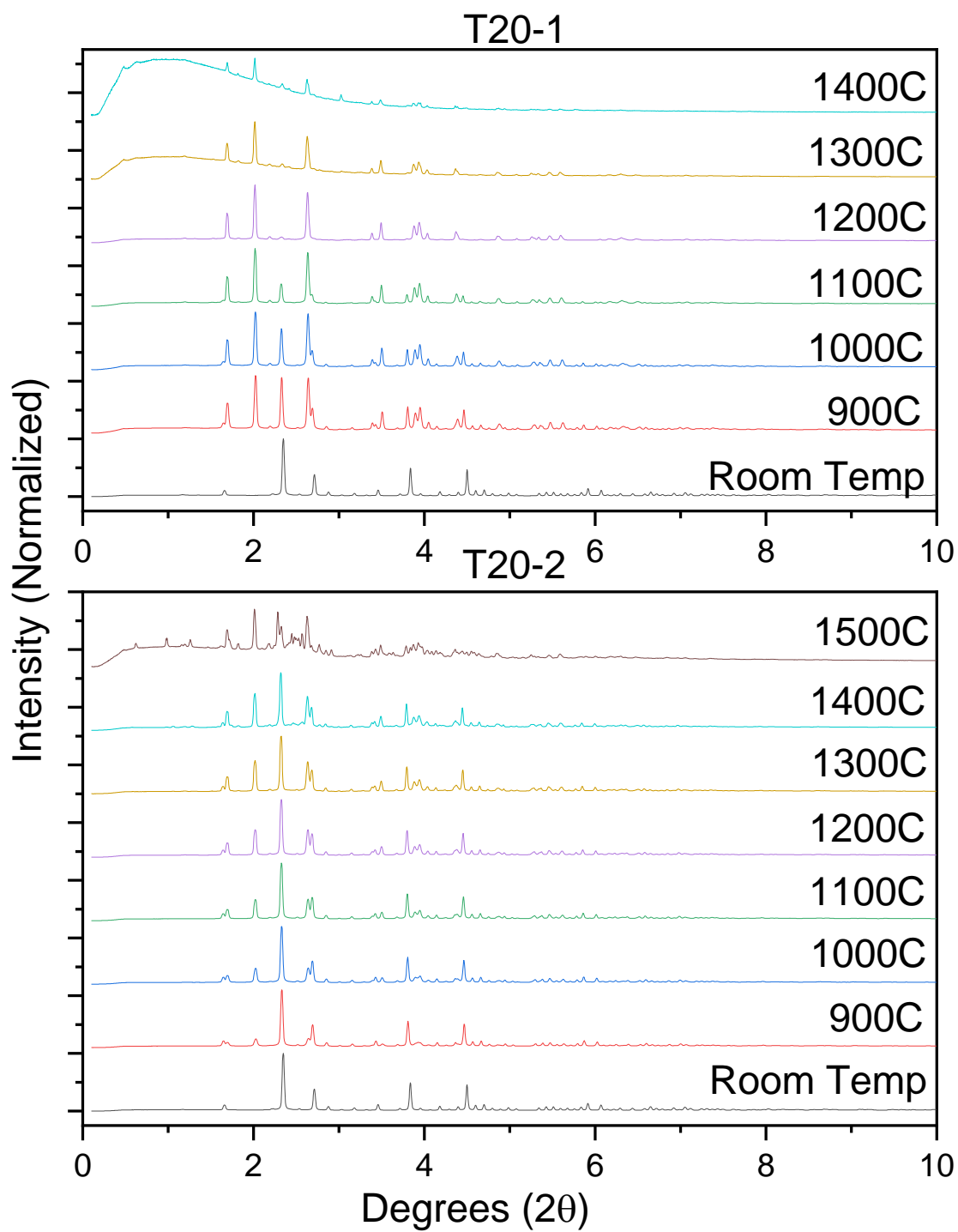
8.2.3 T18: 30% B₂O₃, 40% SiO₂, 30% Yb₂O₃



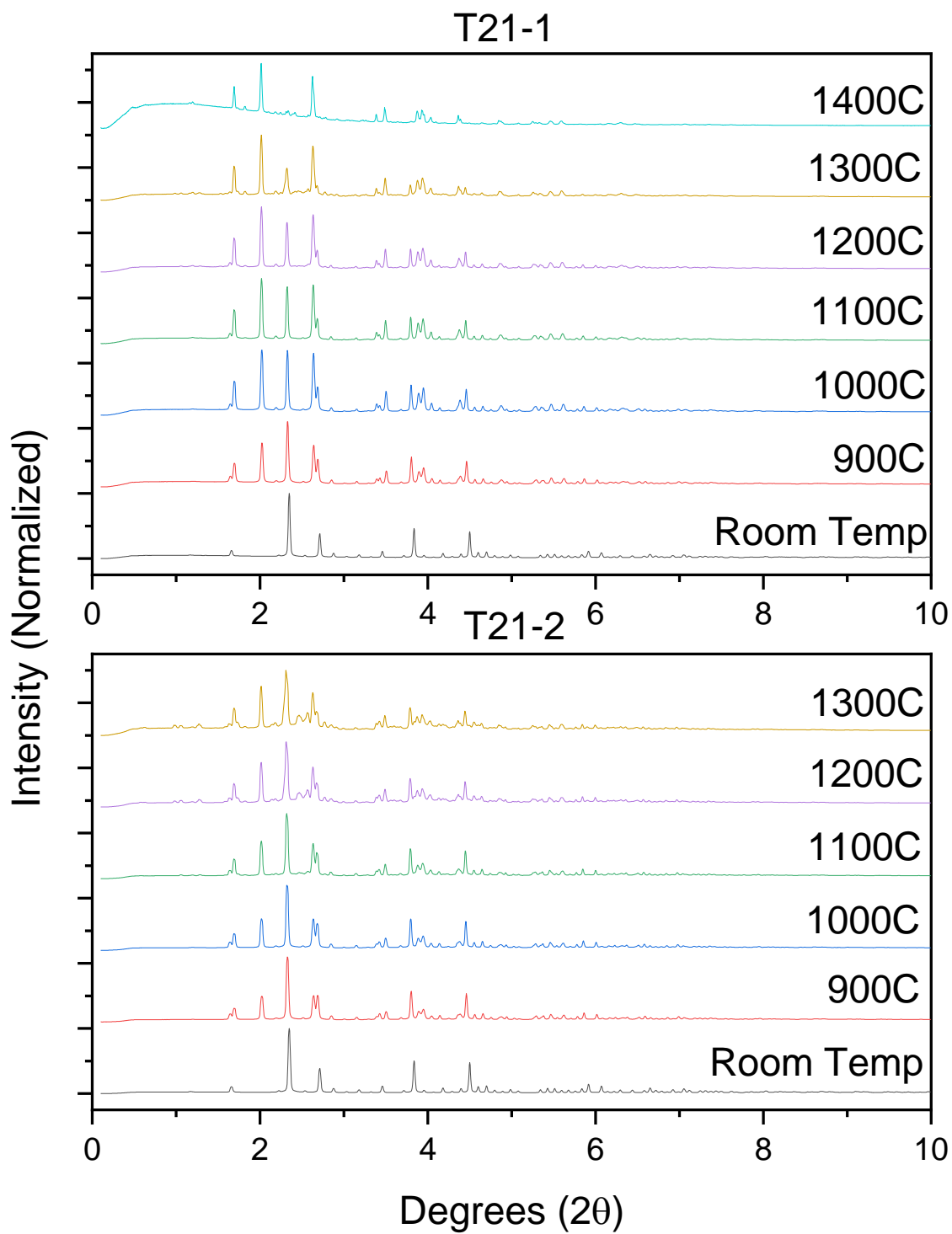
8.2.4 T19: 30% B₂O₃, 30% SiO₂, 40% Yb₂O₃



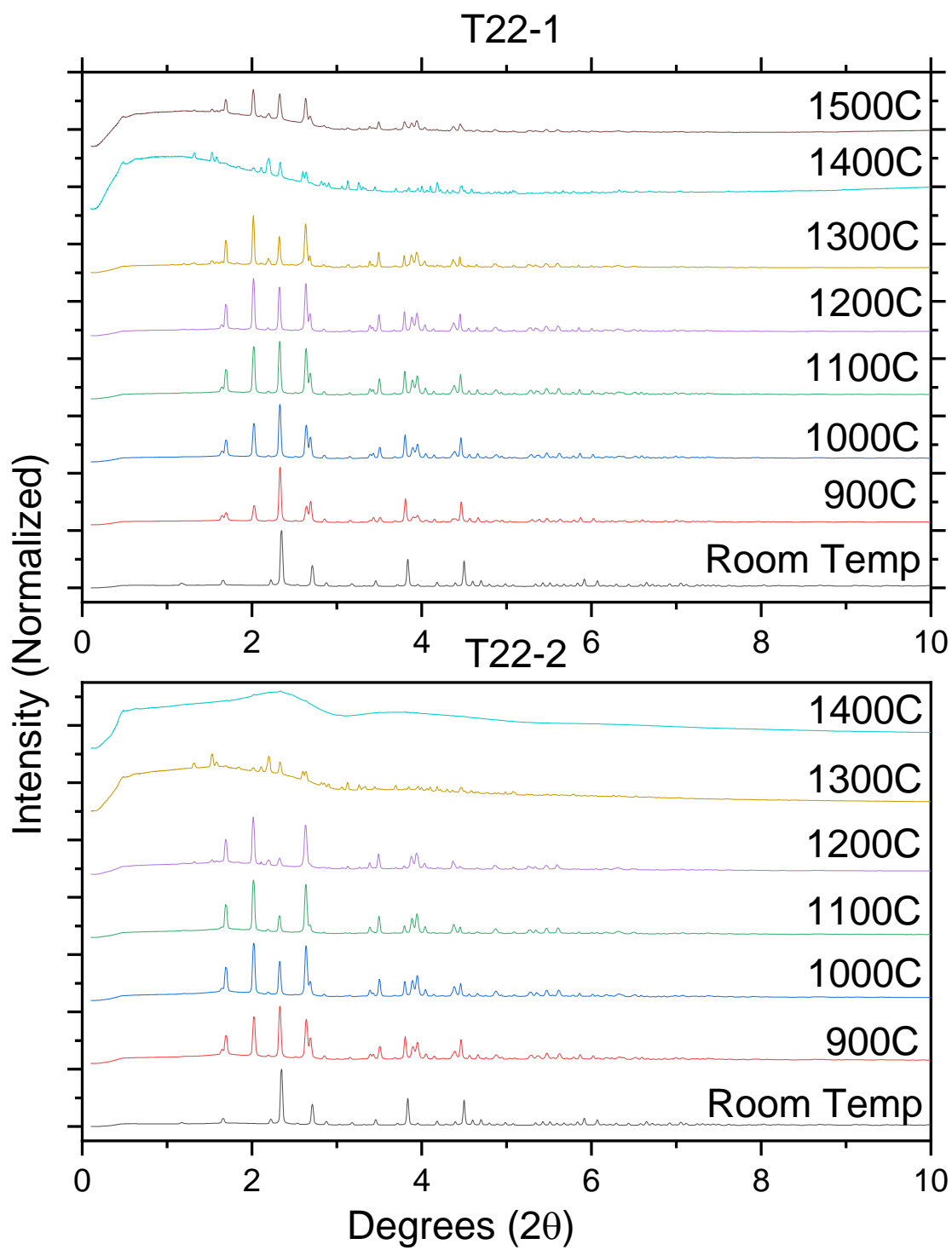
8.2.5 T20: 30% B₂O₃, 20% SiO₂, 50% Yb₂O₃



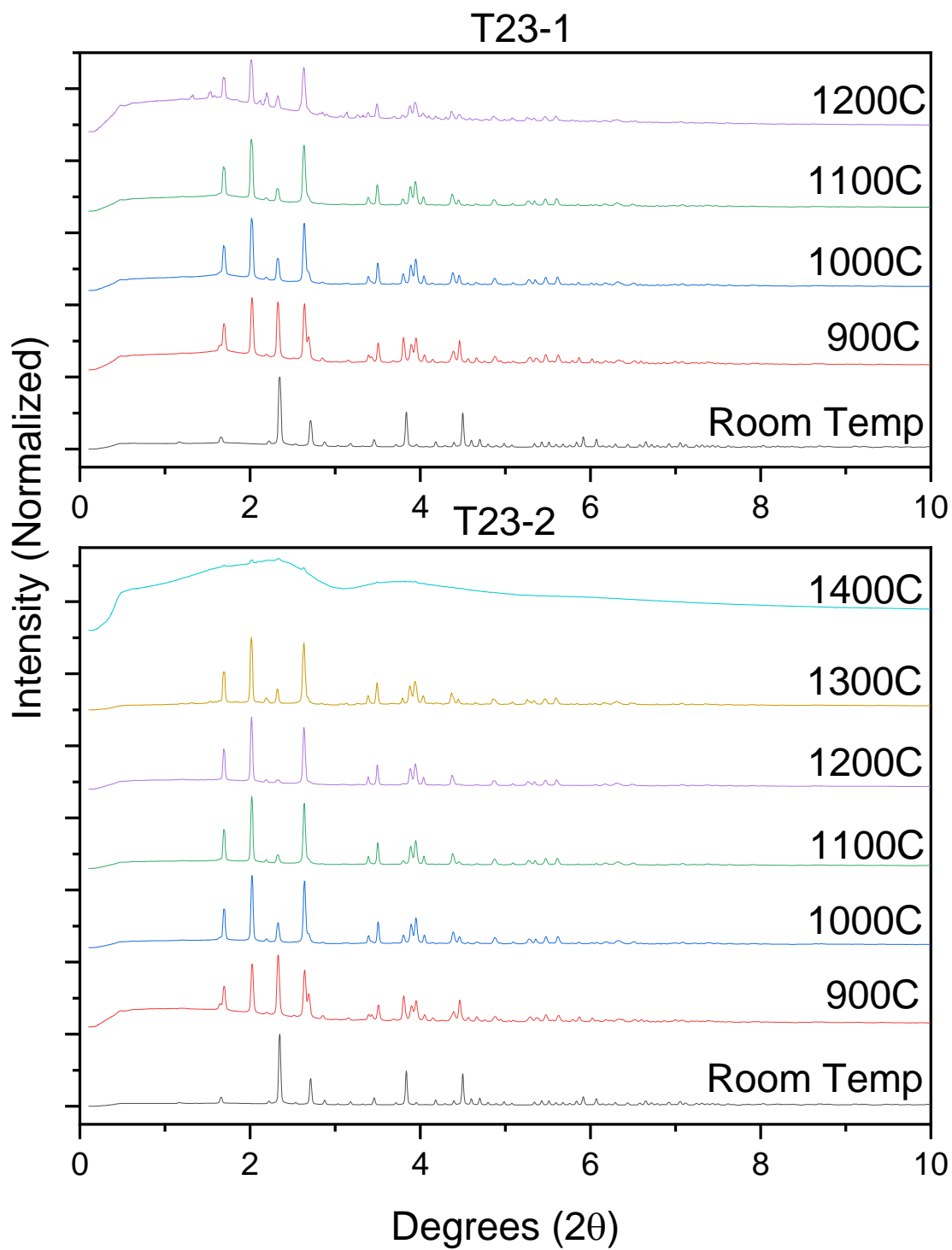
8.2.6 T21: 30% B₂O₃, 10% SiO₂, 60% Yb₂O₃



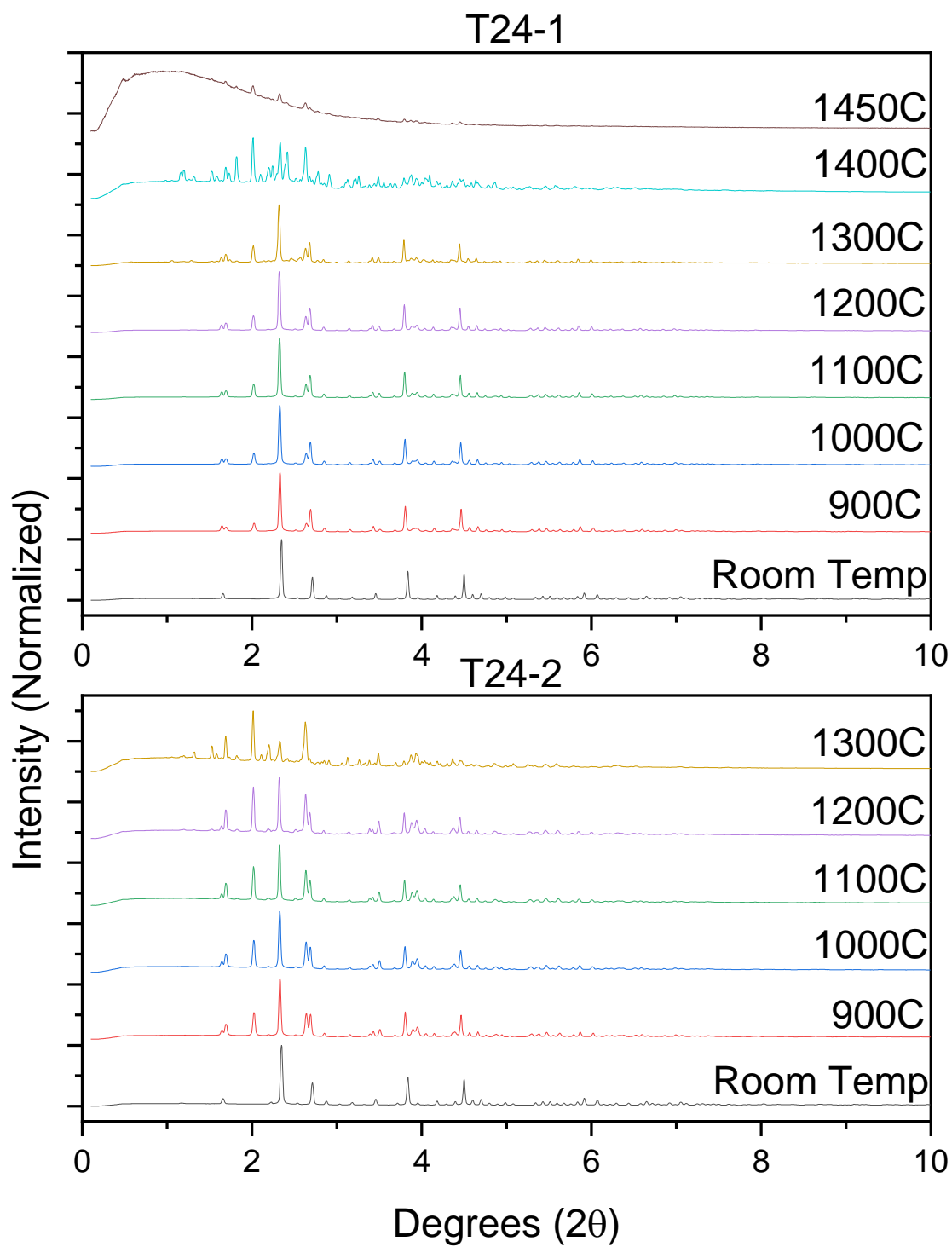
8.2.7 T22: 20% B₂O₃, 70% SiO₂, 10% Yb₂O₃

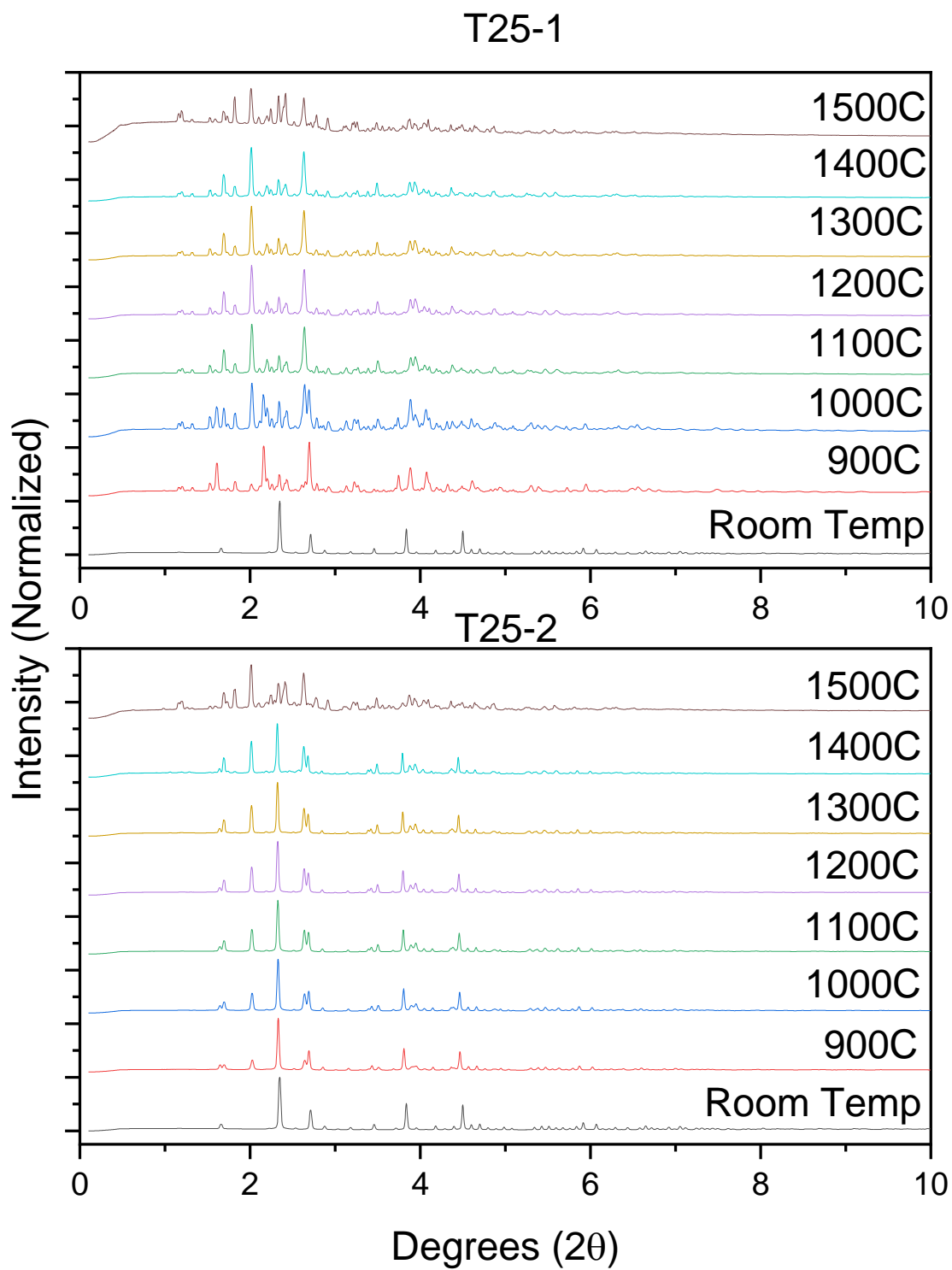


8.2.8 T23: 20% B₂O₃, 60% SiO₂, 20% Yb₂O₃

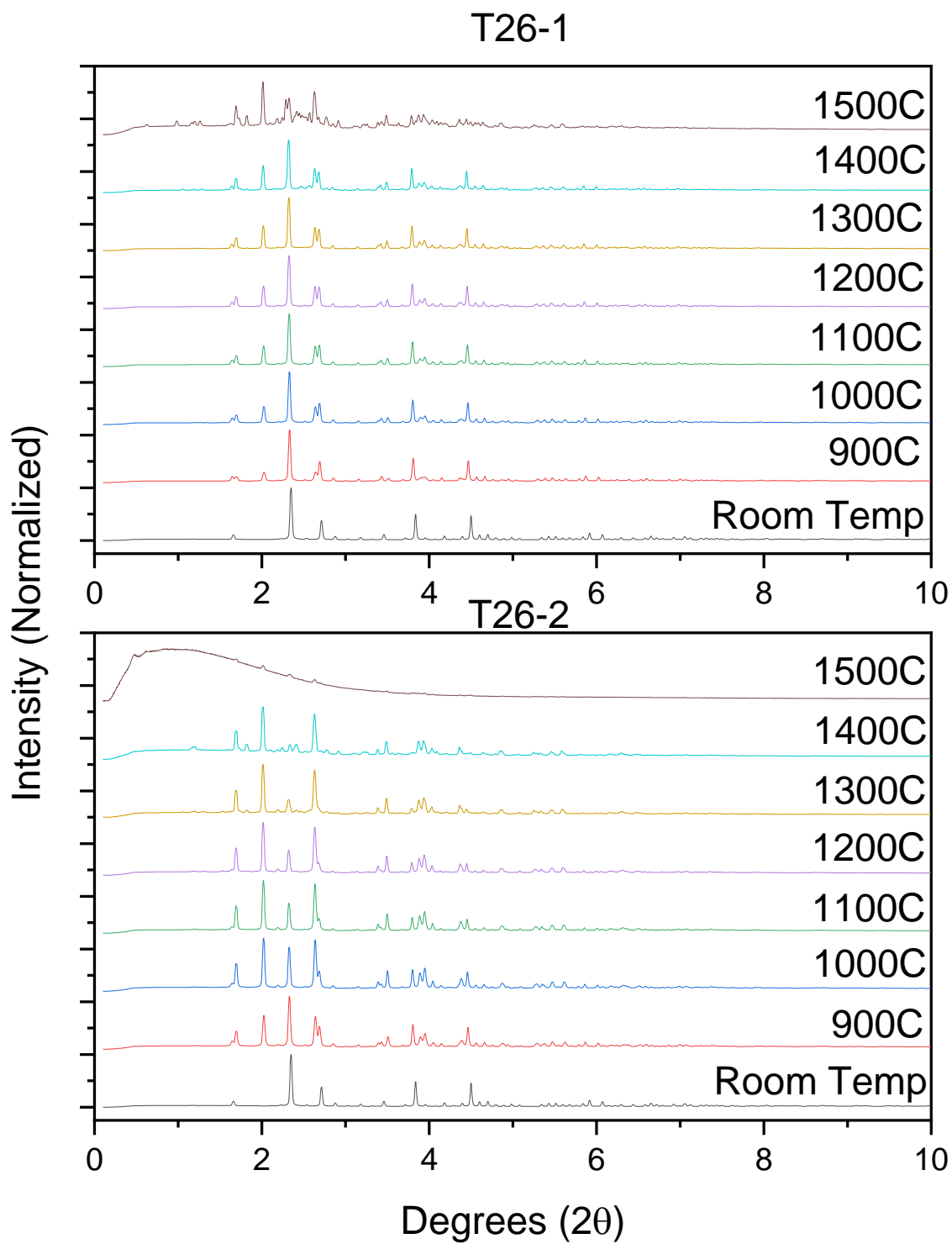


8.2.9 T24: 20% B₂O₃, 50% SiO₂, 30% Yb₂O₃

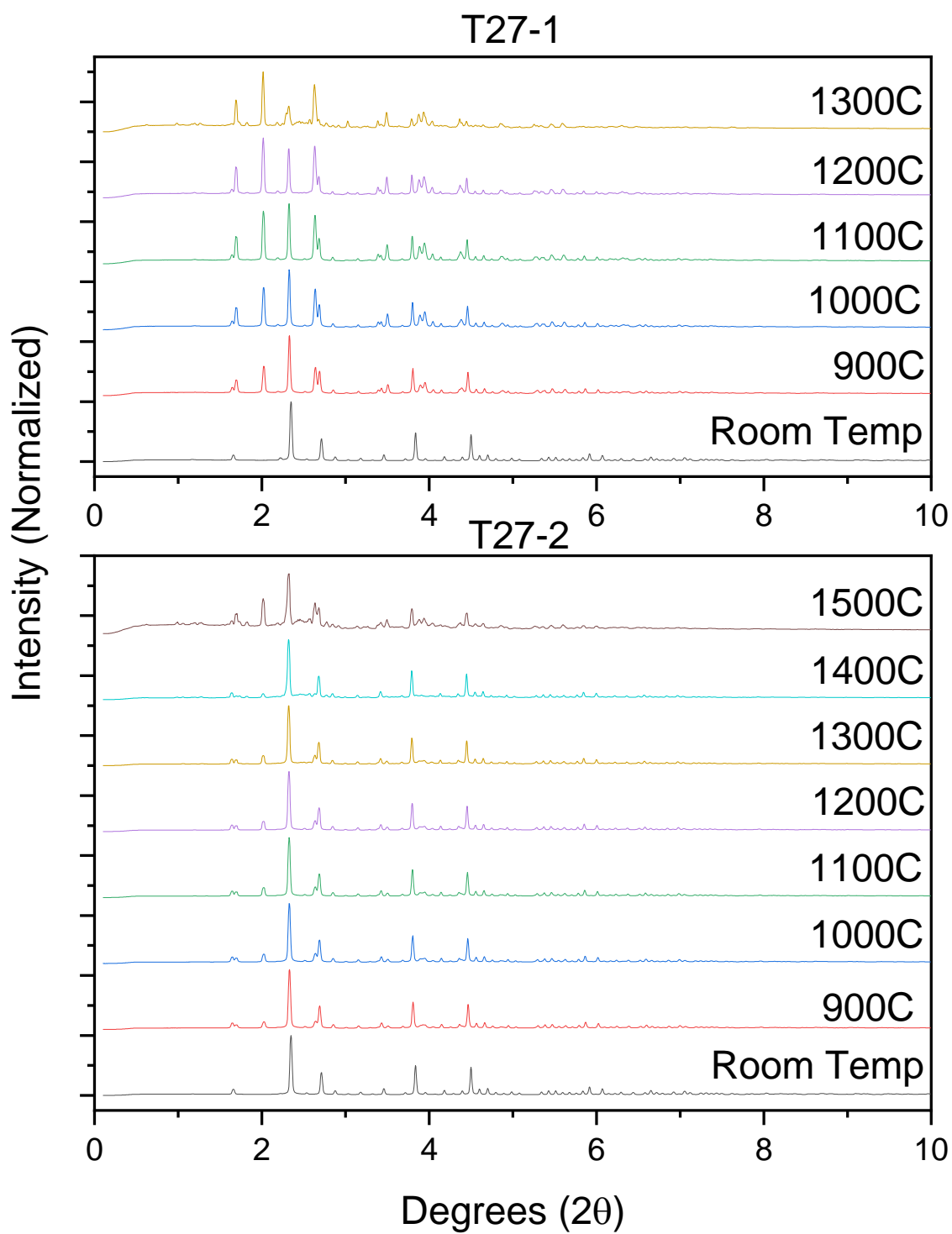




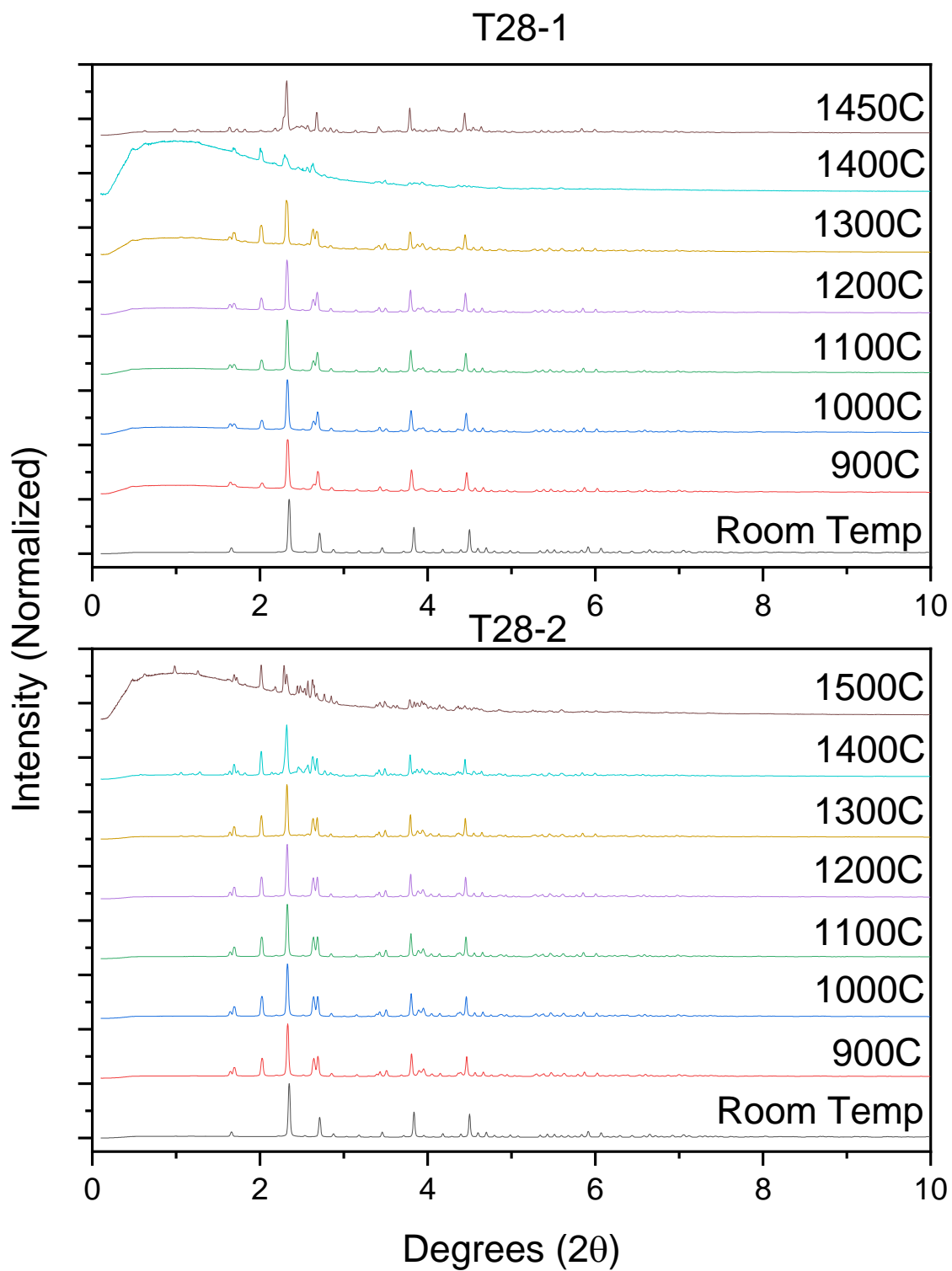
8.2.11 T26: 20% B₂O₃, 30% SiO₂, 50% Yb₂O₃

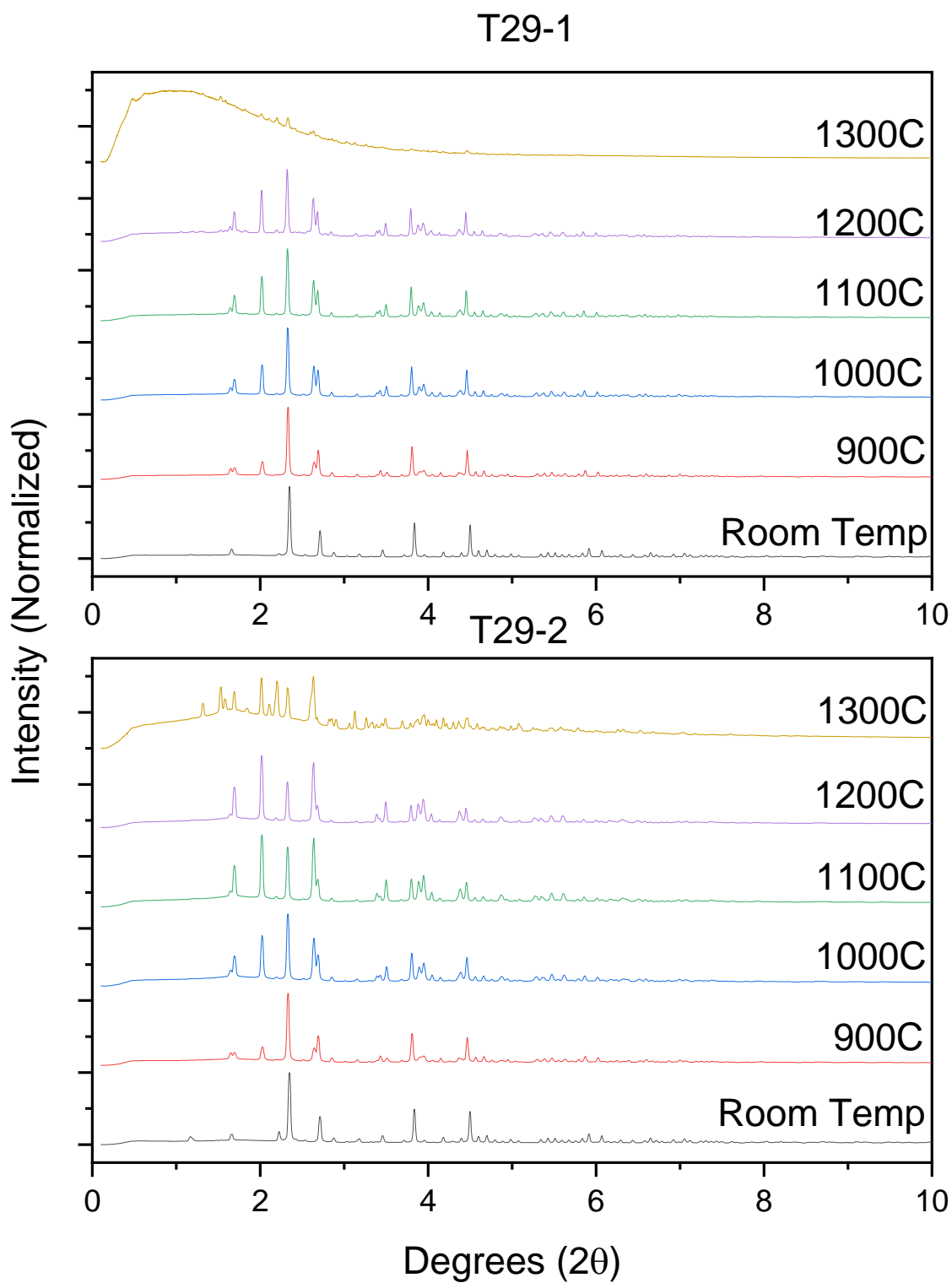


8.2.12 T27: 20% B₂O₃, 20% SiO₂, 60% Yb₂O₃

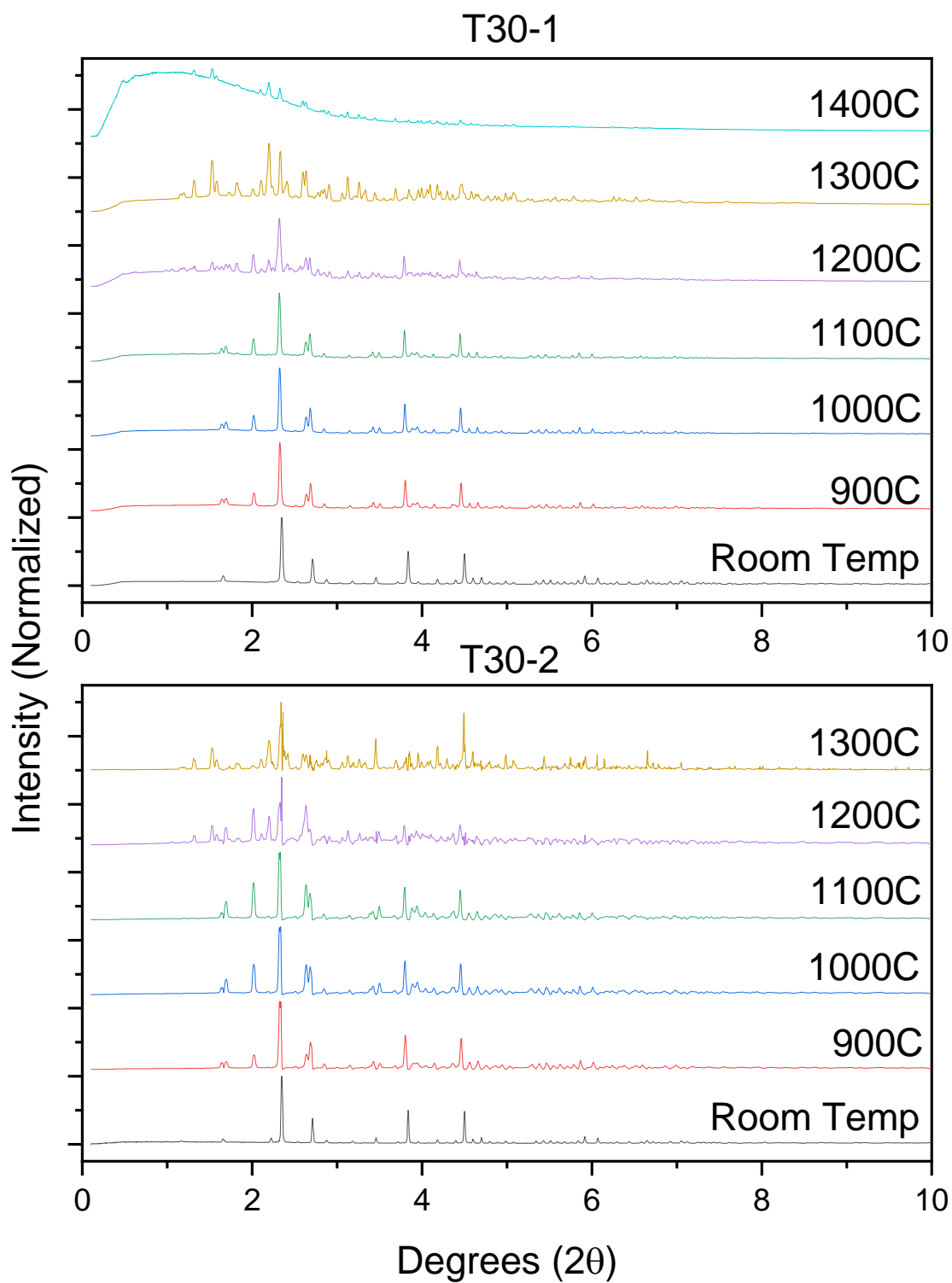


8.2.13 T28: 20% B₂O₃, 10% SiO₂, 70% Yb₂O₃

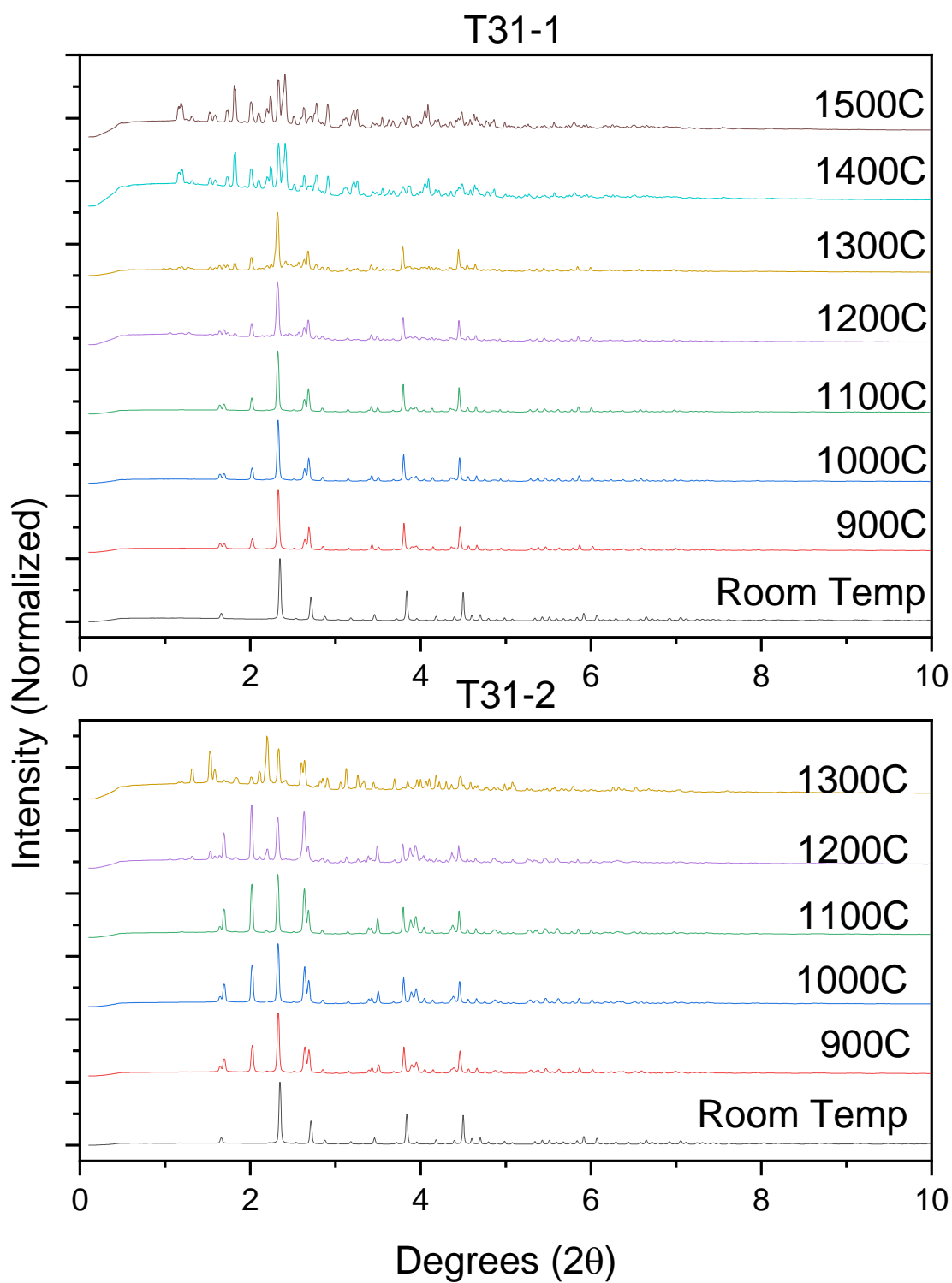




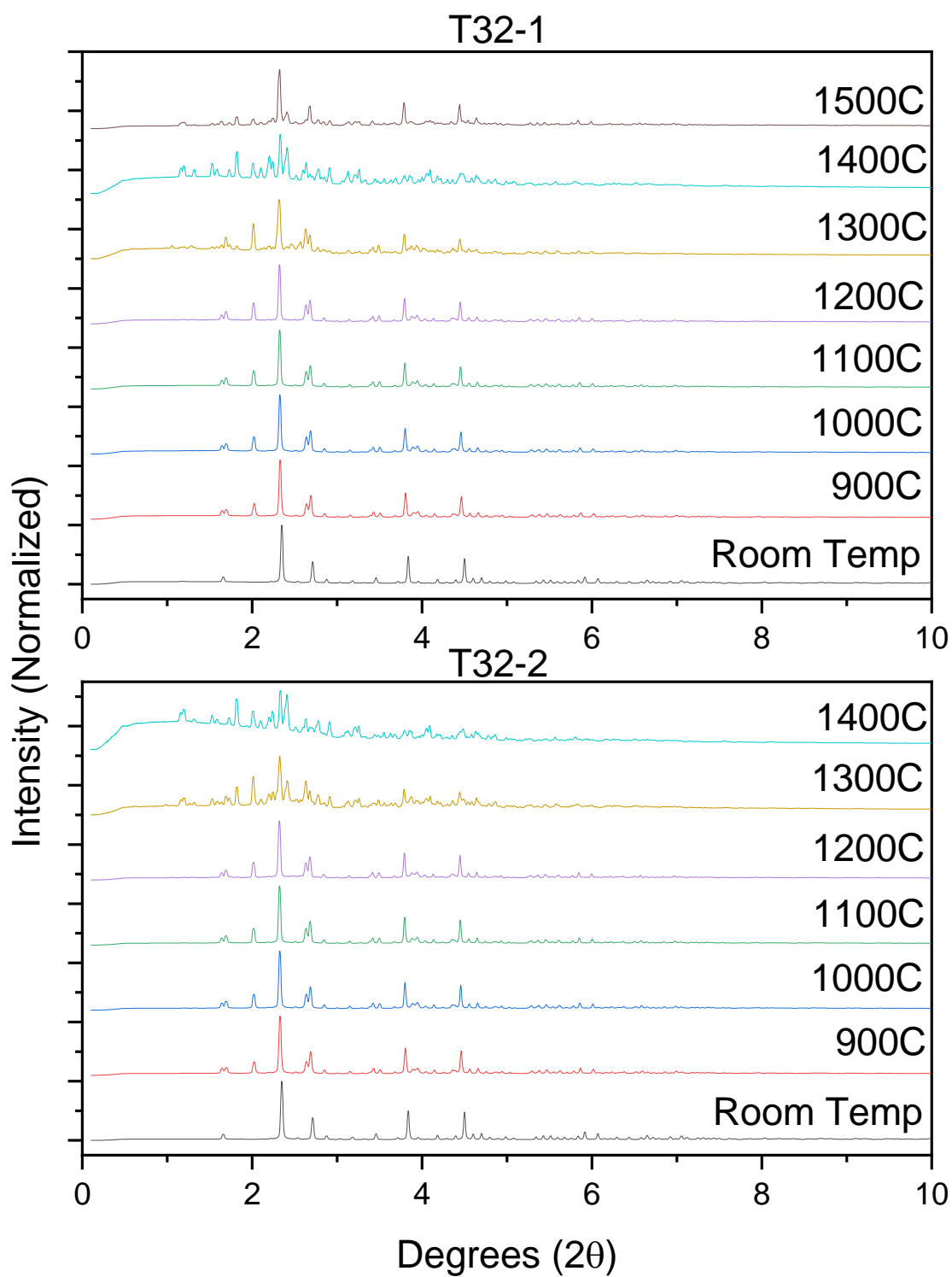
8.2.15 T30: 10% B₂O₃, 70% SiO₂, 20% Yb₂O₃



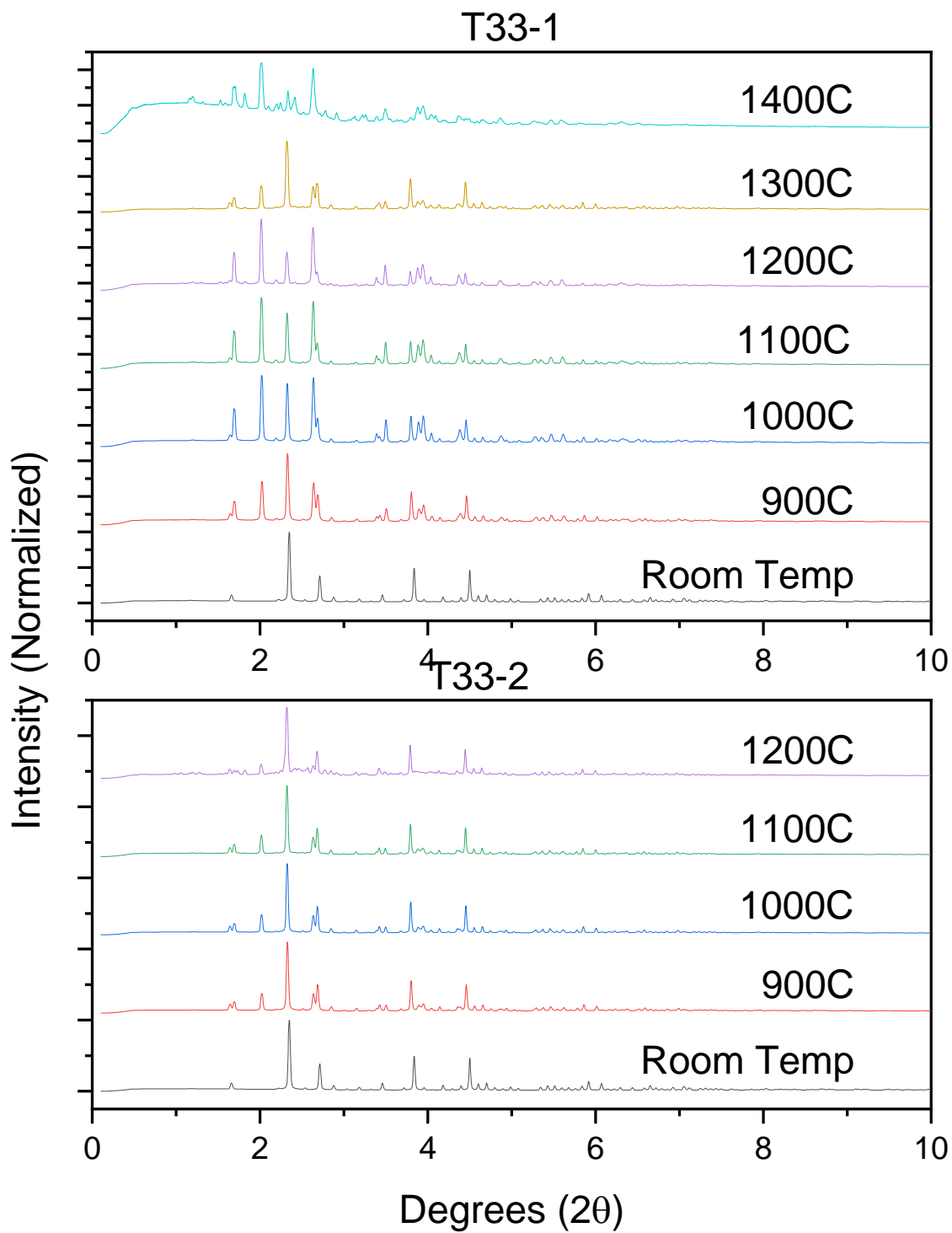
8.2.16 T31: 10% B₂O₃, 60% SiO₂, 30% Yb₂O₃



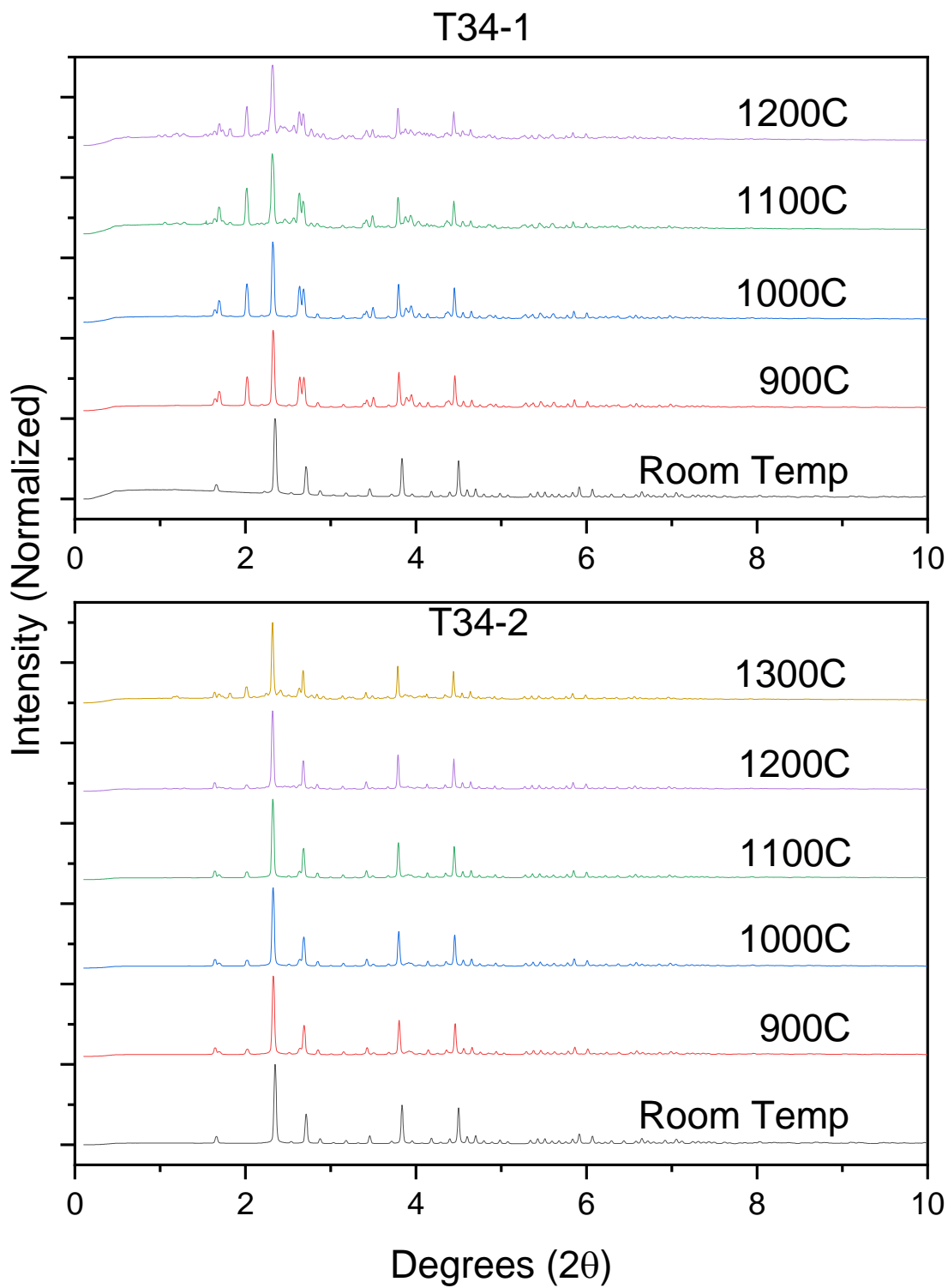
8.2.17 T32: 10% B₂O₃, 50% SiO₂, 40% Yb₂O₃



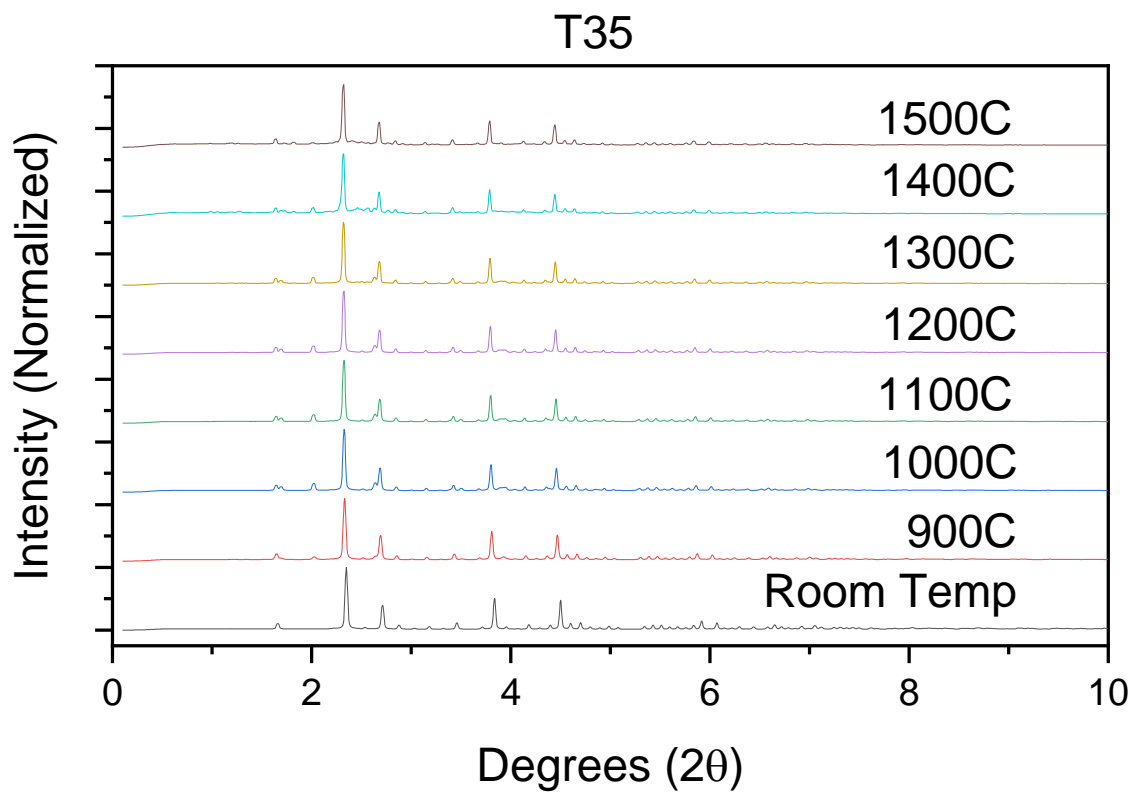
8.2.18 T33: 10% B₂O₃, 40% SiO₂, 50% Yb₂O₃



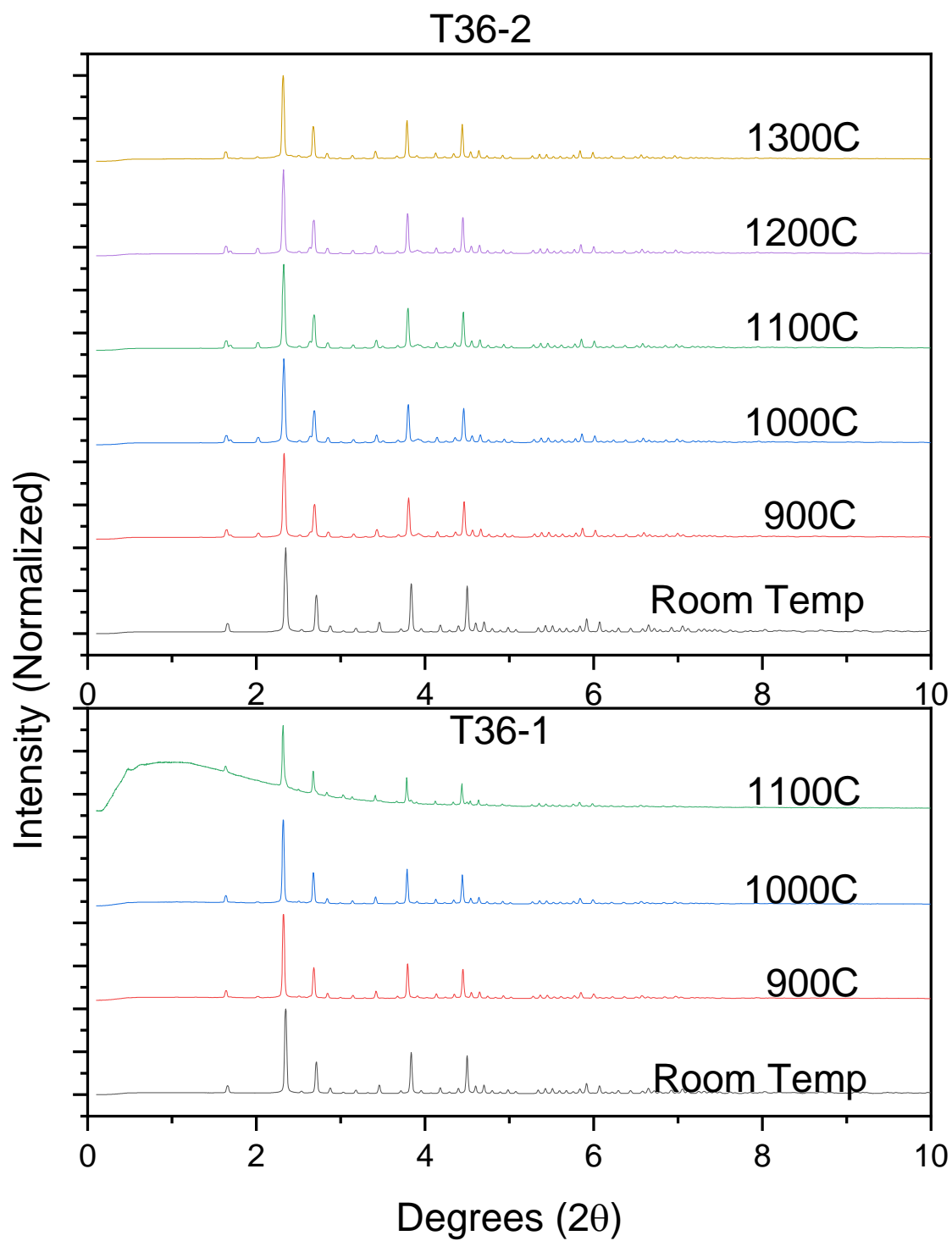
8.2.19 T34: 10% B₂O₃, 30% SiO₂, 60% Yb₂O₃



8.2.20 T35: 10% B₂O₃, 20% SiO₂, 70% Yb₂O₃



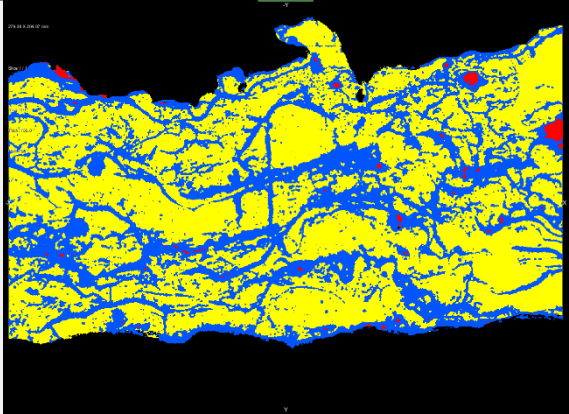
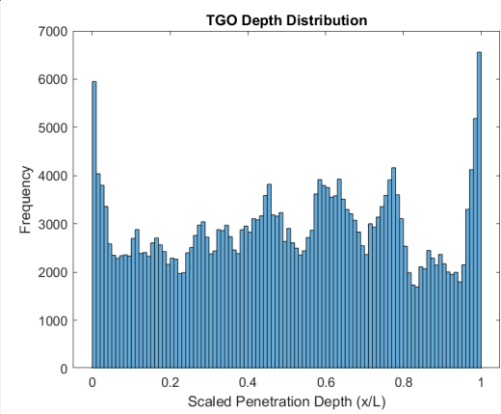
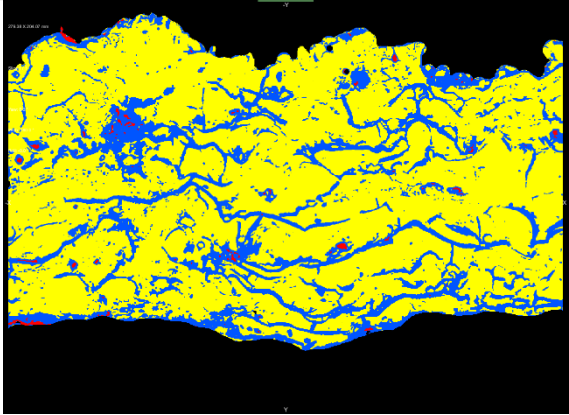
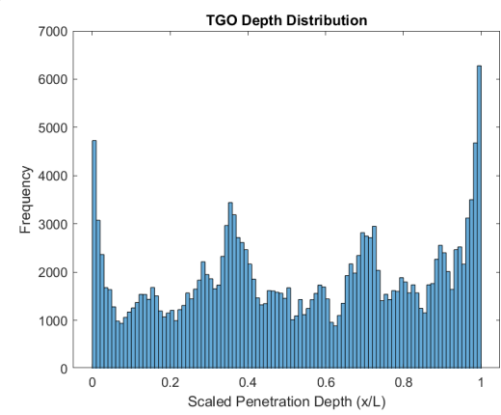
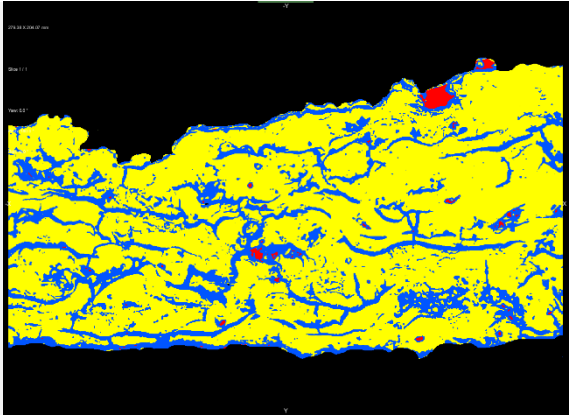
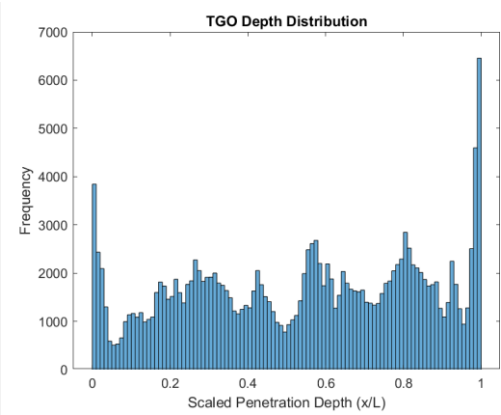
8.2.21 T36: 10% B₂O₃, 10% SiO₂, 80% Yb₂O₃



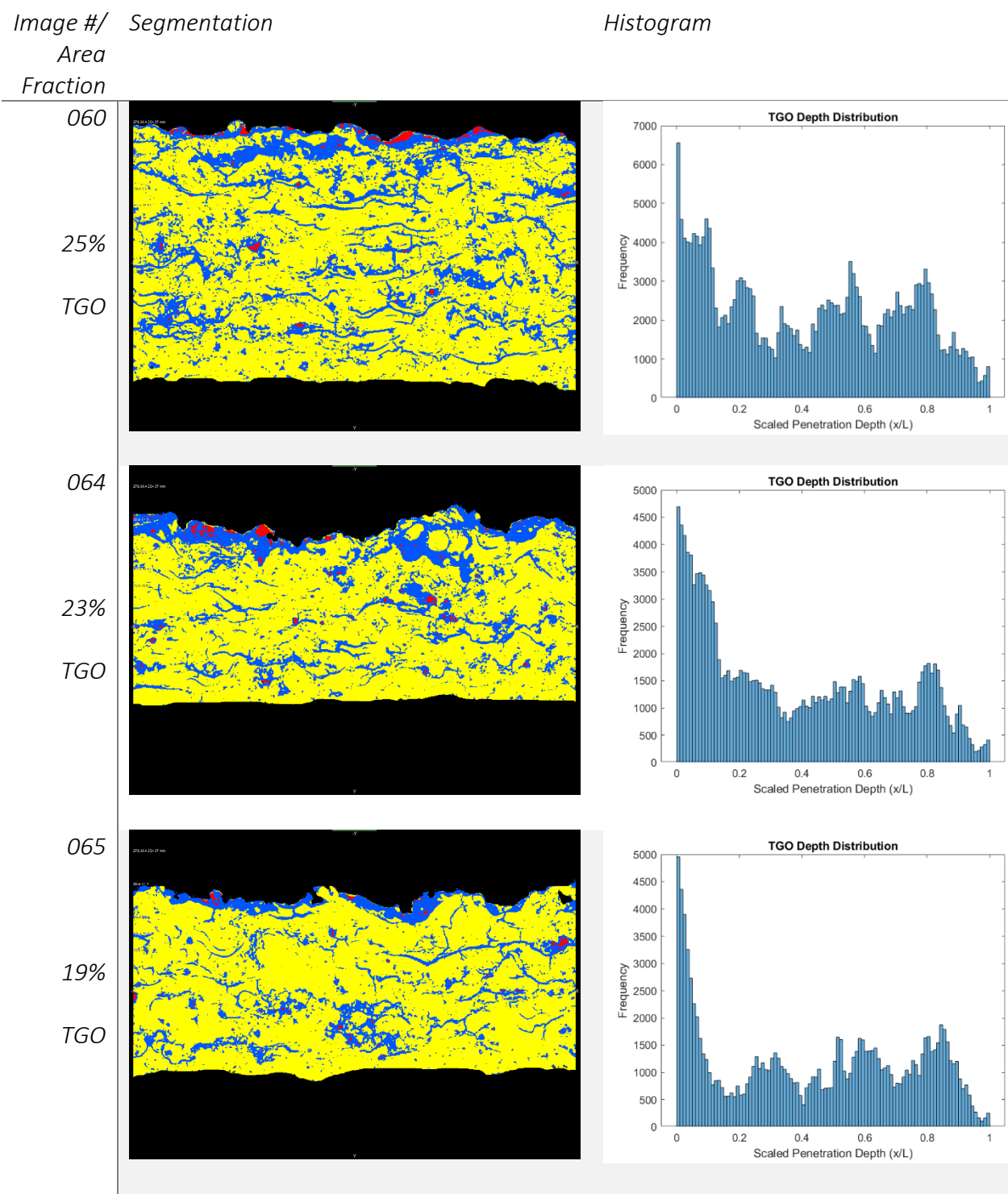
9 Appendix C: Dragonfly Segmentations for TGA & Keiser Rig Exposed Samples

9.1 900°C Exposures, 100h, 1 atm O₂

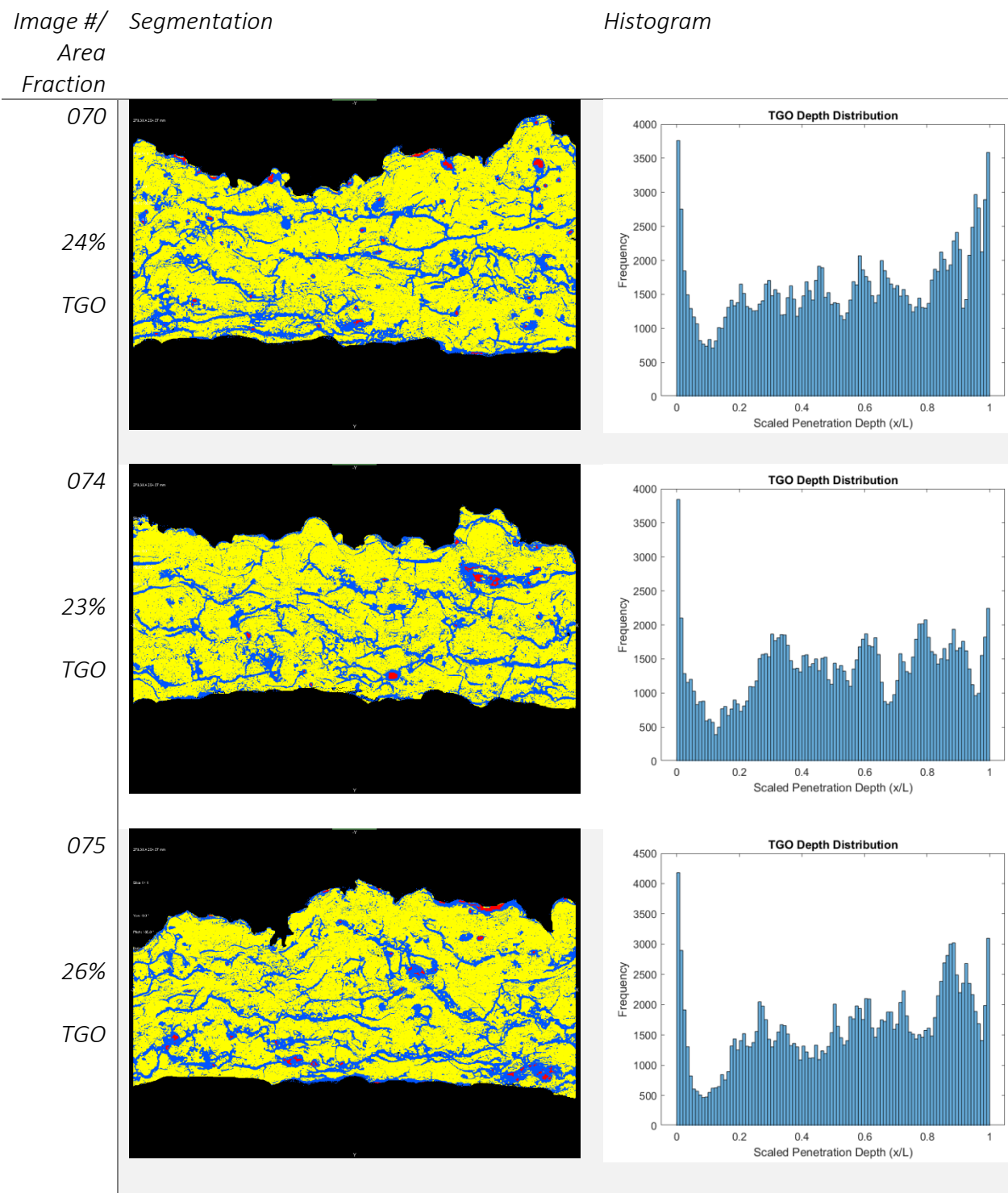
9.1.1 0%B RBSiC Sample- Keiser Rig Exposure

Image #/ Area Fraction	Segmentation	Histogram
051 38% TGO		
056 23% TGO		
057 25% TGO		

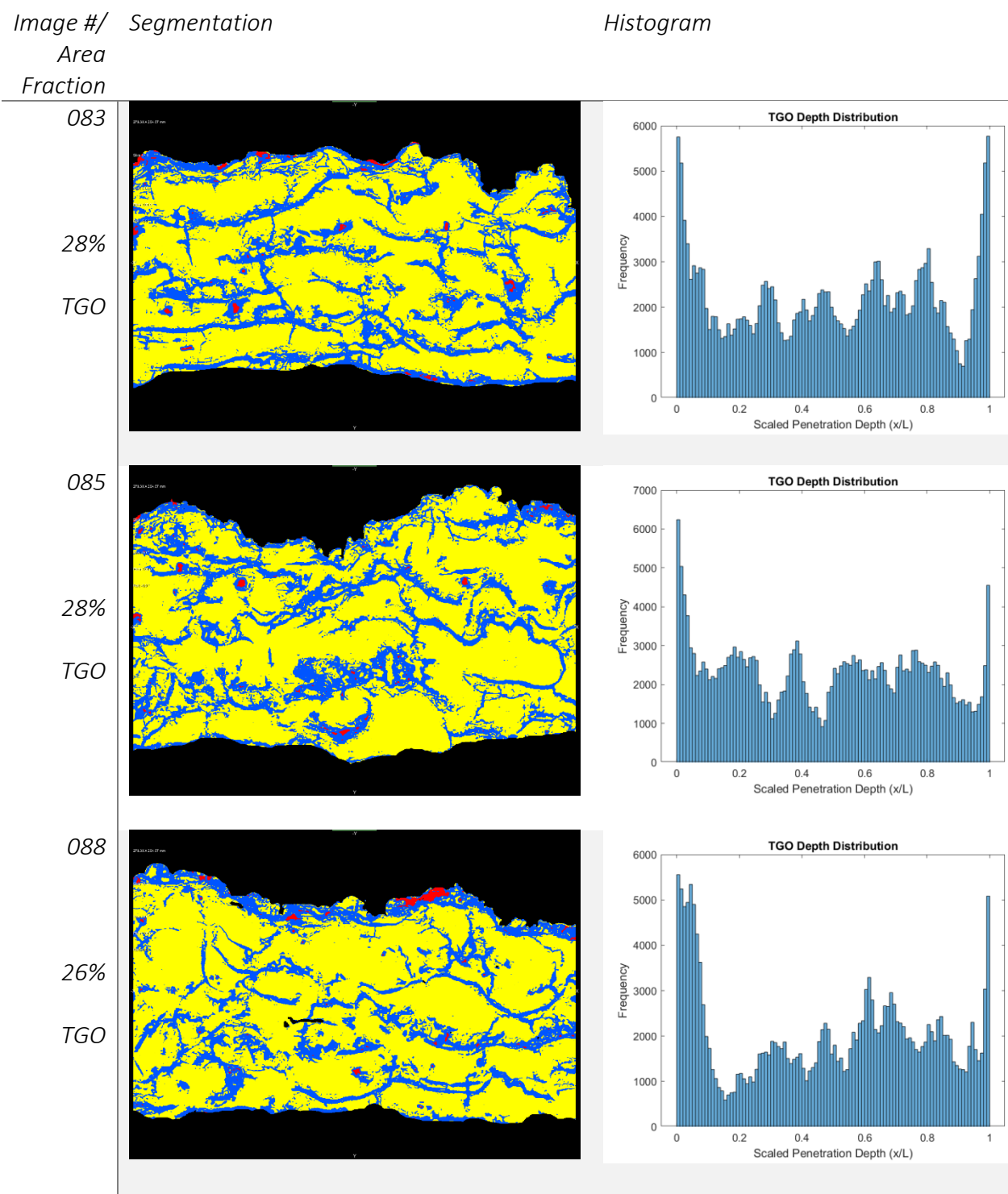
9.1.2 0%B RBSiC Sample- TGA Exposure



9.1.3 4%B RBSiC Sample- Keiser Rig Exposure

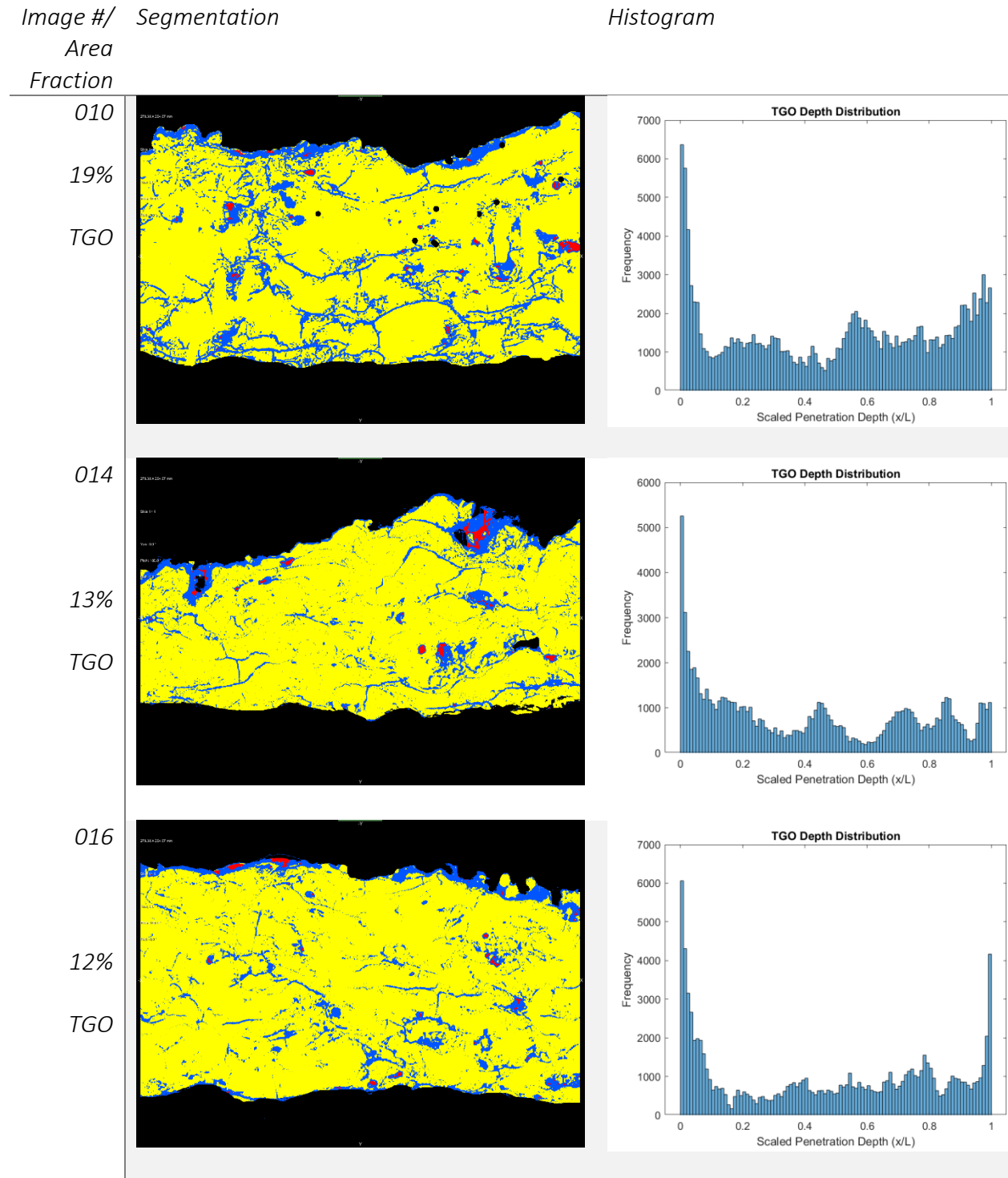


9.1.4 4%B RBSiC Sample- TGA Exposure

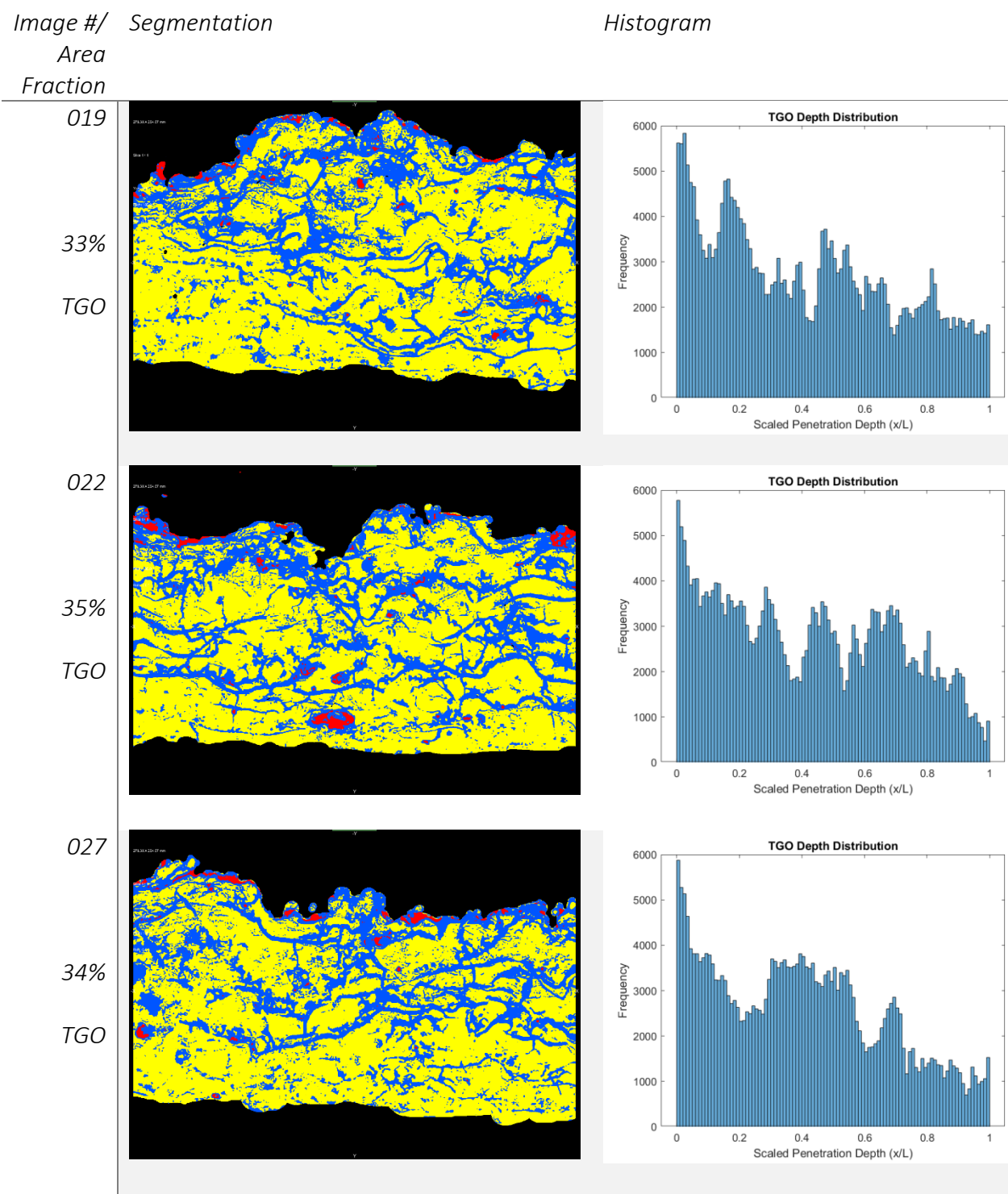


9.2 1050°C Exposures, 100h 1 atm O₂

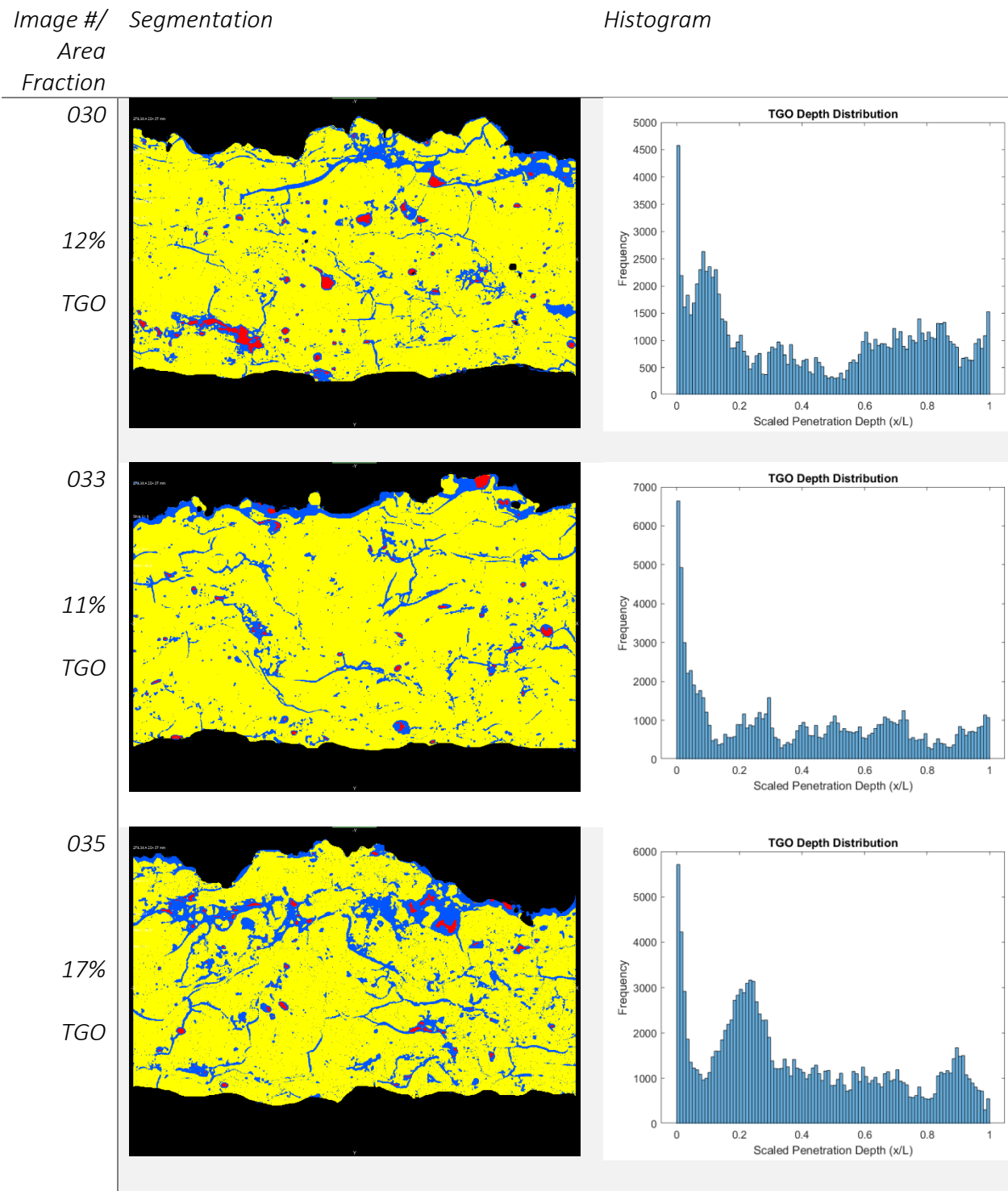
9.2.1 0%B RBSiC Sample- Keiser Rig Exposure



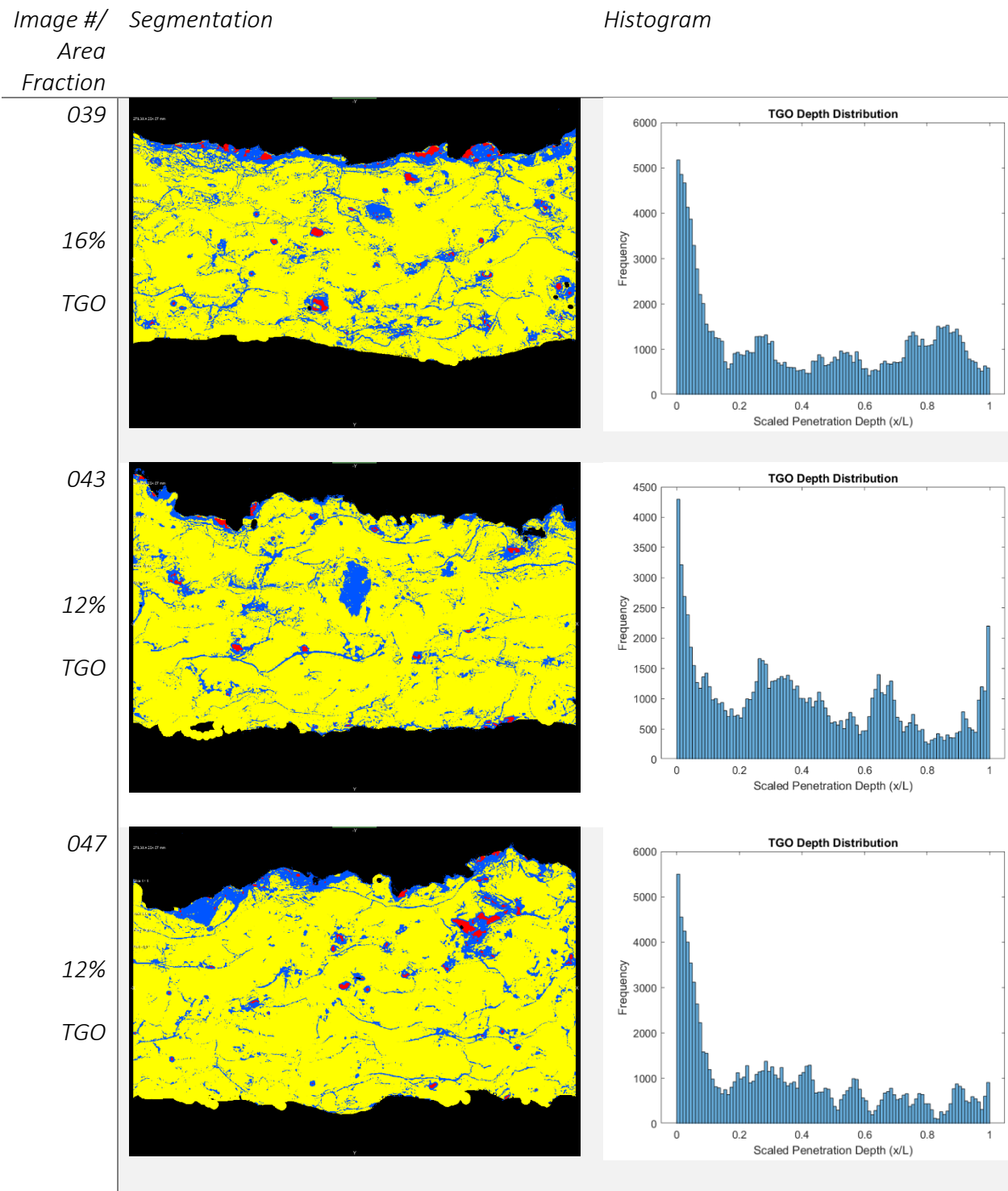
9.2.2 0%B RBSiC Sample- TGA Exposure



9.2.3 4%B RBSiC Sample- Keiser Rig Exposure

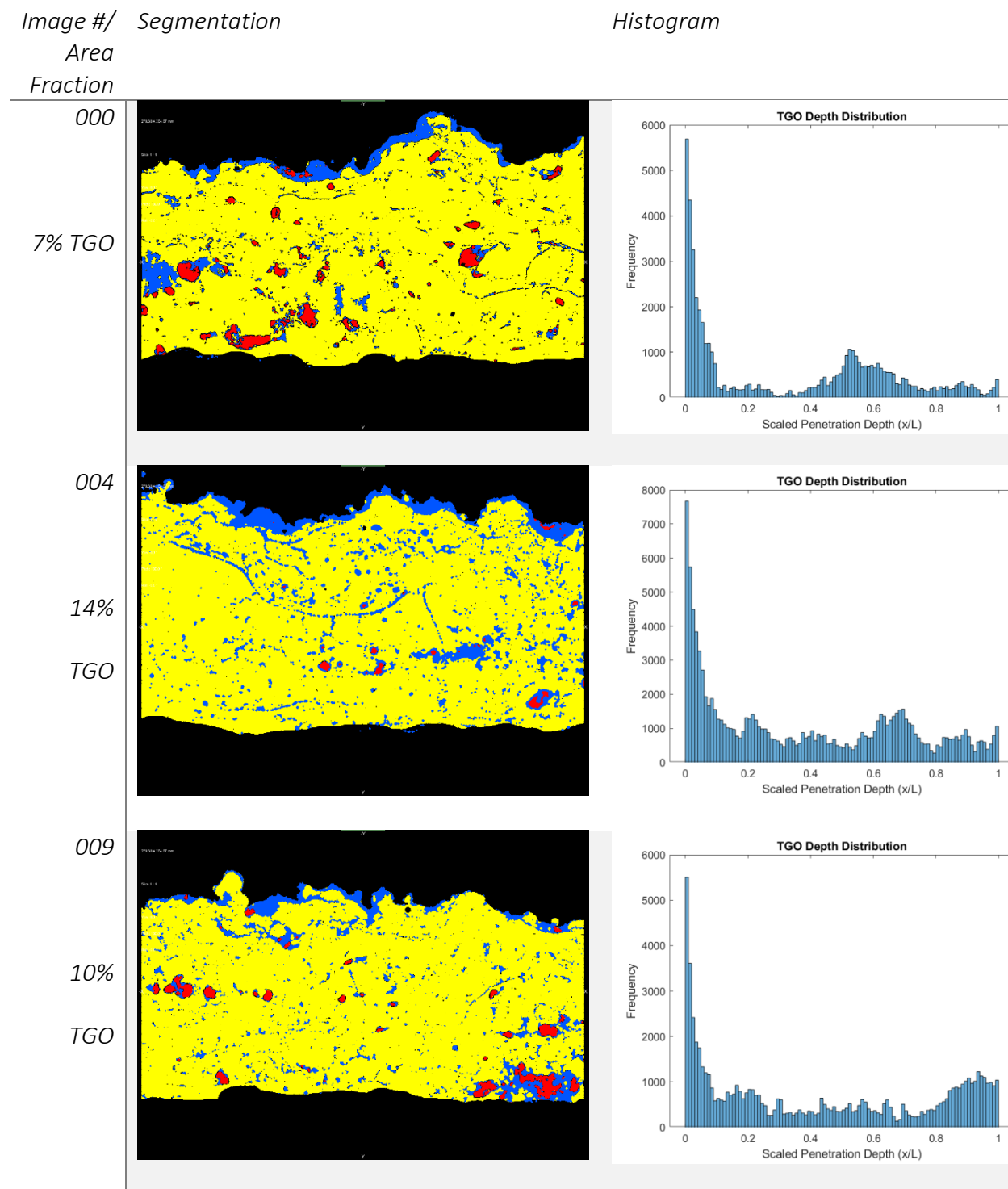


9.2.4 4%B RBSiC Sample- TGA Exposure

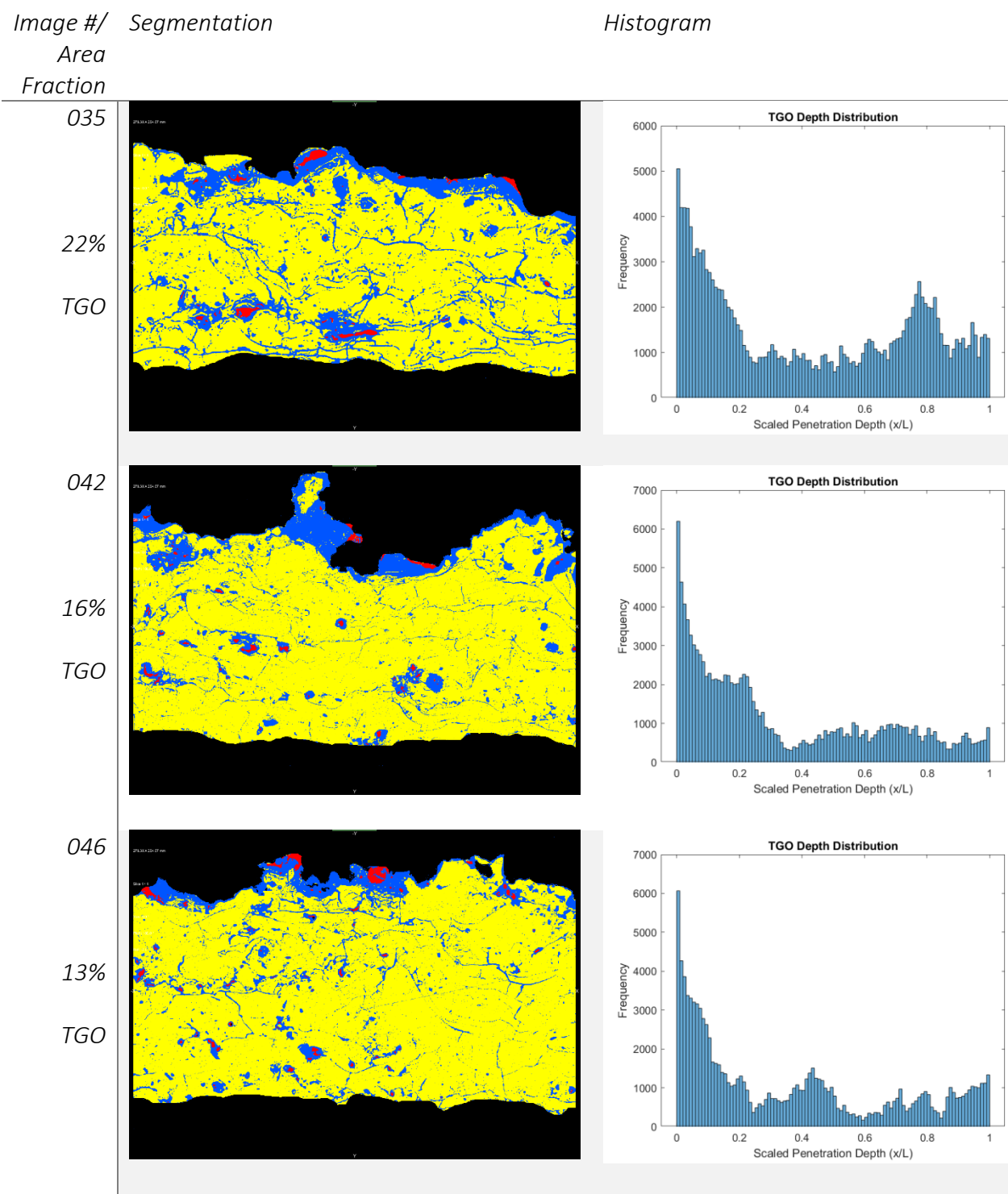


9.3 1200°C Exposures, 100h 1 atm O₂

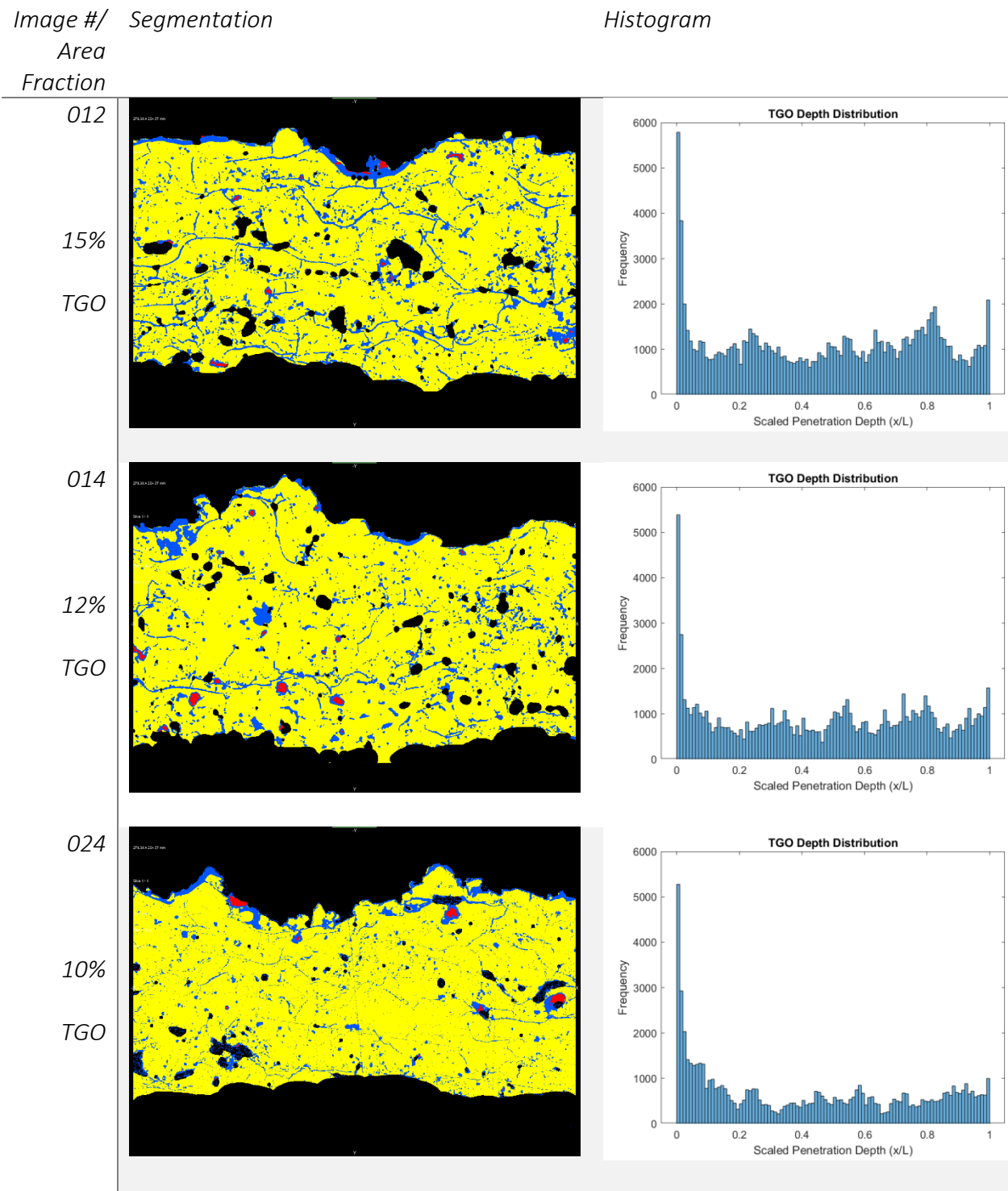
9.3.1 0%B RBSiC Sample- Keiser Rig Exposure



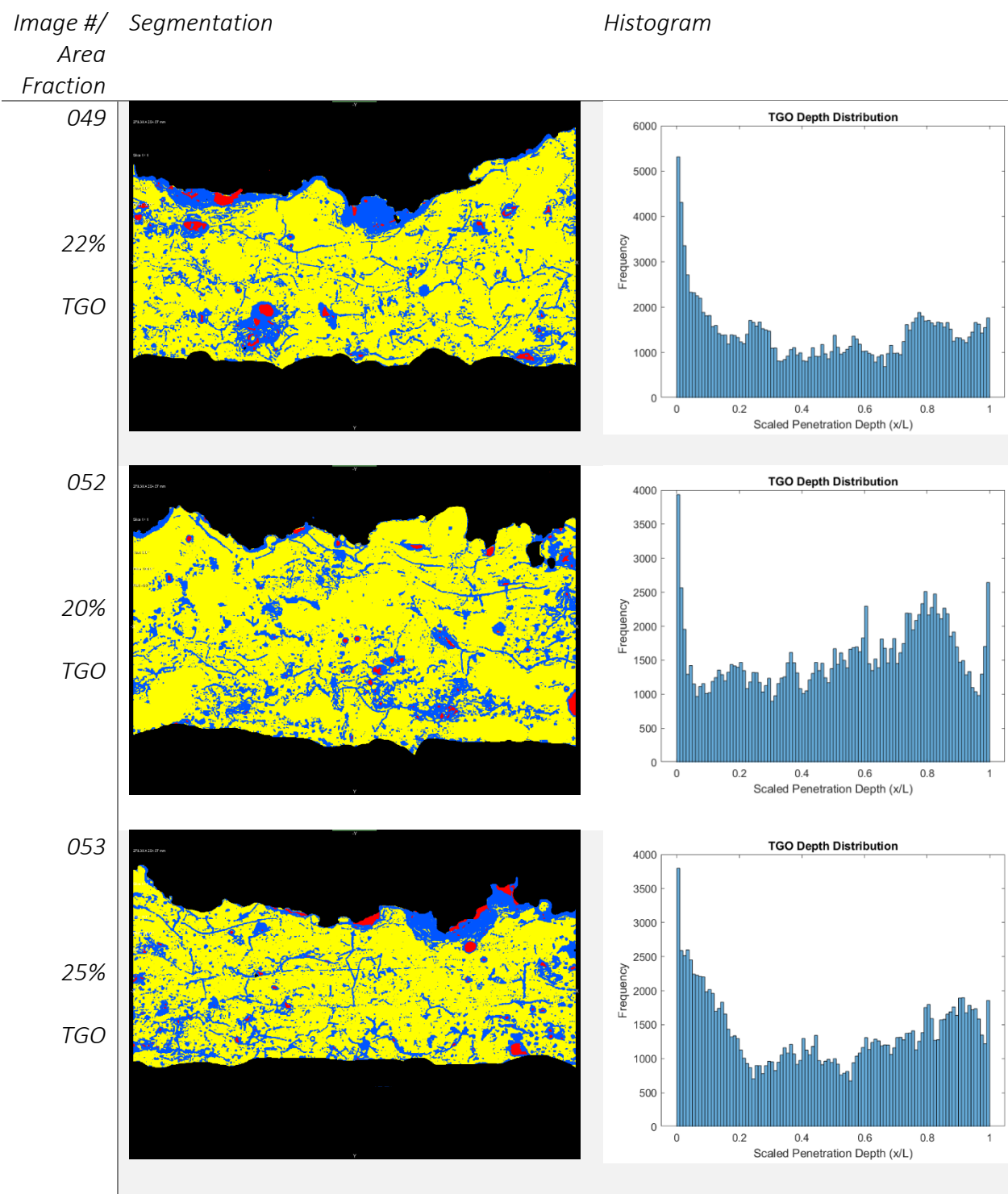
9.3.2 0%B RBSiC Sample- TGA Exposure



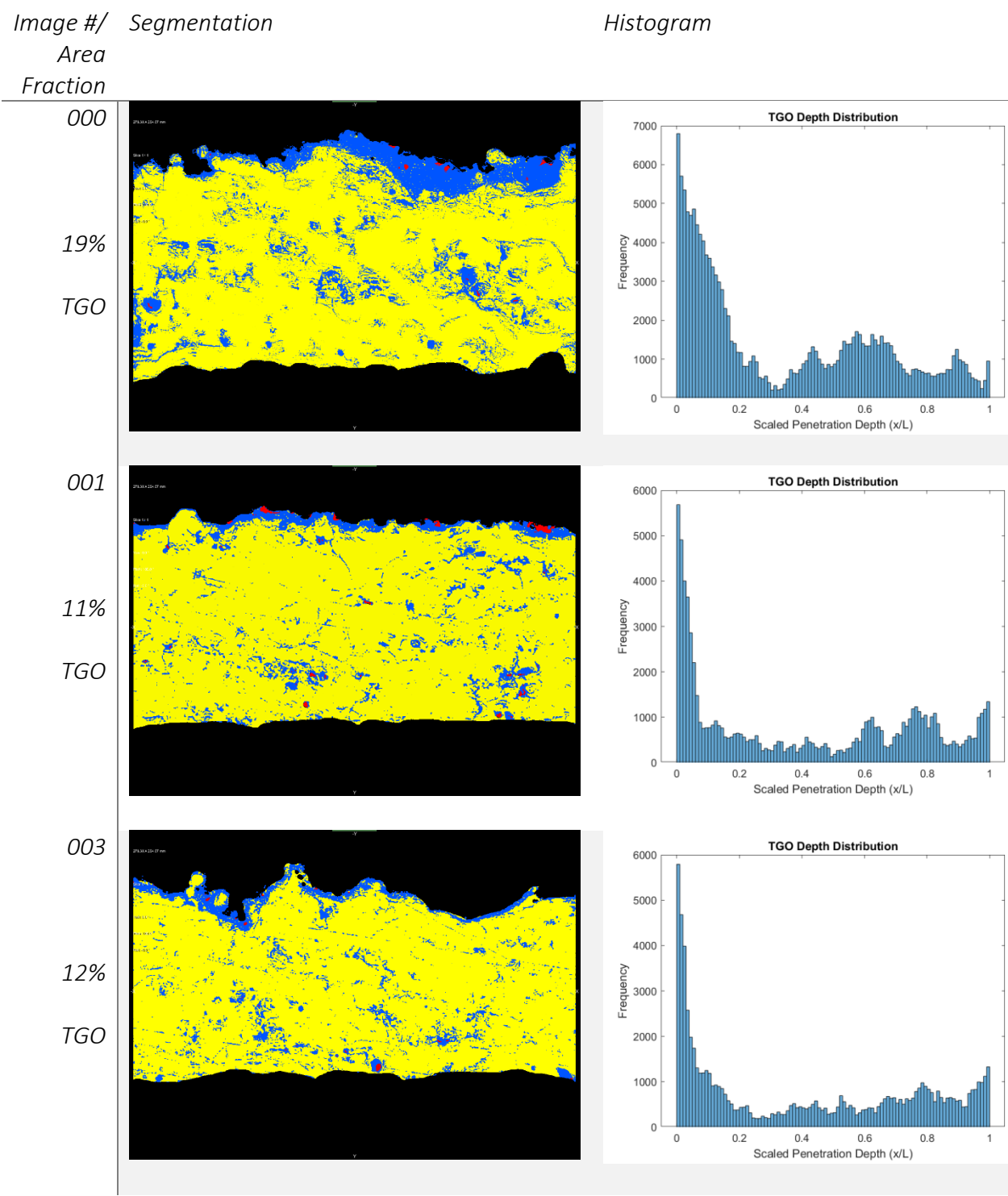
9.3.3 4%B RBSiC Sample- Keiser Rig Exposure



9.3.4 4%B RBSiC Sample- TGA Exposure



9.3.5 CMC Sample- Keiser Rig Exposure



9.3.6 CMC Sample- TGA Exposure

